Multigap superconductivity at oxide interfaces

Guilhem Saïz

PSL UNIVERSITÉ PARIS

THÈSE DE DOCTORAT
DE L'UNIVERSITÉ PSL

Préparée à l'ESPCI Paris, au LPEM

Multigap superconductivity at oxide interfaces

Supraconductivité multi-condensat à l'interface d'oxydes

Soutenue par

Guilhem SAÏZ

Le 26 septembre 2022

École doctorale n°564

Physique en Ile-de-France

Spécialité

Physique

Composition du jury :

Etienne JANOD Université de Nantes	*Président du jury* *Rapporteur*
Laurence MÉCHIN ENSI Caen	*Rapporteur*
Roberta CITRO Université de Salerne	*Examinateur*
Claire MARRACHE-KIKUCHI Université Paris Saclay	*Examinateur*
Nicolas BERGEAL ESPCI Paris	*Directeur de thèse*

ESPCI PARIS | PSL

Remerciement:

Ces quatre années de thèse ont été une opportunité unique de me former au travail de recherche et d'expérimentation scientifique. J'aimerais remercier ici celles et ceux qui m'ont aidé.

Premièrement, je tiens à remercier chaleureusement mon superviseur de thèse, Nicolas Bergeal, dont la pédagogie, la patience et la rigueur intellectuelle sont une inspiration. Je remercie également Jérôme Lessueur et Cheryl Feuillet-Palma pour leur aide concernant mes expériences et leurs résultats ou encore la fabrication d'échantillon en salle blanche. Je remercie également Laurence Méchin ainsi qu'Étienne Janod d'avoir accepté d'être rapporteur du manuscrit ainsi que Roberta Citro et Claire Marrache-Kikuchi pour leur examen critique.

Je souhaite également remercier nos nombreux collaborateurs, à commencer par Gyanendra Singh, qui m'a accompagné durant le stage d'avant thèse ainsi qu'au début de la thèse, m'a formé sur les mesures micro-ondes et leurs analyses avec pédagogie. Je remercie Gervasi Herranz d'avoir fabriqué les échantillons de LAO/STO(110) au coeur de ce manuscrit, ainsi que Édouard Lesnes et Andréa Caviglia qui nous ont fourni les deux échantillons de LAO/STO(111) étudié dans cette thèse. Enfin, je tiens à remercier l'équipe Oxitronics de l'UMR CNRS-Thales, dirigé par Manuel Bibes, qui nous a fourni de nombreux échantillons de LAO/STO, AlO_x/STO, AlO_x/KTO et Gd/STO. Pami ses membres, je tiens à remercier Luis Moreno, Julien Bréhin et Malik Srijani qui ont fabriqué de nombreux échantillons. Je souhaite remercier également Marco Salluzzo et Daniela Stornaiuolo pour leur fabrication d'échantillons. Je tiens à remercier les collaborateurs de la Sapienza pour leur support théorique concernant l'analyse des mesures micro-ondes et de champs critique du multicondensat dans LAO/STO(110): Marco Grilli, Sergio Caprara et Lara Benfatto. Enfin, je remercie le groupe de Ingrid Martif, à Halle, ainsi que Annika Johansson et Börgue Göbel pour leur support théorique concernant les analyses de données de magnétorésistance.

La recherche dans l'équipe PHASME ne serait pas complète sans le travail de ses doctorants, post doctorant et ingénieur de recherche. À ce titre, je remercie Paul Amari pour qui Labview n'a aucune limite et qui a finalement réussi à trouver ses photons uniques, François Couedo pour avoir passé du temps à m'expliquer la calibration micro-onde entre autres, ainsi que Gerbold Ménard qui a été un soutien considérable pour les expériences et analyses de données -je te souhaite une riche carrière de chercheur, et finalement Etienne Maréchal toujours curieux et ouvert à la discussion. Je remercie également Eliana Recoba Pawlowski, Zoé Velluire, Sergei Koslov et Hugo Witt et je souhaite aux trois dernières une bonne fin de thèse et poursuite du travail de l'équipe.

Je remercie également les autres membres du LPEM : Dimitri, Stéphane, Sergio, et Arthur pour les riches discussions de géopolotique le midi, Marie-Claude et Sophie dont le support est indispensable, Francis toujours capable de résoudre les problèmes techniques, et bien d'autres : Zhuoying, Luca... Désolé pour ceux que j'oublie de citer. Enfin je remercie les membres de mon comité de suivit de thèse pour leur questions toujours pertinente et leurs encouragements: mon parrain Alexandre Zimmers ainsi que mon tuteur Marco Aprili du LPS à Orsay.

Je remercie particulièrement les relecteurs de ce manuscrit, à commencer par Nicolas et Gerbold, j'espère que vous n'aurez plus à corriger autant de "s" à l'avenir. Je remercie également ma soeur Cécile qui a du corriger les fautes d'anglais d'une thèse dont elle n'a probablement pas compris grand chose. Enfin je remercie à nouveau Claire dont les corrections sur l'ensemble du manuscrit le rendent bien meilleur.

Mon amour pour la physique a été entretenu par des enseignants passionnés : Kamel Boukheddaden de l'UVSQ, Elias Khan, Jean-Marcel Rax, Julien Bobroff et Andrès Santander, du magistère de physique d'Orsay, qui, avec Shamashis Sengupta, m'ont initié à la mesure de gaz 2D. Et enfin les enseignant du M2 ICFP Florent Perez, Valia Voliotis, Fabrice Bert... Je remercie tous ces professeurs qui ont su me donner le goût de la physique et répondre à mes questionnements.

Je remercie ma famille, mes parents Catherine et Stéphan qui m'ont toujours encouragé à poursuivre mes rêves et grâce à qui je suis allé si loin, et mes soeurs Cécile et Noémie avec qui passer un moment est toujours un plaisir, comme avec ma famille toulousaine.

Enfin, je remercie mes amis à commencer par le #1, Massine, avec qui j'ai traversé le M2 ICFP ainsi que la thèse, qui m'inspire par la qualité de son travail. Je remercie également Tiphaine, avec qui j'ai traversé presque tout mon cursus du secondaire, je me souviendrais toujours de nos soirées révisions intensives. Je remercie enfin mon amour, Juliette, qui partage ma vie depuis plus de 2 ans, tu m'as transmis ta joie de vivre et ton gout de l'organisation, chaque jour avec toi est un bonheur. ⊛

Résumé:

L'interface $LaAlO_3/SrTiO_3$ (LAO/STO) est connue pour héberger un gaz d'électrons bidimensionnel (2DEG) supraconducteur. Ce gaz a été un terrain de jeu pour l'étude d'oxydes fonctionnels ces dernières années car il abrite divers phénomènes physiques, tels qu'un fort couplage spin-orbite Rashba, de la supraconductivité et une conductivité multibande, entre autres. La densité de porteurs de charge du 2DEG aux interfaces de $SrTiO_3$ peut être contrôlée par effet de champ électrique, qui à son tour influence d'autres propriétés telles que le potentiel de confinement, le couplage Rashba et, plus interessant encore, la température critique de supraconductivité formant un dôme en fonction du dopage. Dans ce manuscrit, nous discutons des propriétés de transport controlable par tension de grille du 2DEG formé aux interfaces des hétérostructures impliquant les matériaux paraélectriques quantiques $SrTiO_3$ ou $KTaO_3$, dont la croissance est réalisée selon différentes orientations cristallines. Des mesures de transport dc et radiofréquence ont été réalisées dans un réfrigérateur à dilution jusqu'à 20mK, sous champ magnétique et avec application d'une tension de grille.

Le chapitre introductif traite des concepts de supraconductivité qui seront utilisés tout au long du manuscrit, tel que l'équation auto-cohérente du gap, ou la théorie Mattis-Bardeen de la conductivité complexe à frequence finie. Dans une deuxième partie, les propriétés électroniques et structurales des cristaux de $SrTiO_3$ seront discutées pour décrire leur influence sur le gaz 2D. Enfin, nous abordons les propriétés électroniques des gaz bidimensionnels aux hétéro-interfaces de $SrTiO_3$ dans les différentes orientations du substrat (i.e. (001) (110) (111)).

Le second chapitre décrit le système expérimental electronique et cryogénique nécessaire aux mesures présentées par la suite. Des concepts relatifs au transport dc et radiofréquence sont abordés, en particulier le montage experimental pour les mesures résonantes micro-ondes de rigidité de phase est détaillé.

Dans le troisième chapitre, nous décrivons les mesures de transport contrôlable par tension de grille, telles que la température critique (T_c) du supraconducteur, le champ magnétique critique (H_{c2}) et la densité de porteurs des interfaces LAO/STO(110) et LAO/STO(111). Nous décrivons ensuite les mesures par micro-ondes résonantes de la rigidité superfluide, ce qui nous donne accès aux propriétés supraconductrices fondamentales de ces 2DEGs. Dans LAO/STO(110), les mesures de champs magnetique critiques et les mesures de la rigidité superfluide montrent l'existence d'une supraconductivité à deux condensats au-delà d'un seuil de dopage qui peut être analysée de manière cohérente par deux modèles indépendants. Nous montrons également que les deux condensats interagissent de manière répulsive pour former un état supraconducteur exotique s±-wave et que la diffusion interbande supprime fortement la température critique T_c. Nous démontrons ainsi qu'à l'interface LAO/STO(110), une transition supraconductrice d'un vers deux condensats a lieu de manière continue et réversible en fonction de la tension de grille, ces condensats formant un état supraconducteur s±-wave. Des mesures similaires du champ critique et de la rigidité superfluide dans LAO/STO(111) ont donné des résultats contrastés. Malgré la preuve d'un transport multibande dans l'état normal, aucune signature claire de supraconductivité à plusieurs condensats n'a pu être observée. En particulier, la dépendance en température des champs magnetique critique est en accord avec un modèle à un seul condensat. Néanmoins des limites sur les paramètres des éventuels deux condensats (coefficients de diffusivité, gap) peuvent être tirés de cette absence de signature d'une supraconductivité multigap. Concernant la rigidité de phase, bien qu'une déviation du modèle BCS soit visible à fort dopage, il n'est pas possible de la reproduire avec

le modèle multigap utilisé pour l'interface LAO/STO(110). Dans les deux orientations, les mesures de rigidité superfluide sont comparées aux prédictions de la théorie conventionnelle BCS/Mattis-Bardeen. Dans ce chapitre, le rôle de l'orientation du substrat sur la structure de bande et les propriétés supraconductrices du gaz d'électrons sont discutés à la lumière des résultats bien connus pour l'interface conventionnelle LAO/STO(001).

Dans le quatrième chapitre, nous analysons le transport non-réciproque de la magnétorésistance anisotrope (AMR) dans le plan de ces 2DEGs (LAO/STO(110) et LAO/STO(111)) comme une sonde pour l'interaction spin-orbite. Nous détaillons l'effet Rashba-Edelstein par lequel un courant de charge est convertie en une polarisation de spin, et ses prédictions sur l'AMR. La magnétorésistance quadratique (QMR) et bilinéaire (BMR) dérivée de ce transport non-réciproque est systématiquement mesurée en fonction du champ magnétique, de la tension de grille et du courant de polarisation. Nos résultats sont comparés aux travaux précédents sur l'interface LAO/STO(001). À partir de la magnétorésistance quadratique, on extrait un temps de diffusion élastique qui est comparable à celui attendu à partir d'un modèle de Drude parabolique. Enfin, le ratio de la BMR et de la QMR permet d'extraire une constante de couplage Rashba effective, dont l'évolution en fonction de la tension de grille est discutée. Nous montrons également que la magnétorésistance anisotrope dans le plan peut être utilisée comme un outil pour observer une transition de Lifschitz dans LAO/STO(110) à partir des données de QMR normalisées.

Dans le dernier chapitre, nous discutons des propriétés de nouvelles interfaces d'oxydes supraconducteurs, fabriquées par un simple dépôt d'aluminium donnant lieu à la formation d'un gaz 2D à la surface d'un cristal de STO ou KTO. Nous rapportons d'abord la supraconductivité contrôlable par tension de grille à l'interface AlO_x/STO aux travers de mesures de la résistance et les champs critiques. Nous montrons que l'interface AlO_x/STO est un substitut de 2DEG aux applications prometeuses car sa méthode de fabrication par pulvérisation est plus facile que la croissance épitaxiale par laser pulsé de LAO. Ensuite, nous présentons des résultats sur le 2DEG supraconducteur récemment découvert dans les interfaces à base de $KTaO_3$(111). Nous montrons que le 2DEG à l'interface AlO_x/KTO(111) est similaire à celui de LAO/KTO(111) de la littérature. Nous présentons les mesures de propriétés de transport telles que la résistance, l'effet Hall, et les champs critiques. Contrairement à LAO/STO, aucune trace de transport multibande n'est présente. Nous discutons enfin de la mesure de la rigidité de phase d'un échantillon d'AlO_x/KTO(111), ces dernières étant étudiées à la lumière de la théorie de Berezinskii Kosterlitz Thouless.

Summary:

The $LaAlO_3/SrTiO_3$ (LAO/STO) interface is known to host a superconducting two-dimensional electron gas (2DEG). This gas has been a playground for the study of functional oxide materials in recent years as it harbours various physical phenomena, such as a strong Rashba spin-orbit coupling, superconductivity and multiband conductivity, among others. The 2DEG carrier density in the $SrTiO_3$-based interfaces can be controlled by electric field effect, which in turn influences other properties such as the confining potential, the Rashba coupling and, most importantly, the critical temperature that exhibits a dome shaped variation upon doping. In this manuscript, we discuss the gate voltage-tunable transport properties of the 2DEG formed at the interfaces of heterostructures involving $SrTiO_3$ or $KTaO_3$ quantum paraelectric materials, in different crystal orientations. DC and RF transport measurements were performed in a dilution refrigerator downt to 20mK, under magnetic field and applied gate voltage.

The introductory chapter is dedicated to the concepts of superconductivity that will be used throughout the manuscript, such as the self-consistent gap equation, or the Mattis-Bardeen theory of complex conductivity at finite frequency. In a second part, the electronic and structural properties of the bulk $SrTiO_3$ will be discussed to describe their influence on the 2D gas. Finally, we discuss the electronic properties of the two-dimensional gas at the heterointerfaces of $SrTiO_3$ in the different orientations of the substrate (i.e. (001) (110) and (111)).

The second chapter describes the electronic and cryogenic set-up required for the measurements presented here. Concepts related to dc and radio frequency transport are discussed, in particular the setup for microwave resonant phase stiffness measurement is detailed.

In the third chapter, we report the gate voltage-tunable transport measurements, such as the critical temperature (T_c) of the superconductor, the critical magnetic field (H_{c2}) and the carrier density of the LAO/STO(110) and LAO/STO(111) interfaces. We then describe the resonant microwave measurement of the superfluid stiffness, which gives us access to the fundamental superconducting properties of these 2DEGs. In LAO/STO(110), gate voltage-tunable critical fields and superfluid stiffness measurements show the existence of two-condensate superconductivity above a doping threshold that can be analyzed consistently by two independent models. We also show that the two condensates interact repulsively to form an exotic s±-wave superconducting state and that interband scattering strongly suppresses the critical temperature T_c. We thus demonstrate that at the LAO/STO(110) interface, a superconducting transition from one to two condensates takes place in a continuous and reversible manner as a function of the gate voltage, with these condensates forming a s±-wave superconducting state. Similar measurements of the critical field and superfluid stiffness in LAO/STO(111) have given contrasted results. Despite evidence of multiband transport in the normal state, no clear signature of multicondensate superconductivity could be observed. In particular, the temperature dependence of the critical magnetic field is more consistent with a single-condensate model. Nevertheless limitations on the parameters of the possible two condensates (diffusivity coefficients, superconducting gaps) can be drawn from this lack of signature of multigap superconductivity. Concerning the phase rigidity, although a deviation from the BCS model is visible at high doping, it cannot be reproduced with the multigap model used for the LAO/STO(110) interface. In both orientations, the superfluid stiffness measurements are compared with the predictions of the conventional BCS/Mattis-Bardeen theory. In this chapter, the role of the substrate orientation on the band structure and the superconducting properties of the electron gas are discussed in the light of the well-known

results on the conventional LAO/STO(001) interface.

In the fourth chapter, we analyse the non-reciprocal transport of anisotropic magnetoresistance (AMR) in the plane of these 2DEGs (LAO/STO(110) and LAO/STO(111)) as a probe for the spin-orbit interaction. We detail the Rashba-Edelstein effect by which the Rashba coupling at the interface generates charge to spin conversion, and its predictions on the AMR. The quadratic (QMR) and bilinear (BMR) magnetoresistance derived from this non-reciprocal transport is systematically measured as a function of magnetic field, gate voltage and bias current. Our results are compared with previous work on the LAO/STO(001) interface. From the quadratic magnetoresistance, an elastic scattering time is extracted which is comparable to that expected from a parabolic Drude model. Finally, the ratio of BMR and QMR allows the extraction of an effective Rashba coupling constant, whose evolution with the gate voltage is discussed. We also show that the in-plane anisotropic magnetoresistance can be used as a tool to observe a Lifschitz transition in LAO/STO(110) from the normalised QMR data.

In the last chapter, we discuss the properties of new superconducting oxide interfaces, fabricated by a simple deposition of an Al layer that generates a 2DEG at the surface of a STO or KTO crystals. We first report on the gate voltage tunable superconductivity at the AlO_x/STO interface, through measurement of the resistance and critical magnetic fields. We show that the AlO_x/STO interface is a promising 2DEG substitute for future applications because its sputtering fabrication method is easier than the pulsed laser grow of crystalline LAO. Next, we present results on the recently discovered superconducting 2DEG in $KTaO_3$(111)-based interfaces. We show that the 2DEG at the AlO_x/KTO(111) interface is similar to that of LAO/KTO(111) from the literature. We present measurements of transport properties such as resistance, Hall effect, and critical fields. In contrast to LAO/STO, no multiband transport signatures are present. Finally, we discuss the measurement of the superfluid stiffness of an AlO_x/KTO(111) 2DEG an analyse the results in the light of the Berezinskii Kosterlitz Thouless theory.

Introduction

For decades, semi conducting interfaces have powered the world to achieve technological progress in a vast number of fields. However, the semi-conductor based devices have intrinsic limitations which could be surpassed by spin-based and superconducting devices. Hence, scientists had been searching for new candidates to replace semiconductors in certain applications. In this context, oxide-based 2DEGs have been investigated for years now, and the LAO/STO system is considered as a benchmark in the field. Indeed, STO-based 2DEGs can exhibit many quantum orders such as superconductivity, ferroelectricity, Rashba spin-orbit interaction, and their properties can be continuously tune *via* the application of a gate voltage. The realization of structures similar to those in semiconductors using oxide interfaces is exciting, as it was suggested that topological superconductivity can occur under certain conditions. The non-trivial topological state could then be used as a basis for quantum computers.

Doped bulk strontium titanate ($SrTiO_3$) has been known to be superconducting in a large doping range for more than 50 years. It was only in 2004 that a highly mobile 2DEG was found at its interface with another insulator (Lantanum aluminate LAO), and a few years later that it was found to be superconducting with a $T_c \approx 300\,mK$. Due to its very large dielectric constant, the carrier density of 2DEGs at STO interfaces can be tune by up to $\pm$50%. The unique combination of superconductivity and strong spin orbit coupling both tunable with a gate voltage makes STO-based 2DEGs one of the most exotic 2D system which have consequently became a playground to study functional oxide interfaces.

Despite being intensively studied, STO-based 2DEGs have raised questions which have been left unanswered so far. Superconductivity in these 2D systems are in a peculiar regime, the anti-adiabatic limit, and the exact pairing mechanism for superconductivity remains unknown. The dome-shaped phase diagram of the superconducting transition temperature upon doping is also debated. Adding to the complexity, several different mechanism are proposed to explain the 2DEG formation, and each of them being different we can assume that the resulting 2DEG properties are likely to depend on the sample preparation method. Finally, a point of interest addressed in this thesis is the influence of the crystal orientation on the 2DEG properties.

The purpose of this thesis is to examine the transport properties of LAO/STO interfaces grown along orientations different than that of the conventional LAO/STO(001), with the intent of studying the band engineering *via* cristal orientation. In this regard, we present results from both LAO/STO(110) and LAO/STO(111) interfaces. Other oxide 2DEGs such as AlO_x/STO(001) or the more recent superconducting $AlO_x/KTaO_3$(111) interface are also discussed. Transport measurements at dc and radiofrequency have been performed in a dilution fridge down to 20 mK under magnetic field and back gate voltage.

In the first chapter we introduce the reader to the concepts related to superconductivity which will be used throughout the manuscript. We then discuss the bulk $SrTiO_3$ electronic properties before reviewing LAO/STO 2DEG's origin, electronic band structure and superconducting properties. In the second chapter, we detail the experimental cryogenic and electrical set-up for dc and radiofrequency measurements of the 2DEGs.

The third chapter addresses the normal and superconducting properties of sample at the unconventional (110) and (111) interfaces, namely the LAO/STO(110) and LAO/STO(111) interface. We report gate-tunable transport measurements such as the superconducting T_c, the superfluid stiffness J_s, the upper critical magnetic field H_{c2}, and the carrier density of LAO/STO(110) and LAO/STO(111) 2DEGs. Both orientations show multiband physic in the normal state, and their normal transport properties are discussed in the framework of a tight binding band structure. Regarding the superconducting state however, while the superfluid stiffness and critical field measurements for the

LAO/STO(110) interface show unambiguous multicondensate superconductivity, the same is not true for the LAO/STO(111) interface. In both orientations, the superfluid stiffness measurements are compared with predictions from the conventional BCS/Mattis-Bardeen theory. We conclude this part on the role of the substrate orientation on the band structure and the electron gas superconducting properties by comparing our results to the well-known properties of the conventional LAO/STO(001) interface.

In the fourth chapter, we analyse the non-reciprocal transport of the in-plane anisotropic magnetoresistance (AMR) of these 2DEGs (LAO/STO(110) and LAO/STO(111)) as a probe for spin-orbit interaction and as a way to qualitatively assess the Fermi surface evolution with back gate voltage. The quadratic and bilinear magnetoresistance derived from the AMR are compared to previous work at LAO/STO(001) interface, and an effective Rashba coupling constant is extracted from these measurements. We also show that the in-plane anisotropic magnetoresistance can be used as a tool to observe a Lifschitz transition in LAO/STO(110).

In the last chapter, we discuss the properties of novel superconducting oxide interfaces. We first report gate tunable superconductivity at the AlO_x/STO interface, which is a promising 2DEG substitute for future applications since its sputtering fabrication method is easier than the pulsed laser growth of the LAO layer. Then, we present results on the recently discovered superconducting 2DEG in $KTaO_3$(111)-based oxide interfaces. Transport properties and superfluid stiffness measurement are studied in light of the Berezinskii Kosterlitz Thouless theory.

Contents

Chapter 1

Two dimensional electron gas at oxides interface

This chapter is divided into three parts. First, we will introduce the reader to the concepts of 2D superconductivity theory which will be used throughout the manuscript: coherence length, superconducting gap, complex conductivity and superfluid stiffness. Secondly, we will discuss the bulk $SrTiO_3$ properties such as its crystal and electronic properties. Lastly, we will review the two dimensional electron gas (2DEG) properties of $SrTiO_3$-based hetero-interface which will provide the framework to analyze the measurements presented in this manuscript.

1.1 2D Superconductivity

1.1.1 Ginzburg-Landau theory

Free energy The Ginzburg-Landau theory is a phenomenological description of a superconductor thermodynamics. It was shown by Gor'kov that it constitute a limiting case of the BCS theory close to T_c and when spatial variation of the order parameter ψ are small. The free energy f in the Ginzburg-Landau theory is expressed as a even power of the order parameter ψ. Including only the first two terms necessary to take into account the phase transition, it is expressed as :

$$f = \overbrace{f_{n0} + \frac{h^2}{8\pi}}^{\text{Normal free energy}} \overbrace{+\alpha|\psi|^2 + \beta|\psi|^4 + \frac{1}{2m^*}\left|\left(\frac{\hbar}{i}\vec{\nabla} - \frac{e^*}{c}\vec{A}\right)\psi\right|^2}^{\text{Superconducting free energy}} \tag{1.1}$$

Where α and β are phenomenological temperature-dependant parameters. It is useful to define $|\psi_\infty|^2 = -\alpha/\beta$ with $\alpha < 0$ corresponding to the order parameter deep in the bulk, in the absence of field or gradient. α is considered to be $\alpha(T) = \alpha_0(T - T_c)$, and β is a positive constant. A representation of the Ginzburg-Landau free energy potential is shown in figure 1.1**a.** When there is a magnetic field (potential vector $\vec{A}$) or a spatial variation, the last term of eq. 1.1 plays a role and variational method leads to the equation:

$$\alpha\psi + \beta|\psi|^2\psi + \frac{1}{2m^*}\left(\frac{\hbar}{i}\vec{\nabla} - \frac{e}{c}\vec{A}\right)^2\psi = 0 \tag{1.2}$$

Coherence length in the absence of field When $\vec{A} = \vec{0}$, equation 1.2 can be rewritten in term of the normalized order parameter $f = \psi/\psi_\infty$ as :

$$\xi^2(T)\frac{d^2f}{dx^2} - f + f^3 = 0 \quad \text{where} \quad \xi^2 = \frac{\hbar^2}{2m^*|\alpha(T)|} \tag{1.3}$$

ξ is the Ginzburg-Landau coherence length, the typical scale over which ψ does not vary appreciably. It can be thought of as the typical size of a Cooper pair which is typically much larger than the interatomic distance.

Linearized equation When the magnetic field is close to the critical field of the superconductor, in agreement with the definition of $|\psi_\infty|$ and since $|\psi|^2 \ll |\psi_\infty|^2$ we can drop the β term of equation 1.2:

$$\left(\frac{\vec{\nabla}}{i} - \frac{2\pi\vec{A}}{\phi_0}\right)^2 \psi = \frac{1}{\xi^2}\psi \tag{1.4}$$

where $\phi_0 = \frac{ch}{2e}$ is the magnetic flux quantum.

Critical field We need to solve equation 1.4 for an applied field which vector potential $\vec{\nabla} \wedge \vec{A_z} = \vec{H_z}$ in order to find what is the field at which superconductivity can start to nucleate :

$$\left[-\nabla^2 + \frac{4\pi i}{\phi_0} H_z \frac{\partial}{\partial z} + \left(\frac{2\pi H}{\phi_0}\right)^2 x^2\right] \psi = \xi^{-2}\psi \tag{1.5}$$

It is justified to assume solution of the form $\psi = e^{ik_x x} e^{ik_y y} g(z)$. Then,

$$-g''(z) + \left(\frac{2\pi H_z}{\phi_0}\right)^2 (x - x_0)^2 g(z) = \left(\frac{1}{\xi^2} - k_y^2\right) g(z) \tag{1.6}$$

where $x_0 = \frac{k_z \phi_0}{2\pi H}$. Equation 1.6 is the Schrödinger equation of a particle in an harmonic oscillator of constant force $F = \left(\frac{2\pi H}{\phi_0\sqrt{m^*}}\right)^2$ whose eigens energies are

$$\epsilon_n = (n + \frac{1}{2})\hbar\omega_c \tag{1.7}$$

where $\omega_c = \hbar\frac{2eH}{m^* c}$ is the cyclotron frequency of the charge in the field H. Comparing eq. 1.6 and eq. 1.7, we have :

$$H = \frac{\phi_0}{2\pi(2n+1)}\left(\frac{1}{\xi} - k_y^2\right) \tag{1.8}$$

Which is maximum for n=0 and k_y = 0, thus we can define the upper critical magnetic field H_{c2} as

$$\boxed{H_{c2}(T) = \frac{\phi_0}{2\pi\xi^2(T)}} \tag{1.9}$$

H_{c2} corresponds to the value of applied magnetic field at which there is no room for any additional magnetic flux quantum to be passed through without destroying the superconducting order. At $T = 0$, $H_{c2}(T = 0) = \frac{\phi_0}{2\pi\xi_0}$. Measuring H_{c2} is a direct way to extract the Ginzburg-Landau coherence length and equation 1.9 will be often used in this manuscript, in particular to assess whether a 2DEG is in the dirty limit by comparing it to the mean free path l_{MFP} (dirty limit : $\xi \gg l_{MFP}$). In practice, it is expected that all true 2DEGs are more frequently dirty than bulk superconductor because of dimensionality considerations. A representation of ξ, as well as the London penetration length, at a normal-superconductor interface under a magnetic field is shown in figure 1.1**b.**

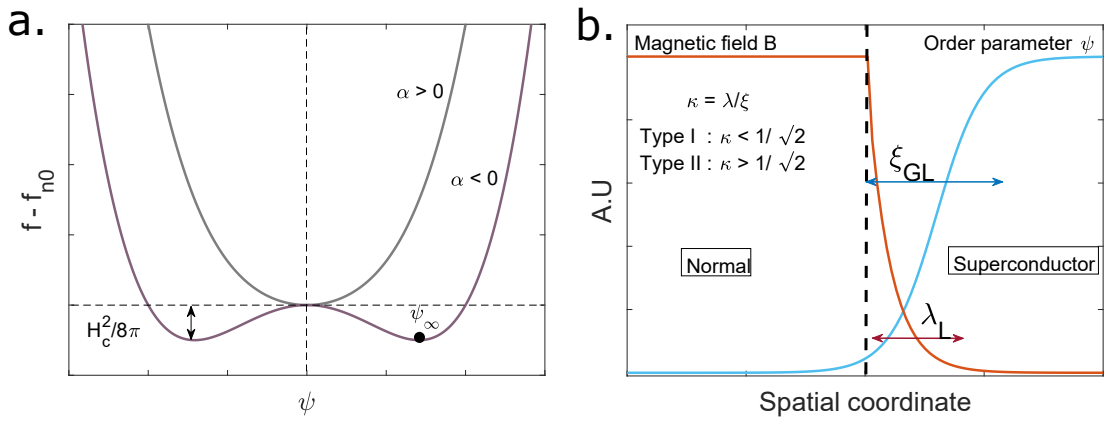

Figure 1.1: **a.** Superconducting free energy f_s in the Ginzburg-Landau theory (from eq. 1.1). $\beta > 0$. For $\alpha < 0$ the minimum of f_s is at order parameter ψ_∞. **b.** Schematic of the magnetic field screened over the London penetration length and the order parameter decaying over the Ginzburg-Landau coherence length.

1.1.2 London equations

In 1935, the London brothers proposed a system of two equations describing the dependence of the supercurrent j_s upon an applied electric E and magnetic field B:

$$\begin{cases} \frac{\partial}{\partial t}(\Lambda \vec{j_s}) = \vec{E} \\ \vec{\nabla} \wedge (c\Lambda \vec{j_s}) = -\vec{B} \end{cases} \tag{1.10}$$

Λ is a phenomenological parameter which relates to the London penetration length λ:

$$\Lambda = \frac{4\pi\lambda^2}{c^2} = \frac{m}{n_s e^2} \tag{1.11}$$

where n_s is the superfluid density, i.e. the density of superconducting carriers (Cooper pairs), c is the velocity of light and e the electron charge. The penetration length λ can be understood as the exponential screening of the magnetic field in the superconductor if we combine the second equation in 1.10 with Maxwell equation $\vec{\nabla} \wedge \vec{B} = \mu_0 \vec{j}$.

$$\vec{\nabla}^2 \vec{B} = \vec{B}/\lambda^2 \tag{1.12}$$

This equation is a main result of the London description of supercurrent because it consistently describes the Meissner effect.

Considering now the first equation in 1.10 and using $\vec{B} = \vec{\nabla} \wedge \vec{A}$ in the Coulomb gauge $\vec{\nabla} \cdot \vec{A} = 0$, as well as the canonical momentum $\vec{p} = (m\vec{v} + e\vec{A}/c)$ we have :

$$\vec{j_s} = -\frac{n_s e^2}{m}\vec{A} = -\frac{1}{L_k}\vec{A} = n_s e\langle \vec{v_s} \rangle \tag{1.13}$$

Which contains both London equations in compact form. $L_k = m/n_s e^2$ is the kinetic inductance

of the Cooper pair. This key quantity will be further discussed in this manuscript when presenting microwave transport measurement in chapter 3.

1.1.3 BCS Theory

BCS Hamiltonian In essence, the BCS theory proposes that electrons at energy $\hbar\omega_D$ around the Fermi sea form bound pairs called Cooper pairs, because any attractive potential V between electron triggers such pairs formation below a certain temperature. ω_D is the Debye energy and represents the maximum energy a phonon can have in the material. The pairing Hamiltonian is :

$$\hat{H}_{BCS} = \sum_{\sigma \mathbf{k}} \epsilon_{\mathbf{k}} c^{\dagger}_{\mathbf{k}\sigma} c_{\mathbf{k}\sigma} + \sum_{\mathbf{k},\mathbf{l}} V_{\mathbf{k},\mathbf{l}} c^{\dagger}_{\mathbf{k}\uparrow} c^{\dagger}_{-\mathbf{k}\downarrow} c_{-\mathbf{l}\uparrow} c_{\mathbf{l}\downarrow} \tag{1.14}$$

Where $c^{\dagger}_{k\sigma}$ is the creation operator of an electron with wave vector k and spin σ satisfying the anticommutation relation $\{c_{k\sigma}, c^{\dagger}_{k'\sigma'}\} = \delta_{k,k'}\delta_{\sigma\sigma'}$ and $\{c_{k\sigma}, c_{k'\sigma'}\} = 0$.

Mean field treatment In the grand-canonical ensemble, which is the framework for systems where the number of electrons is not conserved, and within the mean-field approximation which neglects fluctuations, it can be rewritten :

$$\hat{H}_{MF} = \sum_{\sigma \mathbf{k}} \xi_{\mathbf{k}} c^{\dagger}_{\mathbf{k}\sigma} c_{\mathbf{k}\sigma} + \sum_{\mathbf{k}} \left(\Delta c^{\dagger}_{\mathbf{k}\uparrow} c^{\dagger}_{-\mathbf{k}\downarrow} + \Delta c_{\mathbf{k}\downarrow} c_{-\mathbf{k}\uparrow} \right) \tag{1.15}$$

Where $\xi_k = \epsilon_k - \mu N$ and $N = \sum_{\sigma \boldsymbol{k}} c^{\dagger}_{\boldsymbol{k}\sigma} c_{\boldsymbol{k}\sigma}$.

Bogoliubov-de Gennes Hamiltonian The traditional way to solve eq. 1.15 is to perform a Bogolioubov transformation, where we substitute the electron operator $c_{\boldsymbol{k}\sigma}$ for a Bogolioubov quasiparticule (Bogoliubon) $\chi_{\boldsymbol{k}\sigma}$ which is mixture of an electron and a hole with weight $u_{\boldsymbol{k}}$ and $v_{\boldsymbol{k}}$:

$$\begin{cases} c_{\boldsymbol{k},\uparrow} = u^{*}_{\boldsymbol{k}} \chi_{\boldsymbol{k},\uparrow} + v_{\boldsymbol{k}} \chi_{-\boldsymbol{k},\downarrow} \\ c^{\dagger}_{-\boldsymbol{k},\downarrow} = u_{\boldsymbol{k}} \chi^{\dagger}_{-\boldsymbol{k},\downarrow} - v^{*}_{\boldsymbol{k}} \chi_{\boldsymbol{k},\uparrow} \end{cases} \tag{1.16}$$

We define the energy dispersion of the Bogolioubon as $E_{\boldsymbol{k}} = \sqrt{\xi^2 + |\Delta_{\boldsymbol{k}}|^2}$, shown in figure 1.2**a.**, as a function of k. Substituting eq. 1.16 into eq. 1.15 gives the so-called Bogolioubov de Gennes Hamiltonian:

$$\hat{H}_{BdG} = \sum_{\boldsymbol{k}\sigma} E_{\boldsymbol{k}} \chi^{\dagger}_{\boldsymbol{k}\sigma} \chi_{\boldsymbol{k}\sigma} + E_0 \tag{1.17}$$

Where $E_0 = \sum_k \left(\xi_k + E_k + \Delta_k \langle c^{\dagger}_{\boldsymbol{k}\uparrow} c^{\dagger}_{-\boldsymbol{k}\downarrow} \rangle \right)$ is the ground state energy.

To cancel unwanted term, equation 1.17 is derived under the condition:

$$\chi^{\dagger}_{\boldsymbol{k},\uparrow} \chi^{\dagger}_{\boldsymbol{k},\downarrow} = 0 \qquad \Longleftrightarrow \qquad \frac{v_k}{u_k} = \frac{E_k - \xi_k}{\Delta^{*}_k} \tag{1.18}$$

Also, the normalization of the coefficient u_k and v_k yields:

$$|u_{\boldsymbol{k}}|^2 + |v_{\boldsymbol{k}}|^2 = 1 \qquad \Longleftrightarrow \qquad u_{\boldsymbol{k}}^2 = \frac{1}{2}\left(1 + \frac{\xi_{\boldsymbol{k}}}{E_{\boldsymbol{k}}}\right) \tag{1.19}$$

The gap equation The gap function is defined as :

$$\Delta_{\boldsymbol{k}} = \frac{-1}{N}\sum_{\boldsymbol{k}} V_{\boldsymbol{k}\boldsymbol{k}'}\langle c_{-\boldsymbol{k}\downarrow} c_{\boldsymbol{k}\uparrow}\rangle \tag{1.20}$$

Bogolioubon are fermion-like particules obeying the Fermi-Dirac distribution:

$$\langle \chi^\dagger_{\boldsymbol{k},\uparrow}\chi_{\boldsymbol{k},\uparrow}\rangle = \langle \chi^\dagger_{\boldsymbol{k},\downarrow}\chi_{\boldsymbol{k},\downarrow}\rangle = \frac{1}{e^{\beta E_k}+1} \tag{1.21}$$

Injecting eq. 1.18, 1.19, 1.21 into eq. 1.20 gives the general self consistent gap equation:

$$\Delta_{\mathbf{k}} = -\frac{1}{N}\sum_{\mathbf{k}'} \frac{V_{\mathbf{k},\mathbf{k}'}\Delta_{\mathbf{k}'}}{2E_{\mathbf{k}}} \tanh\left(\frac{E_{\mathbf{k}'}}{2k_BT}\right) \tag{1.22}$$

To go further, we have to make assumptions. For phonon-mediated interactions whose maximum energy is the Debye energy $\hbar\omega_D$, we have $V_{k,k'} = -V_0$ when $|\xi_k| < \hbar\omega_D$. For isotropic gap (s-wave), $\Delta_k = \Delta$. Eq. 1.22 simplifies into:

$$1 = \frac{V_0}{N}\sum_{k<k_D} \frac{1}{2E_k}\tanh\left(\frac{E_{\boldsymbol{k}'}}{2k_BT}\right) \overset{\hbar\omega_D \ll \mu}{\simeq} V_0\rho_F \int_0^{\hbar\omega_D} \frac{d\epsilon}{\sqrt{\epsilon^2+\Delta^2}} \tanh\left(\frac{\sqrt{\epsilon^2+\Delta^2}}{2k_BT}\right) \tag{1.23}$$

Where ρ_F is the density of states per spin at the Fermi level.

At T=0, in the weak coupling limit, i.e $\Delta \ll \hbar\omega_D$, eq. 1.23 gives:

$$\Delta(T=0) = 2\hbar\omega_D e^{-\frac{1}{V_0\rho_F}} \tag{1.24}$$

When $T \to Tc^+$ or equivalently $\Delta \to 0^+$ (the subscript + means approaching from the inferior side)

$$T_c = \frac{2e^\gamma}{\pi}\frac{\hbar\omega_D}{k_B} e^{-\frac{1}{V_0\rho_F}} \tag{1.25}$$

Where $\gamma \simeq 0,577$ is the Euler-Mascheroni constant. Combining eq. 1.24 and 1.25 gives the universal ratio of T_c to Δ of the BCS theory for the weak coupling limit :

$$\frac{\Delta(T=0)}{k_BT_c} = \frac{\pi}{e^\gamma} \simeq 1.76 \tag{1.26}$$

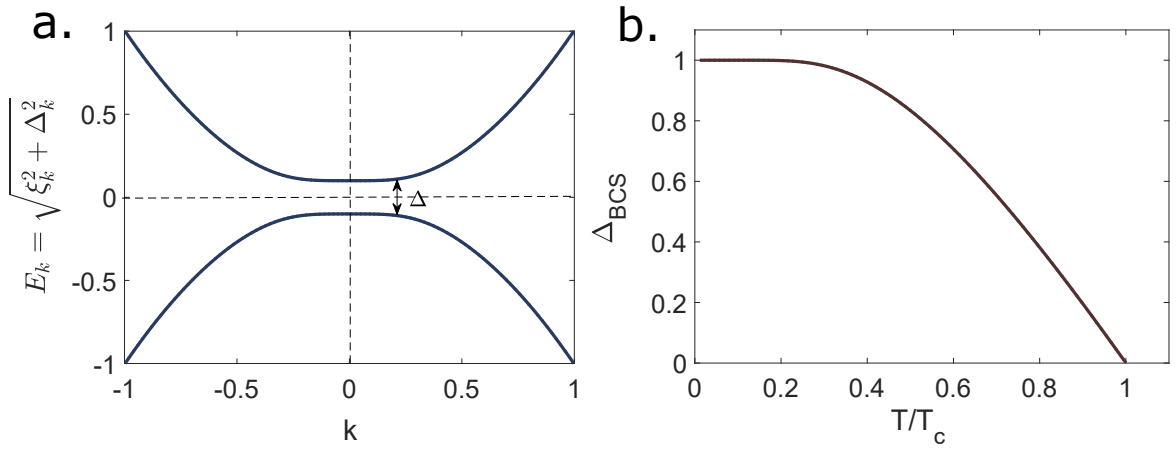

Figure 1.2: **a.** Schematic dispersion relation of Bogolioubons. **b.** Normalized BCS superconducting gap from self consistent gap equation 1.22

Anti-adiabatic limit In eq. 1.23, we have used the adiabatic limit, i.e $\hbar\omega_D \ll \mu$ or without lost of generality in our studies $\hbar\omega_D \ll \epsilon_F$, where E_F is the Fermi energy. In such limit, the cut-off parameter for Cooper pairs is the Debye energy ω_D which appears in eq. 1.23 as a limit in the integral.

However, the opposite limit also exists, the anti-adiabatic limit $\hbar\omega_D \gg \epsilon_F$ and the intermediate regime $\hbar\omega_D \approx \epsilon_F$ as well. Superconductivity in Strontium titanate is a textbook example of such anti-adiabatic limit because in very low doped bulk material, its superconductivity is such that $\hbar\omega_D \gg \epsilon_F$. In this limit, the Fermi energy becomes the cut-off energy and eq. 1.25 becomes

$$T_c = \mathbb{C}\ \epsilon_F e^{-\frac{1}{V_0 \rho_F}} \tag{1.27}$$

Where $\mathbb{C}$ is a constant of the order of unity. This "unconventional" superconductivity is characterized by the absence of the isotope effect [1] [2]. In BCS superconductors, such as mercury, the T_c is enhanced when substituting the atom with lighter isotope, as demonstrated by Reynolds et al. [3]. However, in doped $SrTiO_3$, an opposite trend is observed, which hints at an unconventional pairing mechanism. Reynold et al. attribute this behaviour to a combination of the polaronic nature of the condensate (i.e Cooper pair in the anti-adiabatic limit) coupled to soft phonon modes responsible for ferroelectricity [4] [5].

For 2DEGs where superconductivity emerges at the filling of a second band, which is the case for some samples studied in this thesis, superconductivity exist in a range of a few meV above the Fermi level, which put them in the anti-adiabatic limit.

1.1.4 From Drude complex conductivity to the superfluid stiffness

The Drude model is a classical description of electrons in a solid under an electric field $\vec{E}$ where a simple relaxation process with scattering rate τ prevents the exponential growth of the electron's speed. For an electron of mass m, Newton's second law reads :

$$m\frac{d\vec{v}}{dt} = e\vec{E} - m\frac{\vec{v}}{\tau} \tag{1.28}$$

One can solve this first order differential equation for a time dependent field $\vec{E}e^{i\omega t}$ and find $\vec{v}$. The conductance (σ), defined by the relation $\vec{j} = \sigma\vec{E}$, is deduced from $\vec{j} = ne\vec{v}$ (n is the carrier density, e the charge). The normal and imaginary part of σ are respectively called σ_1 and σ_2.

$$\sigma(\omega) = \frac{ne^2\tau/m}{1 + i\omega\tau} \tag{1.29}$$

$$\sigma_1(\omega) = \frac{ne^2\tau/m}{1 + \omega^2\tau^2} \qquad \sigma_2(\omega) = -\frac{ne^2\omega\tau^2/m}{1 + \omega^2\tau^2} \tag{1.30}$$

The relaxation time is related to the mobility through the relation $\mu = \frac{q}{m*}\tau$. For a normal metal, mobility is $\simeq 10^{-3}\ m^2/V \cdot s$, which would give $\tau \simeq 10^{-15}\ s$. In semi-conductors 2DEG like the one used in high-electron mobility transistors, the mobility is of the order of $1\ m^2/V \cdot s$ giving τ of $10^{-12}\ s$. In LAO/STO, the typical low mobility band band have a mobility of $10^{-2}\ m^2/V \cdot s$ while the higher mobility band have a mobility comparable to that of HEMT, while having a typical scattering time much lower, around 0.1 to 1 ps.

In this thesis, the maximum frequency we used is around 1 GHz, deep in the limit $\omega \ll 1/\tau$, such that equation 1.28 for normal electrons reduces to $\vec{j}_n = \sigma_n\vec{E}$ with

$$\sigma_n = \frac{n_n e^2\tau_e}{m} \tag{1.31}$$

For Cooper pairs however, the scattering is by definition non existent. We can consider the limit $\tau \to \infty$ in equation 1.28 which then corresponds to the first London equation $d\vec{j}_s/dt = (n_s e^2/m)\vec{E}$ (with $\vec{j}_s = n_s e\vec{v}$). We can evaluate the superconducting conductance σ_s just like we did for σ_n and find:

$$\sigma_s(\omega) = \frac{\pi n_s e^2\tau}{m}\delta(\omega) - i\frac{n_s e^2}{m\omega} \tag{1.32}$$

In the London two-fluids model we have to add a parallel conductance contribution from normal (σ_n) and superfluid (σ_s) electrons [6]. In the limit $\omega \ll 1/\tau$, the total conductivity is the sum of the two channels :

$$\sigma(\omega) = \sigma_n + \sigma_s = \frac{n_n e^2\tau_e}{m} + \frac{\pi}{L_k}\delta(\omega) + \frac{1}{i\omega L_k} \tag{1.33}$$

Where $L_k = \frac{m}{e^2 n_s}$ is the kinetic inductance of Cooper pairs in the 2DEG, the same quantity is involved in the Ginzburg-Landau description of the superfluid stiffness equation 1.13.

The London superfluid stiffness $J_s = \hbar^2 n_s/4m$ allows to relate the kinetic inductance of Cooper pairs L_k to the superfluid stiffness J_s, which is the energy scale associated to phase rigidity (energy cost for a phase twist). Combining London superfluid stiffness with the definition of the kinetic inductance of Cooper pairs and the expression of the conductance we obtain :

$$J_s = \frac{\hbar^2}{4e^2 L_k} \qquad \sigma_2(\omega, T) = \frac{1}{L_k(T)\omega} \qquad L_k = \frac{m}{e^2 n_s(T)} \tag{1.34}$$

1.1.5 Superfluid stiffness in Mattis-Bardeen theory

Following the Kubo formalism which relates the current-current correlation function to the conductivity [7], Mattis and Bardeen have described the temperature and frequency dependence of the conductance of a dirty BCS superconductor (i.e. $\Delta \ll \Gamma = \hbar/\tau$) [8]. Although not perfectly valid in the study of 2D superconductors, the formalism is useful to understand the interplay between normal and superconducting electrons in a two-fluid model.

The expressions for the real part $\sigma_1(\omega, T)$ and the imaginary part $\sigma_2(\omega, T)$ of the dynamical conductance are [9] :

$$\frac{\sigma_1(\omega,T)}{\sigma_N} = \frac{2}{\hbar\omega}\int_{\Delta}^{\infty}(f(E)-f(E+\hbar\omega)g(E))\,dE + \frac{1}{\hbar\omega}\int_{\Delta-\hbar\omega}^{-\Delta}(1-2f(E+\hbar\omega)g(E))\,dE \tag{1.35}$$

$$\frac{\sigma_2(\omega,T)}{\sigma_N} = \frac{1}{\hbar\omega}\int_{max(-\Delta,\Delta-2\hbar\omega)}^{\Delta}(1-2f(E+\hbar\omega)g(E))\,dE \tag{1.36}$$

With

$$g(E) = \frac{E(E+\hbar\omega)+\Delta^2}{\sqrt{(\Delta^2-E^2)}\sqrt{(E+\hbar\omega)^2-\Delta^2}} \tag{1.37}$$

f is the Fermi-Dirac distribution. The second term in 1.35 accounts for Cooper pair breaking by photo-excitation and should be nullified when $\hbar\omega < 2\Delta$. The first term in 1.35 accounts for dissipation of the thermally activated quasiparticles. Equation 1.36 accounts for the Cooper pair contribution to the conductance.

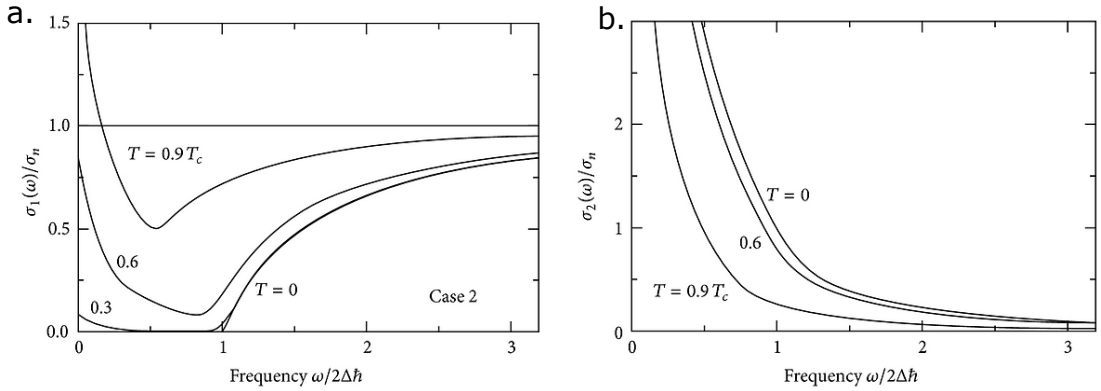

Figure 1.3: **Real and imaginary part of the normalized conductance in a dirty superconductors as a function of frequency. a.** At T=0 for frequency below the gap, no dissipative process occurs. However when T is increased up to T_c a minimum is observed at a frequency below the gap and the conductivity even exceeds the normal conductivity in a certain range of temperature close to T_c and frequency close to zero. **b.** The imaginary conductance diverges as $1/\omega$ at low frequency. From [9].

Figure 1.3 shows the evolution of the normalized real and imaginary part in panel **a.** and **b.** respectively as a function of frequency, while figure 1.4 shows the evolution of those quantities as a function of temperature.

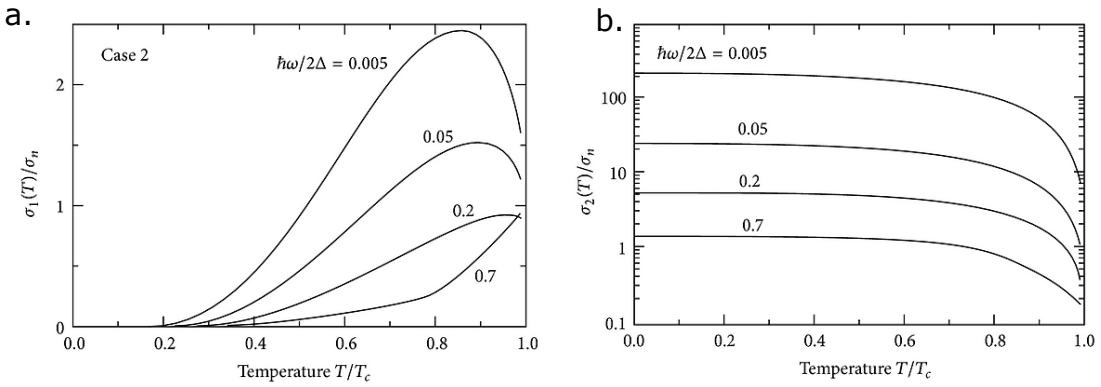

Figure 1.4: **Real and imaginary part of the normalized conductance in a dirty superconductors as a function of frequency. a.** For very low frequency, below T_c the spectral weight condenses into a peak visible in σ_1. When the frequency is close to the gap, the peak is smeared out. **b.** σ_2 varies strongly close to T_c and saturates at low temperature at a value strongly influenced by frequency. From [9].

In the limit $\hbar\omega \ll \Delta$, the expression of σ_2 simplifies as :

$$\frac{\sigma_2(\omega \to 0, T)}{\sigma_N} \simeq \frac{\pi\Delta}{\hbar\omega} \tanh\left(\frac{\Delta}{2k_BT}\right) \tag{1.38}$$

In the limit $T \to 0$, i.e well below the gap, $\tanh\left(\frac{1}{T}\right) \to 1$ and equation 1.38 gives:

$$\sigma_2(\omega \to 0, T \to 0) = \frac{\pi\Delta n e^2 \tau}{\hbar\omega m} \tag{1.39}$$

Where we have used the Drude formula for the normal conductivity. Given that

$$J_s = \frac{n_s\hbar^2}{4m} = \frac{\hbar^2\sigma_2\omega}{4e^2} \tag{1.40}$$

We finally obtain

$$J_s = \frac{R_0}{R_N}\frac{\Delta}{4} \tag{1.41}$$

Where $R_0 = h/e^2 \simeq 25.81k\Omega/\square$ is the quantum of resistance. Equation 1.41 shows that the larger the scattering, the higher R_N and thus the lower J_s. This means that for highly disordered system such as 2DEGs studied in this thesis, only a small fraction of the electrons will condensate into Cooper pairs.

1.2 Bulk $SrTiO_3$ electronic properties

Strontium titanate is a strontium and titanium oxide of formula $SrTiO_3$ with a perovskite structure. In this thesis, $SrTiO_3$ crystals were used as the main element of heterostructures such as $LaAlO_3/SrTiO_3$ or $AlO_x/SrTiO_3$, which accomodate a two dimensional electron gas (2DEG) at their interfaces. In this section, we will introduce the reader to the bulk properties of $SrTiO_3$ as the 2DEG at its interface inherits many of its properties.

1.2.1 Crystal properties

Strontium titanate belongs to the peroskite class of crystals. Perovskites take the origin of their name from the first type of these crystals being naturally found in the Ural mountains in 1839 by Gustave Rose. He named the calcium titanate oxide "Perovskite" after the famous Russian mineralogist, Lev Perovski. Since then, any crystal that has the similar ABO_3 structure has been called a perovskite crystal. The structure is such that the B atom, smaller than the A atom, is at the center of a cubic cell inside an oxygen octahedra where oxygen atoms are centered on each face of the cell, and the A atom occupies the origin of the cell as represented in figure 1.5. Strontium titanate can be classified as a d-band perovskite (meaning the electrons occupy the d orbital of the B atom, here Ti), a class of oxide materials particularly interesting for multi-functional electronics [10].

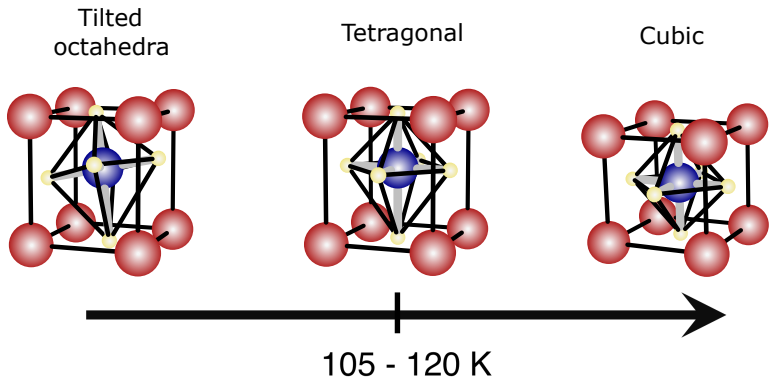

Figure 1.5: Evolution of the crystal structure of Strontium Titanate perovskite with temperature.

The high temperature cubic cell of $SrTiO_3$ transitions to a lower symmetric cell upon cooling. Such transitions can drive new orders such as ferroelectricity, ferromagnetism or anti-ferromagnetism. $SrTiO_3$ undergoes a tetragonal distortion at $T \simeq 105$ K which can be seen in specific heat measurement [11] [12]. The oxygen octahedra inside the tetragonal cell tilts upon further cooling [13] (see figure 1.5). The double-potential well shape felt by the Ti atom should lead to a ferroelectric order below 23K, however it is not the case in $SrTiO_3$ which is a quantum paraelectric.

1.2.2 Quantum paraelectricity

As the cell of $SrTiO_3$ becomes tetragonal below 105 K, the oxygen octahedra starts to rotate, which usually comes in competition with ferroelectricity [14]. Below 20 K, the titanium atom shifts from its center position to one of the two equilibrium positions inside the distorted oxygen octahedra, initiating a ferroelectric order. The onset of the ferroelectricity can be fitted by a Curie-Weiss law between 300 and 60 K, giving a Curie Temperature of ≈ 30 K [15]. However at temperatures below

10 K, quantum fluctuations stabilize the $q = 0$ phonon mode responsible for ferroelectricity, preventing the emergence of this order and freezing the diverging relative dielectric constant to a very large value of $\epsilon_r \approx 20000$ (figure 1.6) [16] [17]. This peculiar order is called quantum paraelectricity and the subsequent high value of the dielectric constant of $SrTiO_3$ allows to dope the 2DEG by electric field effect.

Quantum fluctuations can be suppressed and the low temperature ferroelectric order can be restored by different mechanisms:

- By chemical doping with isotopes [18], substituting Strontium to Calcium atom [19], or equivalently by applying stress [20]

- By applying an external electric field [21] [15] as seen in figure 1.6

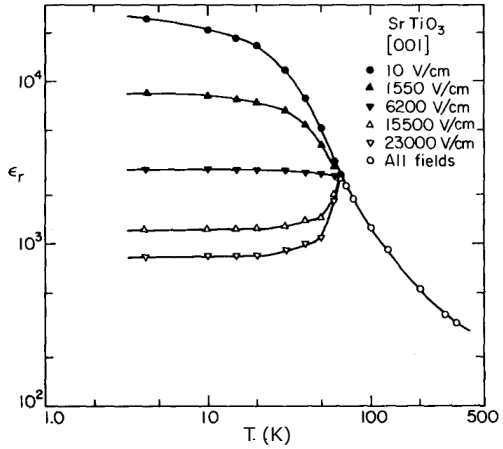

Figure 1.6: Saturation of the dielectric constant of $SrTiO_3$ from ferrolectric fluctuations stabilized by quantum fluctuations under different applied electric fields. Quantum fluctuations are suppressed and the ferroelectric order is restored above an applied field $> 6200\ V/\text{cm}$ (see figure 1.5).

Neville et al. [15] showed that the relative dielectric constant ϵ_r of $SrTiO_3$ varies with applied field $\boldsymbol{F}$ below 65K according to the following law:

$$\epsilon_r(|\boldsymbol{F}|) = \epsilon_r(|\boldsymbol{F}| = \infty) + \frac{1}{A(T) + B(T)|\boldsymbol{F}|} \tag{1.42}$$

where A and B are experimental parameters available in ref [15] for the principal crystal orientations (i.e [001], [110] and [111]). The parameter B becomes non-zero below 60 K.

1.2.3 Electronic properties

The main contributions to the conduction band of $SrTiO_3$ come from the 3d orbitals of the Ti atoms [22], while the valence band, separated from the conduction band by a 3.2 eV gap, mainly involves the oxygen anisotropic 2p orbitals (calculations by Mattheis [23], experiments e.g Benthem et al., [24]). The oxygen octahedron environment of the Ti atoms generates a crystal field which lifts the degeneracy of the five 3d orbitals between three low-energy t_{2g} orbitals (namely the d_{xy}, d_{yz} and d_{xz} orbitals) and two higher energy e_g orbitals ($d_{x^2-y^2}$ and d_{z^2}) [23].

The 105 K tetragonal transition lifts the degeneracy of the three t_{2g} orbitals at the Γ point by introducing anisotropy in the crystal field which can be seen as originating from spin-orbit coupling [25]. The overlap between highly anisotropic t_{2g} orbitals generates parabolic-like bands with different effective masses along the different directions.

Given the geometry of the t_{2g} orbitals, each band with a given orbital character has a light mass along two directions corresponding to large overlaps between orbitals in neighboring atoms and a heavy mass along the third direction corresponding to a weak overlap. For instance, the band associated to the d_{xy} orbitals has a light mass along the [100] and [010] directions and a heavy one along the [001] direction. Other bands with a d_{xz} and d_{yz} character are equivalent to the d_{xy} band by a rotation of $\pi/2$. This reasoning is summarized in figure 1.7. The band structure of STO-based interfaces will be examined in more details in section 1.3.3.

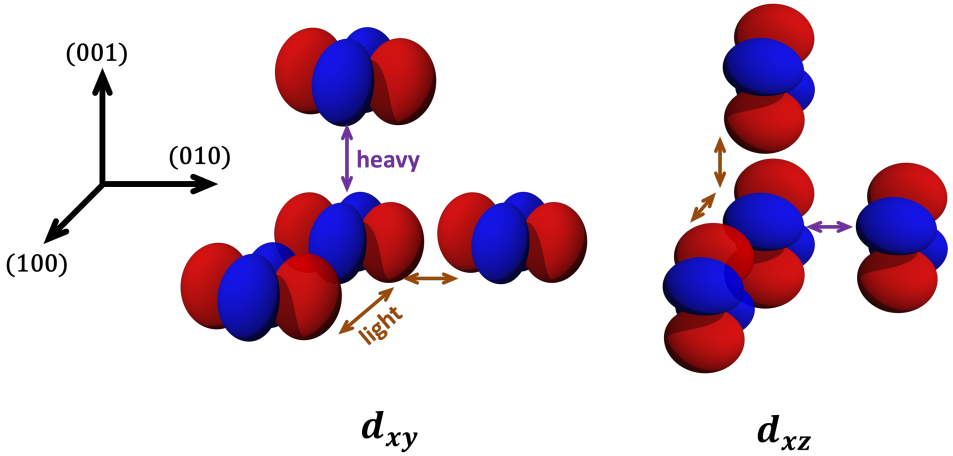

Figure 1.7: Representation of two of the t_{2g} Ti orbitals (left d_{xy}, right d_{xz}) in a cartesian basis and how their relative overlapping leads to different effective band masses along different directions.

1.2.4 $SrTiO_3$ bulk superconductivity

Strontium titanate is an insulator with a 3.2 eV band gap, yet conductivity and superconductivity can occur with very low n-doping. Doping is achieved by replacing the Ti^{4+} atoms with Nb^{5+} atoms, or by creating oxygen vacancies. The typical maximum superconducting transition temperature T_c is $\simeq$ 400 mK. The carrier density at which superconductivity emerges is the lowest observed in superconductors ($\approx 10^{17}\ cm^{-3}$). The critical temperature forms a dome upon doping which extends to more than three orders of magnitude in carrier density [26]. Its first measurement, by Schooley in 1965 [27], is shown in figure 1.8.

Superconductivity in $SrTiO_3$ was discovered in 1964 [28] but the pairing mechanism remains under debate. Early proposals such as the multi-valley model [29], or calculation based on MacMillan strongly coupled superconductors [30], are no longer considered relevant. More recent proposals have included soft-phonon modes from the 105 K tetragonal distortion as the pairing mechanism [31] or ferroelectric phonons and plasmons from first principle calculations [32]. The peculiar dielectric constant of $SrTiO_3$ is often put forward in suggestions for the superconducting pairing mechanism.

As first emphasized by Takada in 1980, at low enough doping, the Fermi energy ε_F is smaller than the Debye frequency ω_D corresponding to an unusual regime for a superconductor where usu-

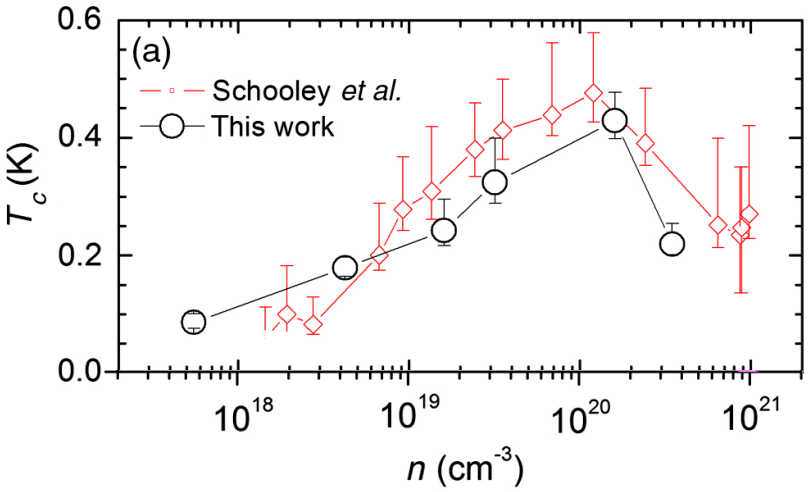

Figure 1.8: Variation of the superconducting critical temperature with carrier concentration in bulk $SrTiO_3$, showing early work of Schooley [27] and recent work of Lin et al [26].

ally $\hbar\omega_D << E_F$ [32]. In $SrTiO_3$, $\hbar\omega_D \simeq E_F$ or even $\hbar\omega_D >> E_F$ which corresponds to the anti-adiabatic limit where the phonon interaction must be greater than the direct Coulomb interaction [2]. In such anti-adiabatic limit, the relevant energy scale is E_F, and not ω_D, and a distinct characteristic of such unconventionality is the absence of isotope effect [1]. $SrTiO_3$ exhibits an opposite trend for the isotope effect : T_c is enhanced by replacing atoms with *heavier* elements such as ^{18}O. This has been seen as a clue that the quantum paraelectricity of $SrTiO_3$, more specifically the soft phonon modes, plays a role in the apparition of superconductivity and its tunability with electric field [5] [4].

Multigap superconductivity has been suggested to take place in doped-$SrTiO_3$, with one report showing two-gap superconductivity in Nb-doped $SrTiO_3$ [33], however such an experiment has never been reproduced and reports of superconductivity in $SrTiO_3$ and its surface 2DEG have been consistent with a single s-wave like gap superconductivity [34] [35] [36]. We will address this issue of multi-gap superconductivity for the LAO/STO(110) and LAO/STO(111) interfaces in more depth in chapter 3.

1.3 2DEG at La(Ti,Al)O_3/$SrTiO_3$ interfaces

1.3.1 History

A. Ohtomo and H.Y. Wang first discovered in 2004 that a conductive layer emerges at the interface of a 60 $\AA$ thick thin film of $LaAlO_3$ grown on top of a $SrTiO_3$ crystal [37]. A measurement of the resistivity as a function of temperature of this 2DEG, for different thicknesses of $LaAlO_3$ and different oxygen pressures, is shown in figure 1.9a. Three years later, N. Reyren and collaborators showed that this interface can be superconducting below $\approx$ 300 mK [38]. Figure 1.9b shows an example of resistance versus temperature curves measured under different magnetic fields. The critical field at which superconductivity disappears can be estimated to be 180 mT. A year later, Caviglia et al. showed that the critical temperature can be tuned by electric field effect using a metallic gate on the back side of the STO [39]. The superconducting critical temperature forms a dome upon gating, with a maximum T_c around 300 mK, as we can see in figure 1.9c. Note however,

that for the interface this dome extends on a rather low carrier density modulation (typically $\delta_n = \pm 50\%$) compared to that of bulk STO that extends on more than three orders of magnitude in density.

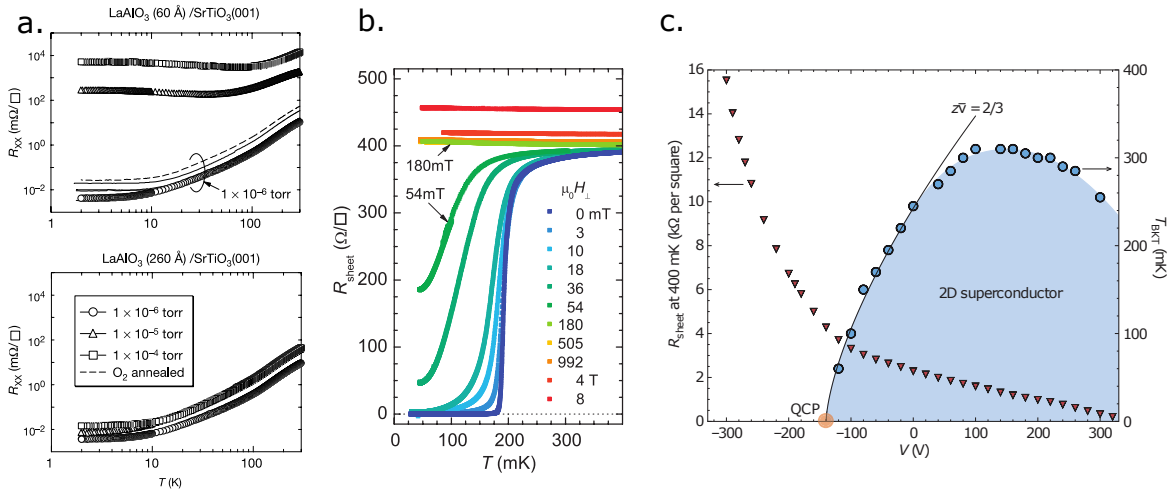

Figure 1.9: **Transport properties of LAO/STO interfaces. a.** First measurement of the temperature dependent resistance of the LAO/STO 2DEG [37]. **b.** Suppression of the superconducting transition in a LAO/STO 2DEG upon increasing magnetic field. [38]. **c.** Tunable critical superconducting temperature via electric field effect (right axis) and resistivity (left axis) [39].

1.3.2 Microscopic origin of the 2DEG

The most studied oxide interface so far is the LAO/STO one. The growth of the crystalline $LaAlO_3$ layer is done on a TiO_2-terminated $SrTiO_3$ commercial substrate by pulsed laser deposition (PLD) with a laser fluence of typically 1 J/cm^2, monitored by reflection high energy electron diffraction (RHEED) in ultra-high-vacuum (UHV). In this thesis, we have measured samples fabricated by M. Bibes group (CNRS-Thales lab), M. Salluzzo group (CNR, Naples), G. Herranz (ICMAB Barcelona) and A. Caviglia (TU Delft).

Experimentally, a 2DEG only forms at the TiO_2 terminated crystaline $LaAlO_3/SrTiO_3$ interface above a 4 unit cells critical thickness of $LaAlO_3$ ($\simeq$ 16 $\mathring{A}$) [40]. Two main mechanisms have been proposed to explain the origin of the 2DEG, which are complementary, and later a proposal merging the two approaches was developped by L. Yu and A. Zunger [41].

Polar catastrophe

In the polar catastrophe scenario, the 2DEG originates from a charge transfer due to the divergence of the electrostatic potential that accumulates as polar layers of $LaAlO_3$ are built on top of each other (see figure 1.10). This mechanism has first been proposed in 2006 by Nakagawa et al. [42]. In their article they showed that, by transferring half a charge per unit cell, there is a renormalization of the electrostatic potential, preventing it from diverging. They analyzed the two possible interfaces possible: the SrO-terminated $AlO_2/SrO/TiO_2$ interface and the TiO_2 terminated $AlO_2/LaO/TiO_2$ interface. Using electron energy loss spectroscopy (EELS) on a scanning transmission electron microscopy (STEM), they showed that for the TiO_2 terminated interface, a net -1/2 charge per unit cell

is expected at the interface whereas for the SrO terminated interface no net charge is expected, as the expected 1/2 charge per unit cell is neutralized by a higher concentration of oxygen vacancies.

The polar catastrophe mechanism is described in figure 1.10. In panel **a.** and **b.**, we see what happens when layers of polar $LaAlO_3$ are stacked onto a substrate of $SrTiO_3$ which is either TiO_2-terminated (panel a.) or SrO-terminated (panel b.). In both cases, the charge accumulation (ρ) gives a non-zero average electric field (E) leading to a diverging electrostatic potential (V), either positive in the case of TiO_2 termination or negative in the case of the SrO termination. Panels **c.** and **d.** of figure 1.10 show the polar reconstruction of the system, where half a charge is transfered from the top of the $LaAlO_3$ crystal to the interface. This charge transfer is such that the field E becomes, on average, zero, and thus the electrostatic potential V does not diverge anymore. Experimentally, only the situation described in panel **a.** and **c.** has been observed, that is, only the TiO_2 termination of a $SrTiO_3$ substrate is known to accommodate a 2DEG at the $LaAlO_3/SrTiO_3$ interfaces.

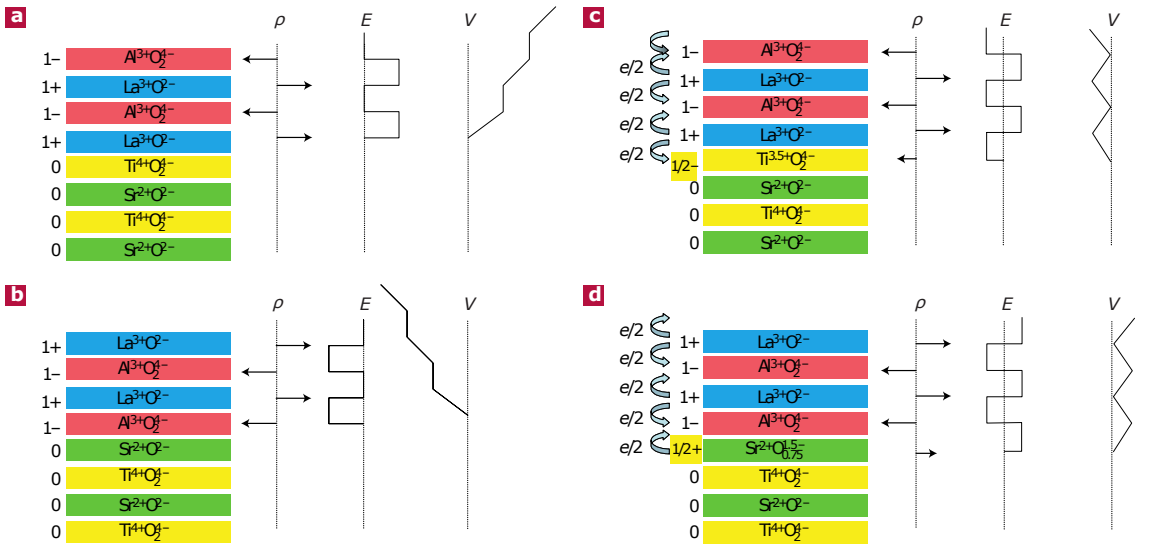

Figure 1.10: **Polar catastrophe scenario for the 2DEG formation.** Panels **a.** and **c.** show the n-type interface reconstruction, where -1/2 charge is transferred to the interface to prevent divergence of potential. Similarly, the **b.** and **d.** panels show the p-type interface reconstruction where +1/2 charge is transferred to the interface to prevent divergence of potential as seen from [42].

In a crystalline $LaAlO_3/SrTiO_3$ heterointerface, the metallic electrons at the interface come mainly from the polar reconstruction of the surface. However, when the structure is not annealed in oxygen atmosphere under certain conditions that are meant to fill the eventual oxygen vacancies, or if $LaAlO_3$ is amorphous, the conductivity comes from both oxygen vacancies and the polar catastrophe, as shown by Lui et al. [43]

The importance of in-situ annealing is emphasized in figure 1.11 below. Figure 1.11**a.** describes a conductive-tip atomic force microscopy (AFM) measurement along the side of an LAO/STO sample. When the sample is not annealed, the conductivity extends deep in the substrate and decays smoothly over depths larger than several micrometers (figure 1.11**b.** left panel). When the sample is annealed at 400°C for 7 days under 20 bars of oxygen pressure, the system becomes truly two-dimensional: the conductivity occurs within a layer of thickness lower than the experimental resolution of 7 nm (figure 1.11**b.** panel) [44]. In practice, samples studied in this thesis were not exposed for 7 days under oxygen pressure, but rather a few hours which is sufficient avoid the

presence of oxygen vacancies.

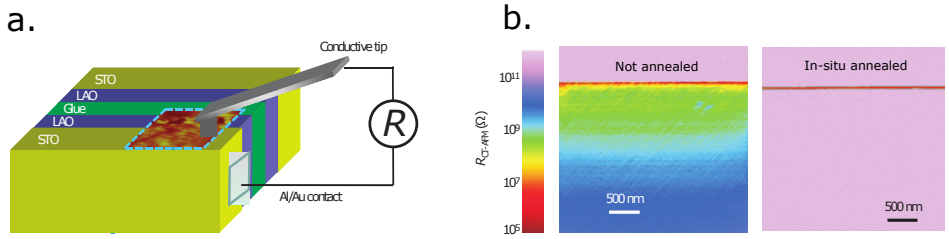

Figure 1.11: Basletic et al., mapped out the metallic charges distribution in a LAO/STO interfaces. **a.** Principle of the conductive-tip AFM measurement which acquires resistivity map. **b.** Cross sectional resistance profile of two interfaces, one annealed and one not annealed showing the importance of oxygen annealing to get a 2DEG at the LAO/STO interface [44].

The polar catastrophe scenario predicts that the electronic reconstruction can only take place above a critical thickness of 4 unit cells of crystalline LAO which is in agreement with experimental observations. Such charge transfer and electronic reconstruction at the interface has been described using DFT calculation [45] [46] [47]. In this paradigm, the lattice polarization from stacking LAO layers leads to an insulating behavior for thicknesses lower than 4 unit cells. The gap is reduced by approximately 0.4 eV per LAO unit cell, until it reaches 0 above 4 unit cell, allowing charge transfer and electronic reconstruction of the surface [45].

However, the polar catastrophe scenario has several limits, the first one being that the predicted carrier density is not observed experimentally. According to the polar catastrophe scenario, the 2DEG should have a carrier density of $\simeq 3 \times 10^{14}$ cm^{-2}, corresponding to half a charge per unit cell. However, most of measured densities are typically ten times smaller than this prediction [48] [49]. One could argue that these missing charges are trapped in local impurities at the interface, and indeed it has been observed that under visible light, the carrier density can quadruple compared to the situation in absence of light [50]. However, even after accounting for these photo-excited charges, there still is not half a charge per unit cell. The second mechanism partially answers the limit that the polar catastrophe cannot address.

Oxygen vacancies

The year following Nakagawa's polar catastrophe proposal, other groups suggested that oxygen vacancies could be the main provider of free electrons, depending on the growth conditions. Under an oxygen pressure equal or lower than 10^{-4} mbar, the metallicity seems to be 3 dimensional, whereas when the oxygen pressure is higher than 10^{-4} mbar, weak localization characteristic of 2D electronic transport is observed [51] [52] [53].

The oxygen being charged 2- in the crystal, to keep electronic neutrality, a charge of -2 is left free when one oxygen vacancy is created. Annealing the sample in high oxygen atmosphere has the effect of filling the oxygen vacancies and thereby decreasing the total carrier density. In amorphous $LaAlO_3/SrTiO_3$ heterostructures, oxygen vacancies are the main contributor to conduction because the polar catastrophe scenario requires a crystalline structure.

It has been shown by ARPES that a 2DEG can form at the surface of a cleaved STO crystal due to a high number of oxygen vacancies [54]. Another method to induce oxygen vacancies consist in evaporating aluminium atoms on a clean TiO_2 terminated strontium titanate substrate. Aluminum

pumps oxygen at the surface of STO to form an insulating Al_2O_x layer, ($x \leq 3$) as shown in figure 1.12a. Researchers have reported that above a critical thickness of a few $\mathring{A}$ of aluminium oxide, less than the few nm required with $LaAlO_3$, a conducting 2DEG appears similar to that of the LAO/STO interface. [55] [56]. It also has light and heavy bands crossing the Fermi surface, with similar (but not totaly equal) effective masses, which are shown figure 1.12c. for the heavy and figure 1.12d. for the light band. This 2DEG (sample figure 1.12b.) can also become superconducting with a similar $T_c \approx 300$ mK, tunable with gate voltage [57]. The samples fabricated using this method will be discussed in chapter 5.

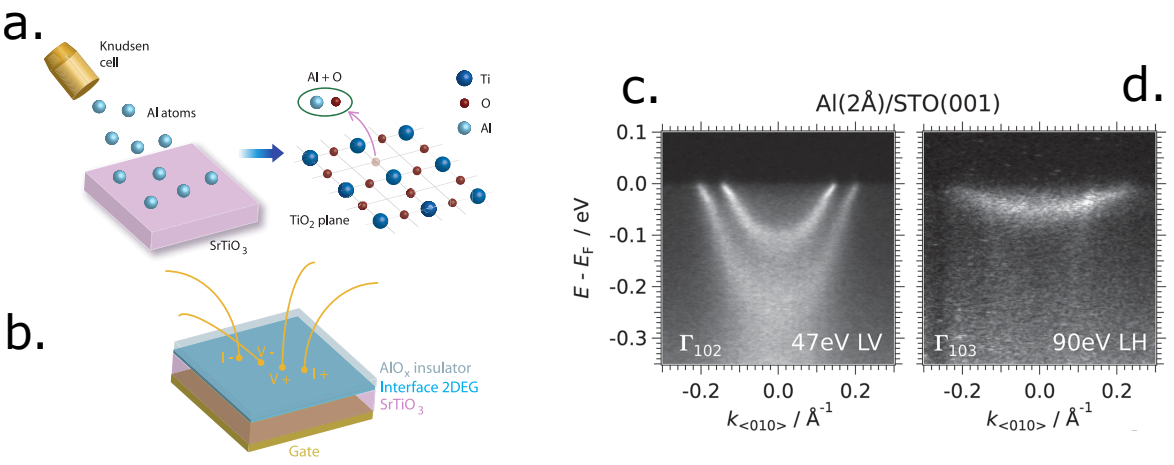

Figure 1.12: **Formation of a 2DEG at the STO surface by controlling oxygen vacancies. a.** Aluminum evaporated on the top of a $SrTiO_3$ substrate pumps oxygen atoms in the first atomic layers leaving two electrons as free charges per vacancy. **b.** The 2DEG is buried under a thin layer of insulating aluminium oxide suitable for DC measurement [57]. **c.d.** Conduction bands of a 2DEG at $SrTiO_3$ interface as seen in ARPES along the <010> direction. Panel **c.** shows the two light bands in the <010> direction, with a d_{xy} and d_{yz} orbital characters while panel **d.** shows the heavy d_{xz} band [55].

Adding a metallic capping layer on top of 2 unit cells of $LaAlO_3$ has been proven to also trigger the creation of a 2DEG at $SrTiO_3$ heterointerface. D. Vaz studied in his thesis the properties of such 2DEG created by depositing a few nanometers thick layer of various metals such as Pd, Co, Nb, Ta among others. He showed that conductivity occurs and that the mobilities and densities are affected by the type of metal deposited, which makes oxide-based 2DEG very versatile. The formation of the 2DEG dependence for a given capping material is understood in terms of enthalpy of formation of oxygen vacancies, which was also experimentally assessed *via* the degree of oxidation of the Ti donor site with XPS [58].

The former polar catastrophe mechanism is referred to as "intrinsic" doping of the interface, while the oxygen vacancies are referred to as "extrinsic". In this manuscript, we will present results from both $LaAlO_3/SrTiO_3$ interfaces where it is believed that polar catastrophe plays a role in the formation of the 2DEG, as well as results from $AlO_x/SrTiO_3$ interfaces where oxygen vacancies is the main doping mechanism. We will also present results on 2DEGs created by aluminium capping of another quantum paraelectric material, $KTaO_3$, for which the mechanism responsible for the formation of the 2DEG is also based on oxygen vacancies.

Polarity-induced defect

In 2014, L. Yu and A. Zunger [41] summarized four proposed mechanisms for conductivity at LAO/STO interfaces, the polar catastrophe (or intrinsic electronic reconstruction) and three kinds of interfacial defects : oxygen vacancies at the interface, on the $LaAlO_3$ side and interfacial cation intermixing. They noted that none of the mechanism could, by itself, take into account all the major experimental observations. They proposed an unified mechanism in which the polar discontinuity thermodynamically favors the spontaneous formation of defects at the interface that cancels the polar field. Recent work confirmed that the reconstruction occurs at a $LaAlO_3$ thickness too thin to be from pure electronic reconstruction, suggesting that indeed defects cancel the polar field [59]. Figure 1.13 below summarizes the results of Yu and Zunger:

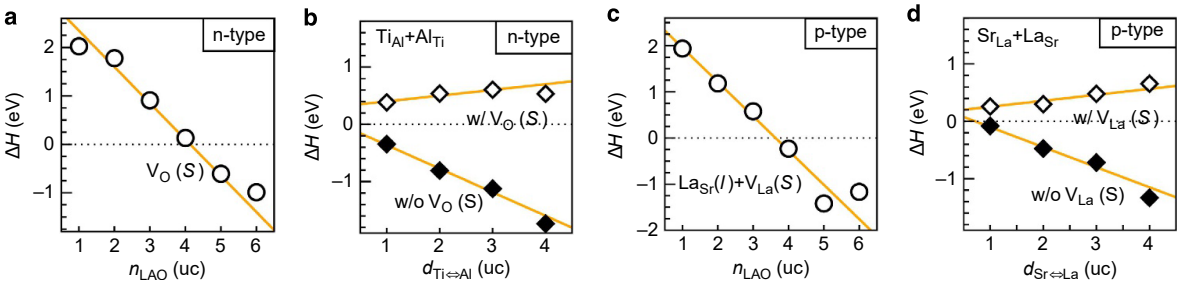

Figure 1.13: Enthalpy of formation of defects at LAO/STO interface as a function of $LaAlO_3$ layers or distance between exchanged atoms. **a.** Formation of oxygen vacancies defects in n-type interfaces. **b.** Formation of Titanium and aluminium pair defects with and without oxygen vacancies present at the interface. **c.** Formation of La, La vancancies and Sr defects. **d.** Formation of Sr-La exchange defect pairs with and without La vacancies. In all panels the dashed line separates the zone of favorable formation (negative enthalpy) from the zone of unfavorable formation (positive enthalpy). From [41].

First, we consider the n-type interface, panels **a.** and **b.** in figure 1.13, which corresponds to the TiO_2-terminated STO substrate where the 2DEG effectively develops. When the thickness n_{LAO} is lower than the critical thickness n_c, the enthalpy of formation ΔH of oxygen vacancies (noted V_O(S) in the figure) is positive thus such defects don't form (fig. 1.13**a.**). However exchange of charges from Ti at the interface and Al from $LaAlO_3$ at the surface create antisite pairs which cancel the polar field. Indeed the decrease of ΔH with increasing donor-acceptor distance below 4 unit cell of $LaAlO_3$ (filled symbol in fig. 1.13**b.**) is a sign of the polar field compensation. As we can see, these defects are too deep, or too far from the interface, to generate free carriers. For $n_{LAO} > n_c$, the polar field is cancelled by oxygen vacancies which now have negative enthalpy of formation (fig 1.13**a.**) and are energetically more favorable than the Ti $\leftrightarrow$ Al exchange pair, represented using empty symbol in figure 1.13**b.**.

We now consider the p-type interface, panels **c.** and **d.** in figure 1.13, which corresponds to the SrO-terminated STO substrate where no interfacial 2DEG has been observed. For $n_{LAO} < n_c$ (figure 1.13**d.** filled symbol) the donor acceptor defect pairs are La atoms from the interface with Sr from the substrate. Just like for the Ti-Al pairs, they can cancel the polar field but do not provide free carriers. For $n_{LAO} > n_c$, charges are transferred from La at the interface to La vacancies at the overlayer surface. In p-type interfaces, the enthalpy of formation is much higher for oxygen vacancies so they do not develop, nor give free carriers to the interface. The calculated equilibrium for p-type interface for $n_{LAO} > n_c$ is in the $SrTiO_3$ band gap, hence this interface is insulating.

Considering the carrier density, which is typically much lower than the 0.5 electrons per unit cell, authors consider that the Ti-Al pairs forming below n_c trap much of the electrons. They point to the fact that in $GdTiO_3/SrTiO_3$, such Ti-Al trapping pairs do not exist and that the carrier density observed indeed correspond to 0.5 electrons per unit cell [60].

Discussion

The polar catastrophe is a simple and rather seductive picture. However, first observed by Thiel et al. [40] and confirmed by DFT calculations, it fails to take into account the correct carrier density. Most charges are likely trapped without possibility to be observed in transport. The sensitivity of the polar LAO surface to the interface has been evidenced by Y. Xie et al. [61] and reinforces the idea that the polar catastrophe is driving the conductivity at LAO/STO interfaces. Annealing at high temperature in an oxygen rich atmosphere also limits the formation of a significant amount of oxygen vacancies.

Other researchers have used oxygen vacancies to generate 2EGS for instance on cleaved STO for ARPES measurement or by oxygen reduction with Aluminum sputtering [55] [56]. Such methods allow to get rid of the epitaxial growth, making simpler and more cost-effective the fabrication of the 2DEG. However, such mechanism does not explain the observed critical thickness for the 2DEG formation. The same argument holds for cation intermixing, where atomic exchanges at the interface such as Ti↔Al, can dope the interface.

Yu and Zunger proposed a unified view where the polar field is cancelled by various defects formation at the interface, which is an elegant way to articulate the different mechanisms together[41].

Still, today the fabrication of STO-based 2DEGs is not sufficiently well understood to be able to predict the properties of a 2DEG and its origin based solely on experimental growth parameters. In the future, we might understand how to design a 2DEG with chosen carrier density and mobility, and through a controlled mechanism.

1.3.3 Electronic properties of the 2DEG

Simple picture of confined $SrTiO_3$ 2DEG

Considering that the conduction band of STO-based 2DEGs is built on the t_{2g} orbitals of Ti ions as described in section 1.2.3, the Hamiltonian of the system can be described in first approximation by an (x,y) in-plane free electron model and out-of-plane confinement under a triangular shape potential along the z axis. In the basis $|\Psi_{k,\sigma}\rangle = (c^{xy}_{k,\uparrow}, c^{xy}_{k,\downarrow}, c^{yz}_{k,\uparrow}, c^{yz}_{k,\downarrow}, c^{xz}_{k,\uparrow}, c^{xz}_{k,\downarrow})^t$, where $c^{xy}_{k,\sigma}$ is the creation operator of an electronic state of spin σ in the band formed from d_{xy} orbitals, the Hamiltonian reads:

$$H = \Sigma_{k,\sigma} \langle \Psi_{k,\sigma} | H_0 | \Psi_{k,\sigma} \rangle \quad \text{where} \quad H_0 = \begin{pmatrix} \frac{\hbar^2 k_x^2}{2m_l^*} + \frac{\hbar^2 k_y^2}{2m_l^*} & 0 & 0 \\ 0 & \frac{\hbar^2 k_x^2}{2m_l^*} + \frac{\hbar^2 k_y^2}{2m_h^*} + \epsilon_\Delta & 0 \\ 0 & 0 & \frac{\hbar^2 k_x^2}{2m_h^*} + \frac{\hbar^2 k_y^2}{2m_l^*} + \epsilon_\Delta \end{pmatrix}$$

where $\epsilon_\Delta = E^{xz/yz} - E^{xy}$ is the splitting due to confinement.

The conduction occurs in the (x,y) plane and so different orbital symmetries yield different properties. In this case, the d_{xy} orbitals have a strong overlap in plane, while the d_{yz}, d_{xz} have a weaker

overlap. In the first case, the effective mass of the electron will be smaller than in the two later cases. Indeed ARPES experiments at the surface of cleaved STO provide an effective light in-plane mass of $m_l \approx 0.7m_e$ in plane and an effective out-of-plane heavy mass $m_h \approx 10 - 20m_e$ [54]. DFT calculations on $LaAlO_3/SrTiO_3$ interfaces give similar results : $m_l = 0.41m_e$ and $m_h = 6.8m_e$. [62]. Values of $m_l = 0.7m_e$ and $m_h = 14m_e$ are chosen by many authors in the literature.

Quantum confinement: self-consistent Schrödinger-Poisson equations

Each band is further split into subbands via the effect of quantum confinement. We can see the 2DEG as being at the LAO/STO interface, on the STO side, and its conduction band is bent toward the $LaAlO_3$ side modeled by an infinite potential wall. The position of each band in energy can be determined by solving Schrödinger's equations for the states inside the potential well, coupled with Poisson equations to described how the electronic density affects the well and vice-versa in a self-consistent way.

We consider a frame of reference where the confinement occurs along the z direction. The electronic states Ψ_{xy}, Ψ_{yz} and Ψ_{xz} are described by a free wave function of the form $\Psi_{i,j}(x,y,z) = \Psi_{i,j}(z)Ae^{i(k_x \cdot x + k_y \cdot y)}$ $(i,j = x,y,z)$, where A is a normalization constant. The z-components $\Psi_{xy,yz,xz}(z)$ obey the following equations :

$$\frac{\hbar^2}{2m_z^{xy}}\frac{d^2\Psi_{xy}(z)}{dz^2} + [E_{xy} + e\phi(z)]\Psi_{xy}(z) = 0 \tag{1.43}$$

$$\frac{\hbar^2}{2m_z^{xz/yz}}\frac{d^2\Psi_{xz/yz}(z)}{dz^2} + [E_{xz/yz} + e\phi(z)]\Psi_{xz/yz}(z) = 0 \tag{1.44}$$

where m_z^{xy} is the effective mass of the bands with d_{xy} character along the z-axis, which is 14 m_e and $m_z^{xz/yz}$ are the effective masses along the z axis of the bands with d_{xz} and d_{yz} character which is 0.7 m_e. $\phi(z)$ is the electrostatic field confining carriers at the interface.

The electronic density n must satisfy the Poisson equation (1.45) involving the electric field dependent relative dielectric constant ($\epsilon_r(F)$) of $SrTiO_3$ (1.46):

$$\nabla\left(\epsilon_0\epsilon_r(F)\nabla\phi(z)\right)) = -n(z) \tag{1.45}$$

$$\epsilon_r(F) = \epsilon_r(F=\infty) + \frac{1}{A(T) + B(T)|F|} \tag{1.46}$$

A resolution method was proposed in J. Biscaras thesis manuscript [63] and optimized later on by A. Jouan [64]. The idea is to solve Schrodinger's equation 1.43 and 1.44 to find the energy dispersion of the bands. These energies are then used to estimate the Fermi level. We then solve equation 1.45 for the estimated 2D density, and find the electrostatic potential of this charge distribution. The process is repeated by taking the potential from the last step and injecting it into the first step until the difference between the two is lower than a chosen threshold. At the end, the Fermi level, positions, filling of the bands and charge distribution are known. In this process, a density of trapped charges is also introduced based on experimental observations.

The ingredients needed for a resolution are the effective mass taken from other studies, the experimental 2D density n_{2D} and parameters A and B from equation 1.46.

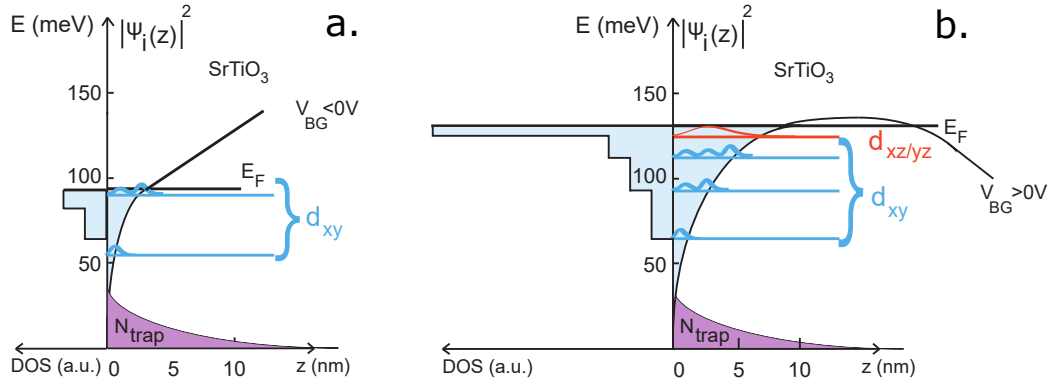

Figure 1.14: **Poisson-Schrödinger simulation in LAO/STO(001).** The d_{xy} lower subbands wave functions squared densities are represented in blue. The higher degenerate d_{yz} and d_{xz} bands are represented in red. Their spatial extensions are plotted as a function of the distance z into the substrate and their corresponding DOS is shown in arbitrary unit. We see that the DOS of the higher band is much larger than the one of the lower bands. A density of trapped charges (N_{trap}) at the bottom of the well is also represented. The ordinate axis shows the energy level of the location of the different bands as well as the Fermi energy E_F. Panel **a.** shows the underdoped regime ($V_G < 0$), where only the lowest bands are populated, while panel **b.** shows the overdoped regime ($V_G > 0$) where the higher bands are also populated.

Examples of simulations are presented in figure 1.14. Panel **a.** shows a situation where $V_G < 0\,V$, meaning the 2DEG is depleted and only the lower d_{xy} bands (in blue) are populated. On the left, the density of state associated with each subbands is shown. Are shown on the right the electrostatic potential in solid black line, as well as the spatial extension of the traped charges. The Fermi level is indicated on the ordinate axis, in solid black line, as well as the energy of the d_{xy} subbands. Figure 1.14**b.** also shows a resolution of the Schrödinger-Poisson model, but in the case where $V_G > 0\,V$. In this situation, the 2DEG is doped and the higher $d_{xz,yz}$ bands are also populated (in red). The trapped charge distribution is taken to decay exponentially from the interface with a characteristic length and amplitude which are chosen to reproduce the experimental behavior of the 2DEG. In particular, it ensures that at the maximum gate voltage, the Fermi energy should lie exactly at the top of the quantum well.

Spin-orbit coupling

Two types of spin-orbit coupling (SOC) are at play at $LaAlO_3/SrTiO_3$ interface: the atomic "$l \cdot s$" spin-orbit coupling (ASO) and the Rashba spin-orbit coupling (RSOC). Spin-orbit interaction originates from relativistic correction to the Schrödinger equation when an electron travels in a potential. If this potential has a certain symmetry, which is the case for the spherical potential of an atom or a translational invariant potential in a solid, the expression of the SOC in the Hamiltonian is of the form $\xi(r)\,\overrightarrow{l}\cdot\overrightarrow{s}$ where $\xi(r)$ denotes the strength of the interaction, and $\overrightarrow{l}$ and $\overrightarrow{s}$ are the orbital and spin momentum respectively. Here the ASO couples the spin of the electron to its momentum via the field of the ionic nuclei in the solid.

In the same basis $(c_k^{xy}, c_k^{yz}, c_k^{xz})^t$ as before, given the symmetry of the t_{2g} orbitals, the non-zero element of the spin orbit interaction for a (001)-oriented interface can be written as [65] [66]

$$H_{ASO} = \Delta_{ASO} \begin{pmatrix} 0 & -i\sigma_y & \sigma_x \\ i\sigma_y & 0 & i\sigma_z \\ -i\sigma_x & -i\sigma_z & 0 \end{pmatrix} \tag{1.47}$$

Where Δ_{ASO} denotes the strength of the spin orbit coupling and $\sigma_{x,y,z}$ are the Pauli matrices.

This SOC Hamiltonian is independent on the orientation of the 2DEG and is the same for 2DEG at the (110) or (111) orientation for instance, which is not the case for the Rashba spin-orbit coupling. The SOC mixes different bands around their crossing point, hence the eigenstates of H_{ASO} at these points are no longer pure $d_{xy,yz,xz}$ states.

The effect of the SOC on the band structure is shown in figure 1.15**b.** that can be compared to the diagonal hopping Hamiltonian from equation 1.3.3 which is represented in figure 1.15**a.**

The second kind of spin-orbit coupling present in these 2DEGs is the Rashba spin-orbit interaction (RSOC) which originates from breaking an inversion symmetry. From the electron perspective the electric field at the interface acts as an effective magnetic field, leading to a coupling between electron spin and momentum. Such phenomena can in principle be described by a phenomenological term of the form $H_{RSOC} = \alpha(\hat{\boldsymbol{\sigma}} \wedge \hat{\boldsymbol{P}}) \cdot \hat{z}$ where α denotes the strength of the Rashba coupling, $\hat{\boldsymbol{\sigma}} = (\hat{\sigma_x}, \hat{\sigma_y}, \hat{\sigma_z})^t$ and $\hat{\boldsymbol{P}} = (\hat{P_x}, \hat{P_y}, \hat{P_z})^t$ are the spin and momentum vector operator. However, the way we introduce RSOC at oxide interface is by considering polarisation of the orbital and introducing new hopping terms between orbitals of different character.

In our system, the confining electric field perpendicular to the 2DEG at the interface breaks the inversion symmetry along the z axis. This field polarizes the Ti orbital and tilts the angle between the p orbital of the oxygen and the d orbital of the titanium. This small polarization allows previously forbidden hoping between the atoms Ti - O - Ti, through the orbitals $d_{xy} - p_x - d_{xz}$ along the y axis and $d_{xy} - p_y - d_{yz}$ along the x axis. In the basis $(c_k^{xy}, c_k^{yz}, c_k^{xz})^t$, it can be written [65] [62]:

$$H_{mix} = \Delta_{mix} \begin{pmatrix} 0 & i\sin(k_y a) & i\sin(k_x a) \\ -i\sin(k_y a) & 0 & 0 \\ -i\sin(k_x a) & 0 & 0 \end{pmatrix} \tag{1.48}$$

The addition of this mixing term to ASO generates a Rashba-like coupling by introducing a breaking of inversion symmetry, which has an effect of spin-splitting at the crossing points between bands (figure 1.15**c.**.)

It has been shown that the Rashba effect in LAO/STO interfaces can be controlled by gate voltage, and Δ_{RSOC} can vary from 2 meV to 10 meV when the back gate voltage is changed from -300 to +100 V [67]. The relatively high spin-orbit coupling in $LaAlO_3/SrTiO_3$ interfaces has attracted much attention due to potential spintronics applications, in particular related to spin-to-charge conversion [68] [69]. The unique combination of 2D superconductivity with large spin-orbit coupling, both of them being tunable by a gate voltage, have made $SrTiO_3$-based-interface an ideal playground to create functional interfaces.

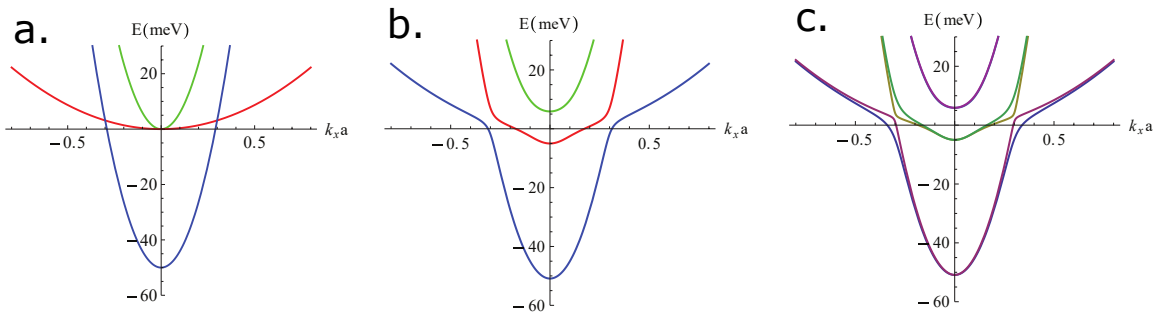

Figure 1.15: **Evolution of the dispersion relation with the addition of spin-orbit couplings.** Dispersion along x at Γ point **a.** for $\hat{H} = \hat{H}_0$ with $\epsilon_\Delta = 50\ meV$. **b.** for $\hat{H} = \hat{H}_0 + \hat{H}_{ASO}$ with $\Delta_{ASO} = 5\ meV$. **c.** for $\hat{H} = \hat{H}_0 + \hat{H}_{ASO} + \hat{H}_{RSOC}$ with $\Delta_{RSOC} = 10\ meV$. From [65]

Crystal orientation influence on the 2DEG band structure

Although much of the research efforts on the superconducting STO-based 2DEG have focused on the (001)-oriented interface, the (110) and (111) interfaces have specificities which are worth looking at. Because the 2DEG arises from Ti 3d states confined along the growth direction, the relative orientation of the t_{2g} orbitals with respect to the growth directions influences the band structure of the 2DEG. In a 2DEG, a large hopping parameter t originates from a good overlap between two neighbouring orbitals. In the Drude model the mobility is defined by $\mu = e\tau/m^*$ so a good in-plane overlap (low mass) of wave functions and long scattering (τ) means that electrons in the band have a high mobility. The in-plane effective mass also determines the 2D density of states. For an isotropic parabolic band, $g_{DOS} = m^*_{||}/\pi\hbar$, where g_{DOS} is the 2D density of state. The effective mass along the confinement direction determines the energy of the band in the potential well. The higher is the mass, the deeper is the band.

In the conventional (001)-oriented interface, the interface has a square geometry (neglecting the small tetragonal distortion). The d_{xy} subbands are energetically the lowest lying orbitals with a pronounced 2D character. Sitting higher in energy in the quantum well, the degenerate $d_{xz,yz}$ subbands delocalize deeper in the $SrTiO_3$ substrate, where they recover bulk-like properties, including a high dielectric permittivity and reduced scattering. A tight binding band structure of a (001)-2DEG is shown figure 1.16**d.** considering a kinetic energy term only and a representation of d_{yz} orbitals in the crystal are represented in figure 1.16**a.**

In the (110) orientation, the band hierarchy is reversed with respect to the conventional (001)-orientation: at the Γ point the d_{xy} band has higher energy than the degenerate $d_{xz,yz}$ ones but the energy splitting between these bands of different orbital character is less pronounced than in the (001) orientation. Two different orbitals with their hopping terms are represented in figure 1.16**b.** and the band structure of a (110)-2DEG is provided figure 1.16**e.**

The (111) interface is fundamentally different from the (001) and (110) interface because of its hexagonal symmetry [70]. At the Γ point, all bulk t_{2g} bands are degenerate. In a confined 2DEG however, the bands have been found to be anisotropic. Rödel and McKeown's respective teams have studied the (111)-oriented 2DEG and found similar value for the effective masses of the two bands, along the two high symmetry directions, despite noticeable differences in the type of samples studied. The light band mass is roughly $0.3\ m_e$ in both directions, but while the heavy band mass along the $[1\bar{1}0]$ direction is roughly the bare electron mass, it is 8.7 times larger along the less dispersive $[1\bar{1}2]$ direction [71] [72]. A small splitting of $\approx 5\ meV$ between the bands is expected

but has not been observed so far. A top view of the orbitals are presented in figure 1.16**c.** and a tight binding prediction is shown in figure 1.16**f.**

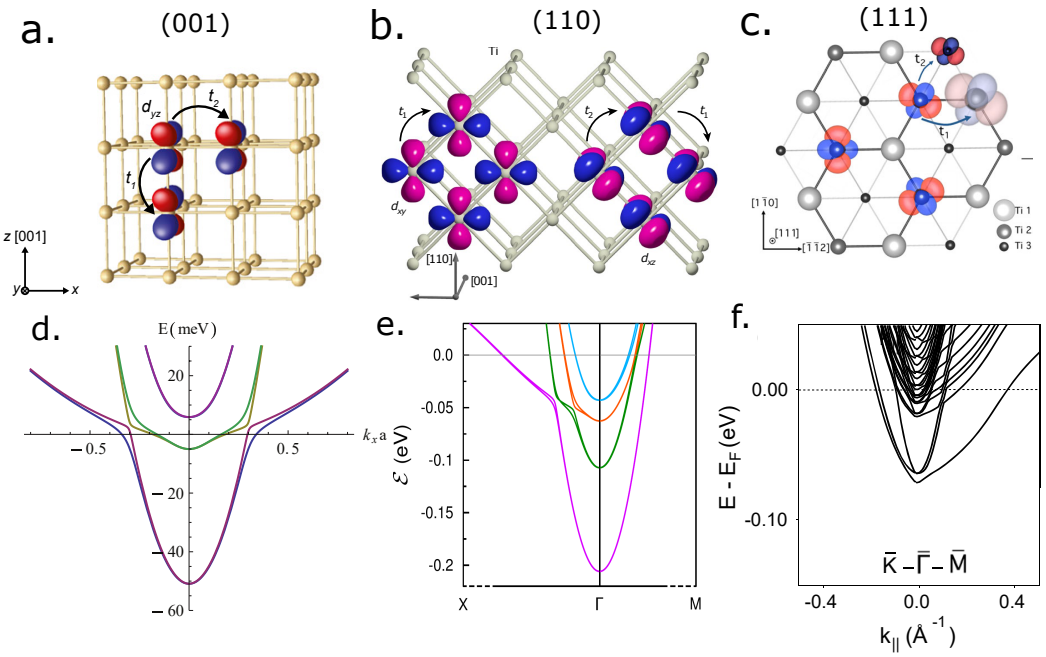

Figure 1.16: **Band engineering via crystal orientation in $SrTiO_3$-based 2DEG** View of the crystal stucture and t_{2g} orbitals in the **a.** (001)-oriented interface with d_{yz} orbital represented **b.** (110)-oriented interface with d_{xy} an d_{xz} orbital **c.** (111)-orientated interface (view from above). **a. b.** and **c.** panels indicate hopping term t_1 and t_2 taken into account in the kinetic term of the 2DEG Hamiltonian. **d.** band structure of the (001)-oriented interface, (From [65]) **e.** idem for the (110) orientation, simulations by B. Göbel. In **e.** a spin splitting which have not been discussed so far is visible at crossing points. **f.** Band structure of the (111)-orientated 2DEG, with multiple subbands visible. (From [72])

1.3.4 Superconductivity in SrTiO3 based 2DEG

Overview

In $SrTiO_3$-based 2DEG, superconductivity can occur when the fabrication is done under certain conditions. As discussed in section 1.3.2, the process requires preparing an atomically-flat TiO_2-terminated interface, either grow crystalline $LaAlO_3$ (polar catastrophe mechanism) or deposit Al via sputtering (oxygen vacancies mechanism), and then anneal the sample under a high partial oxygen pressure. When the sample is cooled down, until the cryostat reaches mK temperature, there is no way to really know if the sample will be superconducting or simply metallic. Similar samples grown under the same conditions can be metallic or superconducting, our understanding of the differences are that inhomogeneities of the sample, as well as non truly reproducible steps in the growth process like annealing, or exposure to atmosphere can play a role in determining the superconducting properties of the sample. Samples with very low carrier density ($n \leq 10^{12}\ cm^{-2}$) are usually not superconducting.

There are two important energy scales in a superconductor, the pairing energy (superconducting

gap Δ) that determines T_c, and the superfluid stiffness J_s which is associated to the phase rigidity of the condensate and determines the superfluid density. The first scale relates to the amplitude of the superconducting condensate wave function while the stiffness relates to its phase. In conventional superconductors, the stiffness is of the order of the Fermi energy and therefore it is much larger than the gap so the physics of the system is largely determined by the gap. In LAO/STO, this is not always the case and the study of the superfluid stiffness, which is a major part of this manuscript, can tell us a lot about the underlying physic of the 2DEG superconductivity.

Gate tunable superconductivity

The main reason why $SrTiO_3$-2DEGs have gathered such attention is that the carrier density of the superconductor can be tuned by applying a gate voltage. This doping is continuous and reversible and can be applied in-situ during the experiment. The peculiar form of the T_c variation as a function of gate voltage (fig 1.9c.) reminds of the famous cuprate superconducting dome as a function of hole doping. In a regime where the T_c is almost suppressed, the superconductivity in the 2DEG consists of puddles, coupled via Josephson effect, giving a peculiar situation where the superfluid stiffness is of the order of the superconducting gap. [34]

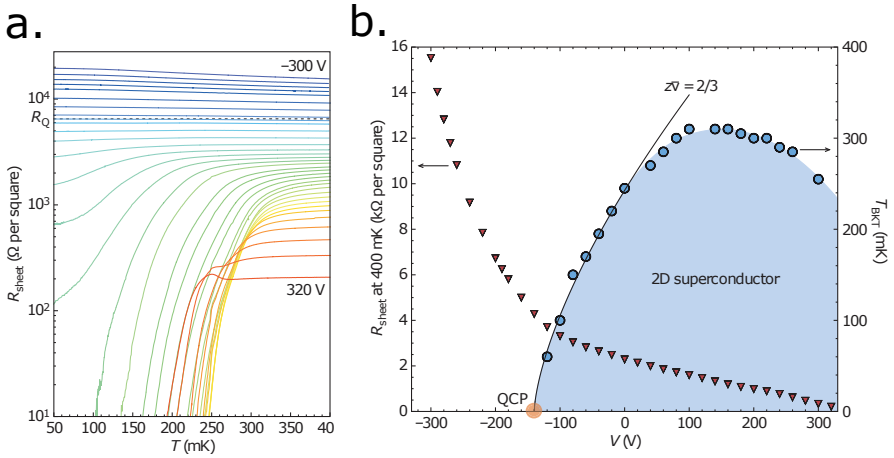

Figure 1.17: **Gate-tunable gap Δ. a.** resistivity as a function of temperature for various gate voltages. **b.** Left axis: Resistivity at 400 mK as a function of gate voltage. Right axis: Superconducting critical temperature as a function of gate voltage, the superconducting region is in blue, from [39].

Reyren et al., who first measured superconductivity in LAO/STO 2DEG, found a superconducting critical temperature of 0.3 K, which is equivalent to a BCS gap in the weak coupling limit of $\Delta \simeq 40\ \mu eV$ [38]. Later tunnel spectroscopy of the gap confirmed this value [73]. Measurements from Caviglia et al. are presented in figure 1.17. Panel **a.** shows the resistivity as a function of temperature for various gate voltages between -300 and +320 V. While the sheet resistance in the normal state varies by orders of magnitude from $10^2\ \Omega$ to $10^4\ \Omega$, the critical temperature varies non monotonically from 0 to 250 mK, and is reported in panel b. When electrons are added with a back gate voltage, the superconducting T_c rises to a maximum value, $T_c^{max} \approx 350\ mK$, before decreasing as doping is further increased. An optimal doping point ($V_G^{opt} = +100\ V$) separates the overdoped regime ($V_G > V_G^{opt}$) from the under doped regime ($V_G < V_G^{opt}$). The current understanding of the metal-to-superconductor transition on the negative gate voltage side is that it correspond to the filling of the second, higher degenerate $d_{xz,yz}$ band which is superconducting while the lower d_{xy} bands are not [74] [34]. We do not still understand why the T_c decreases at very high positive gate voltages.

The first measurement of the superfluid stiffness was carried by J. Bert and collaborators [75] who assessed the local superfluid density from local suceptometry using a scanning SQUID. Their measurements are shown figure 1.18. Panel **a.** shows the superfluid density n_s (proportional to the superfluid stiffness J_s) for a gate voltage of 110 V, as a function of temperature. The grey area is the systematic error. Panel **b.** shows the superfluid density as a function of temperature for various gate voltages. Overall, the superfluid density is between 1 and $3{\times}10^{12}\ cm^{-2}$, representing 1 to 10% of the total carrier density. This corresponds to a stiffness between 15 and 45 μeV assuming an effective mass of 10 m_e for the superconducting band, which is comparable to the superconducting gap. Finally, figure **c.** shows the normalized superfluid density curves as a function of temperature. We notice that they all collapse onto a fit (in dashed line) derived from a BCS model with disorder where $n_s \propto 1-(T/T_c)^{2a}$. They found $a = 1.4$, which is different from the $a = 1$ in a clean superconductor scenario. For the T_c to match experimental data, they went beyond the weak coupling $\Delta = 1.76 k_B T_c$ to $\Delta = 2.2 k_B T_c$.

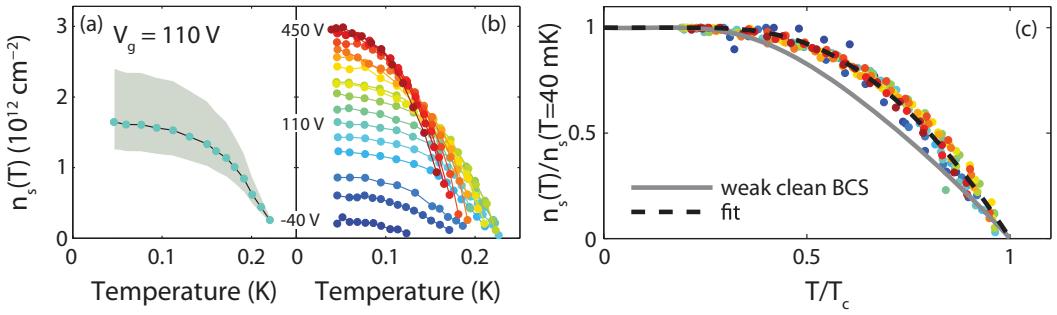

Figure 1.18: **Gate-tunable superfluid density. a.** n_s as a function of temperature for $V_G = 110\ V$, the grey area is the systematic error. **b.** Superfluid density as a function of temperature for all gate voltages. **c.** Normalized superfluid density as a function of temperature, with clean BCS in weak coupling limit in grey line, and a fit of a modified BCS model with $\Delta = 2.2 k_B T_c$ and $n_s \propto 1-(T/T_c)^{2.8}$, from [75].

Other measurements of the superfluid density point to similar value $n_s \simeq 10^{12}\ cm^{-2}$ [34] [76] [77] [78], corresponding to a small fraction (1-10%) of the total carrier density. This means that the 2DEG is deep in the dirty limit, as opposed to the clean limit for which $n_s = n$ (all electrons condense).

Length scales

Two length scales can be extracted from critical magnetic fields measurements. The first one is the Ginzburg-Landau coherence length from the upper critical field in perpendicular geometry $H_{c2} = \phi_0/2\pi\xi^2$ (eq. 1.9). For STO-based superconducting 2DEGs, it has been measured to be around $\xi = 10-100\ nm$ [38] [79] [80] [81]. This is much larger than the typical mean free path ($\simeq$10 nm) computed from sheet resistivity measurements, which further confirm the dirtiness of the superconductivity in the 2DEG. This is not surprising as almost all 2D superconductors are in the dirty limit since scattering events have a higher probability to take place in 2D than in 3D, at constant impurities concentration.

The second length scale is the thickness d, which is obtained by combining the coherence length ξ and the parallel critical field $H_c^{\parallel} = \sqrt{3}\phi_0/\pi\xi d$. It has been estimated to be 7 nm from conductive

tip AFM experiment [44] and 12 nm [79] from critical field measurement. However, as the value of $H_c^{\parallel}$ exceeds by far the Pauli limit, the value of d extracted from the critical field can only be considered as an upper bound. $d \ll \xi$ means that the 2DEG is a true 2D superconductor, where Beresinsky-Kosterlitz-Thouless (BKT) physics is expected to occur.

Measurements of N. Reyren and collaborator [79] of the perpendicular and parallel critical magnetic fields are provided in figure 1.19 as an example. Panel **a.** and **b.** show the resistivity as a function of temperature of the 2DEG under different perpendicular (**a.**) or parallel (**b.**) magnetic fields. We see a suppression of the superconductivity around $H^{\perp} = 80\ mT$ and $H^{\parallel} = 1.7\ T$. Panel **c.** shows the temperature at which the resistance is 50% of the 400 mK resistance, for each field. The inset is a zoom of the data for a perpendicular magnetic field. From $H^{\perp}(0)$ and $H^{\parallel}(0)$ we can estimate the superconducting coherence length to be $\xi = 70\ nm$ and the thickness of the 2DEG to be $d = 10\ nm$. Having $d \ll \xi$, we can conclude that this 2DEG was indeed 2D.

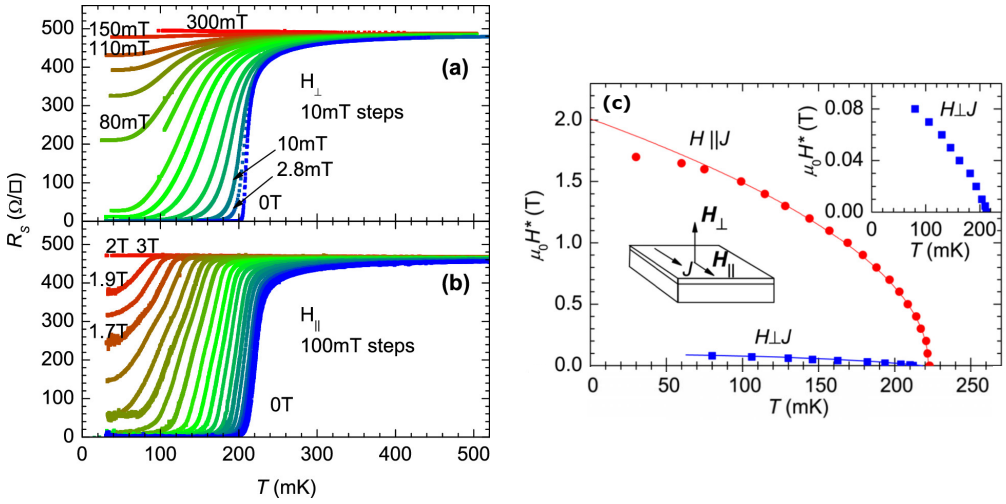

Figure 1.19: **Critical field measurements in LAO/STO. a.** Resistivity as a function of temperature under different perpendicular magnetic fields. **b.** Resistivity as a function of temperature under different parallel magnetic fields. **c.** Field-Temperature superconducting phase diagram for parallel (red) and perpendicular (blue) magnetic field. From [79].

Structural inhomogeneity in superconducting 2DEG

Below 105 K, the tetragonal transition of STO leads to the formation of multiple domains at the interface whose c axis can be along the x, y or z direction. It has been shown by B. Kalisky and collaborators that the conduction occurs in micrometer wide channels, either along tetragonal domain walls or along domains with a given direction [82]. Other work at another superconducting interface $KTaO_3$(111), shows similar stripes where the conduction preferably occurs, which further confirms that micron-size inhomogeneities are present in most oxide 2DEGs [83]. The transport properties we measure, such as the conductivity, are thus global average on wide conducting channels.

Spatial inhomogeneities over micrometers scale can have different effects on superconductivity. They can generate small variations in the chemical potential, gap, and other properties over large pads. At the superconducting transition, we can have nucleation of superconductivity in different places of the 2DEG, and the superconducting islands are connected through proximity effect. This

situation has been observed in a LAO/STO(001) 2DEG by our group and described in more detail in ref [34].

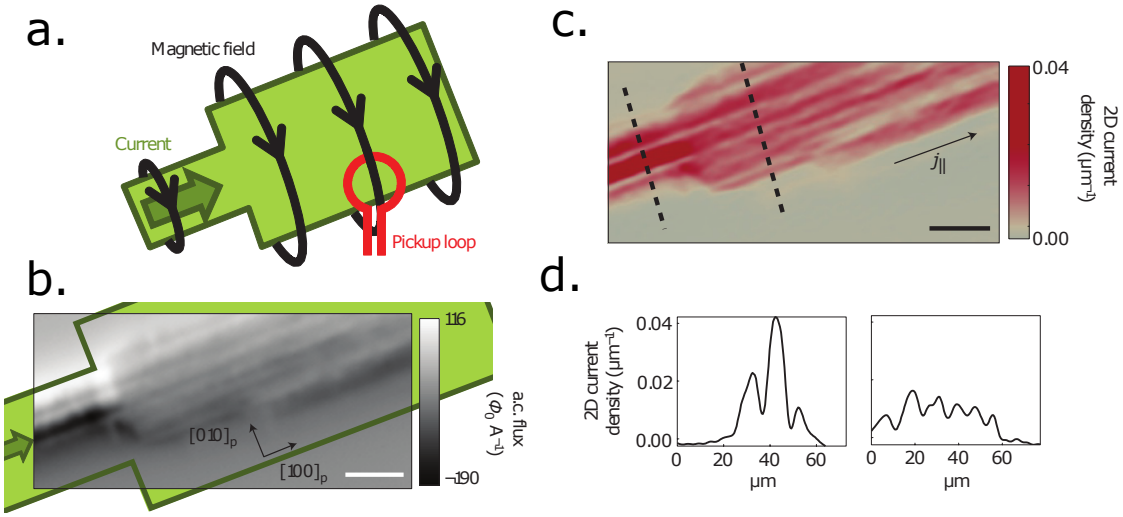

Figure 1.20: **Measurement of micrometer wide conducting channels at LAO/STO 2DEG by B. Kalisky et al. [82] a.** The pick up loop in red measures the current flowing in the sample as a function of position. **b.** Magnetic flux image of current passing through the 2DEG. In green is shown the dimension of the sample. **c.** Current densities reconstructed from flux imagery. **d.** 2D density cuts along the dashed line in **c.**

Chapter 2

Experimental setup and fabrication

2.1 Cryogenic setup

2.1.1 Cryo-free refrigerator

All experiments presented in this thesis, besides a few high field measurements or angle-dependant magnetoresistance measurements, were conducted in a dilution refrigerator from Cryoconcept. It includes five different temperature stages (see figure 2.1a.). It is a dry refrigerator, meaning that cooling to 3K is ensured by a two stages pulse tube, contrary to a wet refrigerator where liquid He is used to cool down to 3K. The cooling power at the first stage (50K) is 40 W, while it is 1.5 W at 3 K. The refrigerator is equipped with mechanical dampers to lessen the effect of vibrations on the measurements and temperature stability at mK temperature. The refrigerator is also equipped with a superconducting coil providing a magnetic field up to 7 Tesla below 4 K.

2.1.2 Dilution regime

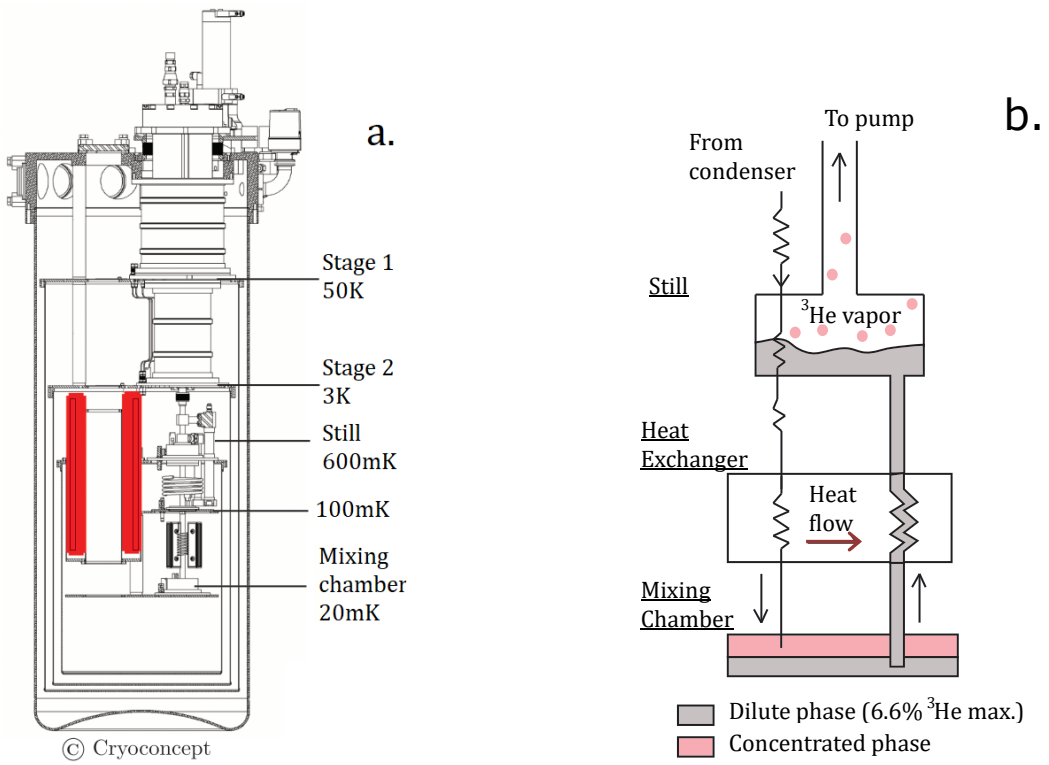

Figure 2.1: **Sub-kelvin Cryogenic setup. a.** Cryo-free dilution refrigerator from Cryoconcept. **b.** Dilution circuit with helium circulation (black arrow) and heat flow (red arrow) flow.

When the mixing chamber stage reaches 3.5 K, it is possible to initiate the dilution regime. A scheme illustrating the principles of operations is represented in figure 2.1b. At the still stage, below 870 mK, the helium separates into a ^{4}He superfluid in grey on the figure and a ^{3}He vapor in pink due to the fact that ^{3}He has a much higher partial pressure than ^{4}He at these temperature. The ^{3}He vapor is compressed by a pump and sent to the mixing chamber through a condenser. On its way down, ^{3}He is cooled by the still and the up-going fluid from the mixing chamber *via* a heat exchanger. In the mixing chamber, the Helium mixture is separated in two phases: a higher concentrated phase of almost pure ^{3}He and a lower dilute phase made of $\approx$ 6.6 % of ^{3}He, separated by a phase boundary.

When the in-going ^{3}He crosses the boundary between the concentrated and the dilute phase, it lowers its entropy, thus cooling the mixing chamber. The ^{3}He is pumped from the dilute phase through the still (^{4}He is at rest) and the cycle goes on. In our setup, this system allows to cool down the mixing chamber plate at a base temperature of 13 mK (or more depending on the heat of the load) with a cooling power of a 250 μW at 100 mK. In practice, due to limitations in the size of the heat exchange area, no dilution refrigerator can cool down below a few mK.

2.1.3 Physical Properties Measurement System (PPMS)

During this thesis, we also used a Physical Properties Measurement System (PPMS) to perform higher magnetic field and angle dependant magnetic field measurements. It is represented in figure 2.2a. In contrast with the Cryoconcept dilution refrigerator, the PPMS is a wet refrigerator, composed of an outer shell filled with liquid nitrogen and an inner shield filled with liquid helium. The temperature of the sample holder, can be precisely controlled between room temperature and 3 K. The PPMS is equipped with a superconducting coil producing a magnetic field up to 13 T and various sample holders allow for angle-dependant field measurements, such as the in-plane anisotropic magnetoresistance one (AMR) (see figure 2.2b.). Although the PPMS comes with its own electronics for transport measurements, we prefer to use external instruments (voltages and current sources, lock-in, amplifiers...) that offer a better control.

Figure 2.2: **Physical Properties Measurement System** From left tor right : Monitor, ^{4}He refrigerator, probe and sample holder for in-plane angle-dependant field measurement.

2.2 Transport measurement wiring and setup

2.2.1 Wiring

Very low frequency (<10kHz)

12 resistive twisted pairs (24 wires) made of constantan are used for dc measurements. They are thermalized at each temperature stages (except 100 mK) with gold platted copper strips on thin Kapton. Thermalization also provides a natural capacitance to ground which together with the resistance of the wire and their inductance ensures distributed low pass filtering.

Outside the cryostat, the twisted pairs are connected to a breakout box with a 24 channels BNC connector panel with LC filters (1 MHz) and then to the commercial Qdevil box. At the lowest temperature stage, the twisted pairs are connected to a sample holder with a 25 miniature sub-D. Figure 2.3**a.**, **b.** and **c.** show example of dc sample holders that have been used in this thesis. All sample holder are closed by a lid to avoid thermal radiation hitting the sample.

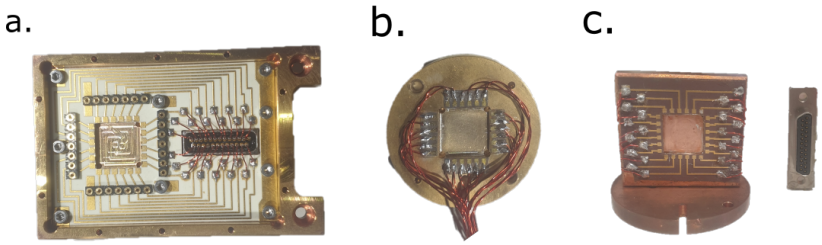

Figure 2.3: Sample holder for dc measurement **a.** for base plate anchoring **b.** for perpendicular magnetic field measurement **c.** for parallel magnetic field measurement, with sub-D visible.

For the most sensitive experiments, a two stages low-pass filter box provided by QDevil was mounted in series, anchored on the mixing chamber plate connected and directly to the sample holder. The first stage contains a RF filter made of three reflective 7-pole Pi filter, attenuating above 80 MHz with a maximum current of 10 mA. The second filter is a RC filter made of one reflective 7-pole Pi filter followed by 2 dissipative RC filters which attenuates above 50 kHz and allow a maximum current of 6.5 mA.

Intermediate frequency (2MHz)

14 micro-coaxial shielded lines made of stainless steel are used for AC measurements. They are ended by SMA connectors at the input of the cryostat and SMC to SMA connectors at the sample holder level. As for the DC lines, they are also thermalized through connectors at each stage of the refrigerator. At the input of the refrigerator, each line is filtered with a Mini-Circuits SLP5+ (Low pass filter, DC to 5 MHz). At the bottom of the refrigerator, home-made copper powder filters (fig 2.4a.) are used to cut high frequencies. Characterization of this filter is shown in figure 2.4b.

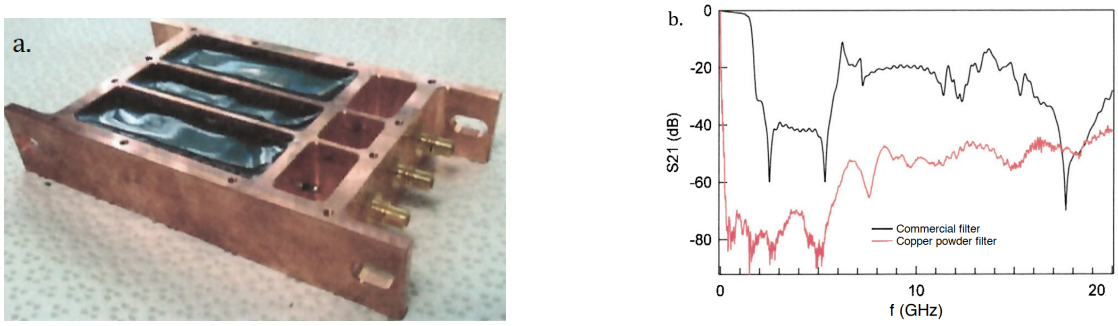

Figure 2.4: **a.** Copper powder filter made of 14-25 μm diameter copper particle mixed with stycast (Sigma Aldrich 32G453). **b.** Transmission of the copper filter compared with a commercial 1.2 GHz LC filter.

Two sample holders used for AC measurement, one to be anchored on the base plate and one to be used in perpendicular magnetic field, are shown figure 2.5**a.** and **b.** respectively.

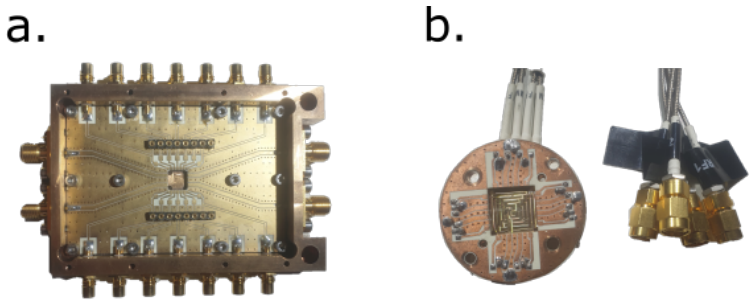

Figure 2.5: Sample holder **a.** with SMC connectors, anchored to the base plate **b.** with SMA connectors visible, for perpendicular magnetic field measurements.

Microwave frequencies

The cryostat is equipped with up to four microwave lines made of semi-rigid coaxial cables terminated by 2.92mm or SMA connectors enabling in principle measurements up to 40 GHz (frequency can be limited by microwave passive and active components used in different experiments). Input lines that are used to carry signals to the sample are strongly attenuated at the different temperature stages to suppress thermal noise while return lines usually involve a cryogenic amplifier. In this thesis, a microwave set-up has been used to measure the superfluid stiffness of the superconducting 2DEGs. It will be described in section 2.3.

2.2.2 Instruments

Low frequency measurements instruments

A Yoko7651 is used as dc source, and for finer measurement a Keitlhey 6221 nano-volt source is used. The dc measurement signal is amplified using a Stanford amplifier SR570 usually with a gain G=100 or 1000, typically with an internal low pass filter of frequency f=3 or 10 Hz set to 12 dB attenuation. The reading is done using a Keithley 2000 or nanovoltmeter Keithley 2182A.

AC measurements are performed using Signal Recovery 7265 DSP Lock-in Amplifiers as voltage source and measurement instrument.

Current and Voltage polarisation

We mainly have performed transport measurement under current biasing for most of the samples presented in this manuscript. For that, a dc or ac source was used to feed a home-made polarisation box that converts a voltage into a current. The box is made of a large resistance which fixes the current, and a smaller resistance for current reading. The circuit is represented below in figure 2.6a.

When we perform voltage biasing, we use a home-made voltage divider box to send a very small voltage signal. The box is a voltage divider, with a resistance in series to read the current presented in figure 2.6b. The RC filter has a frequency cut-off of $f \approx 833$ Hz ($R = 1.2$ kΩ, $C = 1$ μF). The voltage divider is composed of a first resistor $R_1 = 130$kΩ and a second resistor $R_2 = 1.2$kΩ giving

a maximum division of the applyied tension of $\frac{130+1.2\text{k}\Omega}{1.2\text{k}\Omega} \approx 108$ when $R_{load} \gg R_2$. A simulation of the voltage divider as a function of the load resistance is represented figure 2.6c.

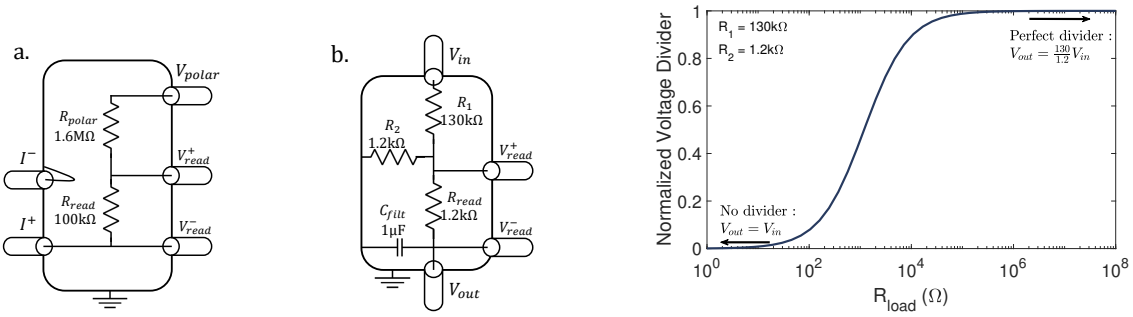

Figure 2.6: **a.** Current polarisation box circuit. **b.** Voltage divider polarization box. **c.** Effective division of the voltage divider as a function of the load resistance.

2.2.3 DC measurement of resistance

During this thesis, we measured a variety of STO and KTO based 2DEGs on the form of plain samples or patterned devices (like Hall bars for instance). Basic transport measurements in the superconducting state, such as resistivity vs. temperature or current-voltage curves were performed in four points configuration under current bias. The 2DEGs were connected to the sample holder pads with Al wire bonds. For plain samples, we used the Van der Pauw configuration (fig 2.7**a.**) in which the sheet resistance of the 2DEG is given by the formula [84]

$$R_{\square} = \frac{\pi}{\ln 2} \cdot \frac{\Delta V}{I} \approx 4.53 \frac{\Delta V}{I}$$

where ΔV is the potential drop and I the current.

For Hall bars, the sheet resistance is simply obtained by dividing the total four points resistance by the number of squares between the voltage leads (see figure 2.7**b.**, where the factor 2 account for the two square of the bar). An additional contact V_H allows measuring the transverse Hall voltage under magnetic field. Note that in all the experiment, the bias current is chosen to be much smaller than the critical current, of order of 100 μA for a typical 5*5 mm sample in a Van der Pauw geometry and of order 1 μA for a typical few micron wide Hall bar.

Superconducting transition in the resistance was measured in current-bias, with a Yoko 7651 voltage source followed by the box described figure 2.6a. used to apply a current of tens to hundreds of nA which is read through the resistance directly by a Keithley 2000. The sample resistance is read through a Stanford 570 amplifier by a second Keitlhey 2000.

Another possible geometry to measure the resistivity of a 2DEG is to use four equally-spaced aligned contacts in the middle of the sheet (fig. 2.7**c.**). Small deviations in term of alignment or spacing are easily corrected by multiplying by a known geometrical factor [85]. However this method was only marginally used during my PhD for two reasons. The first one is mainly aesthetic : having four contacts in the middle of the sample is undesirable, especially if we want to measure it multiple times while ensuring the homogeneity of the 2DEG on the surface. The second reason is that this geometry, while probing the ρ_{xx} component of the resistivity tensor, doesn't allow for simultaneous measurement of the ρ_{xy} component *via* the Hall effect

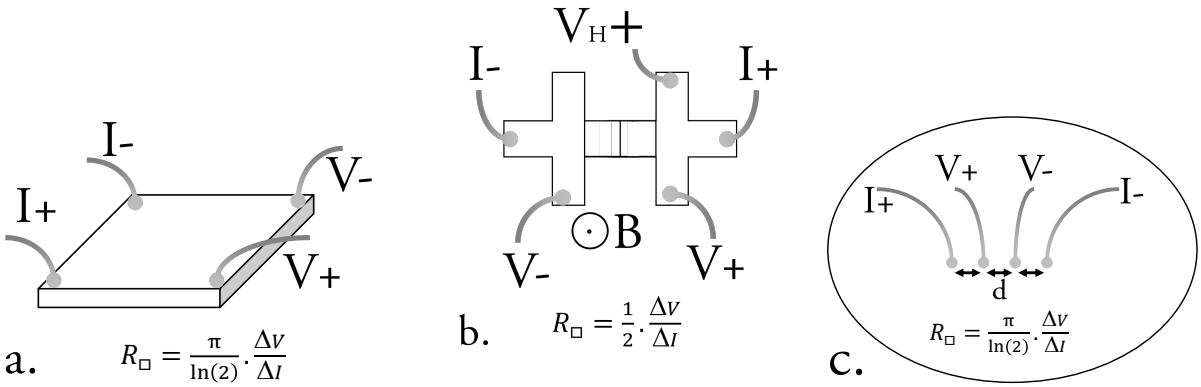

Figure 2.7: **Various contact geometry used to measure sheet resistance of 2DEGs. a.** Van der Pauw. **b.** Hall bar. **c.** Valdes' method.

2.2.4 DC measurement of Hall effect and magnetoresistance

Hall effect and magnetoresistance were measured using the same setup as described above for resistivity measurements, only the contacts used as current source and probe changed. We used perpendicular set of diagonal contacts in Van der Pauw geometry for the plain sample and the transverse V_H contact for the Hall bar (see fig 2.7). Because the Hall effect signal is expected to be small, a gain of G=1000 or 10000 was typically used.

The magnetic field is applied using a superconducting coil from Cryomagnetics Inc with a power supply providing a current up to 42 A, corresponding to around 7 Tesla. The Ampere to Tesla conversion factor is 6.0208 A/T. The coil is anchored to the 2nd stage of the refrigerator and remains at fixed temperature of 3-4 K. A shield anchored on the still stage (500 mK) protect the sample from thermal radiation coming from the magnet. Measurements can be performed at any temperature (for the sample stage) between 13 mK and 4 K. Thanks to a thermal switch, the superconducting magnet can be operated in a persistent configuration in which the current circulates only through the coil, and not through the power supply.

2.2.5 AC capacitance measurement setup

In this thesis, we used the electric field effect to control the carrier density n_{2D} of the 2DEGs. For this purpose, in most of our samples, a metallic gate is deposited on the back-side of the STO or KTO substrate. The 2DEG is usually grounded at the negative current contact (I^-). When a positive (negative) back-gate voltage is applied with respect to ground, electrons are added in (removed from) the 2DEG. As we will see in the next chapter, transport in these 2DEGS can involve different bands making difficult the extraction of the carrier density by Hall effect in some doping regimes. For this reason, it is extremely useful to measure the cate capacitance C_G, i.e the capacitance of the capacitor made of the STO (or KTO) dielectric material between two plates consisting of the metallic gate on one side and the 2DEG on the other side that determines how many electrons are added or removed by a change in gate voltage. As both STO and KTO are quantum paraelectric, their dielectric constant is electric field dependent which means that the gate capacitance depends on the voltage applied on the gate.

The capacitance measurement setup presented in figure 2.8 is composed of a DC voltage source for gating, an AC voltage source, a transformer and two lock-in amplifiers for measurements. A

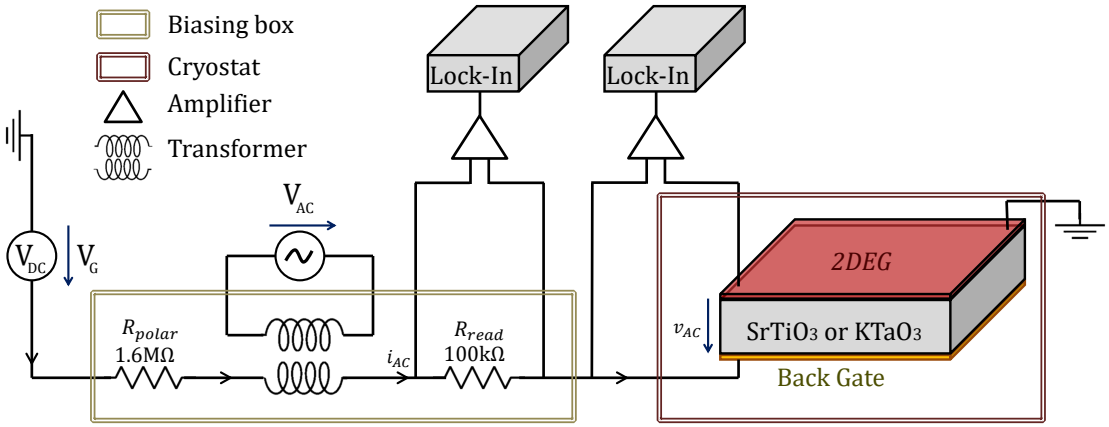

Figure 2.8: setup for capacitance measurement

small AC voltage of frequency ω (typically 10-100 Hz) is added through a transformer, on top of the gate voltage, between the backgate and the 2DEG. The current i_{ac} is obtained by measuring the ac voltage drop across R_{read}. The second lock-in amplifier measures the voltage drop v_{AC} across the sample substrate. The complex impedance of the sample is then given by:

$$Z_{AC} = \frac{i_{AC}}{v_{AC}} = \frac{1}{i\omega(C_G + C_{para})} \tag{2.1}$$

where C_{para} denotes parasitic contribution to the measured capacitance due to the set-up (sample holder, cables etc) which is usually smaller than C_G. In a plane capacitor geometry, the gate capacitance is given by:

$$C_G = \epsilon_0 \epsilon_r \frac{A}{d} \tag{2.2}$$

where ϵ_0 is the vacuum permittivity, ϵ_r is the relative permittivity of the material (STO or KTO), A is the area of the plane capacitor and d is the thickness separating the two plane capacitors.

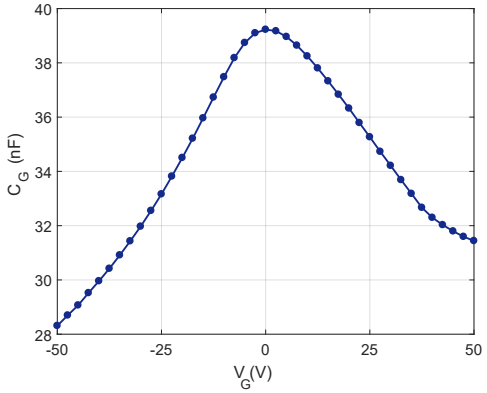

Figure 2.9: Capacitance as a function of gate voltage, measured in a $LaAlO_3/SrTiO_3(110)$ sample.

Figure 2.9 shows a typical measurement of the gate capacitance as a function of gate voltage for a LAO/STO sample of size 5×5mm. The capacitance is found to be maximum for V_G=0 V and

decreases roughly symmetrically on both sides for $V_G < 0$ and $V_G > 0$ as expected from the expression of the relative dielectric constant of STO (eq. 1.42).

Carrier density from gate capacitance

The capacitance as a function of gate voltage is used to compute the relative variation of carrier density with gate voltage. If we can reliably determine the carrier density by Hall effect for a given gate voltage, then we can compute how many electrons are added or removed upon gating, knowing the substrate capacitance C_G. The carrier density as a function of gate is given by:

$$n(V) = n(V_G^{min}) + \frac{1}{eA}\int_{V_G^{min}}^{V} C_G(V)dV \tag{2.3}$$

where A is the area of the plane of the capacitor.

In practice, the determination of the carrier density in oxides 2DEGs is reliable in the low doping regime, where we usually have a linear Hall effect characteristic of single band conductivity. We will therefore use the gate capacitance to extrapolate the variation of n with V_G in the high-doping regime where multiband conductivity can occur, with non-linear Hall effect as a signature of this regime. A parasitic capacitance arises from the measurement set-up, which is to be accounted for. In practice, it is deduced by matching the evolution of the carriers in the low-doping regime, if we know at least two points in the $n(V)$ curve from Hall effect. For this purpose, we simply consider that the measured capacitance is $C_{measured} = C_G + C_{parasitic}$. Typically the parasitic contribution is 10 times smaller than the substrate contribution.

2.3 Resonant micro-wave setup

2.3.1 Overview

During this thesis, we measured the superfluid stiffness of various 2DEGs using the microwave set-up shown in figure 2.10. The general idea is to measure the microwave reflection coefficient of a RLC equivalent circuit in the frequency range [0.1 - 1 GHz], and link the shift of the resonance frequency in the superconducting state to the kinetic inductance of the superconducting 2DEG. The latter is inversely proportional to the superfluid stiffness J_s which is the energy scale associated to the phase rigidity of the condensate.

In figure 2.10**a.**, we see a LAO/STO sample connected *via* aluminium wire bonding between the central line and the ground of a coplanar wave guide (CPW). Surface Mounted Devices (SMD) are soldered to create an equivalent RLC circuit. Their values are chosen to obtain the desired resonance frequency and impedance of the circuit in order to maximize the microwave absorption.

We now focus on figure 2.10 b. : a vector network analyzer sends a signal from port 1, which is attenuated at each stage of the dilution refrigerator. The signal is then weakly coupled to the sample circuit of impedance Z_L through a directional coupler. After reflection, the signal is amplified at 3 K by a HEMT (Low-Noise Factory HMET-based LNC1_12A amplifier with 40 dB gain in the 0.3-12 GHz range) and is measured on port 2 of the VNA. Lastly, we measure the complex ratio of the amplitude of the collected wave at port 2 by what is sent at port 1, which we call S_{21}. A bias-tee, placed between the sample circuit and the directional coupler, allows a simultaneous measurement of the RF and dc response of the sample.

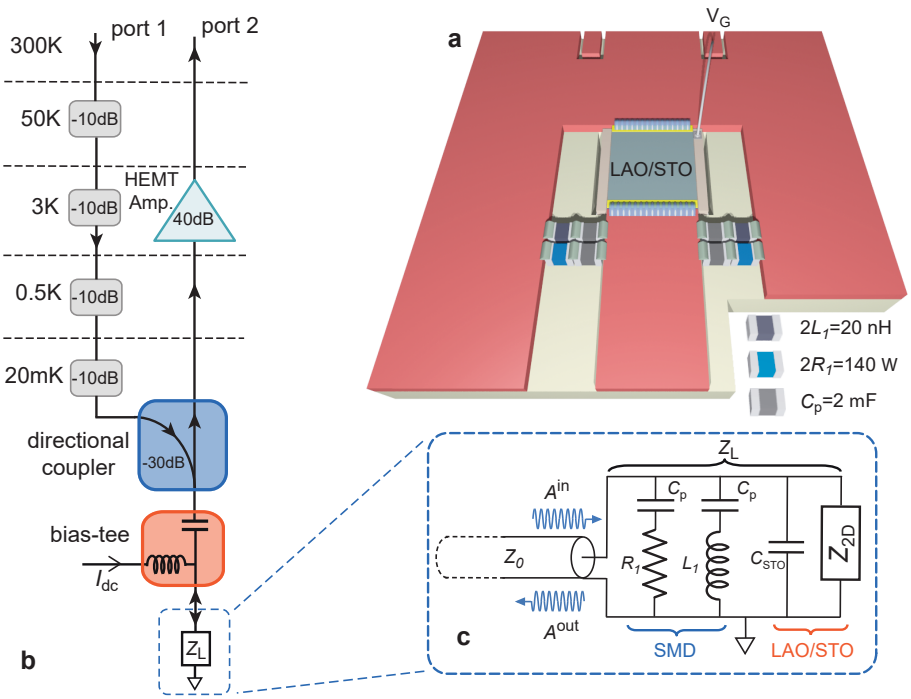

Figure 2.10: **Microwave setup for superfluid stiffness measurement a.** 2DEG connected between the central line and ground of a CPW, in parallel with SMDs to design the RLC equivalent circuit **b.** Schematic of the micro-wave setup: the signal sent from port 1 is attenuated at each stage of the refrigerator, weakly coupled and sent to the sample circuit (Z_L). Part of it is absorbed, the rest is reflected and sent back to port 2 after amplification. The bias tee allows us to also perform a simultaneous DC measurement. **c.** RLC equivalent circuit of the load, of impedance Z_L, modelled by the complex impedance of the 2DEG Z_{2D} in parallel with the substrate capacitance C_{STO}, in parallel with a resistor R_1 in parallel with an inductor L_1. High SMD C_p values are used in order to avoid a short circuit when measuring in DC.

Finally, we consider the equivalent electronic circuit, shown in figure 2.10**c.** A line of impedance $Z_0 = 50\ \Omega$ transmits the source signal between its central line and the ground. The sample circuit impedence Z_L is made of: a chosen resistance R_1, an inductance L_1, the 2DEG we are interested in measuring and a parallel capacitance from the substrate C_{STO}. Two protective capacitance C_p are also added to prevent a short circuit to L_1 or R_1 when simultaneously measuring the 2DEG in DC *via* the bias-tee. The large value of C_p ensures that they do not play any role in the RF measurement. The values of the SMD R_1 and L_1 are chosen so that the equivalent R of the circuit is close to 50 Ω, and the resonance frequency is in our frequency range [0.1 - 1 GHz], respectively. The reflection coefficient at the sample circuit level, $\Gamma = A_{out}/A_{in}$ is related to the transmission coefficient S_{21} via a calibration procedure described in appendix A.

2.3.2 From microwave reflection to superfluid stiffness

The microwave setup is designed to measure the reflection coefficient Γ of the sample circuit which is related to its impedance through the relation $\Gamma = \frac{Z_L(\omega)-Z_0}{Z_L(\omega)+Z_0}$ where $Z_0 = 50\ \Omega$ is the impedance

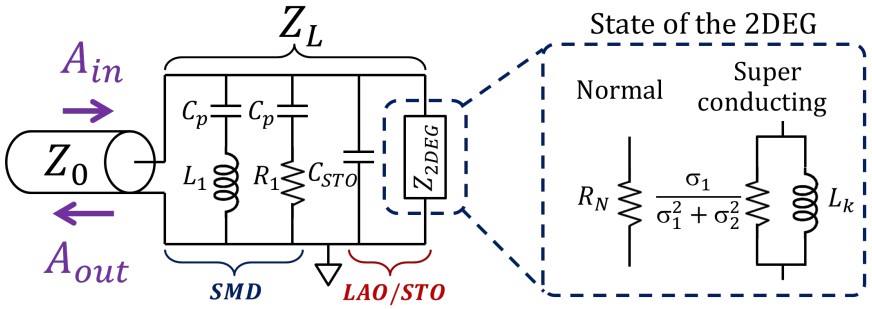

Figure 2.11: Load impedance Z_L, adapted to a $Z_0 = 50\ \Omega$ line. The circuit is composed of surface mounted devices (SMD) L_1, R_1 and C_p. C_p prevents shorting the circuit to the ground during DC measurements. The sample (here LAO/STO) is composed of the capacitance $C_{STO}^{\parallel}$ in parallel with the impedance Z_{2DEG} which is purely resistive in the normal state but develops a parallel kinetic inductance from Cooper pairs in the superconducting state.

of the line and Z_L is the sample circuit's impedance. According to figure 2.11:

$$Z_L(\omega)^{-1} = \frac{1}{iL_1\omega} + iC_{STO}\omega + \frac{1}{R_{sub}} + \frac{1}{R_1} + \frac{1}{Z_{2DEG}} \tag{2.4}$$

Here, R_{sub} represents the losses due to the substrate, C_{STO} is the parallel substrate capacitance and Z_{2DEG} is the complex impedance of the 2DEG.

An example of a typical measured Γ, after the calibration procedure described in appendix A, is shown figure 2.12 below for a given set of R, L and C values specified in the legend.

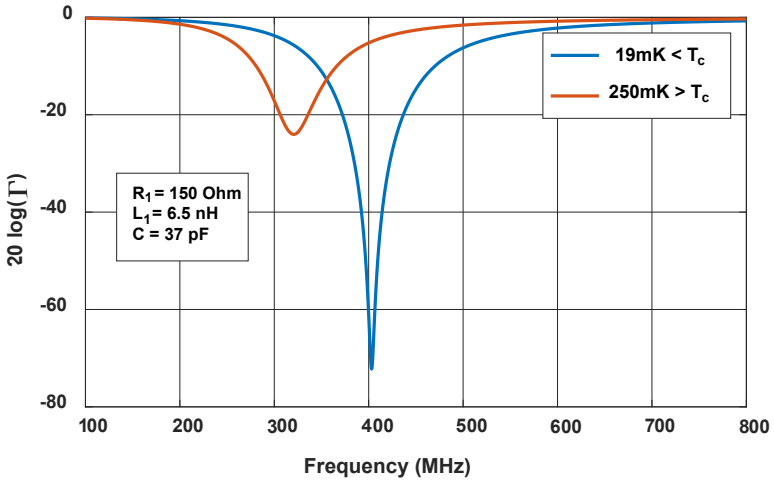

Figure 2.12: Magnitude of the reflection coefficient in dB of a LAO/STO(111) 2DEG, embedded in a RLC circuit which SMD R_1 and L_1 are specified in the figure. The red line correspond to the normal state signal where $Z_{2DEG} = R_s$ and the blue one is the signal in the superconducting state where L_k is significant and shifts the resonance frequency $\omega_0 = 1/\sqrt{(L_{tot}C_{STO})}$.

At the resonance frequency, the impedance becomes purely real (eq. 2.4), the signal is dissipated in the sample circuit, and the reflection coefficient Γ exhibits a dip, along with a 2π phase shift. The frequency of this absorption dip is $\omega_0 = 1/\sqrt{(L_{tot}C_{STO})}$, and the height of the deep is determined by the impedance mismatch between the circuit and the line of impedance 50 Ω.

In the normal state, the 2DEG impedance Z_{2DEG} is assumed to be given by the normal state resistance ($Z_{2DEG} = R_s$) as $\omega \ll 1/\tau$ and the geometrical inductance of the 2DEG is negligible. In the superconducting state, however, we have a contribution from the normal electrons σ_1 and Cooper pairs σ_2 such that

$$\frac{1}{Z_{2DEG}(\omega)} = \sigma_1(\omega) + i\sigma_2(\omega)$$

In the dirty limit ($\xi \gg l_{MFP}$ where ξ is the coherence length and l_{MFP} is the mean free path) and low frequency regime ($\hbar\omega \ll \Delta$), the imaginary part of the conductance σ_2 is :

$$\sigma_2(\omega, T) = \frac{1}{L_k(T)\omega} = \frac{n_s(T)e^2}{m^*\omega}$$

where L_k is the inductance of the superconducting 2DEG Cooper pairs, n_s is the superfluid density and m^* the effective mass of the superconducting carriers.

In the superconducting state, the kinetic inductance of the Cooper pairs adds in parallel with the SMD inductance (L_1) and the resonance frequency $\omega_0 = \frac{1}{\sqrt{L_{tot}C_{STO}}}$ shifts according to $L_{TOT}(T) = \frac{L_1 L_K(T)}{L_1 + L_k(T)}$ from $L_{TOT} = L_1$ to its maximum value $L_{TOT}(0) = \frac{L_1 L_K(0)}{L_1 + L_k(0)}$ at T $\simeq$ 18 mK when the superfluid density n_s is maximum.

The superfluid stiffness J_s, kinetic inductance of Cooper pairs L_k and superfluid density n_s are all linked together through the Mattis-Bardeen formula 1.34 derived in the dirty-limit and low frequency regime in section 1.1.4:

$$J_s(T) = \frac{\hbar^2}{4e^2 L_k(T)} = \frac{\hbar^2 n_s(T)}{4m^*} \tag{2.5}$$

Therefore, tracking the evolution of $L_k(T)$ provides both the evolution of $J_s(T)$ and the superconducting density n_S.

The resonant method described in this section can provide an accurate determination of J_s in most of the gating and temperature ranges. However, in some rare cases, the resonance may be less visible for instance because of parasitic oscillations in S_{21} due to standing waves in the microwave set-up. For this reason and to provide the best possible quality data, we apply a calibration procedure that relates the measured S_{21} coefficient to the reflection coefficient Γ at the sample circuit level. This procedure is described in appendix A.

2.3.3 Directional coupler

A directional coupler is a passive device made of two lines which can be used to separate incoming and outgoing waves in a reflection measurement (figure 2.13). While most of the signal fed to port 1 is dissipated in the load Z_0, a tiny fraction (-30 dB) of it is coupled to port 3 which is connected to the sample load. After reflection, the signal containing the information on the superconducting

2DEG state is fully transmitted to port 4 before being amplified at the 3K stage. The one used in the setup decribed in previous chapter is a Krystar suited for experiments in the 0.3 - 18 GHz range.

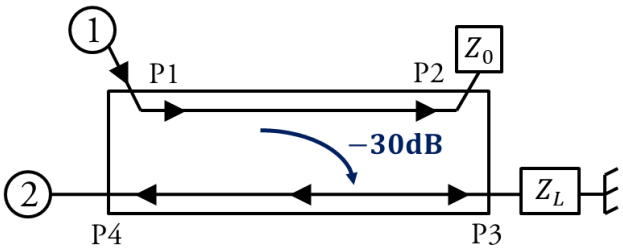

Figure 2.13: Directional coupler: The port 1 of the VNA is used to sent a wave on P1. Most of its power is dissipated on P2 where a $Z_0 = 50\ \Omega$ closes the circuit. The signal is transmitted with a 30 dB attenuation to the sample through P3. The reflected signal travels from P3 to P4 and ultimately to port 2 of the VNA. In a real setup, there might be a bias-tee after P3 to allow simultaneous DC measurement

2.3.4 Bias-tee

A bias tee is a passive device made of three ports used to separate DC and RF signals. It splits the outgoing signal from the sample into a capacitive and inductive line, where only the AC and DC signal propagate respectively.

2.3.5 Sample holder and SMD

SMD components used for the RF setup are certified for milli-kelvin temperature. Printed circuit board containing the coplanar wave guide (see figure 2.10) was made from high frequency laminate RO3010 supplied by Rogers.

Chapter 3

Multiband superconductivity at the LAO/STO(110) and LAO/STO(111) interfaces

At LAO/STO interfaces, the 2DEG conductivity is ensured by the t_{2g} electrons of the Ti atom, thus, a change in crystal orientation is expected to significantly modify the physics of the system. Indeed, the resulting band properties, such as their effective mass and hierarchy in the quantum well, change, leading to different superconducting properties. In this chapter, we will first present resonant-microwave measurements of the superfluid stiffness and critical magnetic field in $LaAlO_3/SrTiO_3$(110) and show that superconductivity occurs in both the d_{xy} and the degenerate d_{xz} and d_{yz} bands, in contrast with the (001) orientation. We will make the case that the LAO/STO(110) 2DEG is a multicondensate superconductor, as predicted a long time ago for bulk STO. In a second part, we will present similar measurements for the $LaAlO_3/SrTiO_3$(111) interface, showing that despite evidences for multiband transport in the normal state, it appears to mostly behave as a single condensate superconductor.

3.1 Overview of the systems

3.1.1 Band structure of LAO/STO(110)

In $LaAlO_3/SrTiO_3$(110) samples, the growth of the LAO layer takes place along the (110) direction, which is more challenging than the (001) and has been less studied. High-angle annular dark field images of the two interface (001) and (110) are presented in figures 3.1**a.** and **b.** Panels **c.** and **d.** show how the t_{2g} orbital involved in the conductivity are coupled to each other for the (001) and (110) orientation respectively. These t_{2g} 3d orbitals have different overlap and thus different effective masses than in the (001) interface, leading to different transport properties.

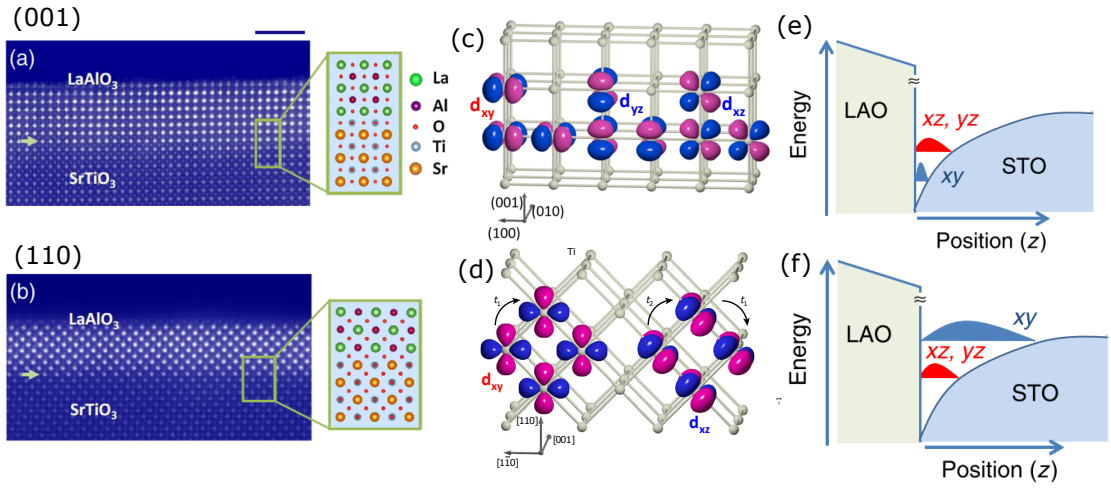

Figure 3.1: **Comparison of the (001) and (110)-oriented LAO/STO interfaces.** High-angle annular dark field scanning transmission electron microscopy of 8ML of LAO on STO for the (001) **(a)** and (110) **(b)** orientation, from [86]. Sketch of the relative orientation of the t_{2g} orbitals with respect to the interface in the (001) **(c)** and (110) **(d)** orientation. Band hierarchy and location in the LAO/STO quantum well at the (001) **(e)** and (110) **(f)** orientation, from [87].

Using XAS (X-Ray absorption spectroscopy) and XLD (X-ray linear dichroism) Pesquera et al. have shown that the band hierarchy is reversed in the (110) orientation compared to the (001) one [86], i.e. in the (110)-2DEG the d_{xy} orbital is higher in energy compared to the $d_{xz,yz}$ orbitals, contrary to the (001) situation (fig. 3.1**e.** and **f.**).

In this section, we will introduce the reader to the tight binding model proposed by Wang et al. [88]. They consider a three bands Hamiltonian justified by the fact that inter-orbital hopping is negligible based on Wannier projection of DFT calculations [89]. It is composed of two kinds of first neighbour hopping terms, t_1 which is the hopping between two co-planar orbitals and t_2 which is the hopping between two orbitals staked on top of each other. Given that the three t_{2g} orbitals are decoupled, the analytical expression of the bulk Hamiltonian is:

$$\begin{aligned} H_{xy}(kx,ky,kz) &= \epsilon_0 + 2t_1\cos(k_x a) + 2t_1\cos(k_y a) + 2t_2\cos(k_z a) \\ H_{yz}(kx,ky,kz) &= \epsilon_0 + 2t_2\cos(k_x a) + 2t_1\cos(k_y a) + 2t_2\cos(k_z a) \\ H_{xz}(kx,ky,kz) &= \epsilon_0 + 2t_1\cos(k_x a) + 2t_2\cos(k_y a) + 2t_2\cos(k_z a) \end{aligned} \tag{3.1}$$

where a is the lattice constant, and $t_1 = -0.455\ eV$ and $t_2 = -0.04\ eV$ have been found by fitting ARPES data with DFT calculation. In the following chapter however we take $t_1 = -0.380\ eV$ and $t_2 = -0.016\ eV$ in order to have masses around $14\ m_e$ and $0.7\ m_e$.

When $\epsilon_0 = -4t_1 - 2t_2$, the energy at the Γ point is zero, which allows for Taylor expansion of the cosines in equations 3.1 and gives the effective masses of the bands $m^* = \frac{\hbar^2}{\frac{d^2E}{dk^2}} = \frac{\hbar^2}{2a^2t}$ where the value of t is given by the path required to connect the two orbitals along the direction k.

For the (001) orientation, the energy dispersion of the confined t_{2g}-based bands are:

$$\begin{aligned} E_{xy}(k_x,k_y) &= -4t_1 - 2t_2 + 2t_1\cos(k_x a) + 2t_1\cos(k_y a) + 2t_2\cos(\frac{\pi n}{(N+1)}) \\ E_{yz}(k_x,k_y) &= -4t_1 - 2t_2 + 2t_2\cos(k_x a) + 2t_1\cos(k_y a) + 2t_1\cos(\frac{\pi n}{(N+1)}) \\ E_{xz}(k_x,k_y) &= -4t_1 - 2t_2 + 2t_1\cos(k_x a) + 2t_2\cos(k_y a) + 2t_2\cos(\frac{\pi n}{(N+1)}) \end{aligned} \tag{3.2}$$

where n is the index of the subband considered and N is the total number of atoms. We thus have $N \gg n$. The development around Γ gives effective masses of $m^* = \frac{\hbar^2}{2a^2t_1}$ along the x direction for bands d_{xy} and d_{xz} and $m^* = \frac{\hbar^2}{2a^2t_2}$ for the d_{yz} orbital.

For the (110)-oriented 2DEG, we consider the two in-plane directions $\vec{z}$ ([001]) and $\vec{x} - \vec{y}$ ([1$\bar{1}$0]), and the out of plane direction $\vec{x} + \vec{y}$ ([110]) where x, y and z are the basis of real space directions. They simply are the x,y and z basis after applying a $\pi/4$ rotation along the z axis. In the real space, along the direction [001] the distance between two atoms is the lattice constant a and in the other in-plane direction [1$\bar{1}$0], this distance is $\sqrt{2}a$. In $\vec{k}$-space, the distance in the reciprocal space between Γ and Z is $2\pi/a$ while it is $\sqrt{2}\pi/a$ between Γ and M or M'. The energy dispersion along the two in-plane directions Z ([001]) and M ([1$\bar{1}$0]) of the bands are :

$$\begin{aligned} E_{xy}(k_z,k_M) &= -4t_1 - 2t_2 + 2t_2\cos(k_z a) + 2\left(2t_1^2 + 2t_1^2\cos(k_M\sqrt{2}a)\right)^{\frac{1}{2}}\cos(\frac{\pi n}{(N+1)}) \\ E_{yz}(k_z,k_M) &= -4t_1 - 2t_2 + 2t_1\cos(k_z a) + 2\left(t_1^2 + t_2^2 + 2t_1t_2\cos(k_M\sqrt{2}a)\right)^{\frac{1}{2}}\cos(\frac{\pi n}{(N+1)}) \\ E_{xz}(k_z,k_M) &= -4t_1 - 2t_2 + 2t_1\cos(k_z a) + 2\left(t_1^2 + t_2^2 + 2t_1t_2\cos(k_M\sqrt{2}a)\right)^{\frac{1}{2}}\cos(\frac{\pi n}{(N+1)}) \end{aligned} \tag{3.3}$$

A similar Taylor expansion around Γ for the (110)-oriented 2DEG allows computing the effective band masses.

As opposed to the (001) case, here the band made of d_{xy} orbitals, as well as the one from $d_{yz,xz}$ are anisotropic and their development in k_M and k_z gives different results.

Because of the square root mixing t_1 and t_2 in eqs. 3.3, the effective mass along k_M is $m^{yz,xz}_{[1\bar{1}0]} = \frac{2t_1t_2}{t_1+t_2}\cos\frac{\pi n}{N+1}$. Note that in macroscopic sample, $\cos\frac{\pi n}{N+1} \to 1$. The results of the effective masses are reported in table 3.1.

	(001)-oriented			(110)-oriented		
	$\perp$	$\parallel$		$\perp$	$\parallel$	
direction	[001]	[100]	[001]	[110]	[1$\bar{1}$0]	[001]
m^*_{xy}	14	0.7	0.7	0.35	0.7	14
$m^*_{yz/xz}$	0.7	0.7	14	0.7	7.34/0.7	0.7/7.34

Table 3.1: Predicted effective in-plane-masses from tight binding calculations in the (001) and (110)-oriented 2DEG at LAO/STO interface.

We present results of simulations for three subbands ($N = 3$) in figure 3.2 below. Panels **a.** and **b.** display results of equations 3.2 and 3.3. Panel **c.** shows ARPES data of a STO(110) sample from ref [88] with a tight binding fit in dotted line. Finally panel **d.** shows the anisotropic Fermi surface of the (110)-oriented 2DEG

The out-of-plane effective mass is a quantity that determines the energy of the band in the well, *via* $E \propto 1/m^*_\perp$. It is defined as $m^*_\perp = \frac{\hbar^2}{2a^2t}$ where t can be t_1, t_2, or a combination of both, depending on the path required to connect one orbital to the other in the confinement direction displayed figure 3.1**c.** and **d.** We can already see from the hierarchy in figure 3.1e. and f. that while in the (001) orientation, $m^{xy}_\perp > m^{yz/xz}_\perp$, in the (110) orientation $m^{xy}_\perp < m^{yz/xz}_\perp$, which is confirmed by expanding the energy dispersion around Γ to find the masses displayed in table 3.1.

Because in 2D the density of state (DOS) ρ depends only on the effective in-plane mass ($\rho_{2D} = m^*_\parallel/\pi\hbar$), this quantity is of great interest. In LAO/STO(001) 2DEG, the d_{xy} electrons have a single in-plane effective mass $m^*_{||}$ given by the effective mass along k_x. The band of character $d_{yz,xz}$ have a anisotropic dispersion and thus different effective in plane masses. In a first approximation one can take the average in plane mass $m^*_\parallel = \sqrt{(m_{k_y}m_{k_z})} = 3.13\ m_e$.

For the LAO/STO(110) 2DEG, which is confined along the (110) direction, both the d_{xy} band and the degenerate $d_{yz,xz}$ bands have different effective masses along the two orthogonal in plane directions k_z and k_M. If we consider an average in-plane effective mass $m^*_{||} = \sqrt{(m_{kM}m_{kZ})}$, the DOS of the d_{xy} band is larger than for the d_{yz}/d_{xz} bands by approximately a factor 1.5. The DOS plays a role in a BCS picture of superconductivity, where the gap Δ is proportional to $e^{-1/V\rho}$. While we can not pronounce ourselves on the pairing strength V in each band, we can discuss the capability of the different bands to accommodate superconductivity based on ρ. In the (001) oriented interface, the low energy d_{xy} band is confined deep in the quantum well and has a low DOS which make difficult the emergence of superconductivity. By contrast, the high energy $d_{xz/yz}$ bands which extend much deeper in the STO substrate have a much larger DOS, making more favorable the emergence of superconductivity. In the (110) oriented interfaces, the d_{xy} and degenerated $d_{xz/yz}$

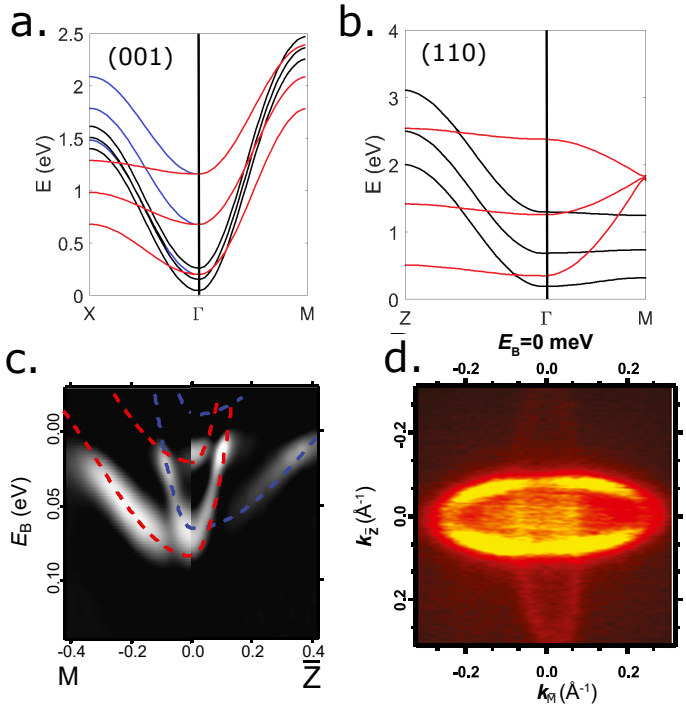

Figure 3.2: **Band structure and Fermi surface of the 2DEG at the (110)-oriented LAO/STO interface from [88] a.** Energy dispersion of the bands in a (001)-2DEG. Along ΓM red and blue indicates $d_{yz,xz}$ and d_{xy} characters respectively while along ΓK they indicates d_{yz} and d_{xy} and black represent a d_{xz} character. **b.** Same for (110). Red lines indicates $d_{yz,xz}$ character while black line indicates a d_{xy} character. **c.** ARPES measurement (blue : d_{xy}, red : $d_{xz/yz}$) and **d.** Fermi surface of a (110)-oriented 2DEG with the two ellipses visible, from [88]. The lower intensity band in **d.** is the d_{xy} band.

bands have more similar out of plane masses and DOS suggesting that they could both accommodate superconductivity.

3.1.2 About the LAO/STO(111) interface

The $LaAlO_3/SrTiO_3$(111) is challenging to grow, because the lowest energy state of the surface is not an atomically flat TiO_2. Despite these challenges, G. Herranz et al. have successfully grown both (110) and (111) interfaces with conducting 2DEGs, showing that there is also, as in the (001) orientation, a critical thickness required to forge the 2DEG. The critical thickness at which a 2DEG appears at room temperature for the (001),(110) and (111) orientation are respectively 4, 8 and 9 monolayers of $LaAlO_3$ [70]. The abrupt jump from an insulating to a conducting state at the critical thickness of the three orientations is displayed figure 3.3. They also showed that epitaxial growth was not required to obtain 2DEG: especially in the (110) orientation which is not made of polar capping LAO and should not promote electronic reconstruction, a conducting 2DEG gas still forms.

The (111) interface breaks the tetragonal symmetry of the lattice into a trigonal symmetry. The subsequent Fermi surface has been found to have a honey-comb/hexagonal symmetry in DFT [90], confirmed by ARPES measurement [71] [72] as depicted in figure 3.4. The six-fold symmetry of the system, which some authors have called "A Three-Orbital Strongly Correlated Generalization

of Graphene" [72], is expected to play numerous roles in the 2DEG properties and distinguish it from the (001) and (110) orientation. Indeed, the three fold rotation symmetry of the hexagonal lattice intrinsically breaks the time reversal symmetry of the system which may be an ingredient for unconventional superconducting order parameter [91] [92]. The first report of superconductivity in this interface dates back to 2017 by Monteiro et al., [81] with a T_c of 117mK, concomitant with Davis et al, [93] with a T_c of $\approx$ 350 mK.

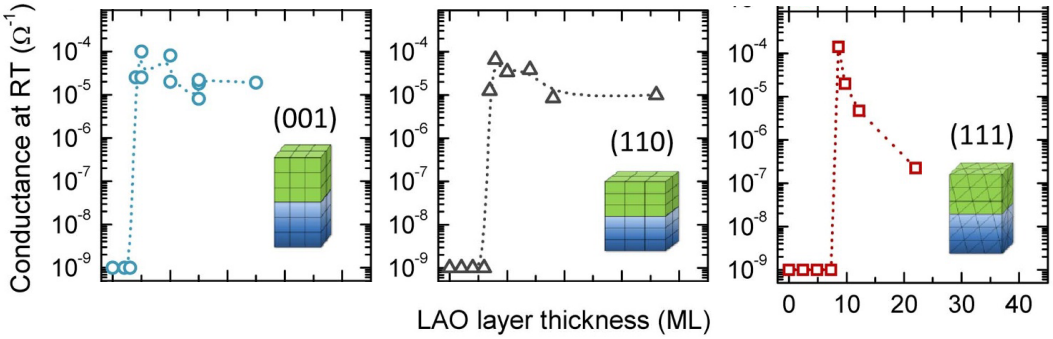

Figure 3.3: The conduction appears at around 4 monolayers for (001), and 8 to 9 monolayers for (110) and (111) From [70]

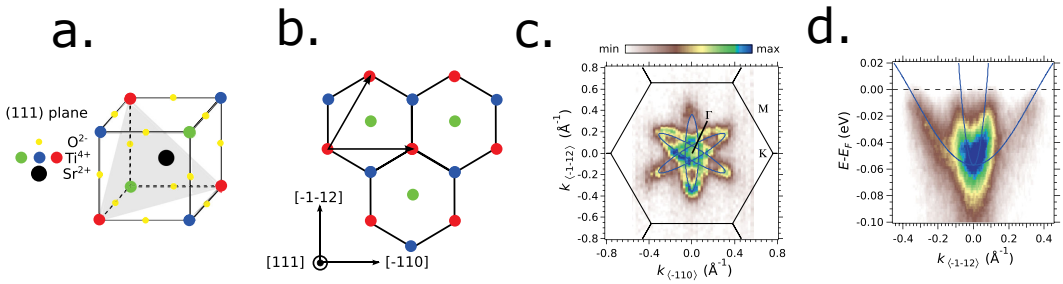

Figure 3.4: **a.** $SrTiO_3$ structure with (111) plane visible, **b.** Hexagonal lattice at the (111) interface, **c.** In-situ ARPES hexagonal Fermi surface around Γ_{222} point, **d.** Bands along the $[\bar{1}\bar{1}2]$ direction seen in ARPES. From [71].

The anisotropy of the system has been largely studied because it is believed to be linked in a non trivial manner to the possibility of an exotic state. Davis et al. showed in multiple articles, and his thesis, that the (111) interface of LAO/STO heterostructure is highly anisotropic. They showed that the Hall coefficient gating dependence is different when the current is applied in the two orthogonal in-plane directions $[1\bar{1}2]$ and $[1\bar{1}0]$ in the depleted regime [94][93][95][96]. The resistivity as a function of magnetic field in the normal and superconducting state has been found to be hysteretic and anisotropic as well, suggesting coexistence of superconductivity and magnetism [93]. Measurement of T_c, n_{Hall} and SdH oscillations by Khanna et al [97] showed to be uncorrelated, which the author ascribed to be due to stronger electronic correlations using a mean-field tight binding model. In any cases, this anisotropy between the two orthogonal $[1\bar{1}2]$ and $[1\bar{1}0]$ directions appears at much lower temperature than the tetragonal transition (around 120 K) which led some scientists to propose that there might be nematicity induced by electron correlations breaking the hexagonal symmetry [98].

While T. Rödel et al. [71] have considered a tight binding Hamiltonian between the lower t_{2g} orbitals, considering them as independent, other reseachers such as U. Khanna et al. [97] consider that the crystal field induced by the triangular symmetry mixes the lower t_{2g} orbitals to form a new basis: a lower a_{1g} band and two higher degenerates e'_g bands. In both cases, the Fermi surface is

hexagonal and at high enough doping, two bands contribute to the conductivity : a light band lower in energy and a heavy band higher. Although Rödel et al. model predicted no splitting at the Γ point, they could not resolve the eventual 5 meV splitting predicted by Khanna et al. model due to experimental limitations.

From ARPES measurements in ref [72] and [71] we can estimate the effective masses in $SrTiO_3$(111) 2DEGs, reported in table 3.2.

	$\Gamma M'$	ΓK
direction	$[1\bar{1}0]$	$[1\bar{1}2]$
m_L^*	$0.3^a - 0.27^b$	$1^a - 0.33^b$
m_H^*	$2.2^a - 1.08^b$	$7^a - 8.7^b$

Table 3.2: Effective in plane masses of the two lower band in $SrTiO_3$(111)-based 2DEG from ARPES measurement. ^{a} : from ref [72]. ^{b} : from ref [71].

3.2 LAO/STO(110) Sample preparation

Samples were grown in the group of G. Herranz at the ICMAB Barcelona with the following recipe:

The $SrTiO_3$(110) substrate was heated from room temperature to the deposition temperature (850°C) in an oxygen partial pressure of P_{O2}=0.1 mbar. The growth of a 10 unit cells thick $LaAlO_3$ thin film by PLD (Pulsed-Laser-Deposition) ($\lambda = 248$ nm) was monitored by high pressure reflection high-energy electron diffraction (RHEED). The deposition occurred under a P_{O_2}=10^{-4} mbar oxygen partial pressure, with a 1 Hz repetition rate and a laser pulse energy of 26 mJ. To avoid formation of oxygen vacancies, which would lead to an extrinsic mechanism of conduction, samples were cooled down from 850°C to 750°C under 0.3 mbar of partial oxygen pressure P_{O_2} and under 200 mbar of partial oxygen pressure from 750 °C to room temperature with a rest time of 1 hour at 600 °C.

Sample name	A	B
Measurements	DC (Hall effect, superconducting phase diagram) RF (superfluid stiffness)	DC (Hall effect, superconducting phase diagram) Critical field (H_c)
Preparation	10 monolayers LAO by PLD Polished substrate (d $\simeq 250\mu$m) Cr back gate deposited Integrated in an RLC circuit	10 monolayers LAO by PLD No polishing Silver pasted onto gold gate
Transport properties @ $V_G = 0V$	$R_{4K} = 0.6\ k\Omega.\square^{-1}$ $n = 7.8 \times 10^{13}\ cm^{-2}$ $T_c = 215\ mK$	$R_{4K} = 0.6\ k\Omega.\square^{-1}$ $n = 9.5 \times 10^{13}\ cm^{-2}$ $T_c = 265\ mK$

Table 3.3: Description of the two samples of $LaAlO_3/SrTiO_3$(110), which results are presented in this chapter.

In this chapter, we will now discuss the results obtained on two samples, which we will call A

and B and which relevant characteristics are shown in table 3.3.

3.3 Superconducting phase diagram and carrier density in LAO/STO(110)

This section presents the DC measurements of Hall effect for various gate voltages, the resistance as a function of temperature for different magnetic fields to extract the upper out-of-plane critical field $H_{c2}^{\perp}$, and capacitance measurements performed on sample A (see table 3.3).

3.3.1 First polarisation:

When we cool down the sample, the 2DEG can have hysteretic properties upon gating that we want to avoid in order to get a reliable determination of the physical parameters such as the carrier density, T_c or Rashba coupling. The effect of irreversibility upon gating in LAO/STO has been studied and described in details in [99]. Although this study has been performed on a (001) oriented sample, the same conclusions can be drawn for the (110) orientation.

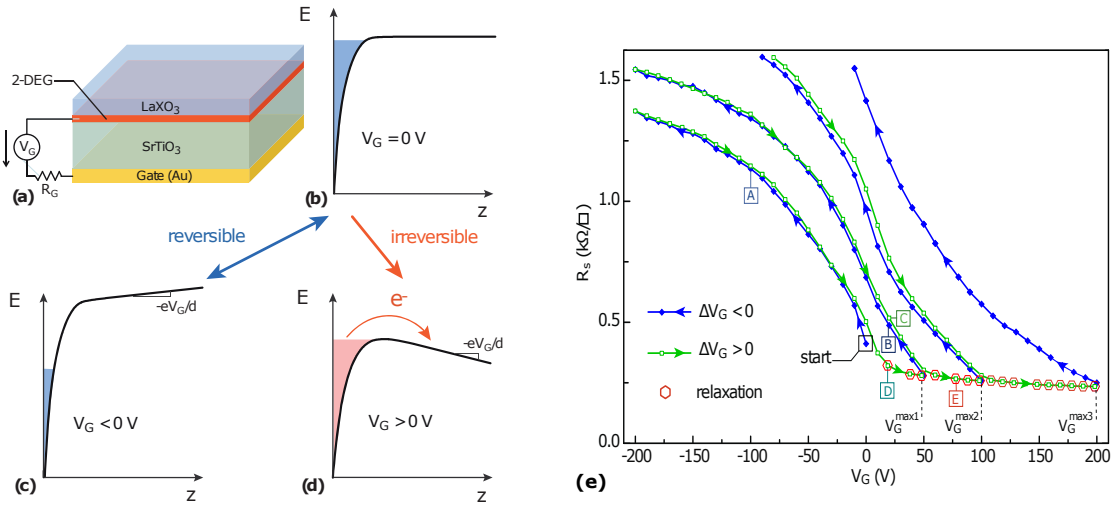

Figure 3.5: **Limit of the electrostatic doping in LAO/STO interface** a) Schematic of the 2DEG at the LAO/STO interface, with a back-gate used for electrostatic doping. b) Shape of the confining potential well when no gate voltage is applied c) Band bending and deep Fermi level when negative gate is applied d) Band bending and shallow Fermi level when positive gate voltage is applied. The electron can escape the well by thermal activation. e) Resistance of the 2DEG with several backward and forward step in gate voltage, starting from V_G = 0. From [99].

In LAO/STO, the formation of the interfacial quantum well results from the accumulation of free metallic electrons at the interface and the unavoidable presence of non-mobile trapped electrons. Because free electrons represent the majority of the charges, in absence of gate voltage during the initial cool down, the Poisson equation imposes that the Fermi energy lies close to the top of the well. As seen on the illustration presented in figure 3.5, the direction of the first gate polarization, i.e. positive or negative has strong consequences on the next measurements. On the one hand, when a negative gate voltage is applied (figure 3.5c.), the number of electrons decreases and the Fermi level decreases. On the other hand, when a positive gate voltage is applied for the first time(figure 3.5d.), the number of electrons in the 2DEG increases up to the point where the Fermi level reaches the

top of the quantum well. The potential on the backgate tends to attract electrons, which can escape out of the well by thermal activation above the barrier potential (figure 3.5d.). It is therefore not possible to further dope the 2DEG.

This is clearly illustrated in figure 3.5e.: Starting from zero gate voltage, when a negative voltage is applied, the sheet resistance of the 2DEG (and thus its electronic density) is fully reversible up to the zero-gate voltage starting point. However, whenever a positive gate voltage is applied, the sheet resistance follows a new, shifted to the right, R vs. V_G curve where the lowest resistance is reached at the highest gate V_G^{max}, where electrons start to escape. The sheet resistance is fully reversible in the range (V_G^{min}, V_G^{max}) where V_G^{min} can be arbitrary low (in practice it is often -200 V because of experimental limitations).

These results can be explained by a model where thermally excited electron can easily escape at V_G^{max}, when the Fermi level is at the top of the well. However, the escape rate is low when V_G < V_G^{max}. Increasing the gate to a higher V_G > V_G^{max} only shifts the physics of the gated-system to the new highest V_G^{max}.

Unless stated otherwise, all measurements reported in the manuscript were performed after a so-called "first polarisation", meaning that the gate is first increased to its maximum value (usually +50 to +200 V), then to the opposite value (-50 to -200 V) to prevent hysteresis. Further measurements are done in the same range [V_G^{min} V_G^{max}] where the gate-dependent characteristics are then fully reversible.

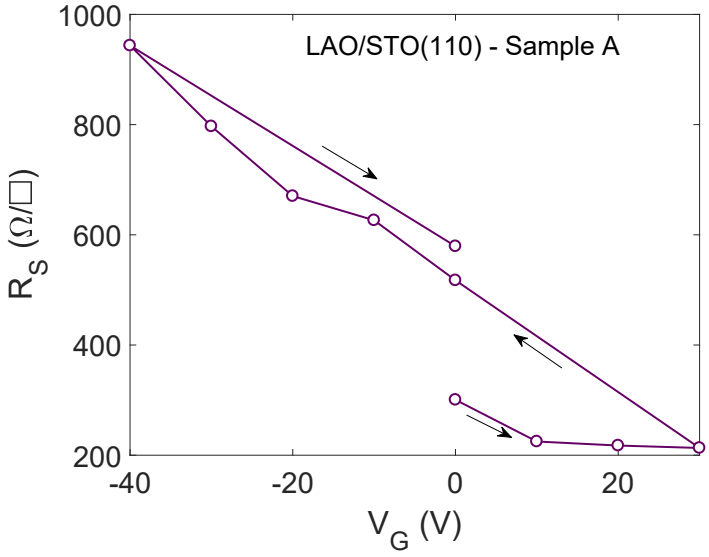

Figure 3.6: First polarization curve, taken on a LAO/STO(110) sample at 300 mK.

3.3.2 Superconducting phase diagram in LAO/STO(110)

Using the set-up described in section 2.2.3, we have measured the resistance as a function of temperature for various gate voltages. The results for sample A are shown in fig. 3.7.

The T_c (defined here as $R(T_c) = 0.25\ R(450\ mK)$) varies from ≃100 to ≃200 mK and the normal resistance from ≃200 to ≃ 5000 Ω between the maximum doping at V_G = +50 V and the

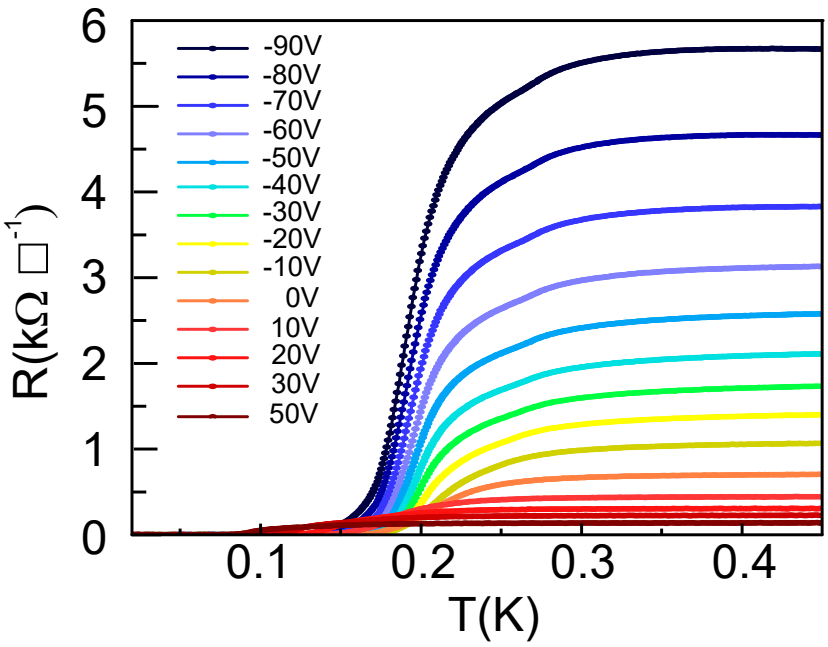

Figure 3.7: **DC measurement of LAO/STO(110) interface.** Sheet resistance as a function of temperature for different gate voltages from -90 V to +50 V.

minimum doping at V_G = -90 V. Both T_c and sheet resistance are similar to other STO-based 2DEG: Han et al. (R_s = 800Ω/□) [100], Herranz et al. (R_s = 200 to 1000Ω/□) [70] and Annadi et al (R_s = 20 to 1000Ω/□) [101].

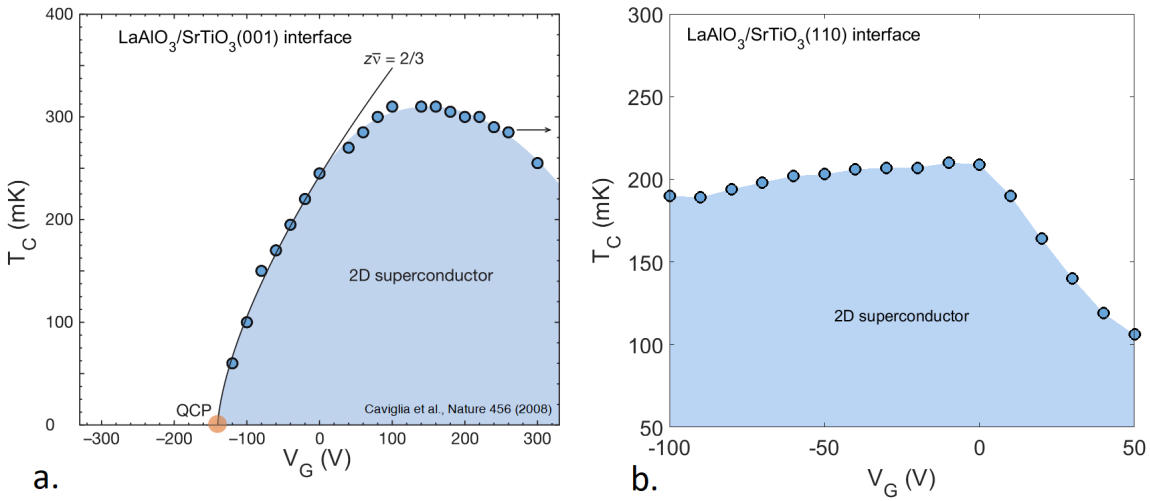

Figure 3.8: **Comparison of superconducting phase diagram of 2DEG at LAO/STO interface a.** in the (001) orientation (from [39]) **b.** in the (110) orientation (this work)

Figure 3.8**b.** is a T_c, V_G superconducting phase diagram derived from the data represented in figure 3.7, showing the superconducting region in blue. A comparison with the similar phase diagram

of the (001)-2DEG is provided figure 3.8**a.** The most striking distinction between the two interfaces is that T_c is not suppressed upon depletion in the (110)-2DEG, whereas the superconductivity is suppressed in (001)-2DEG in the negative gate region.

To understand the qualitative difference in behaviour between the (001) and (110)-2DEG, we have to recall that the ability to host superconductivity depends on the DOS of the material ($T_c \propto e^{-1/(\rho V)}$ where V is the pairing potential and ρ the 2D DOS). The DOS is proportional to the in-plane effective mass, and we will consider the pairing fixed and similar between the two orientations.[1] In the (001)-2DEG, low-DOS d_{xy} band ($m^*_{\|} \simeq 0.7\ m_e$) is sitting at the bottom of the well, and the higher DOS $d_{yz,xz}$ bands ($m^*_{\|} \simeq 7\ m_e$) are closer to the top of the quantum well. In the underdoped regime, there is no superconductivity because the DOS of the d_{xy} band is low and the band is strongly confined. Upon gating, the superconductivity emerges, concomitant with the population of the filling of the higher d_{yz}/d_{xz} bands which have higher DOS and more mobile electrons.

On the contrary, in the (110)-oriented 2DEG, the lower d_{yz}/d_{xz} bands have an effective mass of $\simeq 4.2\ m_e$, which is high enough to induce superconductivity, and it is less confined than the lower band of the (001)-2DEG. This is the reason why even when we are depleting the (110) 2DEG, it remains superconducting : the DOSs of the lowest bands are high enough to host superconductivity. The higher d_{xy} band has an in-plane-mass of $\sqrt{14 \times 0.7}\ m_e = 3.1\ m_e$ equal to that of the superconducting d_{yz}/d_{xz} band masses in the (001) orientation (see table 3.1).

Qualitatively, we still have to explain why the T_c drops in the overdoped region. In a single band BCS picture, the T_c only depends on the DOS ($\Delta \propto e^{-\frac{1}{\rho_{2D} \times V}}$), which is constant in 2D ($\rho_{2D} = \frac{m^*_{\|}}{\hbar \pi}$), so this behaviour cannot be simply explained. We will see that it is explained by a multi-condensate superconductivity. For now, the Hall effect that we will discuss next subsection will give us a first element of answer.

3.3.3 Multiband transport in the normal state of LAO/STO(110)

In this section we explore the signatures of a single-to-two band transition driven by gate voltage, starting with the Hall effect.

Hall effect measurement in LAO/STO(110) intefaces

Hall effect measurement was performed on sample A at 4 K in a Van der Pauw geometry. We apply a DC current of the order of 1 μA between two diagonal contacts and measure the transverse voltage drop. The Hall voltage V_H is the anti-symmetric part of the voltage drop measured between cross-diagonal contact of the Van der Pauw contact. The anti-symmetrization procedure prevents a parasitic magnetoresistance contribution to the Hall effect which can originate from small contacts misalignement. The figure 3.9 below summarizes this measurement.

We start by analyzing the Hall data in the gate voltage range from -90 V to 0 V. In this regime, the Hall resistance is fully linear with the magnetic field as expected for single band transport. The 2D carrier density can be safely extracted from the slope of the $R_{Hall}(B)$ curve using the formula :

[1] In order to take anisotropy properly into account, we should, in principle integrate the effective mass along the contour of the Fermi sea. However, taking the average $m^* = \sqrt{m_{k_Z} \times m_{k_M}}$ is a good first order approximation of the average effective mass.

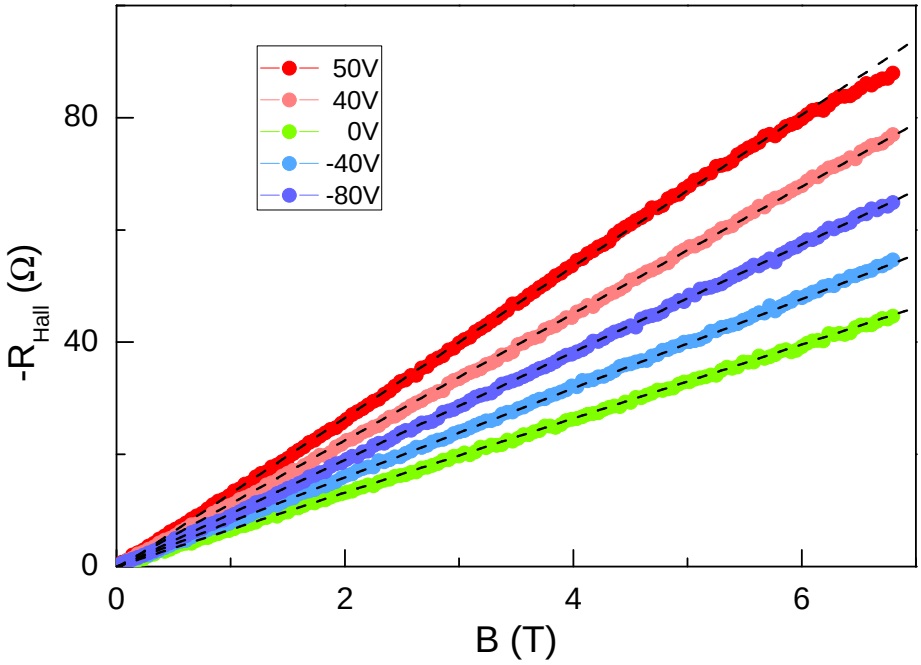

Figure 3.9: **Hall effect measurement for various gate voltages in LAO/STO(110) interfaces sample A.** Experimental data in color symbol and linear fit in dashed line. For $V_G = 40$ and $50\ V$, the linear fit fails and we use equation 3.5 instead.

$$V_{Hall} = \frac{1}{ne} I|B| \tag{3.4}$$

Where n is the carrier density and e is the electron charge.

The drop of R_{Hall} from 60 Ω to 40 Ω at $B = 7\ T$ corresponds to an increase in density from 8.9×10^{13} cm^{-2} to 1.6×10^{14} cm^{-2}, which is almost a two-fold increase in density.

We now address the Hall effect in the gate voltage range from 0 V to 50 V, i.e the overdoped regime. We notice two features: (i) Hall resistance is no longer linear in field B, (ii) the slope of the $R_{Hall}(B)$ curve increases with gate voltage which would suggest an unphysical decrease of carrier density with gate voltage. Both features are in fact signatures of a single band to two band transport transition that occurs around $V_G = 0\ V$.

In a multiband system, the resistivity and Hall effect becomes non-linear when two types of carriers having different mobilities, or more, contribute to the conductance. The Hall coefficient R_H for a two band system is expressed as: [102]

$$R_H = \frac{B}{e} \frac{\frac{n_1\mu_1^2}{1+\mu_1^2B^2} + \frac{n_2\mu_2^2}{1+\mu_2^2B^2}}{\left(\frac{n_1\mu_1}{1+\mu_1^2B^2} + \frac{n_2\mu_2}{1+\mu_2^2B^2}\right)^2 + \left(\frac{n_1\mu_1^2B}{1+\mu_1^2B^2} + \frac{n_2\mu_2^2B}{1+\mu_2^2B^2}\right)^2} \tag{3.5}$$

Where e is the electron charge, B the magnetic field in Tesla, μ_1 is the mobility of the first band,

μ_2 the mobility of the second band, and n_1 and n_2 are the electronic density of the first and second band respectively.

Extracting the different parameters (μ_1,μ_2,n_1 and n_2) requires to perform measurements at a quite high magnetic field where the non-linearity of the $R_H(B)$ curves is well pronounced. For instance, such analysis was done in ref [48] based on Hall effect data obtained at 50 T in pulsed magnetic field.

Gate capacitance measurement

As an alternative, for measurements performed in the lab under smaller magnetic fields (typically less than 13 T in our case), it is possible to get additional information on the relative gate variation of the total carrier density of the 2DEG from a simple measurement of the gate capacitance, i.e the capacitance between the 2DEG and the metallic gate.

The carrier density at any gate voltage relates to the carrier density in the underdoped regime, at the lowest gate voltage V_G^{min}, where there is only one type of carriers by the following formula :

$$n(V) = n(V_G^{min}) + \frac{1}{eA}\int_{V_G^{min}}^{V} C_G(V)dV \tag{3.6}$$

where A is the surface area of the 2DEG, e is the electron charge, and $C_G(V_G)$ is the gate-dependent substrate capacitance.

To obtain the substrate capacitance, we measure the complex impedance $Z = v_{ac}/i_{ac}$ of the plate capacitor whose two electrodes are the 2DEG on one side and the metallic gate on the other side, and the dielectric material is the STO substrate. The measurement set-up was described in chapter 2, section 2.2.5, figure 2.8. The capacitance evolution which is roughly symmetric with the gate voltage, varies from 30 to 40 nF as shown in figure 3.10.[2]

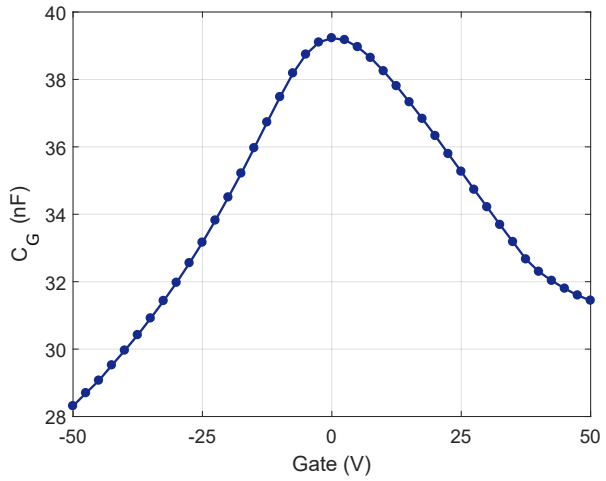

Figure 3.10: Capacitance as a function of gate in LAO/STO(110).

[2]The capacitance of the substrate between the back-gate and the 2DEG, that we have called C_G, is different from the parallel capacitance of the substrate which plays a role in the superfluid stiffness measurement that we shall call C_{STO}. The first one is a few tens of nano-Farad while the second one is tens to hundreds of pico-Farads.

Gate dependent carrier density and multiband transport in LAO/STO(110)

Figures 3.11**b.** and 3.12**b.** show the carrier density as a function of gate voltage, extracted from low magnetic field linear fit (black empty symbol) or integrated from the measurement of the capacitance (black line). Once we have the correct total carrier density, we can perform a two-band fit following Drude formula for multiband system (equation 3.5), with the following constraints: $n_{tot} = n_1 + n_2$ and $1/R_s = n_1\mu_1 + n_2\mu_2$. Performing the fits for all gate voltages allows to extract the individual contribution of each band to the carrier density as shown in blue and red figure 3.11b., as well as the gate voltage evolution of each band's mobility, shown in figure 3.11a. below.

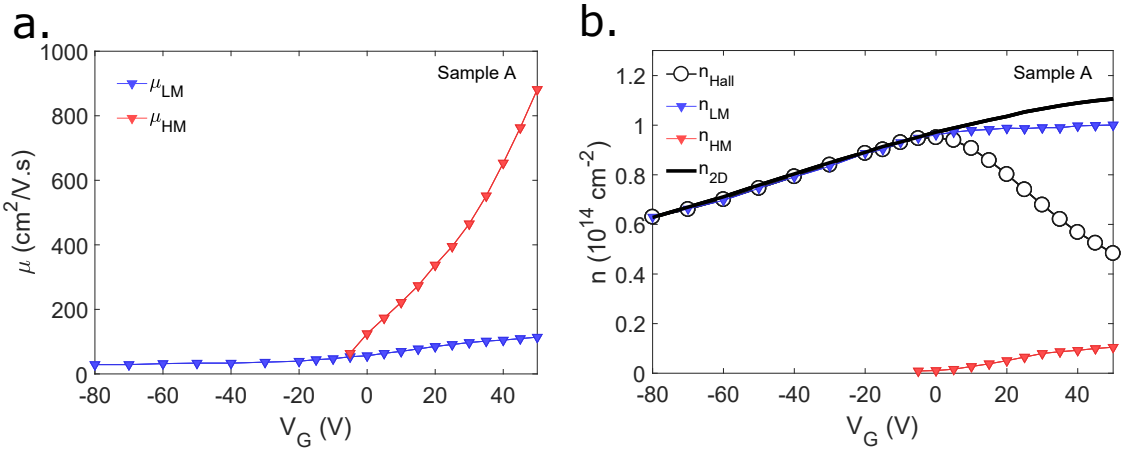

Figure 3.11: **Two-band fitting parameters of the Hall effect in LAO/STO(110) sample A. a.** Electron mobility as a function of gate voltage. **b.** Carrier density as a function of gate voltage.

We see in figure 3.11**a.** that the main band n_1 has a low mobility (LM) of around 100 $cm^2/V \cdot s$ which doesn't change much with gate. The second band which is populated at $V_G > -10\ V$ has a high mobility (HM) which increases from 100 $cm^2/V \cdot s$ at zero gate to $\simeq$ 1000 $cm^2/V \cdot s$ at maximum doping. These figures are comparable to that for other 2DEGs at (001) interface [48], or (110) and (111) interface [70].

The total carrier density of the 2DEG is shown in figure 3.11**b.**. It changes from 6×10^{13} to $10 \times 11^{13}\ cm^{-2}$ between -90 and $V_G = +50\ V$ corresponding to 30% of the total carrier density. At $V_G \approx -10V$, the high mobility band is also populated (orange symbol fig 3.11) but it represents only a fraction of a few % of the total carrier density even at $V_G = 50V$. The carrier density n_{Hall} (dark circle figure 3.11 extracted from low-field Hall effect only matches the true n_{2D} (in black line) in the single band regime. Above $V_G \approx -10\ V$, it fails to capture the real variation of carrier density calculated from integrating the capacitance.

The transition from linear to non-linear Hall effect supports the idea that a second band, with a different orbital character, is filled above $V_G = -10\ V$. In our LAO/STO(110) 2DEG, given the band structure discussed earlier, these results suggest that in the underdoped region ($V_G < -10\ V$) only the lowest degenerate d_{xz}, d_{yz} bands are filled and in the overdoped region ($V_G > -10\ V$), the higher d_{xy} band is also filled.

The same type of analysis leads to similar conclusions for sample B (figure 3.12).

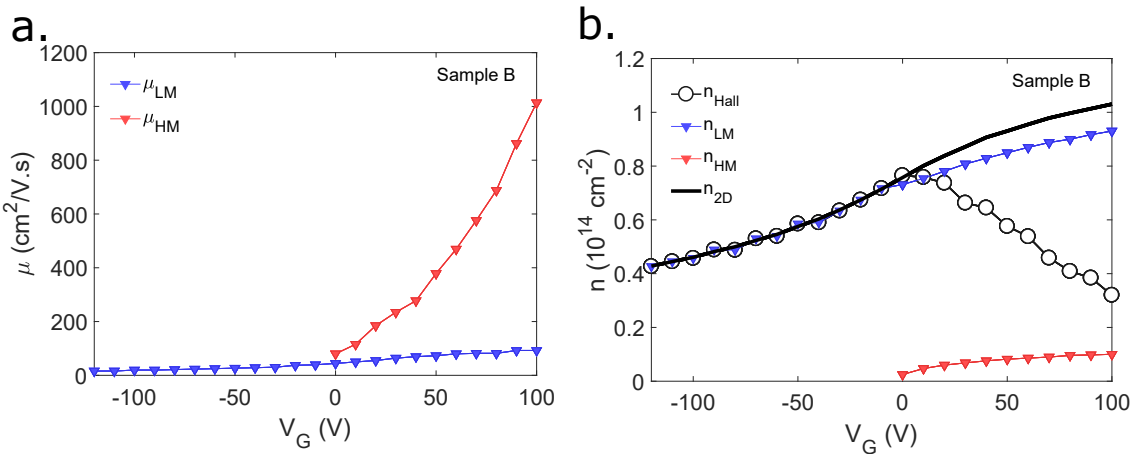

Figure 3.12: **Two-band fitting parameters of the Hall effect in LAO/STO(110) sample B. a.** Electron mobility as a function of gate. **b.** Carrier density as a function of gate.

3.4 Critical field measurement in LAO/STO(110)

3.4.1 Overview of the data

The out-of-plane upper critical magnetic field H_{c2} of superconductors is defined as the field value at which the many vortices leave no room for superconductivity and the zero state resistance is suppressed. The Ginzburg-Landau perpendicular critical field H_{c2} relates to the coherence length of Cooper pair $\xi(T)$ *via* the relation $H_{c2}(T) = \phi_0/2\pi\xi^2(T)$ where ϕ_0 is the magnetic flux quantum.

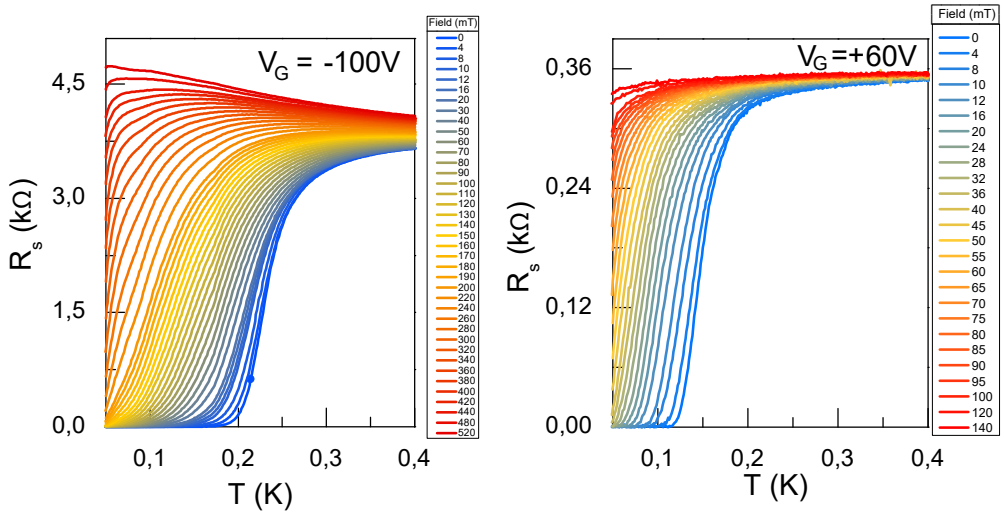

Figure 3.13: **Critical field measurement in LAO/STO(110)** Two set of R vs. T for various fields, at two given gate voltages $-100\ V$ (underdoped regime, left panel) and $+60\ V$ (overdoped regime, right panel).

Experimentally, H_{c2} is extracted from the measurement of R(T) curves under different mag-

netic fields. At each temperature, $H_{c2}(T)$ is defined as the magnetic field that suppresses superconductivity according to a criteria. For instance in the following, we define H_{c2} such that $R(H_{c2}, T) = 0.8\ R(400\ mK)$. Note that the conclusions based on qualitative variations must not depend on the choice of the criteria.

Figure 3.13 shows such measurement of H_{c2} for sample B, for two gate voltages, that is $R(T)$ for various fields H. For $V_G = -100\ V$ the superconductivity is suppressed state at the highest field of 520 mT (left panel), while for $V_G = 60\ V$, superconductivity is suppressed for a field of 140 mT. Figure 3.14 presents $H_{c2}(T)$ curves for all gate voltages, extracted from measurements such as those presented in figure 3.13.

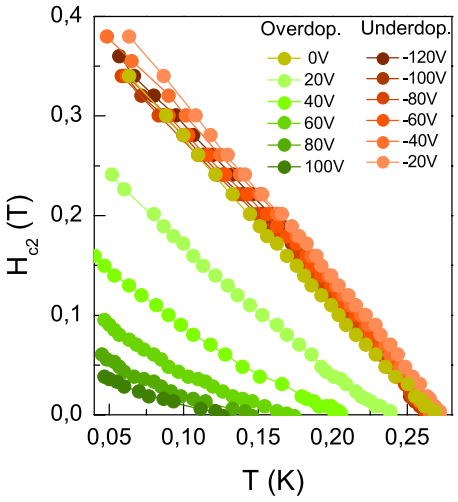

Figure 3.14: $H_{c2}(T)$ for various gate voltages, extracted from critical field measurement such as those represented in figure 3.13.

There are two regimes visible in figure 3.14. In the underdoped regime, all $H_{c2}(T)$ curves exhibit an upward curvature with similar values for both $H_{c2}(0)$ and T_c. As we increase the gate voltage above -10 V in the overdoped regime, the $H_{c2}(T)$ curve starts to acquire a downward curvature and their $H_{c2}(0)$ and T_c are reduced by a factor 8 and 2.5 respectively for $V_G = 100\ V$.

Figure 3.15 presents all $H_{c2}(T)$ curves acquired during the experimental run, normalized by their maximum value $H_{c2}(0)$ plotted as a function of the reduced temperature $t = T/T_c$. In the underdoped regime the curve follows the dependence predicted by Wherthamer, Helfand and Hohenber (WHH) for single gap superconductivity [103] while the overdoped regime shows a deviation growing stronger as the gate voltage is increased. The transition between the two regimes takes place around $V_G = -10\ V$ which corresponds to the single to two band transition observed in Hall effect. We therefore ascribe the change in behavior in the $H_{c2}(T)$ curve to the filling of the high-energy d_{xy} band.

As shown in the lower inset of figure 3.15, the critical field at zero temperature $H_{c2}^{\perp}(T = 0)$ remains constant in the underdoped regime. Its value of $\sim 400\ mT$ gives a Ginzburg-Landau coherence length of $\xi_{UD} \simeq 30\ nm$. $H_{c2}(T = 0)$ decreases when the second band starts to be populated in the overdoped regime down to $\sim 80\ mT$ giving an estimate $\xi(V_G = 100\ V) \simeq 60\ nm$. The upright inset shows the second derivative of normalized H_{c2} as a function of gate at 70% of the T_c, clearly indicating a change from a concave (the second derivative of H_{c2} with respect to gate voltage is negative in the UD regime) to a convex shape (the second derivative of H_{c2} with respect to gate voltage is positive in the OD regime).

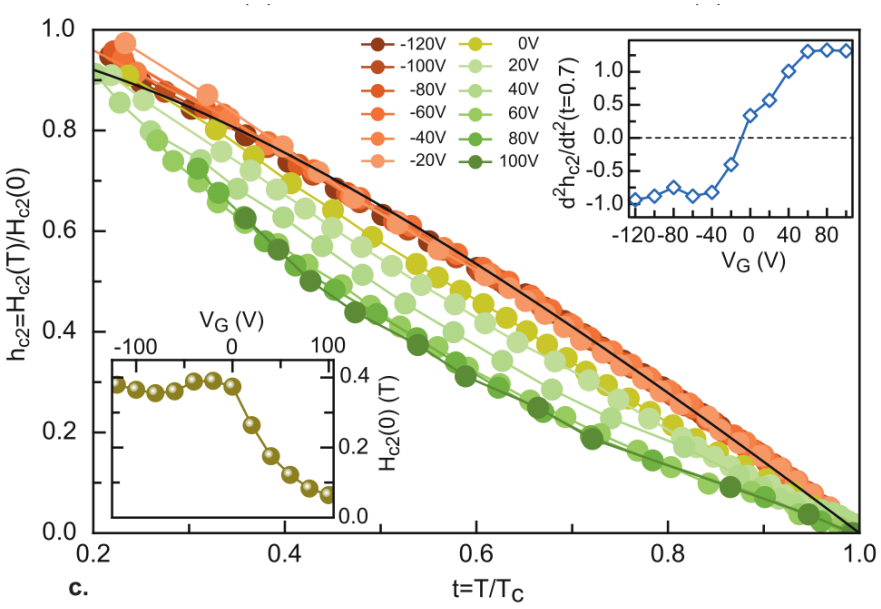

Figure 3.15: **Normalized critical magnetic field $h_c = H_{c2}(T)/H_{c2}(0)$ as a function of the reduced temperature $t = T/T_c$ for different gate voltages in LAO/STO(110).** Lower inset shows the zero-temperature critical field Hc2(0) as a function of V_G. The upper inset shows d^2h_c/dt^2 as a function of V_G that emphasizes the change in curvature of $h_c(t)$ curves in the overdoped regime.

3.4.2 Multicondensate model of H_{c2}

The analysis suggests that a superconducting regime with two condensates could occur in the overdoped regime. To explain this deviation of $H_{c2}(T)$ from the WHH theory concomitant with the emergence of the second band, we use the theory developed by Edge, Balatsky [104] and Gurevich [105]. Following the publication of the BCS theory [106], Gorkov laid down substantial theoretical work on type II superconductor [107] focused on H_{c2}. The later was pushed further by Eilenberger [108] and adapted to the dirty limit by Usadel [109]. The Usadel equations served as a basis for the derivation of the upper critical field in two-band superconductor by Gurevich [110]. In the following section, we present a brief summary of the key points of the calculations from Edge and Balatsky model in ref [104].

Let us consider two superconducting condensates in the dirty limit. Each of the condensates is described by its in-plane, isotropic, diffusivity value $D_{1,2}$ and its superconducting gap $\Delta_{1,2}$. The self-consistent linearised Usadel equations for two superconducting condensates in the dirty limit are :

$$2\omega f_{1,2} = D_{1,2}(\nabla + 2i\pi A/\phi_0)^2 f_{1,2} = 2\Delta_{1,2} \tag{3.7}$$

$$\Delta_m = 2\pi T \sum_{\omega>0}^{\omega_D} \sum_m \lambda_{mm'} f_{mm'}(r,\omega) \tag{3.8}$$

where ω_D is the Debye frequency, $f_{1,2}$ is the anomalous Green's function in each band, in the Nambu-Gorkov formalism which describes the Cooper pair amplitude. $\lambda_{mm'}$ are the intraband ($m = m'$) or interband ($m \neq m'$) superconducting coupling constant. The index m runs from 1 to 2.

After cumbersome calculations, one can show that the temperature dependent critical magnetic field can be obtained by solving equation 3.9 [105]

$$a_0(\ln(t)+U(h))(\ln(t)+U(h\eta))+a_1(\ln(t)+U(h))+a_2(\ln(t)+U(h\eta))=0 \tag{3.9}$$

where $t = T/T_c$ is the reduced temperature, $\eta = D_1/D_2$ is the diffusivity ratio, $h = \frac{HD_1}{2\phi_0 T}$, T is the temperature and ϕ_0 the flux quantum. $U(x) = \psi(x+1/1) - \psi(1/2)$ where ψ is the di-gamma function, and a_0, a_1, and a_2 are defined from the superconducting coupling constants λ's:

$$a_0 = \frac{2(\lambda_{11}\lambda_{22} - \lambda_{12}\lambda_{21})}{\lambda_0}$$

$$a_1 = 1 + \frac{\lambda_{11} - \lambda_{22}}{\lambda_0}$$

$$a_2 = 1 + \frac{\lambda_{22} - \lambda_{11}}{\lambda_0}$$

$$\lambda_0 = \sqrt{\lambda_{11}^2 + \lambda_{22}^2 + 4\lambda_{12}\lambda_{21} - 2\lambda_{11}\lambda_{22}}$$

This model is formally equivalent to the WHH model when $\lambda_{12} = \lambda_{21} = \lambda_{22} = 0$.

Fitting the curve in the overdoped region of figure 3.14 with a solution of equation 3.9 allows to extract the superconducting coupling constants λ and diffusivity constants D of the two bands, i.e. the lowest energy degenerate d_{yz},d_{xz} and the high energy d_{xy}. Constraints allow for the fitting procedure to converge : a weak interband coupling $\lambda_{11,22} \ll \lambda_{21,12}$, $\lambda_{12} = \lambda_{21}$ and starting point close to a set of values from the literature. For instance, one can start with $\lambda_{11} = 0.14$, $\lambda_{22} = 0.13$ and $\lambda_{12} = 0.02$ from Fernandes et al. [111].

3.4.3 Results and discussion

We have systematically fitted the H_{c2} curves using the model described above to find the λ coupling constants, as well as the diffusion coefficients D for all gate voltages. The normalized experimental $H_{c2}(T)/H_{c2}(0)$ curves as a function of temperature for various gate voltages are shown figure 3.16, with their individual fits. Data in panel **a.** to **f.** are fitted using the WHH model, while the data in panel **g.** to **l.** are fitted using the Edge and Balatsky model discussed in the subsection above. We notice that the T_c is constant in the underdoped regime, while it decreases in the overdoped regime, as observed in sample A figure 3.8.

We report in figure 3.17 the gate voltage evolution of the fitting parameters of the $H_{c2}(T)$ curves, namely the value of the intraband superconducting coupling constants λ_{11}, λ_{22} and the interband coupling constants λ_{12} and λ_{21}, as well as the diffusivity ratios η. D_1 and D_2 are independently evaluated from the Drude formula $D = \frac{v_F^2 \tau}{3}$ and reported in the right panel of figure 3.17 in empty symbol, to compare with the result of the fitting procedure (filled symbol). The single λ parameter in

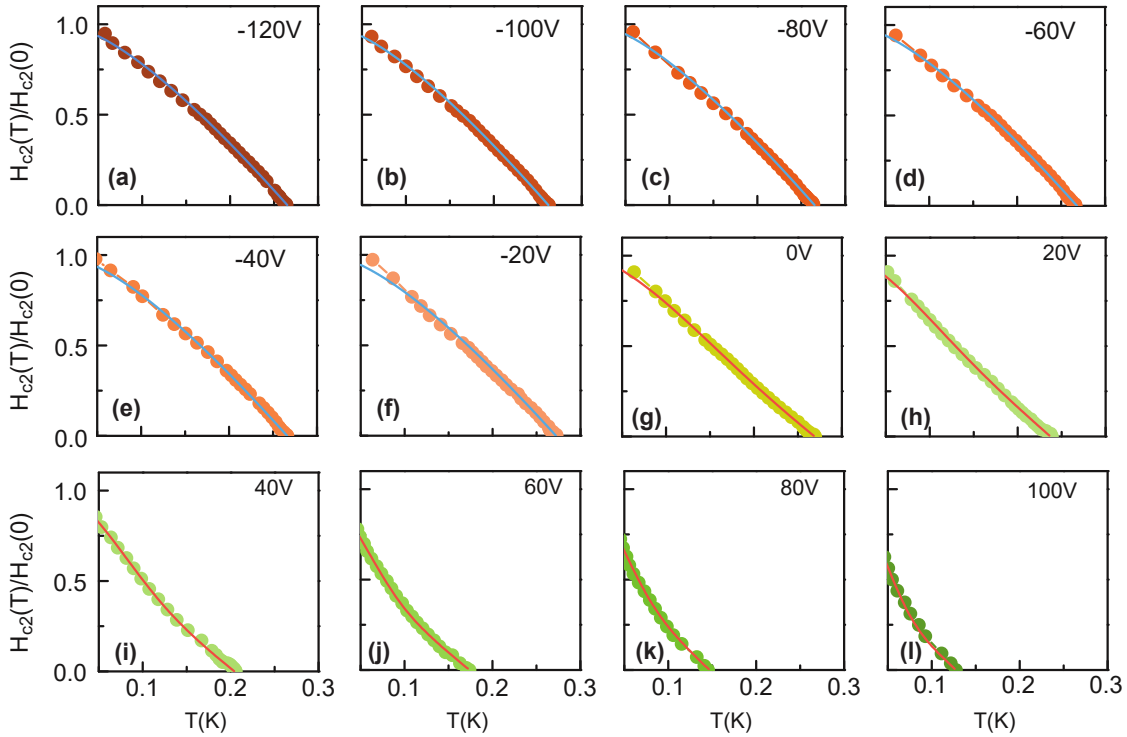

Figure 3.16: **Critical magnetic field measurement in LAO/STO(110) a.** to **l.** show $H_{c2}^{\perp}(T)/H_{c2}^{\perp}(0)$ as a function of temperature every 20 V of gate voltage from -120 V to 100 V. The blue line for negative gate voltages corresponds to WHH fit (which is gate independent) while the red line is the Edge and Balatsky fit, which fitting parameters are shown in figure 3.17.

the underdoped, single band regime is 0.135 (figure 3.17a. inset), which gives a gate-independent gap of value $\Delta \simeq 40\mu eV$ (figure 3.17a.). A second gap opens in the high energy d_{xy} band, we found that λ_{22} is larger than λ_{11}, and so is its gap. Both intraband coupling constants decrease upon increasing the gate as expected from the drop of T_c observed experimentally. The interband coupling constant $\lambda_c = \sqrt{\lambda_{12}\lambda_{21}}$ is much smaller than the intraband coupling constant in the whole doping range (figure 3.17a. inset, right axis).

Figure 3.17b. shows a qualitative agreement between the diffusivity ratios obtained from the fitting procedure and from a normal two-band transport analysis of the Hall effect. This ensures that the results both in the superconducting and the normal state are consistent. The decrease of T_c above the Lifshitz transition (i.e the filling of the second band) challenges the BCS theory of superconductivity in which adding the filling of a new band with a significant DOS should only increase the critical temperature. We will come back to this issue in section 3.5.7.

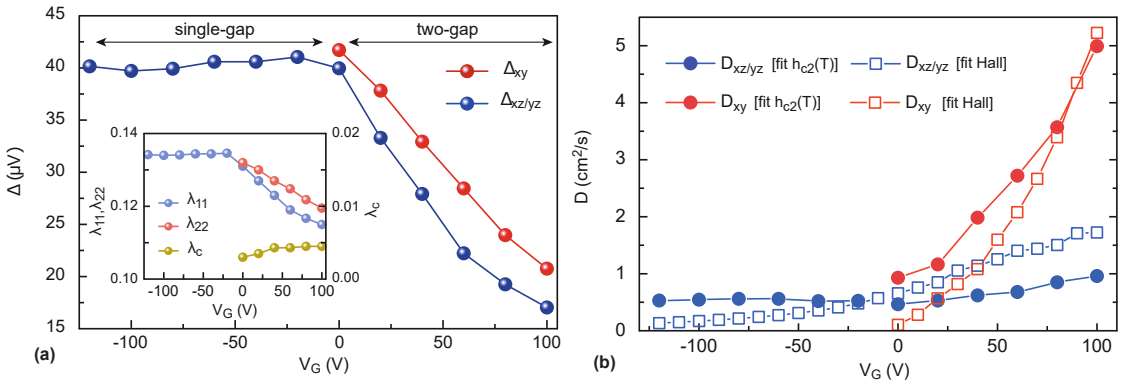

Figure 3.17: **a.** Superconducting gap of the two bands as a function of gate voltage. Inset shows the intraband coupling constants $\lambda_{11,22}$ (left axis) and average interband coupling constant $\lambda_c = \sqrt{\lambda_{12}\lambda_{21}}$ (right axis) **b.** Diffusion constants $D_{xz,yz}$ and D_{xy}, extracted from the fitting procedure (filled symbol) and compared to Drude calculations derived from a two-band model analysis of the Hall effect (empty symbol).

3.5 Microwave measurement of the Superfluid Stiffness in LAO/STO(110)

3.5.1 Kinetic inductance measurement theory

A complete description of the set-up and measurement principle is provided in section 2.3.2 of chapter 2. Here I will recall the basic information necessary to understand the experimental data.

The sample is placed between the ground and the central line of a coplanar wave guide (CPW) transmission line, where surface mounted devices (SMD) are soldered to realise an equivalent RLC circuit. The circuit, also refered to as load, is mounted on the mixing chamber plate of the dilution refrigerator, and connected to RF lines. A directional coupler allows to separate incoming and outgoing signals on the load, and a bias-tee allows for simultaneous DC measurements (see fig. 3.18). A Vector Network Analyser (VNA) sends a RF signal through port 1 and measures the signal at port 2. We thus measure the complex transmission coefficient S_{21} which relates to the reflection coefficient of the load cicruit Γ *via* a calibration procedure described appendix A. The equivalent circuit of the load is depicted figure 3.18 below.

The complex impedance of the load Z_L is the sum of parallel contributions :

$$\frac{1}{Z_L} = \frac{1}{R_1} + iC_{STO}\omega + \frac{1}{iL_1\omega} + \frac{1}{Z_{2DEG}(\omega)} \tag{3.10}$$

where L_1, R_1 are SMD inductors and resistors, C_{STO} is the capacitance of STO parallel to the interface, Z_{2DEG} is the complex impedance of the 2DEG. The purpose of $R_1 = 140\Omega$ is to maintain the real value of the total load impedance close to 50 Ω in the entire gating range (matched with the microwave circuitry) to increase the sensitivity of the experiment. L_1 is added to make the circuit resonates in a practical frequency range both in the normal and superconducting state. In the normal state, $\sigma = \sigma_1 = 1/R_s$ with R_s being the sheet resistance. In the superconducting state, $1/Z_{2DEG}(\omega) = \sigma_1(\omega) - i\sigma_2(\omega)$ where $\sigma_2 = \frac{1}{L_K\omega}$ is the inductive response of the Cooper pairs in the limit $\hbar\omega \ll \Delta$ and the resistive part is $\frac{\sigma_1}{\sigma_1^2+\sigma_2^2}$.

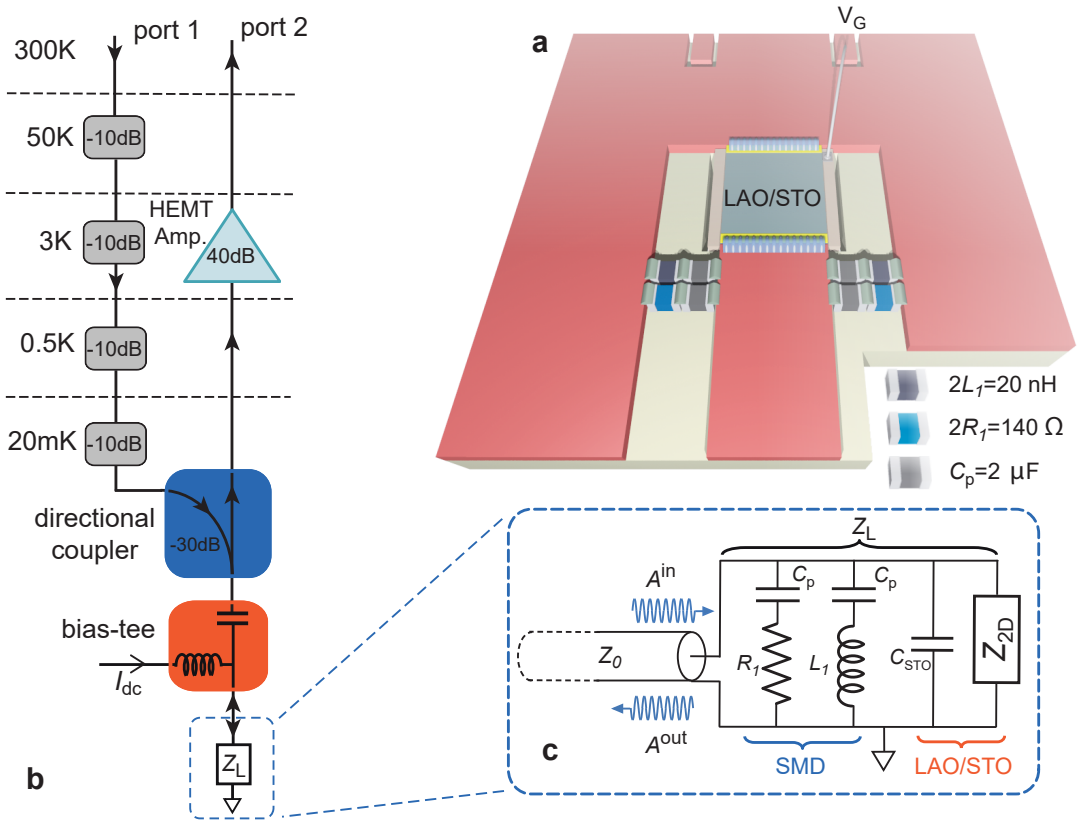

Figure 3.18: **Microwave set-up of the LAO/STO interface for superfluid stiffness measurement a.** LAO/STO sample connected between the central line of a CPW and the ground. SMD are soldered to design an equivalent RLC circuit with an equivalent R close to 50 Ω for maximum contrast and a L_1 such that the resonance frequency close to 300 MHz. Protective capacitance C_p prevent short cut in DC measurement. **b.** Scheme of the load at the bottom of the fridge, two RF line are used to send a signal and measure the reflection. The incoming signal is attenuated at each stage, and the outgoing signal is amplified by a HEMT. A bias-tee is used to send a DC signal simultaneously to the RF signal. **c.** Equivalent circuit of the load with the 2DEG modeled by a complex impedance Z_{2DEG} in parallel with the substrate capacitance C_{STO}, and SMD element L_1 and R_1. The line has a $Z_0 = 50\ \Omega$ impedance. The reflection coefficient $\Gamma(\omega)$ is the complex ratio of the incoming wave $A_{in}(\omega)$ and outgoing wave $A_{out}(\omega)$ at the load's level. From [76].

The SMD elements values (of resistance, capacitance, inductance) do not vary with gate and temperature in the range of interest. Lastly, C_{STO} does not evolve in the low temperature range ($4\ K$ to $10\ mK$) because the dielectric constant of STO saturates below $10\ K$, however C_{STO} is gate dependent since the dielectric constant of STO depends on the applied electric field.

The calibrated reflection coefficient Γ extracted from S_{21} (see calibration procedure described appendix A) is related to the load impedance Z_L *via* :

$$\Gamma(\omega) = \left(\frac{Z_L(\omega) - Z_0}{Z_L(\omega) + Z_0}\right) \tag{3.11}$$

The circuit displays a resonance at frequency $\omega_0 = 1/\sqrt{LC}$. When $\omega \simeq \omega_0$, $Z_L(\omega)$ is purely real (equation 3.10), and the microwave signal is dissipated in the sample circuit. (equation 3.11). As a result, an absorption dip is observed in $\Gamma(\omega)$ along with a 2π shift. A maximum of sensitivity

is obtained when the real part of the load impedance matches the line impedance, $Z_L(\omega = \omega_0) = Z_0 = 50\ \Omega$. Taking the imaginary part of equation 3.10, one can deduce :

$$L_K = \left[\omega\left(\omega C_{STO} + \mathrm{Im}(\frac{1}{Z_L})\right)\right]^{-1} - L_1 \tag{3.12}$$

To summarize, we measure the scattering coefficient S_{21} which is the ratio of the complex amplitude of the wave received at port 2 of the VNA to the amplitude of the wave sent from port 1 as shown in figure 3.18 b). After a calibration procedure detailed in appendix A, the complex reflection coefficient at the level of the load Γ is obtained from S_{21}. From the load impedance we can deduce the kinetic inductance of the superconducting 2DEG (equation 3.12) which in turn gives the superfluid stiffness J_s. Such method of measurement of the kinetic inductance and superfluid stiffness has already been employed as early as 1969 ([112]).

3.5.2 Experimental superfluid stiffness in LAO/STO(110)

Sample preparation is described in figure 3.19. The $LaAlO_3/SrTiO_3$ (sample A) was inserted between the central line and the ground of a coplanar waveguide transmission line. The sample is glued on a MgO substrate and contacted through multiple Al wire-bonds covered by silver epoxy to ensure negligible impedance contacts. A tiny metallic contact on the MgO substrate allows the gate to be connected to an external contact pad through an Al wire-bond. The many wires were then covered with silver paste to fuse them together, ensuring they do not add an inductive contribution to the circuit. Surface mounted devices were added in parallel to design the microwave equivalent circuit described in figure 3.18.

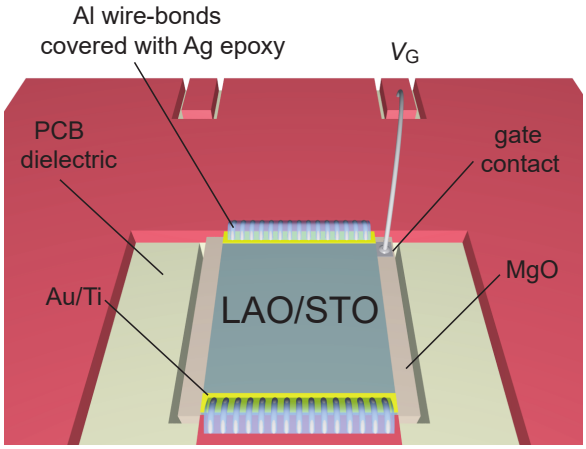

Figure 3.19: **Close up view of a $LaAlO_3/SrTiO_3$(110) sample in the CPW transmission line.**

Figure 3.20 shows the continuous evolution of the magnitude of the calibrated reflection coefficient Γ in dB (color scale) as a function of frequency and temperature, for different gate voltages. The normalized $R(T)$ curves measured in dc are shown on the right axis (white line). Above T_c, the resonance frequency is temperature independent and weakly changes with gate voltage. Below T_c, the resonance shifts to higher frequency due to the inductive response of Cooper pairs. Indeed, the 2DEG starts to have non-zero imaginary conductance $\sigma_2(\omega) = \frac{1}{L_k(T)\omega}$ and its inductance adds

in parallel to the SMD inductance L_1 such that $L_{tot}(T) = \frac{L_1 L_k(T)}{L_1 + L_k(T)}$, changing the resonance frequency $\omega_0 = \frac{1}{\sqrt{L_{tot} C_{STO}}}$. Through the relation 1.34 ($J_s(T) = \hbar^2/(4e^2 L_k(T))$), we extract J_s at all temperatures. In principle, only the position of the resonance is required to compute J_s through the evolution of $\omega_0(T) = \frac{1}{\sqrt{L_{tot}(T) C_{STO}}}$, but we instead use the imaginary part of the impedance in a larger band to extract L_k as described by equation 3.12. For these results the dissipative processes in the 2DEG, which only affects the depth of the microwave absorption peak, are irrelevant.

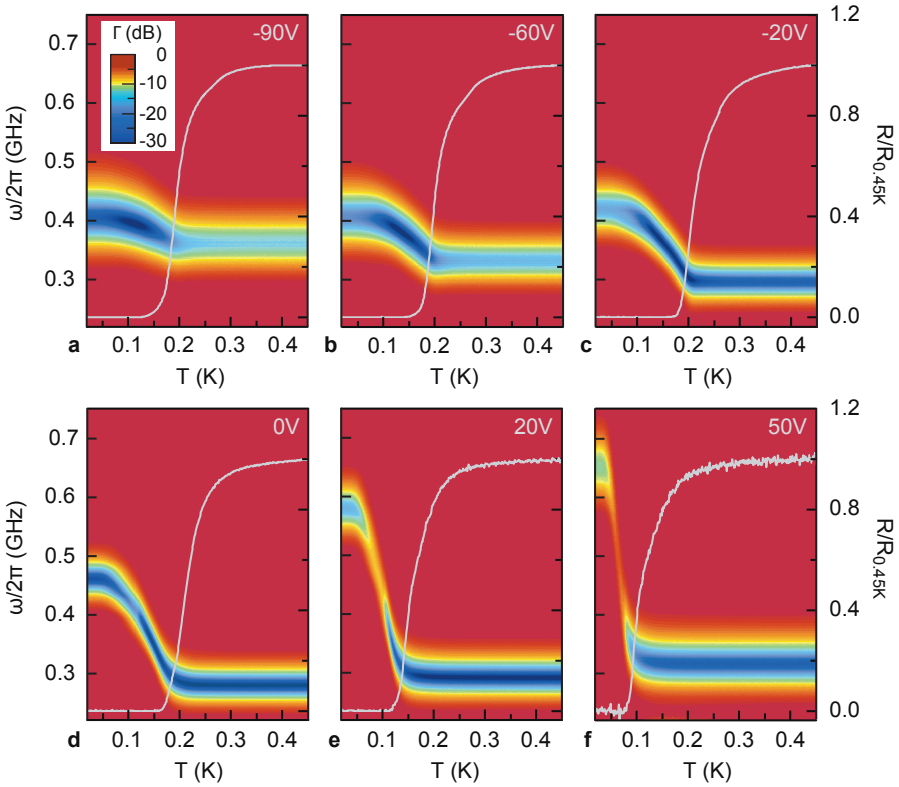

Figure 3.20: **Resonant microwave transport in the superconducting state. a–f**, Magnitude of the reflection coefficient Γ (in dB) as a function of frequency ω and temperature for different values of the gate voltage after calibration (see appendix A). The temperature dependence of the sheet resistance R, normalized by the normal state resistance $R_{0.45K}$ taken at T = 450 mK, is shown on the right axis.

The shift of the resonance is larger in the overdoped regime (figure 3.20 bottom d. e. and f. panel), than in the underdoped regime (figure 3.20 top a. b. and c. panel) indicating that the superfluid stiffness increases with doping, as expected.

Zero temperature stiffness : 2D disordered limit for a superconductor

We first discuss the zero temperature stiffness. From equation 1.34, we express the superfluid stiffness in Mattis Bardeen theory in terms of the normal state resistance R_N and the superconducting gap Δ. Using equation 1.41 discussed in chapter 1, we link the stiffness at zero temperature to the gap at zero temperature of a disordered 2D BCS superconductor through the relation:

$$J_s^{BCS}(0) = \frac{\pi\hbar}{4e^2 R_N}\Delta(0) \tag{3.13}$$

In figure 3.21, we compare the superfluid stiffness extracted at the lowest temperature $J_s(18\,mK)$ to the BCS superfluid stiffness estimated using equation 3.13. Here R_n is taken from dc transport and the gap is obtained from T_c in a weak coupling BCS limit ($\Delta = 1.76 k_B T_c$).

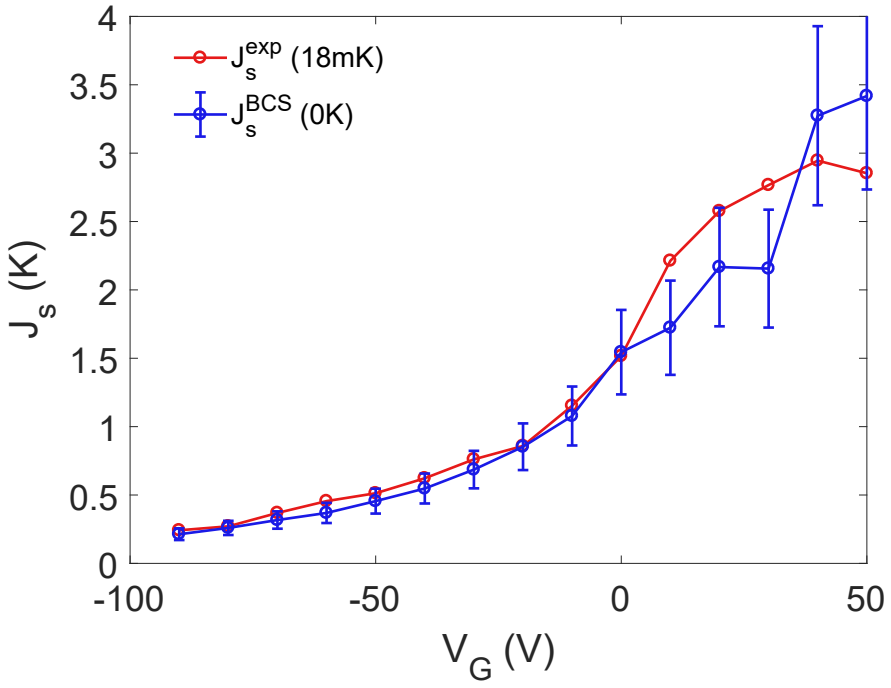

Figure 3.21: Comparison between theoretical Mattis-Bardeen stiffness in the BCS dirty limit $J_s^{BCS}(T=0)$ and experimental $J_s^{exp}(T = 18\ mK)$.

We obtain a very good agreement between the Mattis Bardeen stiffness and experimental J_s^{exp} in the underdoped regime. In the overdoped multiband regime, we have a qualitative agreement with mismatch of maximum 30% averaging out on the total gate range. We can conclude that the 2DEG stiffness seems to be the one expected from BCS theory under our assumption of weak coupling, low excitation and dirty limit. The situation is different from that encountered in the (001) orientation for which strong deviations were observed between the BCS predicted stiffness and the experimental one. Such difference was interpreted as the result of inhomogeneous superconductivity in the underdoped regime [34].

Temperature dependence of the superfluid stiffness

The superfluid stiffnesses normalized by their zero temperature value as a function of normalized temperature T/T_c for all gate voltage are presented in figure 3.22 below.

This figure shows two distinct regimes: in the UD regime, all curves collapse onto the single-band BCS fit. In the OD regime, when the second band start to be populated, the curve deviates from the single-band BCS fit and its curvature changes. For the largest gate value, we see a tail in the

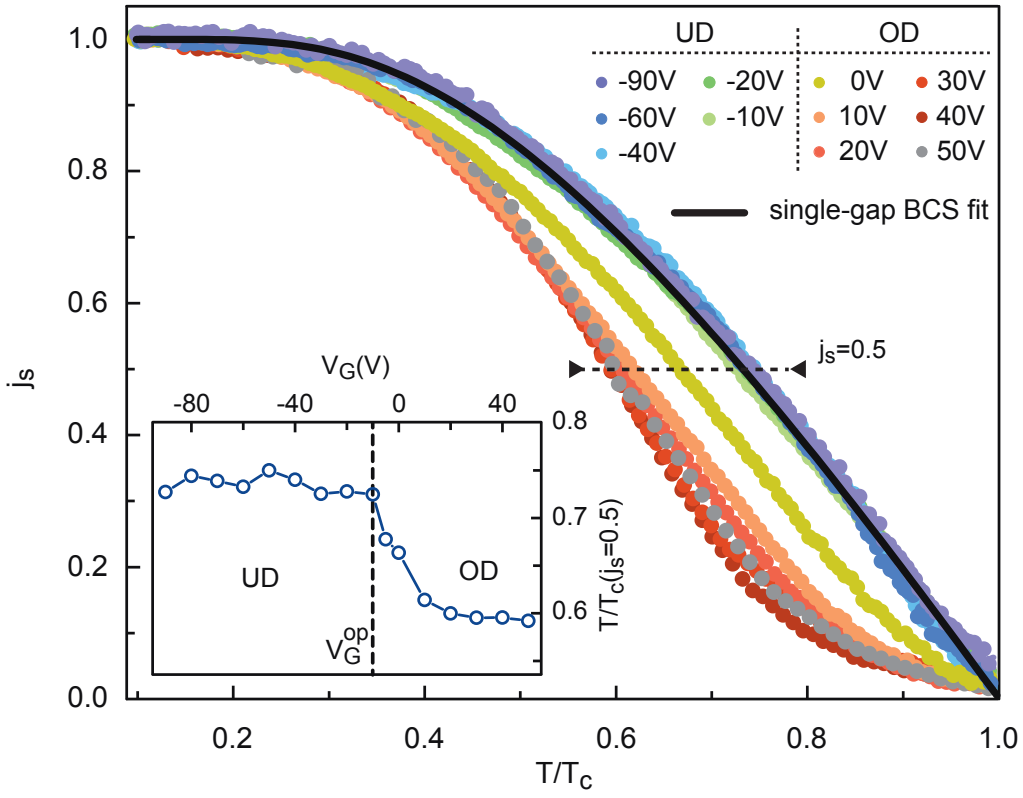

Figure 3.22: **Superfluid stiffness in LAO/STO(110)**. Normalized superfluid stiffness $j_s = \frac{J_s(T)}{J_s(0)}$ as a function of the reduced temperature $\frac{T}{T_c}$ for different gate voltages in the UD and OD regimes (see color code up-right corner). The value of T_c used in the reduced temperature is the one extracted from either a single band BCS fit or a two-band BCS fit (see text). In the UD regime, all the curves are superimposed and follow a single-gap BCS behavior (dashed line). In the OD regime, the temperature dependence of the j_s curves is strongly modified. The absolute value of J_s at $T \approx 0$ as a function of V_G is shown in figure 3.21. The inset shows the reduced temperature $\frac{T}{T_c}$ corresponding to $j_s = 0.5$ as a function of V_G. Whereas the values are constant in the UD regime, an abrupt decrease of the critical temperature takes place at the Lifschitz transition.

curve close to T_c which arises from the interaction between the two condensates. The inset shows the evolution of the normalized temperature where the normalized stiffness reaches 50% of its value, as a function of gate voltage. A clear change in behavior is observed at $V_G \approx -10\ V$ marking the transition between the underdoped and overdoped regime.

The purpose of the next section is to understand why we observe two distinct behaviours depending on the doping regime, and how it can be described.

3.5.3 Superfluid stiffness of a two-gap superconductor

Equiped with our previous results on the critical magnetic field measurements, we now address the issue of two-gap superconductivity in LAO/STO(110) interfaces based on microwave measurement. Kogan et al. have proposed a model in which we can self-consistently calculate the superconducting gap and stiffness evolution of each individual band by introducing intraband and interband coupling

constant $\lambda_{\mu\nu}$ related to the critical temperature *via* a BCS-like gap equation. In this model, we introduce the intraband coupling constant $\lambda_{11,22}$ and the interband coupling constant $\lambda_{12,21}$ with the constraint $n_1\lambda_{12} = n_2\lambda_{21}$ where $n_i = \frac{N_i}{N_{tot}}$ are the density weights of each band. The superconducting critical temperature is determined through a BCS like gap equation:

$$1.76k_BT_c = 2E_De^{\frac{-1}{\tilde{\lambda}}} \tag{3.14}$$

where $\tilde{\lambda}$ is the effective coupling constant $\tilde{\lambda} = \frac{2(\lambda_{11}\lambda_{22}-\lambda_{12}\lambda_{21})}{\lambda_{11}+\lambda_{22}-\sqrt{(\lambda_{11}-\lambda_{22})^2+4\lambda_{12}\lambda_{21}}}$. [3]

By introducing the reduced energy gap $\delta_\mu = \frac{\Delta_\mu}{T_c 2\pi t}$ and the reduced temperature $t = \frac{T}{T_c}$ we can solve a self-consistent gap equation for each band

$$\delta_\mu = \sum_{\mu=1,2}^{\infty} n_\mu\lambda_{\mu\nu}\delta_\mu \left(\frac{1}{\tilde{\lambda}} + \ln(\frac{T_c}{T}) - A_\mu\right) \tag{3.15}$$

$$A_\mu = \sum_{n=0}^{\infty}\left(\frac{1}{n+1/2} + \frac{1}{\sqrt{\delta_\mu^2+(n+1/2)^2}}\right)$$

Running the last sum over a few hundreds iterations is sufficient. The superfluid density is given by the sum of the contributions from both band

$$j_s = \gamma j_{s1} + (1-\gamma)j_{s2} \tag{3.16}$$

where each band's superfluid stiffness is self-consistently calculated from the reduced gap δ_μ:

$$j_{s\mu} = \delta_\mu^2 \sum_{n=0}^{\infty}\left[\delta_\mu^2 + (n+1/2)^2\right]^{-3/2} \tag{3.17}$$

and γ account for the weight of each band to the stiffness, determined experimentally.

3.5.4 Application of the two-gap model to LAO/STO(110) superfluid stiffness measurement

$J_s(T)$ curves presented in figure 3.22 were fitted using a single band BCS model for the underdoped regime or the two-gap model for the overdoped regime, which is described in the section above. Figure 3.23 below shows the results of the fitting procedure for 6 different gate voltages, three in the underdoped regime ($V_G = -90\ V$, $-60\ V$ and $-20\ V$) and three in the overdoped regime ($V_G = 0\ V$, $20\ V$ and $50\ V$).

In the UD regime, a single band BCS superfluid stiffness deduced from the self-consistent gap fits well the data (upper panel figure 3.23 **a.** **b.** and **c.** in linear scale, middle panel for log scale). The bottom panels of figure 3.23 **a.** **b.** and **c.** show the self-consistently calculated BCS gap. In this region, neither the amplitude of the gap ($\Delta \simeq 350\ \mu eV$) nor the $T_c = 200\ mK$ change much.

[3] Note that the coupling constant of the model relates to the electron-phonon interaction λ_{ab}^{ep}, the coulomb interaction μ_{ab}^* and the mass renormalization $Z_a = 1 + \sum_\mu \lambda_{ab}^{ep}$ *via* $n_a\lambda_{ab} = (\lambda_{ab}^{ep} - \mu_{ab}^*)/Z_a$.

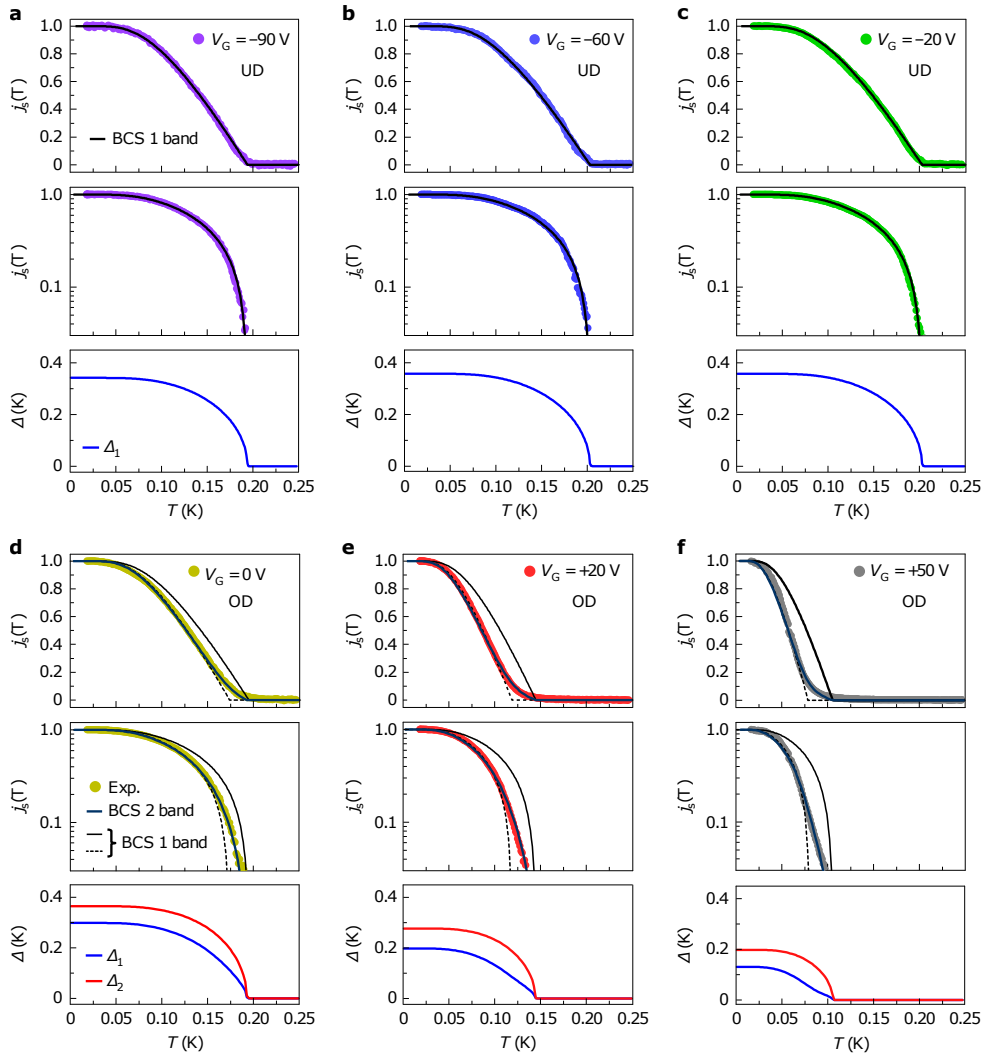

Figure 3.23: **Single-condensate to two-condensate superconductivity transition seen from the superfluid stiffness. a-f.** Temperature dependence of j_s (symbols) in a linear scale (top panels) and logarithmic scale (middle panels) for three gate voltages in the UD regime (V_G = -90 V **a.**, -60 V **b.** and -20 V **c.**) and three gate voltages in the OD regime ($V_G = 0\ V$ **d.**, $V_G = 50\ V$ **e.** and $V_G = 50\ V$ **f.**). In the UD regime, $j_s(T)$ is fitted using the single-band model (black line) assuming in equation 3.15 the gap energy $\Delta_1(T)$ shown in the lower panel for each gate voltage. In the OD regime, $j_s(T)$ is fitted using the two-band model (blue line) corresponding to equation 3.16, assuming in equation 3.15 the gap energies $\Delta_1(T)$ and $\Delta_2(T)$ shown in the lower panel for each gate voltage. Two attempts to fit $j_s(T)$ in the OD using a single-band model are also shown (black solid and dashed lines).

In the OD regime, there is a tail close to T_c (figures 3.23 **d. e.** and **f.** upper and middle panels), which cannot be fitted by the single band BCS model. In the middle panel of figure 3.23 **d. e.** and **f.**, we can see that while none of the two BCS 1-band fit the data, the BCS 2-band model shows a very good agreement. The bottom panels figures 3.23 **d. e.** and **f.** represent the self-consistent gap of the two condensates Δ_1 and Δ_2, calculated from equation 3.15. At $V_G = 0\ V$ the second gap appears and both Δ_1 and Δ_2 are close to $350\ \mu eV$. We notice that the second gap, despite being from a band less populated, has a higher amplitude as anticipated from the DOS. The more we increase the gate voltage, the more $\Delta_{1,2}$ and T_c decrease. Finally, at $V_G = 50\ V$ the two gaps are reduced to less

than 200 μeV, the T_c to $\simeq$ 100 mK and the effect of the coupling of the two condensates is more pronounced and visible close to T_c (bottom panel **f.**).

Note on disorder : Kogan et al., derived the two-band model discussed above in a clean limit, however, we can show that the qualitative results should hold in the dirty limit as well. Indeed, both the behavior close to $T = T_c$ and $T = 0$ is well reproduced in the dirty and clean limit and highlights a universal superconducting behavior.

3.5.5 Summary on superfluid stiffness measurement in LAO/STO(110)

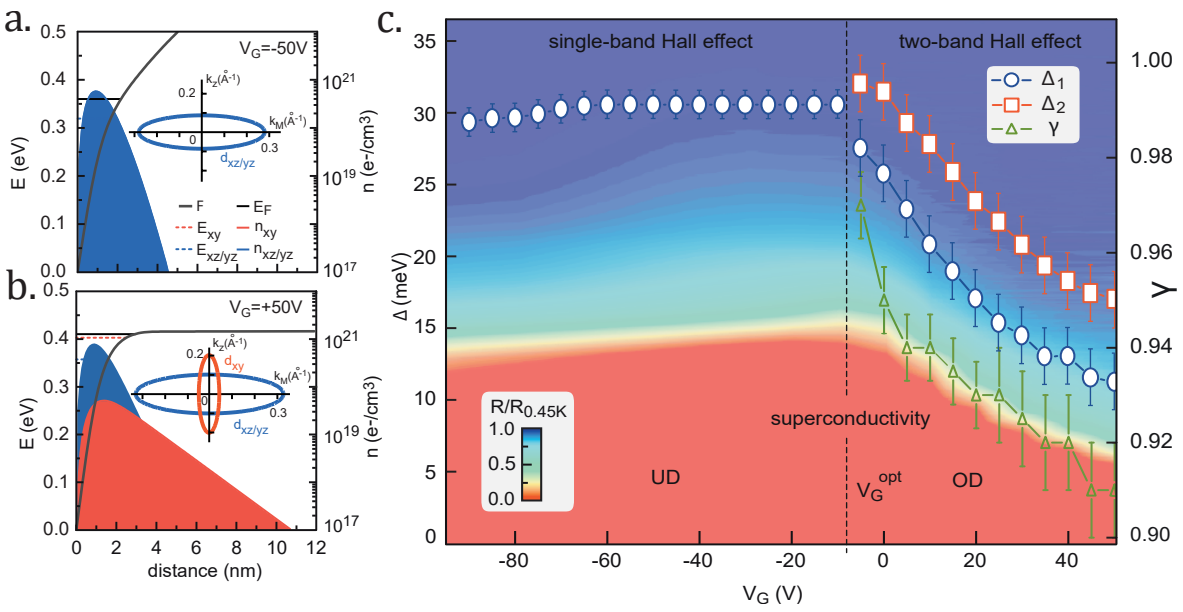

Figure 3.24: **Superconducting phase diagram of the $LaAlO_3$/$SrTiO_3$(110) interface (sample A). a.** and **b.**, Numerical simulations of the band structure in the (110)-oriented interface using self-consistent Poisson-Schrödinger equations for two doping regimes: $V_G = -50\ V$ **a.** and $V_G = +50\ V$ (**b.** same key as in **a.**) The confinement potential ϕ in the energy scale as a function of the distance to the interface, the Fermi energy (E_F) and the energies of the different t_{2g} bands (E_{xy} , $E_{xz/yz}$) are shown on the left axis while the 3D carrier densities associated with each band (n_{xy} , $n_{xz/yz}$) are shown on the right axis. The 2D carrier density used in the simulation corresponds to the one reported on fig. 3.9, that is, $n \approx 0.75 \times 10^{14}\ e \cdot cm^{-2}$ at $V_G = -50\ V$ and $n \approx 1.1 \times 10^{14}\ e \cdot cm^{-2}$ at $V_G = +50\ V$. The inset shows Fermi contours in the (k_z ([001]), k_M ([1–10])) plane for each gate voltage. **c.**, Gap energies $\Delta_1(0)$ and $\Delta_2(0)$ (left axis) and the individual stiffness weight γ (right axis) extracted from the fitting procedure, plotted as a function of V_G and superimposed on the sheet resistance colour map of fig. 3.7. Error bars correspond to the uncertainty in the fitting procedure.

Figure 3.24 summarizes our results on superfluid stiffness. In panel a. and b. we present Poisson-Schrodinger simulations of the electron distribution in the quantum well, as well as the Fermi surfaces. The results are obtained by self-consistently solving the Poisson equation for the electronic density in a given shape of the well, which will in turn influence the electronic density and so on. The procedure is described in section 1.3.3. Panel **c.** presents the superconducting phase diagram with the two gaps.

Let us focus on panel **a.** and **b.**. When only the lowest degenerates $d_{xz/yz}$ are populated as represented in panel **a** in the underdoped regime ($V_G = -50\ V$), the electrons distribution is confined close to the interface ($\simeq 5\ nm$). At higher carrier density, the high energy d_{xy} band is also populated and the corresponding electrons extend deeper in the substrate ($\simeq 11\ nm$). The Fermi surface shows a double elliptical shape as discussed in the section 3.1.1 at the beginning of the chapter.

Figure 3.24c. synthesizes our findings. In the background, it shows the superconducting phase diagram obtained by plotting the normalized resistance in color scale as a function of temperature and gate voltage. Two regimes are visible, separated by a dashed black line corresponding to the optimal doping point of maximum T_c.

In the underdoped regime, the linear Hall effect is characteristic of a single band conduction and, consistently, the temperature dependent superfluid stiffness indicates the presence of a single superconducting gap. In this regime, the T_c remains constant and does not vary with the carrier density as expected in a BCS picture. In the overdoped regime, beyond the optimal doping point, the Hall effect is non-linear revealing the additional filling of the high-energy d_{xy} band. The temperature dependence of the superfluid stiffness indicates a two-gap superconducting regime. Both superconducting gaps follow the T_c and decrease with gate voltage in this regime. The right axis shows γ, an experimental measure of the contribution of the first band to the superfluid stiffness. It decreases suggesting that the relative importance of the second band grows as the gate voltage increases.

3.5.6 Comparison with critical field measurements

From the two different experimental probes, namely the microwave measurement of the superfluid stiffness and the critical magnetic field measurements, we find similar results regarding the superconductivity at LAO/STO(110) interface. First in the underdoped regime ($V_G < 0\ V$), the Hall effect is linear, associated with the filling of the lowest degenerate bands $d_{xy,yz}$ and the superconductivity is well fitted by a single band BCS model, both in terms of stiffness J_s or critical field H_{c2}. Secondly, in the overdoped regime ($V_G > 0$) the Hall effect becomes non-linear, indicating the filling of the higher d_{xy} band, and the T_c decreases upon doping. We have used two different methods to evidence the one-gap to two-gap superconductivity transition. From the superfluid stiffness measurements on sample A in the overdoped regime, we have deduced the superconducting gap by solving equations 3.17 and 3.15 from the Kogan model (see section 3.5.3). We determined the intraband superconducting constant $\lambda_{11/22}$ and interband superconducting constant $\lambda_{12/21}$, which gives the gaps evolution in temperature. At the same time, the critical field measurement on sample B in the overdoped regime was fitted using the model proposed by Edge and Balatsky (see section 3.4.2) of two weakly coupled interacting superconductors in the dirty limit. It has allowed us to find the superconducting coupling constants from a fitting procedure, and thus compute the temperature dependence of the gaps.

Figure 3.25 shows the consistency of the superconducting gaps extracted by the two methods. Each panel presents the gaps as a function of gate voltage, and the inset shows the λ coupling parameters deduced from the fits. In figure 3.25**a.** and **b.** we see the two regimes, separated by a dashed line indicating the transition between the two Hall effect regimes.

In the underdoped regime ($V_G < 0\ V$), where only the lowest degenerate d_{yz}/d_{xz} bands contribute to the superconductivity, the coupling constant λ_{11} is independent of gate voltage. This is in agreement with the constant T_c in this region, as well as the idea that the T_c depends only on the DOS which is constant in 2D for a single band. In both critical magnetic fields (panel **b.**)

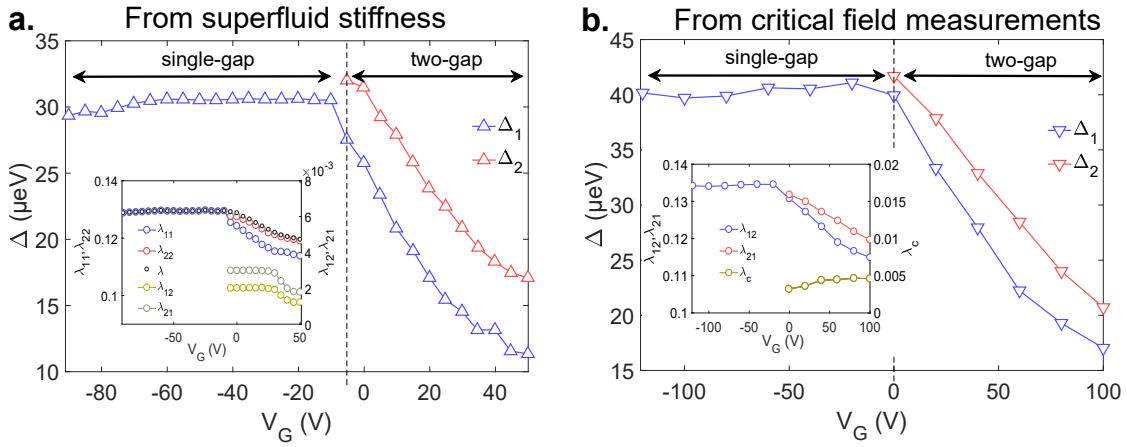

Figure 3.25: **Gate evolution of the superconducting gap(s) and coupling constants in $LaAlO_3/SrTiO_3$(110) a.** From superfluid stiffness measurement on sample A (Kogan et al., model [113]) **b.** From Critical field measurement on sample B (Edge and Balatsky model [104])

and superfluid stiffness (panel **a.**) experiments, we find a similar $\lambda_{11}(UD) \approx 0.13$, yielding a gap $\Delta \simeq 30 - 40\mu eV$.

In the overdoped regime, the higher d_{xy} band starts to be populated and contributes to the superconductivity. The two condensates interact *via* the interband coupling constant called λ_c in the critical field measurement analysis and λ_{21} or λ_{12} in the superfluid stiffness one. The later two are related to λ_c via the weighted density of state. More explicitly, $\lambda_{12} = \lambda_c \frac{N_1}{N_1+N_2}$ where N_1 and N_2 are the DOS of the two bands.

Using Edge and Balatsky's model (from Gurevich calculations) for critical field measurements, and Kogan model for superfluid stiffness measurements, we capture the drop of T_c upon increasing gate in the overdoped regime by assuming that the superconducting coupling constant changes with gate voltage. However such an artificial decrease of the intraband coupling constant is not physical. As we will see in the following, a more detailed microscopic model that includes the effect of disorder is needed to fully explain our data.

3.5.7 s±-wave superconductivity

The phase diagram in the previous sections shows a suppression of superconductivity in the two-gap regime, which is not expected within a simple BCS approach since, at the Lifschitz transition, an increase in the number of electronic states available should enhance T_c. However, such weakening of superconductivity was predicted in multiband superconductors in the presence of disorder when the order parameters associated with each superconducting condensate have opposite sign because of a repulsive coupling, a situation referred to as s±-wave superconductivity [114]. The s±-wave superconductivity is characterized by a negative interband coupling constant ($\lambda_{12,21} < 0$). Golubov and Mazin showed that for anisotropic multiband s±-wave superconductor, nonmagnetic scattering decreases the T_c as the scattering rate τ increases [115]. Their approach was developped for metallic 3D system with a fixed, large DOS, however Trevisan et al. adapted this model for 2DEGs at oxide interfaces, with the possibility of varying the carrier density [116]. In the following, we present a model developed in collaboration with G. Venditti, S. Carrara and M. Grilli from La Sapienza university (Rome). We consider that the superconducting coupling constants λ have to sat-

isfy $N_1\lambda_{12} = N_2\lambda_{21}$, found to be $\approx -N_1\lambda_{11} \cdot 10^{-2}$ with $\lambda_{11} = 0.135$ (the value in the underdoped region).

Figure 3.26 shows a schematic of the density of states. In our experiment, the lowest degenerate $d_{xz,yz}$ band are always in the BCS regime (in the sense that the chemical potential μ is always larger than the pairing from Debye frequency Ω) while the higher d_{xy} band, populated at positive gate voltage, is in the Bose-Einstein condensate regime in the sense that the pairing Ω is stronger than the chemical potential μ. [117]. The Debye energy is taken to be $\Omega = 34.5\ meV$. The two bands have a constant DOS, denoted N_1 and N_2. The lower limit of the lowest band is $w_1 = -\mu$, while the lower limit of the upper band is $w_2 = \epsilon_0 - \mu$, ϵ_0 being the difference between the difference between the bottom of the two bands. The top of the bands, L_i are linked to the chemical potential μ and ultraviolet cutoff Λ *via* $\Lambda_i = L_i - \mu$. Sweeping the back gate in its entire range from -120 V to +100 V is equivalent to shifting the chemical potential from 40 to 95 meV, as represented in the blue shaded area in figure 3.26.

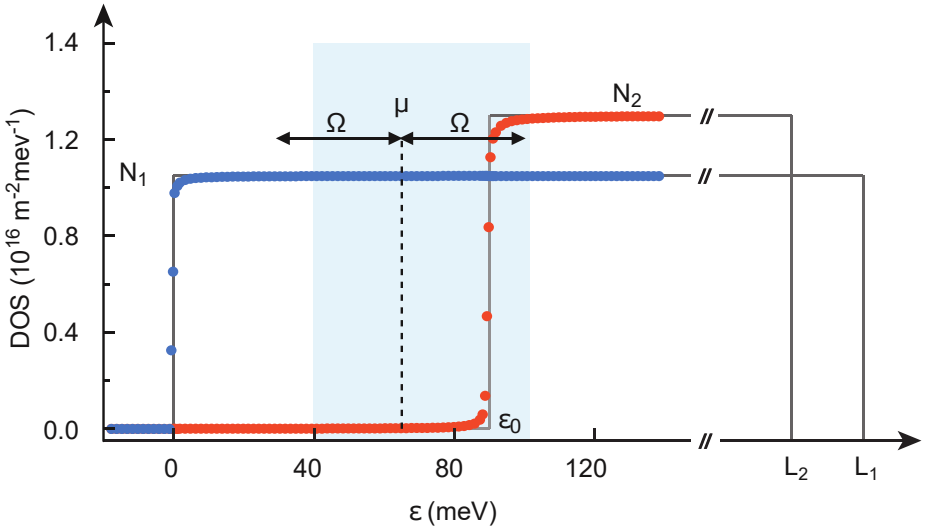

Figure 3.26: Band structure of our two-band model. Solid grey lines show the clean limit (no disorder), while the blue and red symbols show the dirty limit for both bands, with a scattering rate $\tau^{-1} = 0.4\ meV$. The shaded blue area represent the accessible chemical potential window upon gating. Ω is the Debye energy.

The critical temperature is extracted from the linearized equation for the superconducting gaps in the presence of disorder in the Born approximation :

$$\begin{pmatrix}\Delta_1\\ \Delta_2\end{pmatrix} = \begin{pmatrix}\lambda_{11} & \lambda_{12}\\ \lambda_{21} & \lambda_{22}\end{pmatrix}\begin{pmatrix}A_{11} & A_{12}\\ A_{21} & A_{22}\end{pmatrix}\begin{pmatrix}\Delta_1\\ \Delta_2\end{pmatrix} \tag{3.18}$$

where

$$A_{ij} = k_B T \sum_n \frac{M_{ij}}{Det(M)} \int_{\nu_i}^{\xi_i} \frac{d\xi}{\tilde{w}_n^2 + (\xi + h_n)^2}$$

and $\nu_i = \max(-\Omega, w_i)$, $\xi_i = \max(\Omega, w_i)$.

When $\mu \ll L_i$, which is the case in our system, then the renormalized Matsubara frequency $\tilde{\omega}$ and the disordered-renormalized band dispersion h_n are calculated self-consistently as [115]:

$$\tilde{\omega_n} = \omega_n + \frac{\tilde{\omega}_n}{4\tau} \sum_{j=1,2} f_{n,j} \tag{3.19}$$

$$h_n = -\frac{1}{4\pi\tau} \sum_{j=1,2} \int_{w_i}^{\Lambda_j} \frac{(\xi + h_n)}{\tilde{\omega}_n + (\xi + h_n)^2} d\xi \tag{3.20}$$

The Matsubara frequencies are defined as $\omega_n = (2n+1)\pi k_B T$ and the fuction f is:

$$f_{n,j} = \frac{1}{\pi} \int_{w_j}^{\Lambda_j} \frac{d\xi}{\tilde{\omega}_n^2 + (\xi + h_n)^2}$$

The term $M/Det(M)$ enforces the disorder-induced vertex corrections to the coupling constants λ's *via*:

$$M = \begin{pmatrix} 1 - \frac{1}{4\tau} f_{n,1} & \frac{1}{4\tau} f_{n,1} \\ \frac{1}{4\tau} f_{n,2} & 1 - \frac{1}{4\tau} f_{n,2} \end{pmatrix} \tag{3.21}$$

τ is the single scattering time considered here, for simplicity. Finding the root of the determinant of the homogenous linear problem equation 3.18 gives T_c versus μ (remember μ is a function of w_i and L_i). The disordered-broadned DOS $\tilde{N}_{1,2}(\epsilon)$ is solved self-consistently via the equations:

$$\tilde{N}_{1,2}(\epsilon) = \mathrm{Im} \int_{w_i}^{\Lambda_i} \frac{N_i(\xi)}{\epsilon - \xi - \varsigma_i} d\xi = N_i \mathrm{Im}(\varsigma_i) \tag{3.22}$$

$$\varsigma_i(\epsilon) = \sum \frac{1}{2\pi\tau} \ln \frac{\epsilon - w_i - \varsigma_i}{\epsilon - \Lambda_i - \varsigma_i} \tag{3.23}$$

where

$$\varsigma_i^{n=0} = \frac{i}{2\pi\tau} \tag{3.24}$$

Using the relation

$$n(\mu, T) = \int_{-\infty}^{\xi} [\tilde{N}_1(\epsilon) + \tilde{N}_2(\epsilon)] \frac{1}{e^{(\epsilon-\mu)/k_B T} + 1} d\epsilon \tag{3.25}$$

together with the experimental n_{2D}, we can obtain T_c versus V_G. The chemical potential is mapped to the number of particle following the relation:

$$n(\mu) = \sum_{i=1,2} \int_{-\infty}^{\mu} \tilde{N}_i(\xi) d\xi \tag{3.26}$$

Finally, we have the T_c as a function of the gate voltage and chemical potential. The DOS $N_1 = 1.05 \times 10^{16} m^{-2} meV^{-1}$ and $N_2 = 1.3 \times 10^{16} m^{-2} meV^{-1}$ are taken from ARPES study on (110)-oriented STO crystals. [88].

The critical temperature T_c of the two condensates system is computed for different scattering rates τ^{-1}. Its ratio to the single band condensate critical temperature T_{c0}, as a function of the chemical potential, is plotted figure 3.27 below, assuming a splitting between band $\epsilon_0 = 90\ meV$:

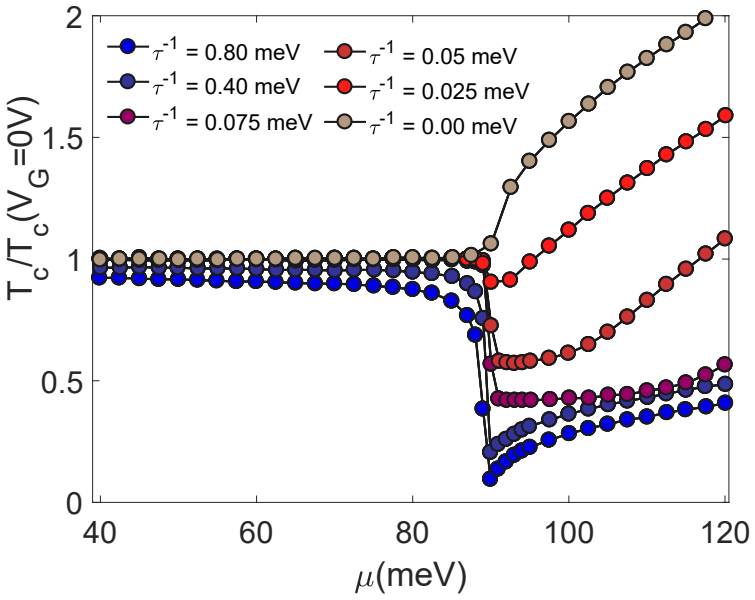

Figure 3.27: Ratio of the calculated T_c to the single-band superconducting critical temperature T_{c0} in the clean limit, as a function of the chemical potential μ for different scattering rates τ^{-1} in the s$\pm$-wave two-condensate case (i.e repulsive interband pairing case $\lambda_{12} < 0$).

It is clear that the ratio T_c/T_{c0} remains constant around 1 in the underdoped region, where only a single condensate contributes below $\mu \approx 90\ meV$. When the second condensate starts to contribute, we observe different behaviours depending on the scattering rate τ. For the two lowest computed scattering times 0 and 25 μeV, T_c is increased upon population of the second condensate. For the four highest computed scattering times of 50, 75, 400 and 800 μeV, T_c is reduced as observed experimentally. However the curves follow a V-shape, characteristic of a BEC scenario. From transport measurement of the diffusion constant, we estimate an upper bound $\tau^{-1} \approx 0.4\, meV$.

To further improve the theoretical description of our experiment, we consider that the 2DEG is made of coupled puddles [118] in which the fluctuations in carrier density, associated with fluctuations of the local chemical potential, lead to fluctuations in T_c such that the average is given by:

$$\langle T_c(\mu) \rangle = \int_{-\infty}^{\infty} T_c(\mu') G\left(\frac{\mu' - \mu}{\sigma}\right) d\mu' \tag{3.27}$$

Where G is the normalized Gaussian distribution with average value μ and variance σ. Such disorder has the effect of smoothing out the V-shape drop of T_c. We find that the value $\sigma = 7\ meV$ leads to a good agreement between the s$\pm$-wave model and the experiment (yellow diamond sym-

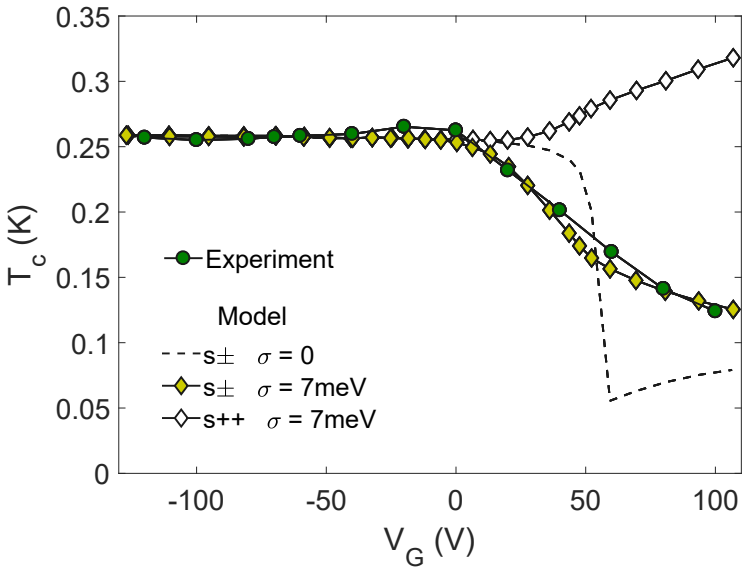

Figure 3.28: Experimental (green circles) and calculated superconducting T_c as a function of the gate voltage V_G. The model correspond to a s$\pm$ superconductor with no mesoscopic disorder (dashed line), a s$\pm$ superconductor with fluctuations of the chemical potential of variance $\sigma = 7\ meV$ (yellow symbol) and a s++ superconductor with the same variance in fluctuation of μ. All curves have been calculated with a scattering time $\tau^{-1} = 0.4\ meV$.

bols in figure 3.28). Such pictures of a network of superconducting island with random T_c have already proven to efficiently describe the (001) interface of the LAO/STO 2DEG [78] [63]. To convince ourselves that this pair breaking effect is induced by s$\pm$-wave superconductivity, we have shown in white diamond a situation similar to the one in yellow symbol, i.e $\tau^{-1} = 0.4\ meV$ and $\sigma = 7\ meV$, but where the intraband pairing λ_{12} is positive, leading to a s++ superconductor. In such a case, the T_c monotonically increases, as opposed to our experimental measurements.

3.6 Discussion on the LAO/STO(110) superconducting 2DEG

We found that the 2DEG in LAO/STO(110) is superconducting below $\simeq$ 250mK in the whole gate voltage range (-100 to +100V), with a constant T_c in the negative gate region and a continuous drop in the positive gate region. Hall effect measurements shows that the 2DEG has a carrier density of 4 to $10 \times 10^{13}\ cm^{-2}$ with a strong modulation in gate voltage of around $\delta n = 50\%$. Around zero gate voltage, there is a transition from a linear Hall effect to a non-linear Hall effect, meaning that the 2DEG evolves from a single band to a multiband regime. From tight-binding calculations, we ascribe this transition to the filling of the high energy d_{xy} band which has a mobility ten times the larger than the low energy $d_{xz,yz}$ bands. In the superconducting regime, both the upper critical magnetic field measurements and superfluid stiffness temperature dependence measurements show a change in curvature at the Lifschitz point (i.e. the filling of the second band) indicating the formation of a second condensate in the high energy band.

For the critical magnetic field measurements, we have performed a fit of the data with the linearized Usadel equation in the dirty limit and shown the gate evolution of the superconducting gaps

and coupling constants. In the microwave resonant experiment, we were able to measure the kinetic inductance of Cooper pairs and deduce the superfluid stiffness from it, for various gate voltages. Using a similar model of weakly coupled superconducting condensates in the dirty limit developed by Kogan, we solved the self-consistent equations for the gaps, and extract the superconducting coupling constants. Both methods yield gate-dependent superconducting coupling constants which are in good agreement between each other.

The unexpected drop of T_c at the filling of the second band is explained by impurity scattering in a so-called $s_{\pm}$ superconductor, that is a superconductor where the two condensates have opposite sign order parameters ($\lambda_{12/21} < 0$), allowing for destructive interband scattering. In this picture, we managed to explain the gate evolution of T_c by disordered pair-breaking scattering in a s$\pm$-wave superconductor considering an inhomogeneous distribution of T_c.

The 2DEG at $LaAlO_3/SrTiO_3$(110) is, to our knowledge, the only known system where a single to two condensates superconducting transition can be reversibly and continuously driven by a gate voltage.

We could have a similar multi-condensate superconductivity in the (001)-oriented sample, as it has been predicted from two-dimensional two gaps models [111] [116] but so far, experiments are more consistent with a single gap. This could be explained by the weak magnitude of the second gap, as $N(0)$ is small, and the rapid suppression of T_c upon doping. Local susceptibility measurements have restrained the magnitude and doping of the second gap [75] but could not rule out definitively the existence of the second gap. Two gaps superconductivity has been observed in bulk Nb-doped $SrTiO_3$ [33] evidenced by a double peak structure in the differential tunnel conductance, but replication of this experiment on a $LaAlO_3/SrTiO_3$(001) 2DEG has failed to capture two gaps [73]. Here, in the (110)-oriented 2DEG, the lowest bands have a higher $N(0)$ leading to a sizeable gap which can be observed by indirect probes such as superfluid measurement, demonstrating the existence of multi-gap superconductivity in STO-based 2EDGs.

3.7 Sample preparation of LAO/STO(111)-2DEG

Sample name	LS253	LS281
Measurements	DC (Hall effect, superconducting phase diagram Critical field ($H_{c2}^{\perp}$)) RF (superfluid stiffness)	DC (Hall effect, superconducting phase diagram) Parallel critical field ($H_c^{\parallel}$)
Preparation	Cr back gate deposited Integrated in an RLC circuit	Two barrels cut in perpendicular directions Silver pasted onto gold gate
Transport properties @ $V_G = 0V$	$R_{4K} = 0.6\ k\Omega.\square^{-1}$ $n = 7.8 \times 10^{13}\ cm^{-2}$ $T_c = 215\ mK$	$R_{4K} = 0.6\ k\Omega.\square^{-1}$ $n = 9.5 \times 10^{13}\ cm^{-2}$ $T_c = 265\ mK$

Table 3.4: Description of the two samples of $LaAlO_3/SrTiO_3$(111), whose results are presented in this chapter.

We have previously seen that the crystal orientation at the interface plays a prominent role in

the physics of the 2DEG. Contrary to the (001) or (110) orientations, the (111)-oriented surface harbors an hexagonal lattice symmetry. This interface is prone to hybridization of t_{2g} orbitals between themselves [97] and the hexagonal lattice is believed to be a condition for the emergence of topological states [90]. We have performed DC and AC transport at LAO/STO(111) interface and we report on the gate-tunable superconductivity and multiband physics in this system. The results which are presented have been obtained from two samples whose characteristics are described in the table 3.4. The LAO/STO(111)-2DEG samples were grown in A. Caviglia group at TU Delft.

3.8 DC measurements of the LAO/STO(111) 2DEG

In this section, we will present DC measurements of resistance as a function of temperature in the entire gating range that allows to derive the superconducting phase diagram. Then we will show Hall effect measurements combined with gate capacitance measurements that enables the determination of the gate dependent carrier density. Finally, multiband physics will be discussed based on critical field H_{c2} measurements and microwave measurements of the superfluid stiffness.

3.8.1 Superconducting phase diagram in LAO/STO(111)

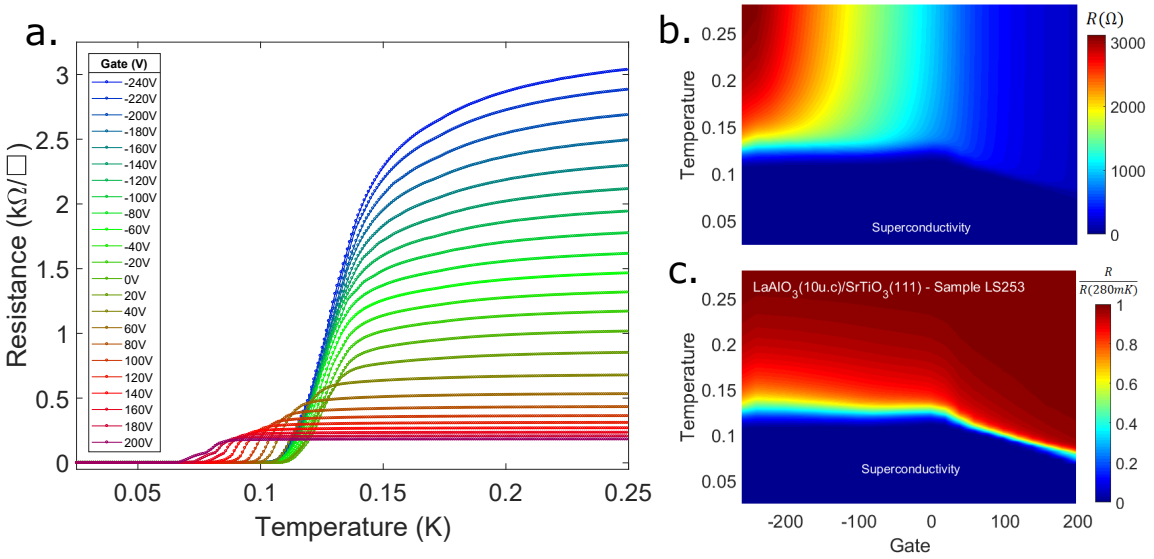

Figure 3.29: **DC measurement of LAO/STO(111) sample LS253 interface. a.** R vs. T curves for different gate voltages from -240V to +200V. **b.** Corresponding color plot. **c.** same as **b.** but normalized by the resistance at 280 mK.

Measurements took place in a dilution fridge down to 15mK, using the set-up described in section 2.2.2 with a bias current I $\approx 1\mu$A. A Van der Pauw geometry was used allowing to extract the sheet resistance from resistivity, as described in section 2.2.3. The resistance vs temperature curves measured for gate voltages ranging from -240V to +200V are shown in fig. 3.29**a**. The T_c varies from 75 to 125 mK and the normal sheet resistance from 200 to 3000 Ω between the maximum doping at V_G = +200 V and the minimum doping at V_G = -240 V.

Figure 3.29**b.** shows the temperature-gate voltage phase diagram of the data in panel **a.**, highlighting the superconducting region in dark blue. Panel **c.** shows the resistance as a function of

temperature in colorscale normalized by the resistance value at 280 mK, which further highlights the superconducting region (in blue) and its border with the metallic state (in red).

The T_c remains almost constant in the negative gate region, whereas it linearly decreases in the positive gate voltage region. We will see that the optimal doping point around $V_G = 0\ V$ corresponds to the point where the Hall effect voltage vs magnetic field curves becomes non linear, suggesting that the occupation of the second band is responsible for the gate dependence decrease in T_c. The overall shape of the superconducting phase diagram, as well as the sheet resistance are very similar to those of the (110) interface.

3.8.2 Hall effect measurement in LAO/STO(111)

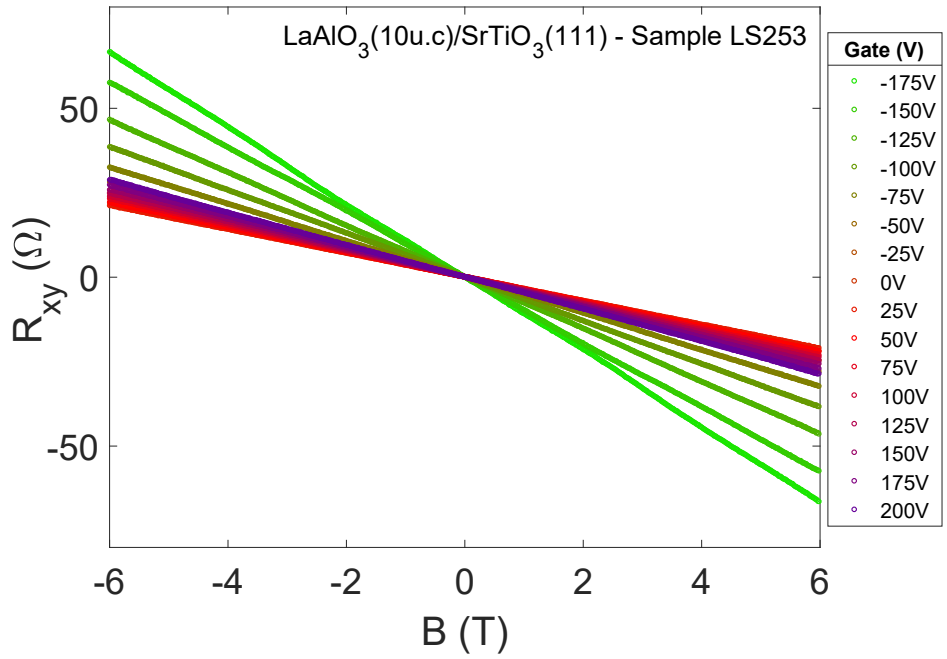

Figure 3.30: **Hall effect measurement and carrier density as a function of gate in a LAO/STO(111) interface**. R_{xy} vs. B for different gate votages. We observe an inverse relation between doping and evolution of the slope above $V_G \sim 0\ V$.

The Hall resistivity R_{xy} as a function of magnetic field for various gate voltages is shown in figure 3.30. Just as for the (001) and (110)-orientated 2DEG, we see an inversion of the coefficient of the slope upon gating, around V_G = 0 V. This indicates that a second band is populated and that the Hall effect becomes non linear at a higher field (not accessible here). In this situation, the low-field Hall effect displays a nonphysical decrease of carrier density upon gating (i.e an increase of the coefficient of the slope) as already discussed for a LAO/STO(110) sample in section 3.3.3.

3.8.3 Gate capacitance measurement

Measuring the gate capacitance is needed to know the total carrier density as a function of gate voltage when the Hall effect is non-linear due to multiple bands being populated. It requires an AC signal on top of a DC signal using the set-up described in figure 2.8 chapter 2. The gate dependence of the capacitance in LAO/STO(111) sample (LS253) is shown figure 3.31. The minimum value of

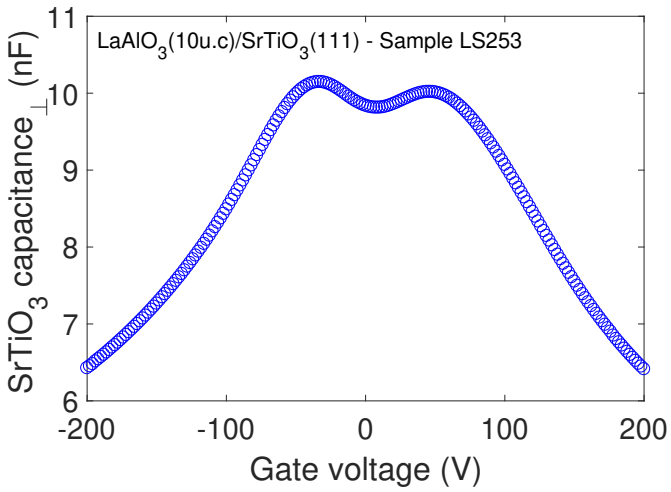

Figure 3.31: **Gate capacitance as a function of gate voltage in LAO/STO(111) sample LS253.**

$\simeq$ 6.5 nF is larger than the parasitic contribution of the set-up estimated to be <1 nF from figure 3.32. The small deep around zero has traditionally been attributed to residual ferroelectricity in the substrate [119].

3.8.4 Carrier density

By measuring the quantum capacitance and integrating its gate dependence we can compute the carrier added to the 2DEG following the formula:

$$n(V_G) = n(V_G = -200) + \frac{1}{eA}\int_{-200}^{V} C_{STO}(V_G)dV \tag{3.28}$$

where A is the surface area of the sample, e is the electron charge, and $C_G(V_G)$ is the gate-dependant substrate capacitance. As usual, a small parasitic contribution of the set-up is to be accounted for by matching the calculated curve to the measured curve in the single band regime ($V_G < 0\ V$). The resulting density n as a function of gate voltage is represented in figure 3.32 with computation of eq. 3.28 for three different parasitic capacitances. We see that the best match is obtained for $C_{para} = 1\ nF$.

The carrier density of the 2DEG at the $LaAlO_3/SrTiO_3$(111) interface that we have measured varies from $\sim 5{\times}10^{13}\text{cm}^{-2}$ to $30 \times 10^{13}\text{cm}^{-2}$. This is larger than typical densities measured at LAO/STO(001) 2DEG: 1-6 $\times\ 10^{13}\text{cm}^{-2}$ [48] [120] [121] [87]. It is also comparable or greater than the density observed at the (110) interface (4 to 12 $\times\ 10^{13}\text{cm}^{-2}$ from [87], 6 to 11 $\times\ 10^{13}\text{cm}^{-2}$ from [76]). The total variation $\Delta n = 25{\times}\ 10^{13}\text{cm}^{-2}$ is also one of the largest observed in this kind of system. For comparison, gating in the LAO/STO(110) in previous chapter "only" increased the carrier density by $\Delta n = 6{\times}\ 10^{13}\text{cm}^{-2}$.

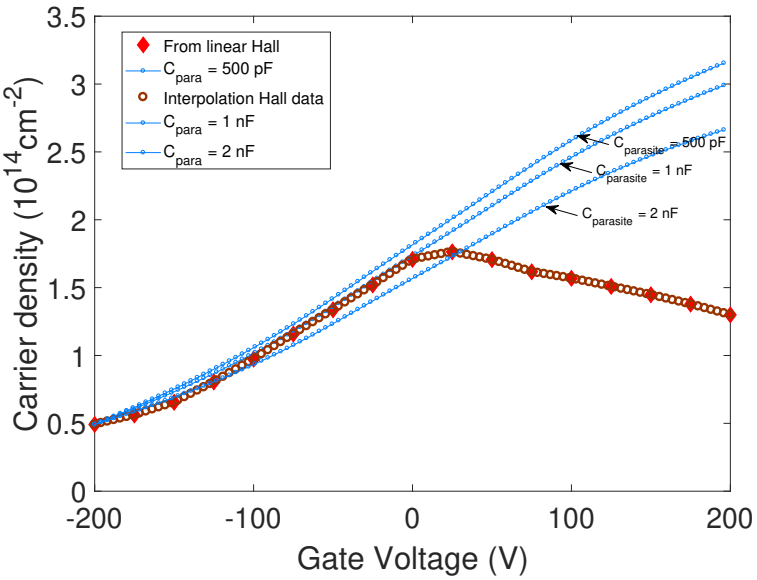

Figure 3.32: **Carrier density as a function of gate voltage in sample LS253**. Linear Hall effect fits (brown circle) fail to predict the carrier density above ∼0V while the capacitance measurement (blue lines), taking into account parasitic contribution, gives a coherent vision of the evolution of the total carrier density.

When the non-linearity is not visible in Hall effect measurement, we can still manage to estimate the individual densities n_1,n_2 and the mobilities μ_1, μ_2 through the following equations :

- $n_1 + n_2 = n_{tot}$
- $\mu_1 n_1 + \mu_2 n_2 = \frac{1}{eR_s}$
- $n_1\mu_1^2 + n_2\mu_2^2 = \frac{1}{e^2 R_s^2 n_{Hall}}$

Where n_{Hall} in the last equation refers to the density extracted from linear Hall effect at low magnetic field. We can assume that the mobility of the lower band μ_1 varies linearly with gate voltage, which is at least rather well verified in the underdoped region where it is the only band contributing to conduction. Once the gate voltage dependence of μ_1 is set, the system can be solved to find n_1, n_2 and μ_2. The gate evolution of these parameters is reported in figure 3.33. Panel **a.** shows the total and individual carrier densities as a function of gate voltage, while panel **b.** represents the evolution of the mobilities with gate voltage. Under our assumption, we can see that the carrier density of the second band n_2 becomes comparable to the first n_1, which is unusual for LAO/STO 2DEG where the second band typically accommodates a maximum of 10% of the total density. The second band is more mobile than the first one ($\mu_1 = 35\ cm^2/V.s$, $\mu_2 =$ up to $200\ cm^2/V.s$) but its mobility is still lower than that from the LAO/STO(110) 2DEG discussed in the previous sections for which μ_2 is as high as 1000 cm^2/V.s.

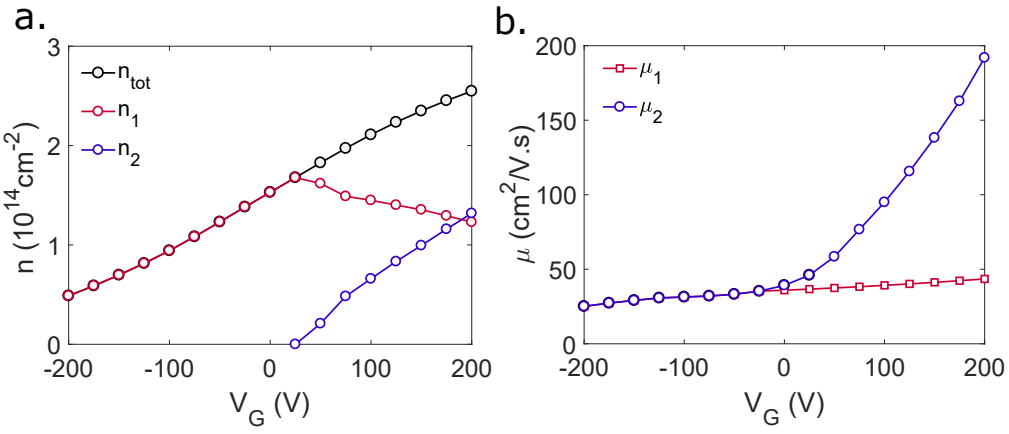

Figure 3.33: **Multiband Hall effect in LAO/STO(111) sample LS253.a.** Carrier density in each band and total carrier density. **b.** Mobilities of the two bands. The mobility μ_1, represented in red square, is an extrapolation of the linear evolution in the underdoped regime.

3.8.5 Critical magnetic field measurement in LAO/STO(111) interfaces

Upper critical field H_{c2}

Just as in the previous chapter on LAO/STO(110) interfaces, we are interested in the evolution of H_{c2} as a function of temperature for all gate voltages, which allows the extraction of the superconducting coherence length. In the following, the out-of-plane upper critical magnetic field H_{c2} is defined as the value at which the resistance recovers 80% of its normal state value.

Figure 3.34 shows the resistivity curve of the LAO/STO(111) 2DEG for various perpendicular magnetic field values. Each panel represents a different gate voltages from $V_G = -100\ V$ in the top left corner to $V_G = 200\ V$ in the bottom right corner. The typical critical field H_{c2} is between 10 and 100 mT which is quite small when compared to previous results in LAO/STO(001) or (110) but consistent with the lower T_c.

From the data presented figure 3.34, we can extract the temperature dependence of the critical field H_{c2}. The results are presented figure 3.35**a.**. Figure 3.35**b.** shows the normalized critical field $H_{c2}(T)/H_{c2}(0)$ as a function of the reduced temperature, with a single band WHH curve (see 3.4.1 for more information) as a guide for the eyes. There is a qualitative agreement between the data and the WHH model, which suggests that either there is only one band which is superconducting, or that both superconducting bands share too many similar properties to be discriminated by the use of critical field measurements.

From equation 1.9, we can compute the superconducting Ginzburg-Landau coherence length ξ ($\xi = \sqrt{\frac{h}{4\pi e H_{c2}}}$.), which is reported figure 3.36.

The 2DEG at (111) orientation studied here has a much larger $\xi(T = 0)$ than in the other orientations : 100 to 300 nm. We can check that the 2DEG is in the dirty limit by calculating $l_{MFP} = \frac{h}{e^2 k_F R_s} = \frac{h}{e^2\sqrt{(2\pi n)}R_s}$ with n = 1.7×$10^{14} cm^{-2}$ and R_s = 4530 Ω at $V_G = 0\ V$, we find $l_{MFP} = 1.7nm$. Since $\xi/l_{MFP} \approx 60 \gg 1$ the 2DEG is indeed in the dirty limit.

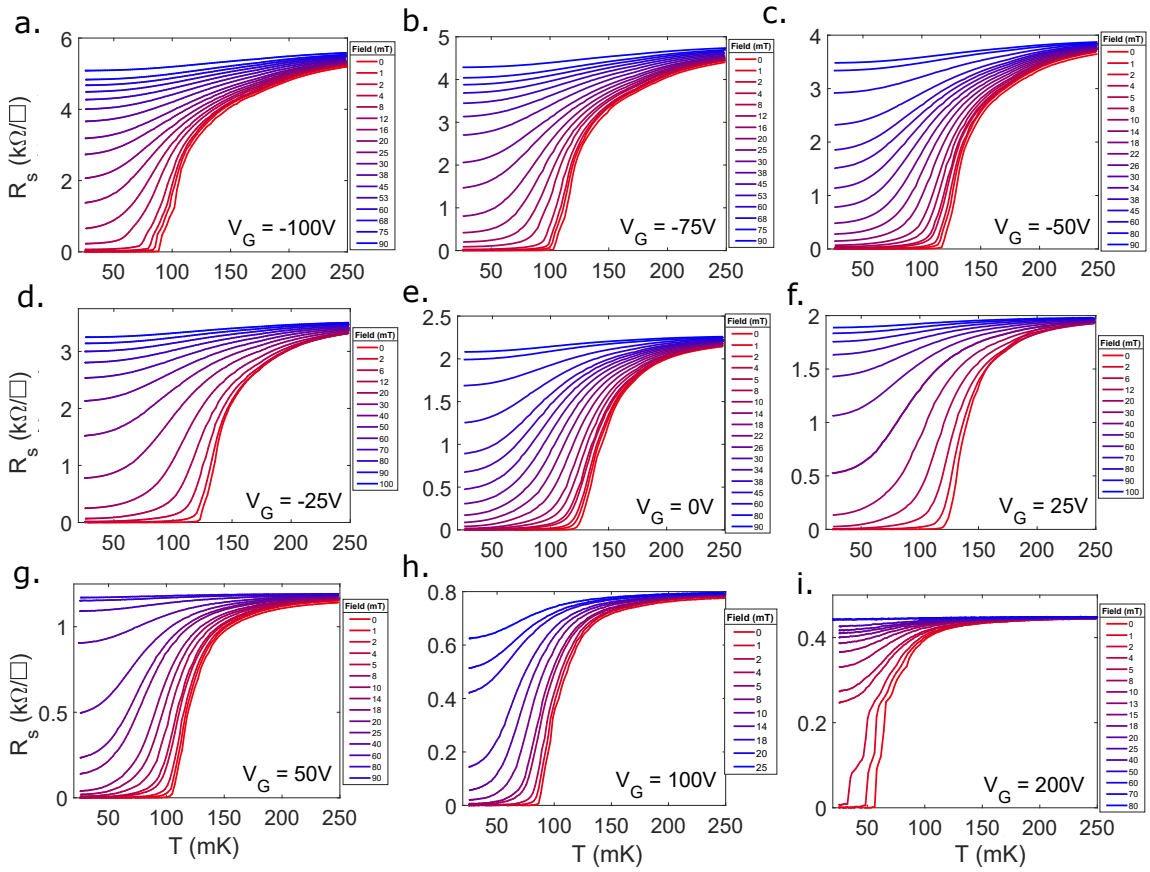

Figure 3.34: **Upper critical magnetic field measurements of the LAO/STO(111) interface sample LS253**. Panels show R vs. T curves for various magnetic fields. Each panel represent a different gate voltage.

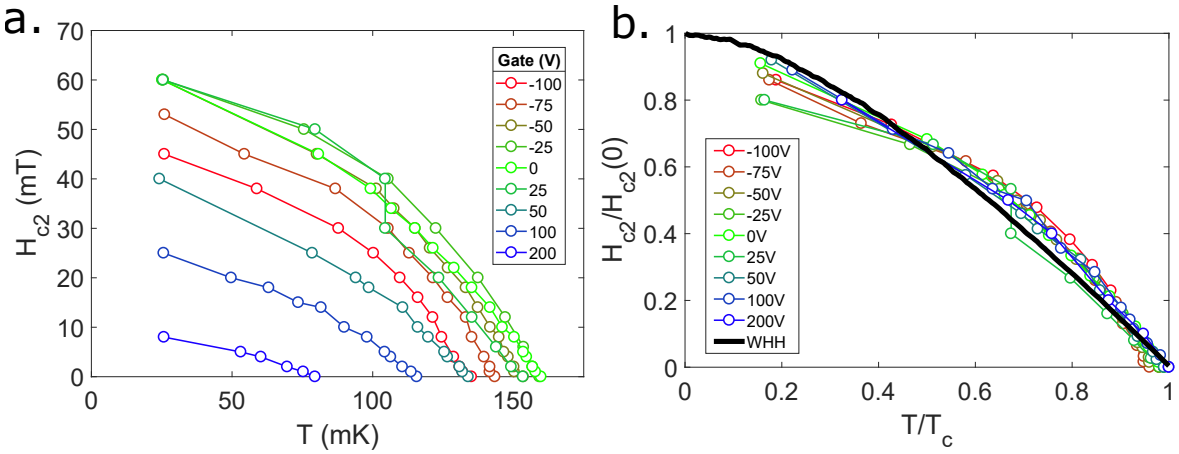

Figure 3.35: H_{c2} **temperature dependence in a LAO/STO(111) 2DEG, sample LS253**. **a.** Critical magnetic field H_{c2} as a function of temperature for all gate voltages considered in figure 3.34. **b.** Normalized curves with a WHH curve as a guide for the eye.

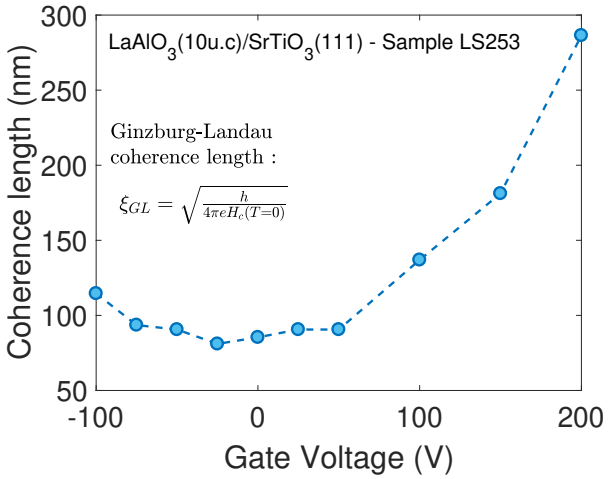

Figure 3.36: Ginzburg-Landau superconducting coherence length extracted from the upper critical field H_{c2} measurements in $LaAlO_3/SrTiO_3$(111)-2DEG sample LS253.

Discussion

So far, the (111)-oriented 2DEG show similarities and differences with the (110)-oriented interface. First, both of them exhibit multiband transport visible in Hall effect curves beyond a certain doping point, a property also shared with the (001) interface. The normal transport properties derived from Hall effect measurements are slightly different: the (111)-2DEG interface has a higher carrier density, but a lower electron mobility than the (110)-2DEG. In both the (110) and (111) interfaces, the doping point which corresponds to the filling of the second band happens to also be the optimal doping point for the T_c, suggesting that the decline of the T_c is caused by the filling of the second band. However, while our experiment show the presence of two condensates in the (110)-oriented 2DEG, the (111) interface does not exhibit any apparent signature of two-gap superconductivity. Indeed by observing figure 3.35 we see that a single condensate WHH curve fits well the experimental curves in the whole doping range, even in the overdoped regime when two bands contribute to the normal state conduction. Several possible explanations can be proposed:

• The high-energy band might not accommodate a superconducting condensate. However, just as for the (001) orientation, this does not explain the decrease of T_c above the optimal doping point. Moreover, in the (001)-oriented 2DEG, the optimal doping point is not concomitant with the filling of the second band in contrast to the (111) interface, so this scenario still need to explain why populating an additional metallic band would decrease the overall T_c.

• The two condensates could have very similar properties, making them impossible to be distinguished *via* a critical magnetic field measurement. In this scenario, the two condensates would have a constant diffusivity and a critical temperature too similar to be noticeable.

• The condensates could have very dissimilar properties and only one condensate imposes its properties in the superconducting state.

Let us investigate the last two scenarios. We can compute an estimate of the diffusivity coefficients of the two bands, based on the normal transport properties discussed in section 3.8.4, in figure 3.32. The elastic diffusion constant of the two band is $D_{1,2} = \frac{v_{F1,2}^2 \tau_{1,2}}{3}$ where $v_{F1,2}$ are the Fermi velocities and $\tau_{1,2}$ are the elastic scattering times. We recall that $\tau_{1,2} = \frac{1}{e} m_{1,2}^* \mu_{1,2}$ and that

$v_{F1,2} = \hbar k_{F1,2}/m^*_{1,2}$, where $k_{F1,2} = \sqrt{2\pi n_{1,2}}$ for a circular Fermi surface can be used as a first order estimate. Then, the diffusion constants are expressed as : $D_{1,2} = \frac{2\pi\hbar^2}{3e}\frac{n_{1,2}\mu_{1,2}}{m^*_{1,2}}$. From tight binding calculations in ref [72], we ascribe the lower band to the low electron mass, a situation similar to the LAO/STO(110) 2DEG. We take the average in plane effective masses from data in ref [72], i.e. $m^*_1 = \sqrt{0.5 \times 2.2} = 1.05\ m_e$ and $m^*_2 = \sqrt{2.2 \times 8.1} = 4.2\ m_e$ and the densities $n_{1,2}$ and mobilities $\mu_{1,2}$ from our Hall effect analysis in figure 3.32. We find that both bands have a low diffusion coefficient, between $D_2 \approx 0.04$ and $D_1 \approx 0.25\ cm^2/s$. In our gating range, the ratio of $\eta = D_1/D_2$ varies between 5 and 40. In figure 3.37**a.** we show a simulation of H_{c2} for realistic λ's for $\eta = 5$ and $\eta = 40$. We see that for the maximum $\eta = 40$, corresponding to $V_G = 75V$, a small deviation should be visible close to T_c. The fact that we do not observe this challenge the validity of the parameter used for this simulation. In figure 3.37**b.** we show simulation for $\eta = 40$ and even $\eta = 100$ but for a multicondensate superconductor where $\lambda_{11}/\lambda_{22} = 3$. We see that in such case where one order parameter dominate over the other, the deviation from the single band model is not visible

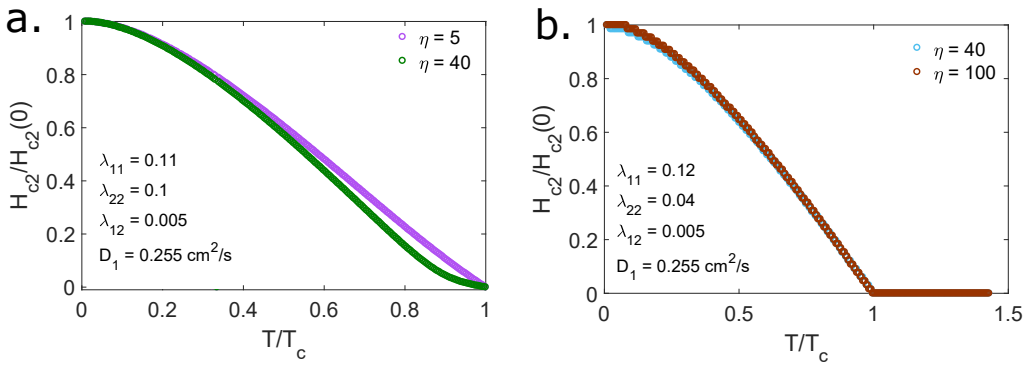

Figure 3.37: **Simulations of two-condensate $H_{c2}(T)$ curves for various parameters. a.** Simulations for various ratios of diffusivity coefficients η for a set of coupling constants close to the one from the (110)-2DEG. **b.** Simulation for various different η for realistic set of coupling constant with $\lambda_{11}/\lambda_{22} = 3$.

We emphasize that this approach is a rough estimate based on the assumption that the Fermi surface is circular. In reality the Fermi surface is a complex 6 points star and such calculation would require a proper calculation of the Fermi wave vector and effective masses in each direction of the Fermi surface. Another way to explore this scenario in more depth would be to perform the same transport measurements analysis on devices oriented in orthogonal directions, since in our case we measured a whole 3×3 mm 2DEG sample in Van der Pauw geometry. Such type of measurement averages the transport properties over the Fermi sea. Nevertheless, our first order estimate of the diffusivity coefficients of the two bands does not allow to rule out multicondensate superconductivity, but it does fix limits on the diffusion coefficients and superconducting gaps. For instance, if diffusivity coefficient are too similar or the gaps amplitude are too dissymmetric, or a combination of both, it would be impossible to tell from H_{c2} measurements only.

One could speculate that the (111)-2DEG is a multigap superconductor just like the (110) interface but that specific circumstances (in terms of diffusivity coefficient and superconducting gaps) make the critical magnetic field measurements blind to multicondensate signatures in this context. It is also possible that only the lower band is superconducting, and the higher band does not condensate. However this scenario does not explains the decrease in T_c upon doping concomitant with the filling of the second band.

Parallel critical magnetic field $H_c^{\parallel}$

For these measurements, a second sample of superconducting $LaAlO_3/SrTiO_3$ (Sample LS281) has been cut into thin bars (width $\simeq 100\mu$m) along the two orthogonal directions $[1\bar{1}0]$ and $[11\bar{2}]$ which have later been assessed by X-ray diffraction. The sample has similar properties than the sample LS253 used for H_{c2} measurements. Figure 3.38 provides data on the gate-tunable superconductivity of this sample, to be compared with fig. 3.29 from the previous section.

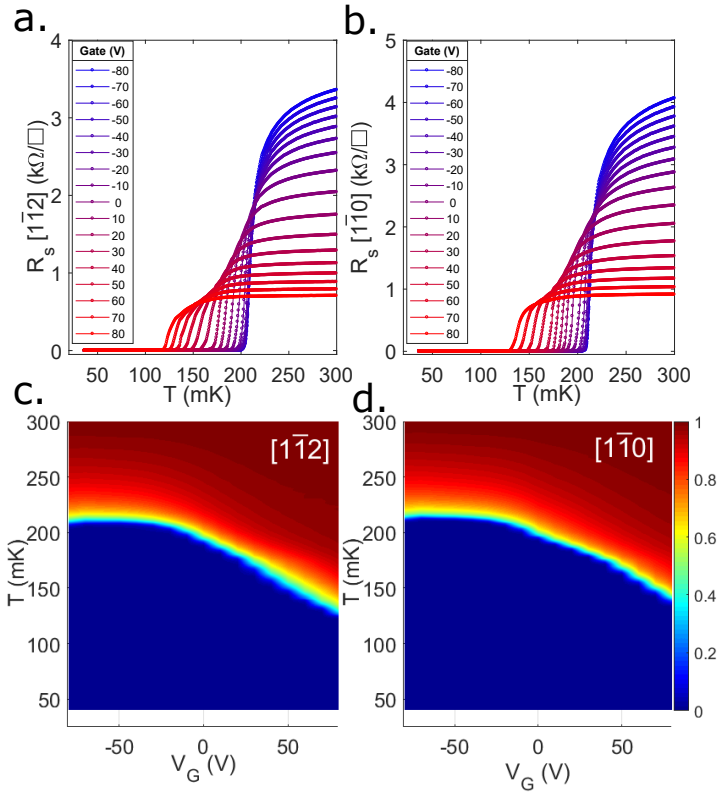

Figure 3.38: **Gate-tunable superconductivity in a LAO/STO(111) sample LS281 for the two orientations. a. b.** Resistance as a function of temperature for different gate voltages measured along the two directions. **c. d.** Color plots of resistance data in **a.** and **b.** normalized by the resistance at 300 mK.

In 2DEGs, the parallel critical field, noted $H_c^{\parallel}$, is given by the following formula, under the assumption that $\xi \gg d$ [6] [105] :

$$H_c^{\parallel} = \frac{\sqrt{3}\phi_0}{\pi \xi d} \tag{3.29}$$

Extensive measurements of R vs. T curves under different parallel magnetic fields for three different gate voltages ($V_G = -80, 0$ and $-80V$) are represented figure 3.39. The top panel represents measurements along the $[1\bar{1}2]$ direction while the bottom panel represent the $[1\bar{1}0]$ direction. We notice that the parallel field is much higher than the perpendicular critical field, ranging from 400 to 1000 mT.

An upper limit on $H_c^{\parallel}$ is set by the Pauli paramagnetic limit. The perfect paramagnetic nature of superconductors means that there should be a field high enough to break superconductivity by

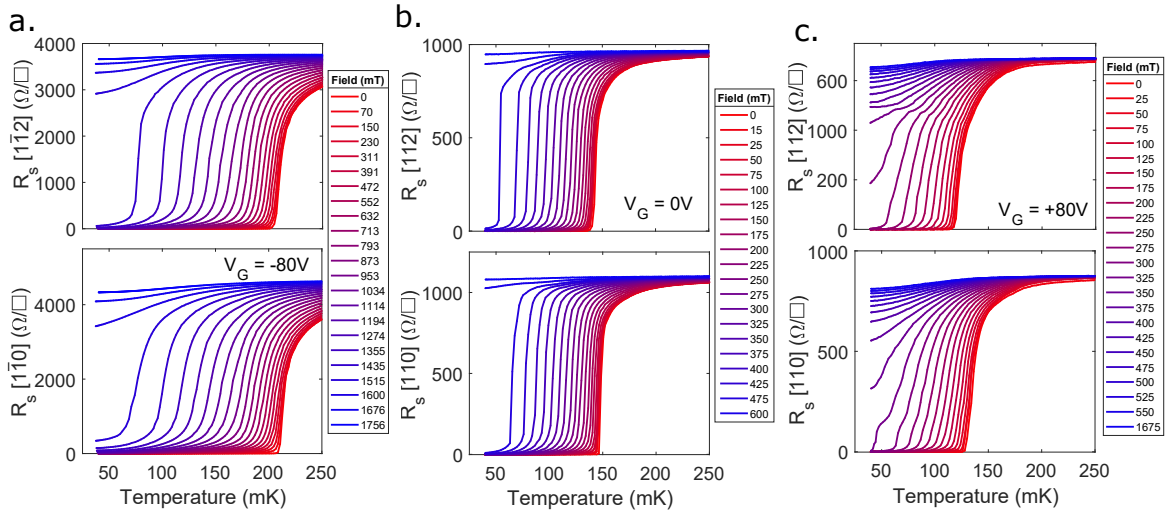

Figure 3.39: **Parallel critical magnetic field in LAO/STO(111) interface, sample LS281**. Each set of panels represents a different gate voltage applied to the 2DEG **a.** $V_G = -80\ V$ **b.** $V_G = 0\ V$ **c.** $V_G = 80\ V$. The upper panels show data taken along the [1$\bar{1}$2] orientation while the lower panels show data taken along the [1$\bar{1}$0] orientation.

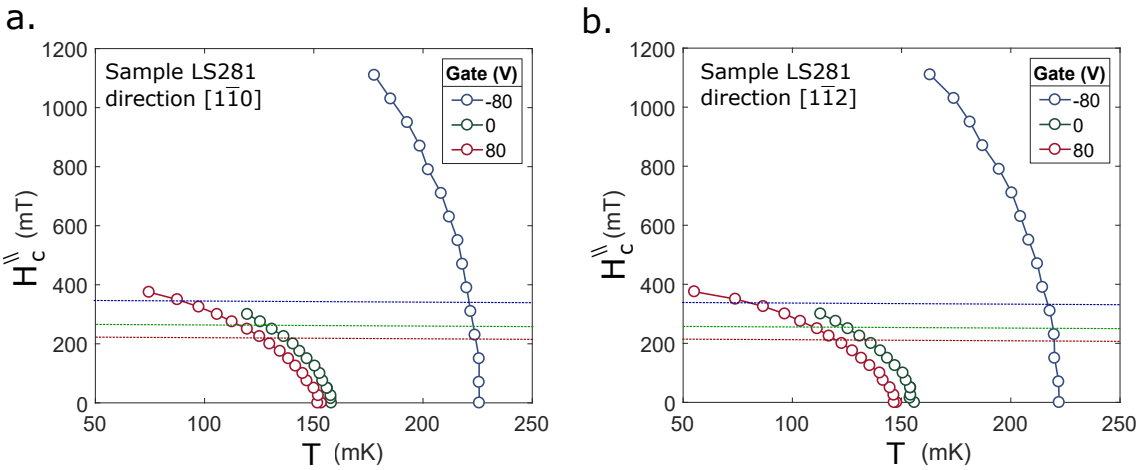

Figure 3.40: Critical parallel magnetic field as a function of temperature extracted from figure 3.39. Measurements performed along **a.** the [1$\bar{1}$0] orientation **b.** the [1$\bar{1}$2] orientation. The dotted color lines indicate the Pauli paramagnetic critical field H_c^p for each gate voltage.

aligning spins within a Cooper pairs. This field is called the Pauli paramagnetic critical field and can be estimated to be $\mu_0 H_c^p = 1.76 k_B T_c/(\sqrt{2}\mu_B)$ assuming a g factor of 2 [122]. This field is an upper bound and the experimental critical field of most materials are lower than H_c^p. However, this Pauli limit doesn't take into account the orbital magnetic energy of the electrons. In 2DEG such as those at $SrTiO_3$ hetero interface, the Pauli limit has been found to be violated [123] [87], which the authors attributed to be a consequence of high spin orbit scattering, whereby the spin is no longer a good quantum number. We show the Pauli limit in figure 3.40 as dotted color-line for each of the corresponding gate voltage. Similarly to the (001) and (110) interfaces, the experimental parallel critical magnetic field of the LAO/STO(111) interface exceeds the Pauli limit by a factor 2 to 5. The violation of H_c^p close to T_c for $V_G = -80\ V$ indicates a stronger confinement than for $V_G = 0$ or $80\ V$.

Estimate of the LAO/STO(111) 2DEG thickness

Combining equations for $H_{c2}^{\perp}$ (eq. 1.9) and $H_c^{\parallel}$ (eq. 3.29), we can obtain an estimate for the 2DEG thickness d:

$$H_c^{\parallel} = \frac{\sqrt{3}\phi_0}{\pi\xi d} \qquad \& \qquad H_{c2}^{\perp} = \frac{\phi_0}{2\pi\xi^2} \qquad \Longrightarrow \qquad d = \frac{\sqrt{H_{c2}^{\perp}}}{H_c^{\parallel}}\sqrt{\frac{6\phi_0}{\pi}} \tag{3.30}$$

Here, measurements of $H_c^{\perp}$ and $H_c^{\parallel}$ have been done on two different LAO/STO(111) samples grown under similar conditions, with similar T_c and R_s. However the gate voltage range for both measurement were different: -200 to 200 V for $H_c^{\perp}$ and -80 to 80 V for $H_c^{\parallel}$. We extract a rough estimate of the 2DEG thickness, by comparing the extremal gate values between the maximum and minimum of the perpendicular (parallel) critical magnetic field at 0 V and 200 V (80 V and -80 V). We find $d(V_G^{min}) = 10\ nm$, $d(V_G = 0\ V) = 30\ nm$ and $d(V_G^{max}) = 15\ nm$ for the extremal and zero gate voltage, confirming the 2D nature of our system ($\xi \ll d$). Note however that these values can only be considered upper bounds since formula 3.29 is only valid for the orbital critical field and that experimentally the critical field exceeds the Pauli limit.

3.9 Microwave measurement of the Superfluid Stiffness of the LAO/STO(111) interface

3.9.1 Experimental superfluid stiffness

In this section, we will present microwave measurement of the superfluid stiffness at the LAO/STO(111) interface. The method is detailed in section 2.3.2 and its application to the LAO/STO(110) interface has been presented in section 3.5.

We recall that the kinetic inductance of Cooper pairs L_k as a function of the load impedance Z_L is :

$$\frac{1}{L_k(T)} = -\left(\mathrm{Im}\left(\frac{1}{Z_L(T)}\right) - \omega C_{STO}\right)\omega - \frac{1}{L_1} \tag{3.31}$$

where C_{STO} is the parallel substrate capacitance and L_1 the parallel SMD inductance.

As for the LAO/STO(110) sample presented before, the LAO/STO(111) sample is inserted in a CPW transmission line to form an equivalent RLC circuit whose reflection coefficient is used to compute the inductance of the 2DEG. Here the equivalent circuit of the set-up for LAO/STO(111) microwave measurement is provided in figure 3.41. The ratio of A_{out}/A_{in} gives, through a calibration procedure described in appendix A, the kinetic inductance of the Cooper pairs, which is inversely related to the superfluid stiffness.

Figure 3.42**a.** shows the magnitude in dB of the measured S_{21} coefficient (color scale) in the normal state at T=300 mK as a function of frequency and gate voltage. Although the resonance is clearly visible, some oscillations due to parasitic standing waves in the microwave set up deteriorate the quality of the signal. Figure 3.42**b.** shows the magnitude of the reflection coefficient Γ for the same data after applying the calibration procedure (see appendix A). The inset of figure 3.42**b.** shows the capacitance C_{STO} as a function of V_G extracted from the resonance frequency in the normal

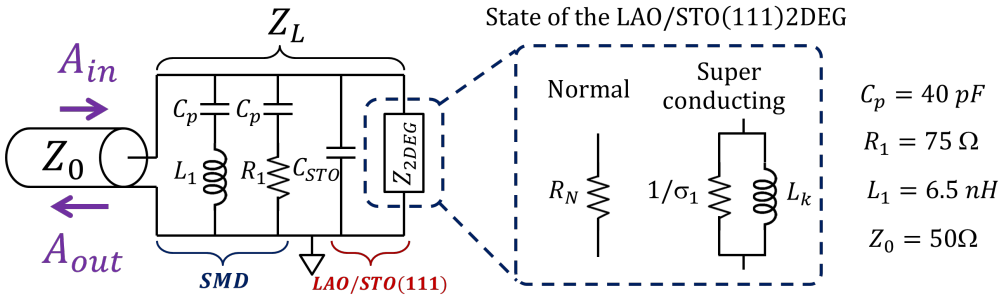

Figure 3.41: **Equivalent circuit for the LAO/STO(111) interface (sample LS253) microwave measurement.** The impedance of the 2DEG varies between the normal and the superconducting state, as shown in the dotted square. The SMD components values are reported on the right.

state. It varies almost symmetrically around 0 V where its maximum value of 60 pF is reached and $\pm 200\ V$ where its minimum value reaches 20 pF.

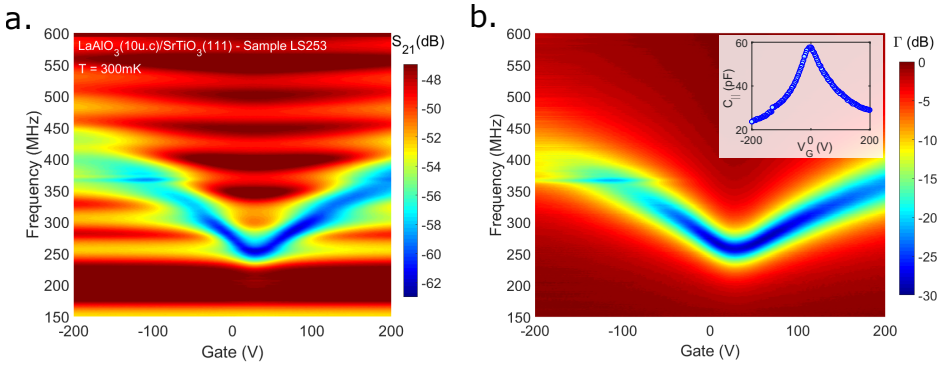

Figure 3.42: **Microwave measurement of the parallel substrate capacitance. a.** S21 (dB) in color at 300mK as a function of gate voltage and frequency. **b.** Calibrated Γ(dB) at 300mK as a function of gate voltage and frequency. Inset : extracted substrate capacitance C_{STO}.

Once the gate voltage dependence of C_{STO} is known, one can find L_K in the superconducting regime using eq. 3.31. In figure 3.43 we show the temperature dependent reflection coefficient Γ in the superconducting state for a selection of gate voltages $V_G = -200$, 0 and 200 V. As already discussed for the LAO/STO(110) sample in section 3.5, we see that the resonance shifts to higher frequencies in the superconducting state because of the contribution of the kinetic inductance of the 2DEG. The temperature dependent superfluid stiffness is then deduced from the kinetic inductance in the entire gating range.

In figure 3.44**a.** we show the temperature evolution of the superfluid stiffness in temperature units for each gate. Its maximum value ranges from J_s = 500 mK at Vg=-200 V to $J_s \simeq 3$ K at Vg=+200 V. The T_c as seen by J_s is in agreement with T_c's from DC measurement: from 70 to 125 mK.

Once the T_c are extracted and $J_s(T)$ are extrapolated to $T = 0$, we can plot the normalized stiffness as a function of reduced temperature, just like we did for the LAO/STO(110) interface in figure 3.22. The resulting curves for the LAO/STO(111) 2DEGs are shown in figure 3.44**b.**. At first glance, it looks like all the curves collapse onto a single band BCS fit, except for the four highest

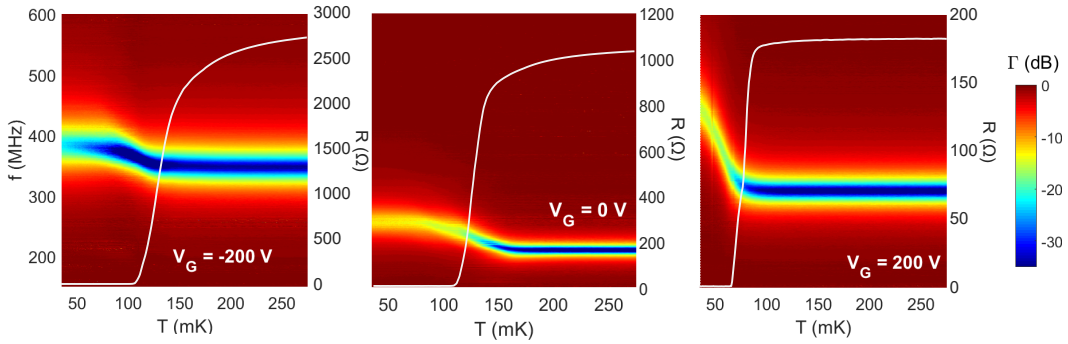

Figure 3.43: **Calibrated microwave refection coefficient for the LAO/STO(111) interface sample LS253** for three selected gate voltages $V_G = -200$, 0, and 200 V. The frequency axis displayed on the left panel is shared with the two other panels. Similarly, the color scale displayed on the right is shared by all panels. For each gate voltage, the resistance as a function of temperature is shown in grey line (right y axis).

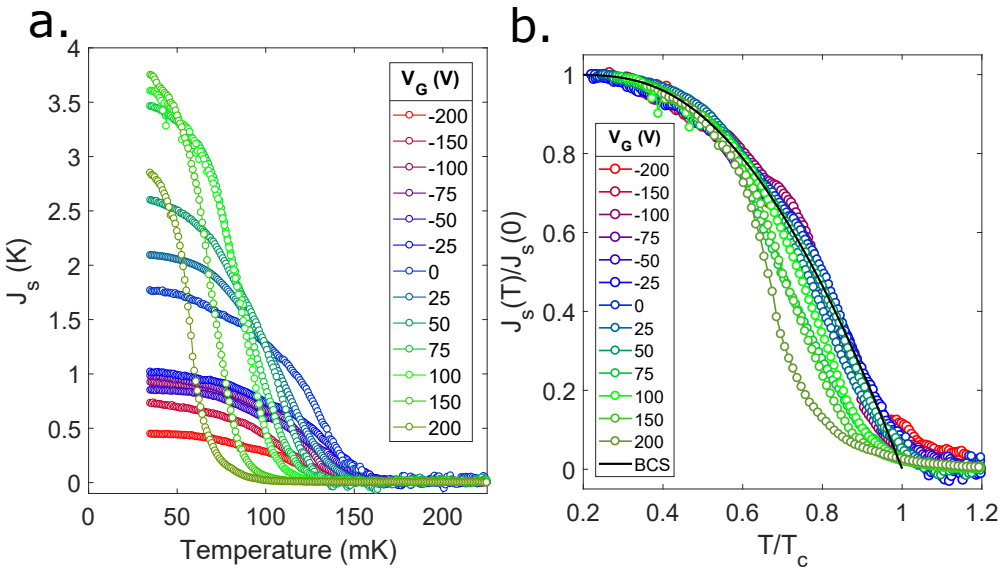

Figure 3.44: **a.** Superfluid stiffness of a LAO/STO(111) 2DEG for various gate voltages as a function of temperature. **b** Normalized stiffness as a function of reduced T_c, with a single band BCS fit in black line.

gate voltages $V_G = 75$, 100, 150 and 200 V.

We have fitted the superfluid stiffness data with a single band BCS fit and the results are provided figure 3.45. We see that in the negative gate region (panel **a.** to **e.**), a BCS fit with the corresponding superconducting coupling constants λ agrees well with the data. In the positive gate region however (panel **f.** to **i.**), the fit deviates from the data close to T_c.

One could think that we are in a similar situation as the LAO/STO(110) interface, where the coupling between two superconducting condensates with different gaps can lead to the formation of a tail close to T_c. However, the two-condensates superconductivity model from Kogan et al. used

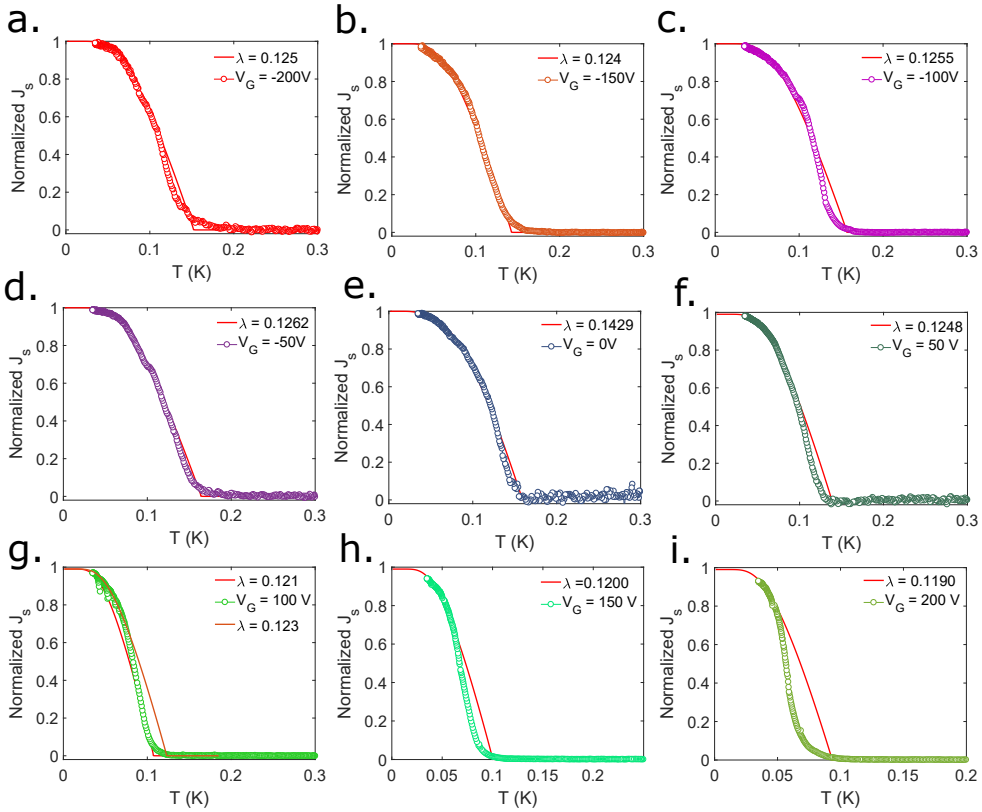

Figure 3.45: **Superfluid stiffness of the LAO/STO(111) 2DEG sample LS253 for various gate voltages as a function of temperature** with a weak coupling BCS fits.

to described the LAO/STO(110) interface does not provide satisfying fit here.

The coupling constants λ extracted from the fits can be used to compute the superconducting gap $\Delta = 1.76 k_B T_c = 2E_D e^{-1/\lambda}$ assuming the Debye energy $E_D = 400\ K$. Their values with systematic error are shown figure 3.46.

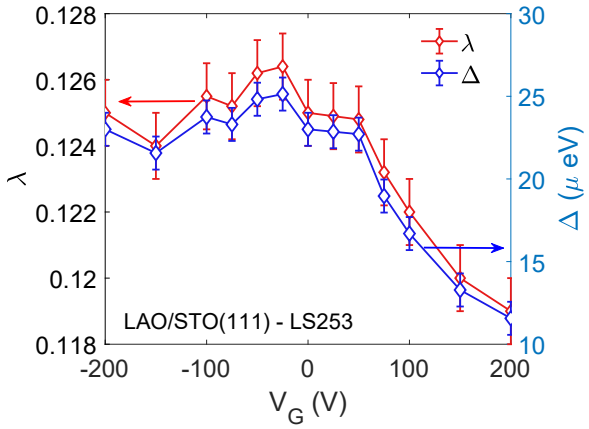

Figure 3.46: Superconducting gap Δ and coupling constant λ for a LAO/STO(111) 2DEG.

3.10 Superconductivity at the LAO/STO(111) interface and Mattis-Bardeen theory

In the dirty limit, as we have seen in chapter 1, according to Mattis-Bardeen formula 1.41 the superfluid stiffness is :

$$J_s^{BCS}(T=0) = \frac{R_0 \Delta(T=0)}{4R_n}$$

Where R_n is the resistance in the normal state (at T=280 mK), $R_0 = \frac{h}{e^2} = 28.813\ k\Omega$ and $\Delta(T=0)$ the superconducting gap at T=0. It has been observed that in the (001) orientation, there is a discrepancy between experimental J_s^{exp} and the expected BCS J_s^{BCS} which was attributed to the onset of superconductivity via coupled superconducting paddles in a Josephson junction array model [34].

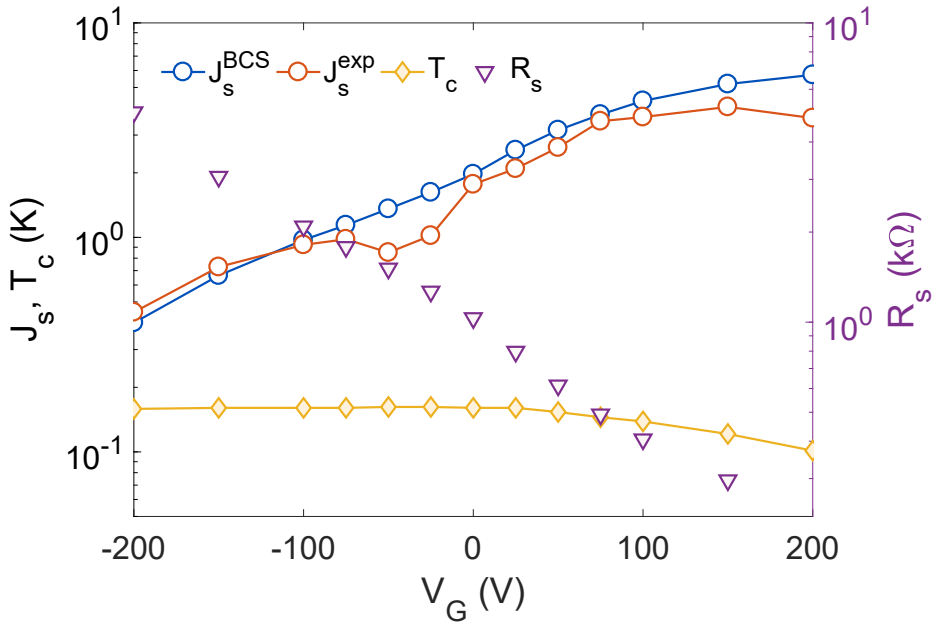

Figure 3.47: **Agreement between Mattis Bardeen theory of dirty superconductors and experimental data.** Experimental zero temperature superfluid stiffness J_s^{exp} as a function of gate voltage (red circle) compared to the expected Mattis-Bardeen stiffness from eq. 1.41 (blue circle), in log scale. Superfluid stiffnesses are expressed in temperature units. The superconducting critical temperature is shown in yellow diamonds, and the resistance in the normal state is shown in purple triangles on the right y axis.

In figure 3.47, we compare the gate evolution of the experimental superfluid stiffness at $T=0$, $J_s^{exp}(0)$, to the Mattis-Bardeen zero temperature stiffness deduced from equation 1.41. We also present the ingredient needed for eq. 1.41: the normal resistance in Ω on the right y axis and the critical temperature. In this formula, the gap is inferred from T_c through a single BCS weak coupling limit ($\Delta = 1.76 k_B T_c$). A very good agreement is obtained between J_s^{exp} and J_s^{BCS}, indicating the formation of a rigid and homogeneous superconducting state in LAO/STO(111) 2DEG. The difference

between the two at $V_G = 200\,V$ is most likely due to the fact that J_s^{exp} is taken at 35 mK, temperature at which the superfluid stiffness has not saturated yet, while J_s^{BCS} is computed for $T = 0$.

3.11 Discussion

The (111)-oriented $LaAlO_3/SrTiO_3$ interface studied here share many similarities with both the (001) and (110) interface. The 2DEG has a low temperature sheet resistance of a few $k\Omega/\square$ and is superconducting with a T_c of around 150 mK, lower than in other orientations. Its gate dependent dependent T_c is very similar to the (110) one : in the negative gate region, the T_c is not affected by the gate voltage but in the positive gate region the T_c drops by a factor $\simeq\ 2$ at maximum gate voltage (fig. 3.29). From Hall effect measurement, we see that this doping point marks the filling of a second band, where the Hall effect is non-linear (fig. 3.30). The total carrier density $n\ \simeq\ 10^{14}\ cm^{-2}$ is a bit higher than the typical $10^{13}\ cm^{-2}$ density of other superconducting 2DEG in the (001) and (110) orientation (fig 3.32).

Upper perpendicular critical field (H_{c2}) measurements do not show any sign of multicondensate physics. The $H_{c2}(T)$ curves approximately follows a single band WHH curve for single gap superconductor (fig. 3.35). The low critical magnetic field of $H_{c2}(0)\ \simeq\ 50\ mT$ gives a large coherence length of Cooper pair of $\xi \simeq\ 150\,nm$ which validates the dirty regime of our 2DEG when compared to the few nm of the mean free path (fig. 3.36). Parallel critical field measurement ($H_c^{\parallel}$) show a much higher value of $\simeq\ 1\ T$ which exceeds the Pauli paramagnetic limit by a factor 5 (fig 3.39 and 3.40). The ratio of $H_c^{\parallel}$ and $H_{c2}^{\perp}$ allows for an estimate of the 2DEG thickness of 10 to 30 nm (upper bound), confirming further the 2D nature of the system.

Resonant micro-wave measurements have been performed on the LAO/STO(111) 2DEG to extract the superfluid stiffness J_s in the entire phase diagram (fig. 3.44). Attempts to fit the data with a two-gap model remains inconclusive despite visible deviation from a single gap behavior. The zero temperature value of the superfluid stiffness was compared to the Mattis-Bardeen prediction of J_s for a dirty 2D superconductor. The agreement between the theory and the results provided figure 3.47 allows us to conclude that this 2DEG accommodate a rather homogeneous superconductivity.

Chapter 4

Anisotropic Magnetoresistance in (110) and (111)-oriented 2DEG

This chapter explores the non-reciprocal transport that occurs in LAO/STO(110) and LAO/STO(111) 2DEGs. Because of Rashba spin-orbit coupling, transport along a given direction (e.g. x) is slightly different from transport along the opposite direction ($-x$). The in-plane anisotropic angle dependent magnetoresistance is used to analyze the bilinear and quadratic magnetoresistances, which provide useful information on the Rashba spin-orbit coupling and the Fermi surfaces.

4.1 Framework

4.1.1 Historical developments

The evolution of the resistance of a material upon applying a magnetic field, also know as magnetoresistance, is an ubiquitous phenomenon in metals. It was first reported in 1857 by W. Thomson [124] that a piece of iron displays an increased resistance along (and a decreased resistance across) the direction of the magnetic polarisation of the material. The relative variation of the resistance with field, which was lower than 5% in Thomson's work, was progressively increased to 100% around 1990 when A. Fert and F. Grunberg independently discovered the now famous "Giant Magnetoresistance" in Cr-Fe alloys [125] [126]. Nowadays, some materials such as topological insulators can exhibit a 20000% magnetoresistance [127].

Magnetoresistance is a generic term which can refer to many observations. In this chapter we focus mainly on the angle-dependant magnetoresistance, i.e. the resistance evolution upon changing the angle between the magnetic field and the applied current. In 2DEGs, the two types of orientation of the field, in-plane or out of plane, can probe different features. When the angle is going from in-plane to out of plane, it allows to study the 2D nature of the gas by extracting its thickness and comparing it to the mean free path. When the angle is changed in the plane of the 2DEG, it gives information on the band structure and scattering mechanisms. In any case, probing the magnetoresistance gives information on the angle dependent in plane conductivity $\sigma_{i,j}(\varphi)$ (or resistivity $\rho_{i,j}(\varphi)$) where $\{i, j\}$ are the spatial coordinates of the 2D conductivity and φ is any of the three Euler angles. In this manuscript, the focus is put on $\{i, j\} = \{x, y\}$ as we deal with a 2DEG and φ is the in plane angle between the bias current and the magnetic field.

Generally speaking, the magnetoresistance can be intrinsic to the crystal which generates natural easy and hard axes, or extrinsic when the symmetry of the system, scattering mechanism or band structure creates a preferable direction, or a combination of both. Regarding the 2DEG at STO or KTO interfaces, the main contribution of the magnetoresistance comes from the band structure, and the spin-orbit effect. Indeed, if the strong magnetoresistance observed at these oxide interface (which can reach 70% of relative variation) was caused by large intrinsic crystal magnetization, we should not observe the presence of superconductivity [128]. Many studies have shown that the anisotropic magnetoresistance can be explained in term of spin-orbit interaction, either a Rashba-coupling [129] or equivalently an atomic spin-orbit coupled with a broken inversion symmetry at the interface [128].

In this manuscript, we are interested in two quantities derived from the anisotropic magnetoresistance (AMR) which are called the bilinear and quadratic magnetoresistances, later called BMR and QMR. The BMR is the average difference between two measurements with opposite current flows (I^+ an I^-) and is linear in magnetic field and linear in current and presents a $\cos(\varphi)$-like variation with in-plane angle. It is expressed in term of the non-reciprocal resistances $\rho_{xx}(I^+, \varphi)$ and $\rho_{xx}(I^-, \varphi)$ as :

$$BMR(\varphi) = \frac{1}{2}\left(\rho_{xx}(I^+,\varphi) - \rho_{xx}(I^-,\varphi)\right) \tag{4.1}$$

The QMR , which is the average sum of two measurements with opposite current flows, is only quadratic in field and does not depend on current; it displays a $\cos 2\varphi$ variation with respect to the angle. It is similarly expressed in term of $\rho_{xx}(I^{\pm})$ as :

$$QMR(\varphi) = \frac{1}{2}\left(\rho_{xx}(I^+,\varphi) + \rho_{xx}(I^-,\varphi)\right) \tag{4.2}$$

For a long time, only the QMR was studied while the BMR was not mentioned. This is due to the fact that most of data aquisition systems average the raw measurements for I^+ and I^- in order to suppress any offset from amplifiers or used an ac signal. If people are not specifically looking for BMR, there is a great chance that they will loose the information about the BMR at the data acquisition level.

The first investigations on the anisotropic magnetoresistance in LAO/STO 2DEG showed heterogeneous results. Shalom et al. suggested that the asymetric AMR they observed could be due to magnetic ordering at low temperature [130] while Fete et al. attributed the symmetric AMR they observed to Rashba effect and calculated electronic parameters such as the effective mass from the measurement of AMR [131]. Joshua et al. were the first to systematically investigate the AMR evolution with gate voltage, and found that there is a region in the electron density and applied field phase space where the AMR becomes asymmetric (at high density and high magnetic field) [49]. It was only later that the BMR and QMR were investigated at LAO/STO interface by several researchers [132] [133].

4.1.2 Semi-classical description of the AMR

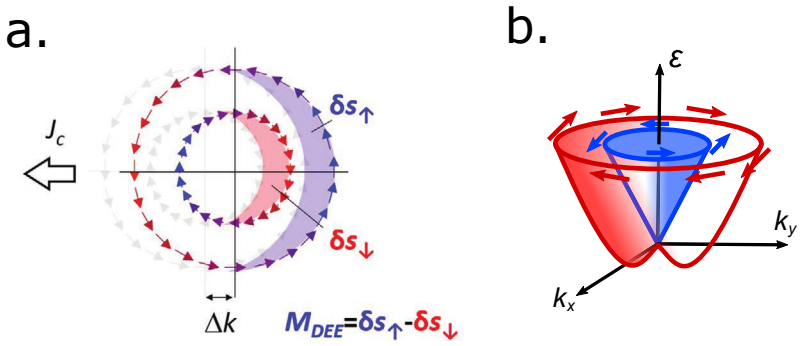

Figure 4.1: **Fermi surface in a Rashba 2DEG, with spin-momentum locking visible. a.** A charge current J_c creates a shift in momentum Δk. Part of the spin down electrons $\delta s_\downarrow$ (clock-wise electrons) accumulate in the inner band (in red) and part of the spin up electrons $\delta s_\uparrow$ (counter clock-wise) accumulate in the outer band (in blue). The imbalance of this spin accumulation generates a magnetization M_{DEE} (for Direct Edelstein Effect). **b.** Schematic representation of the Rashba effect on a spin-degenerate circular Fermi surface. The shift in k is proportional α_R in eq. 4.3.

Let us consider a 2DEG lying in the (x,y) plane. Our 2DEGs have intrinsic Rashba spin-orbit due to the confinement at an heterostructure interface. This interaction splits the spin-polarized surface

and locks the spin to the momentum. At equilibrium, the Fermi surface consists of two concentric circles with opposite helicity (fig. 4.1). Formally, we consider a Rashba Hamiltonian:

$$\hat{H}_R = \frac{\hbar^2 k^2}{2m^*}\hat{\sigma}_0 + \alpha_R(k_y\hat{\sigma}_x - k_x\hat{\sigma}_y) \tag{4.3}$$

Where $\hat{\sigma}_{x,y,z}$ are the Pauli matrices, $\hat{\sigma}_0$ is the identity, m^* is the effective mass of the band which is assumed to be parabolic, and $k^2 = k_x^2 + k_y^2$ is the in plane wave vector. The two eigenvalues of the above Hamiltonian are the two shifted parabolic bands $\epsilon_\pm = \frac{\hbar^2 k^2}{2m^*} \mp \alpha_R k$. The resulting band dispersion is schematically drawn in figure 4.1**b.** When the system is driven out of equilibrium by applying an electric field, the center of the two Fermi contours are shifted. Without loss of generality, let this field E_x be applied along x, then the shift in momentum Δk is expressed as:

$$\vec{\Delta k} = \frac{-e\tau}{\hbar}\vec{E_x}$$

where e is the electron charge and τ is the elastic scattering time.

This shift in momentum leads to a non-equilibrium Rashba term, or an interaction with a current-induced effective magnetic field along y of the form $\vec{H}_{eff} = -\alpha_R\frac{e\tau}{\hbar}|E_x|\vec{y}$. The new Rashba term $\hat{H}_{ne} = -\alpha_R\frac{e\tau}{\hbar}E_x\hat{\sigma}_y$ adds to the total Hamiltonian $\hat{H}_{tot} = \hat{H}_R + \hat{H}_{ne}$. Equivalently, this current induced magnetic field generates a non-equilibrium Edelstein spin-polarisation $S_y = \frac{\alpha_R m^*}{2\pi\hbar}\Delta k$. Figure 4.1**a.** allows the visualization of the spin accumulation from dc current in a Rashba 2DEG. We see the two bands emerging from the Rashba splitting in k with opposite helicity, and in light grey we see the shift in Δk driven by the charge current J_c. Taking into account the non-equilibrium Rashba term induced by Δk results in accumulation of spin mainly 'down' (i.e. along $-y$) in the inner band and mainly 'up' (i.e. along y) in the outer band, noted $\delta s_\uparrow$ and $\delta s_\downarrow$. The difference between $\delta s_\uparrow$ and $\delta s_\downarrow$ gives an effective spin polarization M_{DEE} along $\vec{y}$. This effect by which an electrical current is converted into a transverse spin accumulation in 2D material is the Rashba-Edelstein effect.

To summarize, an applied current will generate an in-plane effective magnetic field perpendicular to the current through a spin imbalance. When measuring the in-plane anisotropic magnetoresistance, at specific angles this field will add or subtract to the external magnetic field. This will translate to a non-symmetric AMR with respect to angle, and an opposite behavior in AMR for opposite current.

A representation of the geometry of the AMR measurement is displayed in figure 4.2**a.**. The 2DEG lies in the (x,y) plane and the current is fixed along a given direction ($y = [010]$ in the figure). The AMR is the measurement of the resistance evolution with the in-plane rotating field φ between external H_{ext} and current induced Rashba field $\vec{H}_{eff}$ which is perpendicular to the current flow. In figure 4.2**b.**, we show an example of the measurement of the normalized 2DEG resistance ρ_{xx} as a function of the in plane angle φ for two opposite biasing currents, j_y and $-j_y$. At the bottom of the figure, we show the relative orientation of the current I (grey arrow) with respect to the Rashba field (green arrow) and the external magnetic field (blue arrow). This geometry is the same as in panel **a.** for $\rho_{xx}(j_y)$ in blue in panel **b.** When φ = $\pi/2$ or $3\pi/2$, I and H_{ext} are parallel and the resistance is maximum as expected for most materials exhibiting AMR. When $\varphi = 0$ or π the current-induced field adds to the external magnetic field field. If $\varphi = \pi$, the effective Rashba field is opposite to the external field and the total field is reduced, leading to a higher resistance with respect to the $\varphi = 0$ case. When the current is reversed, so is the Rashba field and the minimum of resistance of $\rho_{xx}(-j_y)$ occurs for $\varphi = 0$.

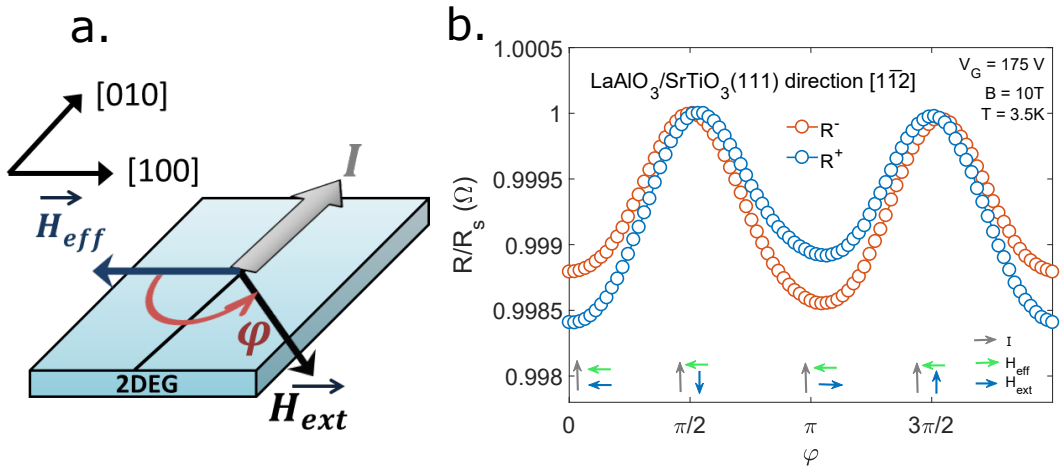

Figure 4.2: **Geometry and measurements of AMR a.** Geometry of the AMR measurement: A current I is applied to a 2DEG and a field $\vec{H_{ext}}$ is rotated from 0 to 2π. The current-induced Rashba field is noted $\vec{H}_{eff}$. **b.** Example of a normalized AMR measurement curve for currents in two opposite directions. The arrow at the bottom shows the relative orientation of H_{eff}, I and H_{ext}

4.1.3 Microscopic description

He and al. (2018) suggested that the bilinear magnetoresistance observed in some topological insulators is a consequence of the hexagonal warping of the Fermi surface [134]. However the same BMR was observed in non-topological, non-hexagonal material such as α-Sn(001) [135] prompting some to search for other mechanisms which could explain this BMR. Dyrdal et al. proposed a theory where the BMR emerges from scattering on inhomogeneities in system where the spin-orbit interaction and a broken inversion symmetry would lock the spin to the momentum [136]. Such theory was successfully applied to the LAO/STO(001) interface by D. Vaz et al. who did the calculation of the angle, field, and current dependence of both the BMR and the QMR [132]. Considering Drydal's theory, they calculated the conductivity σ_{xx} of a Rashba system with the non-equilibrium term induced by the field $\vec{E}$ in presence of short range, zero average interaction impurities. Their model Hamiltonian in k-space is composed of the following terms

$$\hat{H}_{tot} = \hat{H}_R \delta_{kk'} + \hat{V}_{imp} \delta_{kk'} \tag{4.4}$$

Where

$$\hat{H}_R = \frac{\hbar^2 k^2}{2m^*} \sigma_0 + \alpha_R (k_y \sigma_x - (k_x + \Delta k_x) \sigma_y) \tag{4.5}$$

and

$$\langle \hat{V}(r) \rangle = 0 \qquad \text{and} \qquad \langle \hat{V}(r) \hat{V}(r') \rangle = n_i v_0^2 \delta(r - r') \tag{4.6}$$

Where n_i is the impurity density, v_0 is the single impurity potential, $\Delta k_x = -\frac{e\tau}{\hbar} E_x$ from an electric field along the x axis with scattering rate τ and $< \cdots >$ refers to impurity average.

In the Green's formalism under the self-consistent Born approximation, the relaxation rate in presence of magnetic field $\Gamma(b) = \frac{\hbar}{2\tau_b}$ is given by :

$$\Gamma(b) = \Gamma_0 \left(1 + 3\left(\frac{\frac{-2\pi}{m} b S_y}{4\Gamma_0^2} + \frac{b^2}{8\Gamma_0^2}\right)\right) \tag{4.7}$$

Where the field b is understood as the sum of the external and Rashba field, i.e $b = H_{ext} - \alpha_R \frac{e\tau}{\hbar} E$. $\Gamma_0 = \frac{\hbar}{2\tau}$ is the relaxation rate in absence of magnetic field. Then, the longitudinal resistivity is calculated from

$$\sigma_{xx} = \frac{e^2\hbar}{2\pi} \langle Tr \int \frac{d^2k}{(2\pi)^2} v_x G_k^R v_x G_k^A \rangle \tag{4.8}$$

Where G^A and G^R are the advanced and retarded Green's function respectively, and v_x is the renormalized velocity which relates to the vertex correction.

Taking into account the impurity vertex correction and expanding Green's functions with respect to the effective magnetic field b, we arrive at the final expression for the diagonal resistivity:

$$\rho_{xx} = \rho_{xx}^0 + \frac{3\pi}{4}\frac{h}{e^2}\left(\frac{\alpha_R \tau_0 j_x b \sin\varphi}{|e|(\epsilon_R^2 + \epsilon_F^2)} + \frac{\epsilon_F \tau_0 b^2 \cos 2\varphi}{h(\epsilon_R^2 + \epsilon_F^2)}\right) \tag{4.9}$$

The first term is the resistivity in the absence of applied magnetic field, i.e. only when the Rashba field is present:

$$\rho_{xx}^0 = \frac{h\Gamma_0 \epsilon_F}{e^2(\epsilon_R^2 + \epsilon_F^2)}$$

where $\epsilon_R = \alpha_R \frac{\sqrt{2m^*\epsilon_F}}{\hbar}$. The second term in eq. 4.9 is the bilinear magnetoresistance (BMR) which is antisymmetric with respect to the angle φ between the applied electric and magnetic fields and can thus be obtained by taking the average difference of $BMR = (\rho_{xx}(B, j = j_x) - \rho_{xx}(B, j = -j_x))/2$. The last term in eq. 4.9 is the quadratic magnetoresistance, which is symmetric with respect to φ and is thus obtained by taking the average $QMR = (\rho_{xx}(B, j = j_x) + \rho_{xx}(B, j = -j_x))/2$. They take the form BMR = $A_{BMR}\frac{j_x}{j}\sin$ and QMR = $A_{QMR}\cos 2\varphi$ where

$$A_{BMR} = \frac{1}{2}(\rho_{xx}(j) - \rho_{xx}(-j)) = \frac{3\pi}{4}\frac{h}{e^2}\frac{g\mu_B}{|e|}\frac{\alpha_R \tau}{\epsilon_R^2 + \epsilon_F^2} jB \tag{4.10}$$

$$A_{QMR} = \frac{1}{2}(\rho_{xx}(j) + \rho_{xx}(-j)) = \frac{3\pi}{4}\frac{(g\mu_B)^2}{e^2}\frac{\epsilon_R \tau}{\epsilon_R^2 + \epsilon_F^2} B^2 \tag{4.11}$$

These last two quantities of interest can be expressed in simpler term when normalized by ρ_{xx}^0, i.e. by taking $(\rho_{xx}(B, j) - \rho_{xx}(B, -j))/(2\rho_{xx}^0)$ then

$$A_{BMR} = \frac{3\pi}{2}\frac{g\mu_B \alpha_R \tau^2}{|e|\hbar\epsilon_F} jB \tag{4.12}$$

$$A_{QMR} = \frac{3}{4}\left(\frac{g\mu_B}{\hbar}\right)^2 \tau^2 B^2 \tag{4.13}$$

The Rashba coefficient α_R can be found by taking the ratio:

$$\frac{A_{BMR}}{A_{QMR}} = \frac{2\pi\hbar}{|e|g\mu_B}\frac{\alpha_R}{\epsilon_F}\frac{j}{B} \tag{4.14}$$

The determination of α_R thus requires to know some important parameters on the 2DEG, namely, the Fermi energy and the Landé g factor. If we know g from previous studies, ϵ_F from band calculation and filling, we can deduce α_R from eq. 4.14. Note that this equation is in principle only valid for circular Fermi surfaces as implied by the perturbative treatement of the conductivity in Green function's formalism. For highly anisotropic Fermi surfaces and multiband transport however, it is not clear that the formula 4.9 still holds.

Figure 4.3 below shows an example of measurement of normalized BMR and QMR calculated from the AMR shown figure 4.2**b.** above.

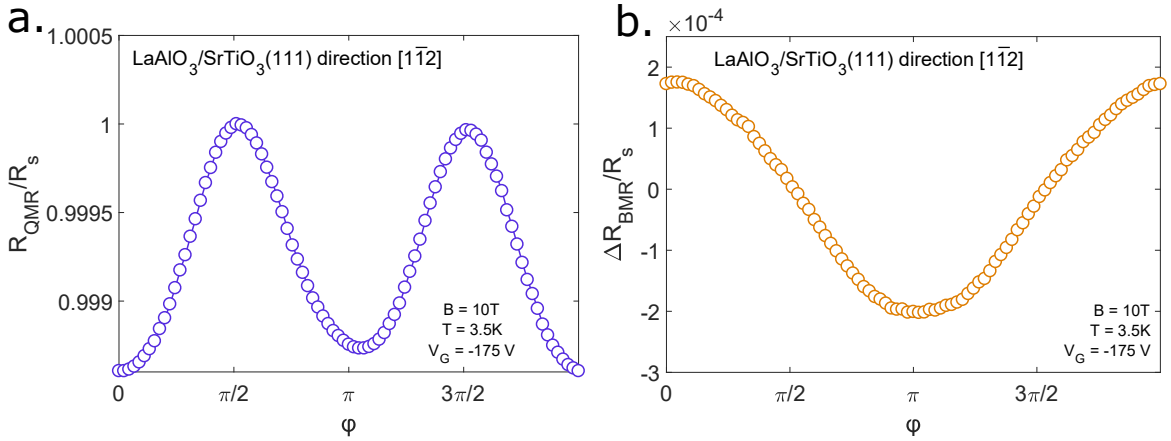

Figure 4.3: **Examples of QMR and BMR curves measured on a LAO/STO(111) 2DEG. a.** Normalized Quadratic Magnetoresistance (QMR) as the average of $\rho_{xx}(j_y)$ and $\rho_{xx}(-j_y)$ in figure 4.2**b.** above. **b.** Normalized Bilinear Magnetoresistance (BMR) as the half difference of $\rho_{xx}(j_y)$ and $\rho_{xx}(-j_y)$ in figure 4.2**b.** above.

4.1.4 State of the art

Few studies have reported transport properties at the LAO/STO(110) interface as the discovery of its superconducting 2DEG only dates back to 2015-2016 ([137] [87]). Shen-Chun and collaborators have shown the anisotropic nature of the 2DEG from magnetoresistance data, and even the superconducting transition was not identical between the two directions of the 2DEG. However it was not until 2021 that a group studied the in-plane angle-dependent magnetoresistance [138]. Following earlier experiments done on LAO/STO(001) interfaces [132], they systematically studied the nonreciprocal transport in LAO/STO(110) interfaces for various magnetic fields and currents but the sample was not gated, which prevents them from exploring the magnetoresistance at different filling of the Fermi sea. Nevertheless, they found that smaller currents were needed to produce the same Rashba field at the LAO/STO(110) interface compared to the LAO/STO(001) interface [138].

While there have been few reports on LAO/STO(001) AMR ([49] [101]) and only one recent report on LAO/STO(110) [138], there have been two reports on the AMR at LAO/STO(111) that we know of. The first one, by Rout et al. shows a strong sixfold anisotropic magnetoresistance in Hall bars which they attribute to the crystal structure of the interface [133]. The other report by P. He

et al. shows no sixfold symmetry, but they have extracted the BMR and QMR as a function of gate and current which are consistent with eq. 4.11 and 4.10 [134].

In this work, we will present the AMR as a function of magnetic field, gate, and current, along the two orthogonal directions of each 2DEG sample. For LAO/STO(110) these are are [001] and $[1\bar{1}0]$ while for LAO/STO(111) these are $[1\bar{1}0]$ and $[1\bar{1}2]$. To ensure that the current was flowing along a single crystallographic direction, we have cut the sample in two orthogonal directions. Each barrel measures around 3 mm in length and 150 μm in width. Their crystallographic orientation was later assessed by X-Ray diffraction.

4.2 Anisotropic magnetoresistance in $LaAlO_3/SrTiO_3$(110)

4.2.1 AMR measurements along the [001] and $[1\bar{1}0]$ direction

Transport measurements were performed in the PPMS described in section 2.1.3. Current was switched from positive to negative after each 2π turn of the rotator, and the angle between each data point corresponds to a 4° variation. A small constant drift of the resistance in angle, likely due to the thermal drift of the amplifier, was removed before any analysis was done.

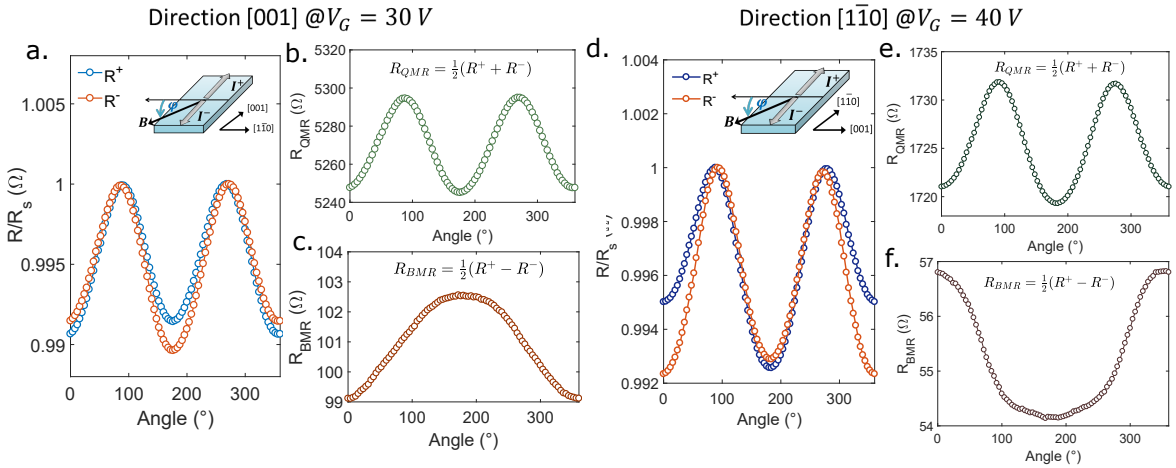

Figure 4.4: **AMR measurement in LAO/STO(110) a.** In plane magnetoresistance for current along the two directions shown in inset I^+ and I^-, i.e R^+ and R^-. **b.** Quadratic magnetoresistance extracted from data in **a.** **c.** Bilinear magnetoresistance extracted from data in **a.** Data taken at $I = 0.6\ mA$ and $T = 3\ K$ for both directions, $B = 9\ T$ for [001] and $B = 8\ T$ for $[1\bar{1}0]$.

Figure 4.4 shows a typical AMR, BMR and QMR measurement in LAO/STO(110) along both the [001] for panels **a.** **b.** and **c.** and the $[1\bar{1}0]$ direction for panels **d.** **e.** and **f.** In panel **a.** and **b.**, we present the normalized anisotropic magnetoresistance as a function of in-plane angle between magnetic field and current, for two directions of the current. The inset defines the zero angle (corresponding to $B \perp I$) as well as I^+ and I^- which are parallel to either [001] for panels **a.** **b.** and **c.** or $[1\bar{1}0]$ for panels **d.** **e.** and **f.**. The corresponding measured resistance are $R^{\pm} = \rho_{xx}(I^{\pm})$. We see a 0.8 to 1% relative variation between maximum and minimum for the two directions. When summing R^+ and R^-, we obtain the quadratic magnetoresistance, displayed in panels **b.** and **e.**. It exhibits the expected $\cos(2\varphi)$ dependence, with a 60 Ω variation along the [001] direction and a 14 Ω variation along $[1\bar{1}0]$. When taking the difference between R^+ and R^-, we obtain the bilinear magnetoresistance, displayed in panels **c.** and **f.**. It has the expected $\sin(\varphi)$ dependence and a small

variation of 3-4 Ω.

Now that we have seen how to obtain the BMR and QMR from the AMR at a given field B and gate V_G, we will analyze systematically the BMR and QMR for various gate voltages, magnetic fields and bias currents.

4.2.2 Field dependence of the BMR and QMR

In figure 4.5, we first present the QMR in a LAO/STO(110) interface as a function of magnetic field, in a moderately doped regime ($V_G = 30 - 40\ V$). In panels **a.** and **c.** we have plotted the QMR normalized by its value at $\pi/2$ for fields between 1 and 12 T, for the directions [001] and [1$\bar{1}$0], respectively. The amplitude of the latter, A_{QMR}, is reported in figure 4.5**b.** and **d.**, and a quadratic fit is provided. The quadratic dependence upon magnetic field follows the prediction of equation 4.11.

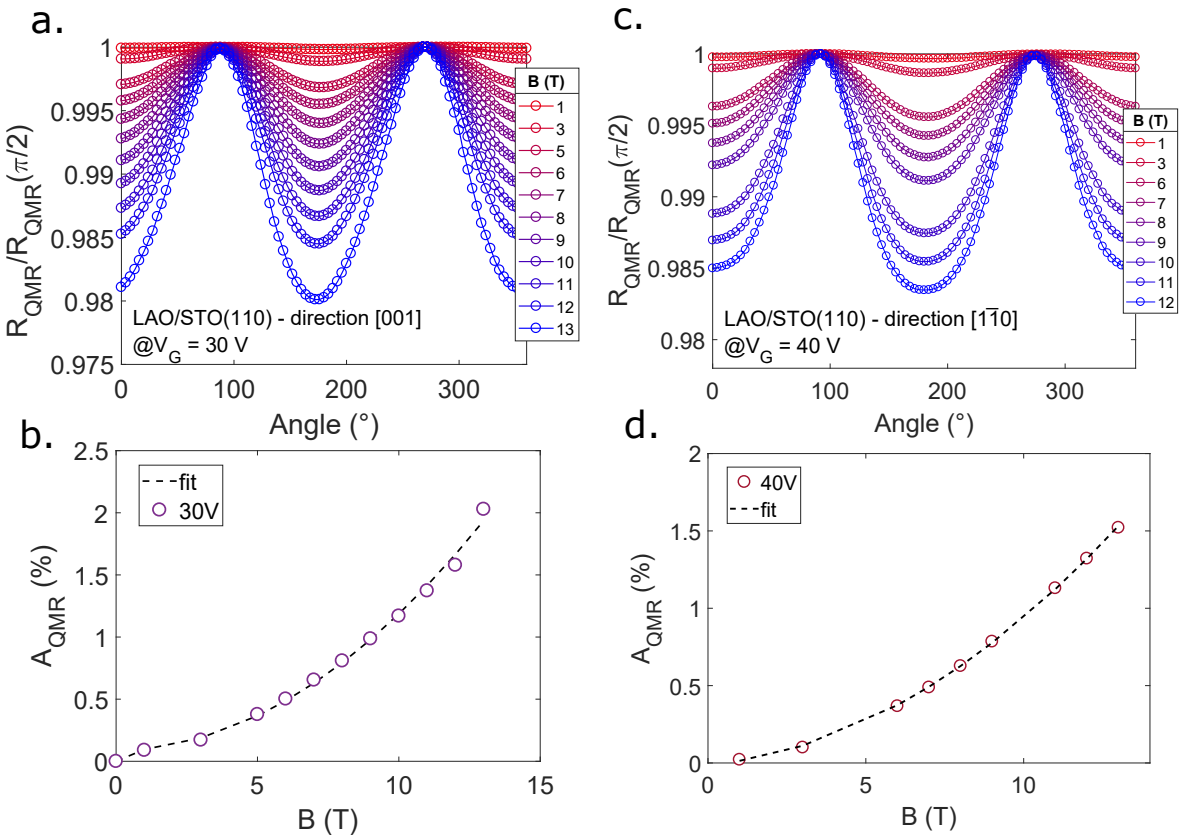

Figure 4.5: **Quadratic Magneto-Resistance (QMR) in a LAO/STO(110) sample** for the two in plane directions, [1$\bar{1}$0] and [001]. **a.** Normalized resistance along the [1$\bar{1}$0] direction as a function of angle for various magnetic fields at $V_G = 30\ V$. **b.** Corresponding evolution of the coefficient of the QMR oscillations (in %) as a function of field. **c. d.** Same but for direction [001] at $V_G = 40\ V$.

Next, we show the magnetic field dependence of the BMR for the same sample, at the same gate. The data are expressed as the ratio of the BMR amplitude ΔR_{BMR} divided by the sheet resistancce. The BMR is shown in panels **a.** and **c.** of figure 4.6 for the directions [001] and [1$\bar{1}$0] respectively. The amplitude of the oscillations is reported in panels **b.** and **d.**. Data are fitted by a linear function as expected from 4.10.

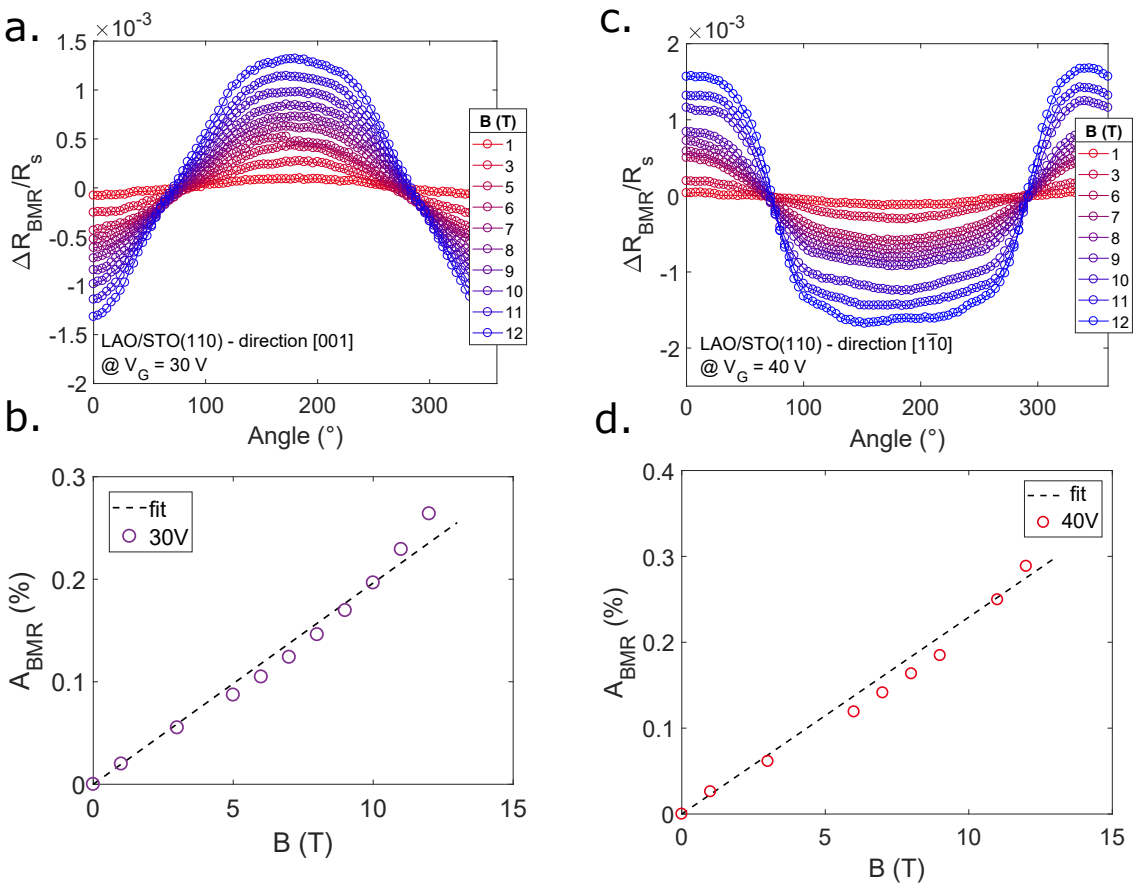

Figure 4.6: **Bilinear Magneto-Resistance (BMR) in a LAO/STO(110) sample a.** BMR angle dependence for transport along the [001] direction plotted for various external magnetic fields. **b.** Evolution of the BMR amplitudes (A_{BMR}), in %, from panel data in **a.** Panels **c. d.** are the same as **a. b.** but for transport along the [1$\bar{1}$0] direction.

4.2.3 Current dependence of the BMR

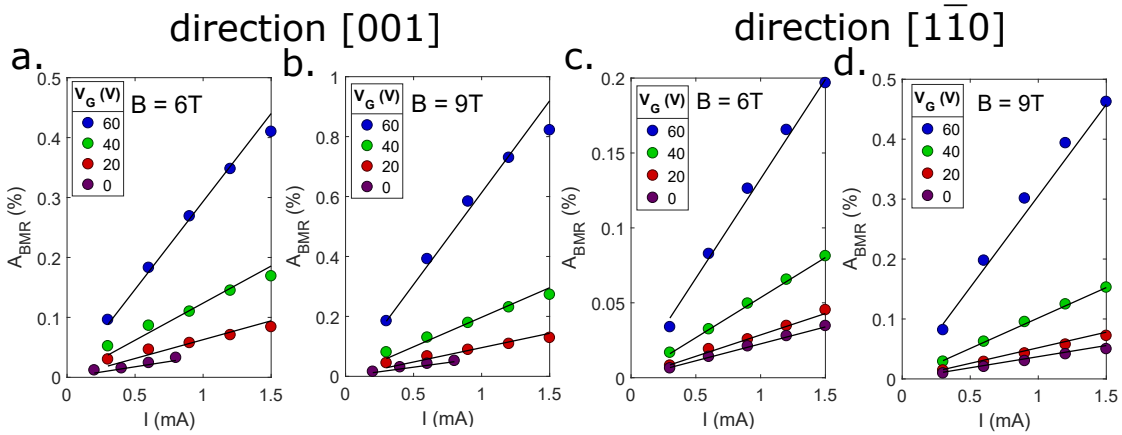

Figure 4.7: **BMR amplitude as a function of current** for different gate voltages between 0 and 60 V, **a. b.** along the [001] direction for B=6 T and B = 9 T and **c. d.** same for the [1$\bar{1}$0] direction.

We have analysed the BMR as a function of bias current, to find out if the linear relation ex-

pressed in eq. 4.10 holds. The AMR was acquired for currents ranging from 1.5 mA to -1.5 mA for a selection of gate voltages and magnetic field. The amplitude of each BMR curve was extracted and the results for all gate voltages are reported in figure 4.7 for two values of the magnetic field. In panel **a.** and **b.** we show the results for the sample oriented along the [001] direction for $B = 6\,T$ and $B = 9T$ respectively while panel **c.** and **d.** show the results for the same sample oriented along the $[1\bar{1}0]$ direction for the same magnetic fields.

We see that equation 4.10 holds, and the dependence of the BMR amplitude with both current and magnetic field is linear (hence the name bilinear). The difference in the slope between each gate voltage at a given field is explained by the variation of the elastic scattering rate τ with gate voltage which we will further investigate in the next subsections.

4.2.4 Gate voltage dependence of the BMR and the QMR

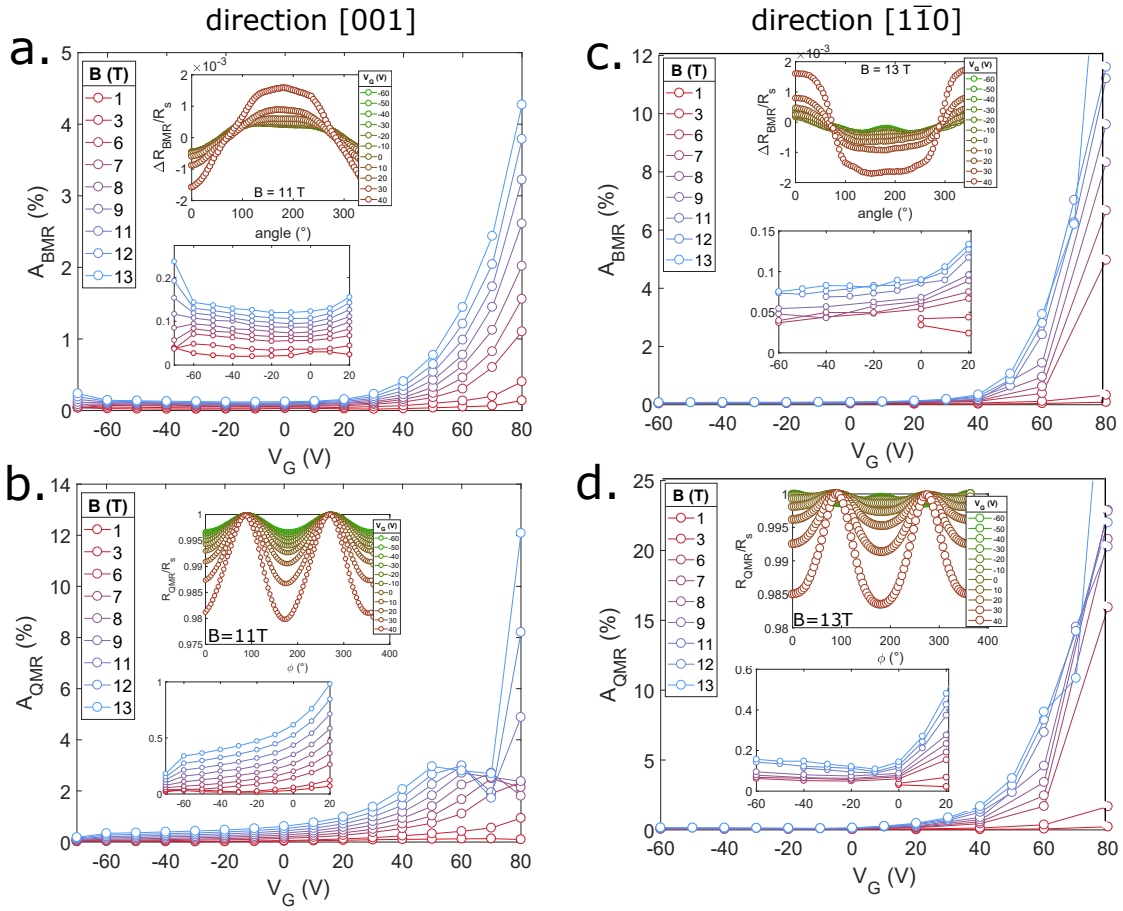

Figure 4.8: **Gate dependence of the BMR and QMR amplitude in a LAO/STO(110) 2DEG** along directions [001] (left) and $[1\bar{1}0]$ (right) **a. c.** BMR amplitude in % of total resistance as a function of gate voltage for various magnetic fields along the direction [001] and $[1\bar{1}0]$ respectively. Insets : zoom in low gate voltage region and normalized BMR for various gate voltages. **b. d.** QMR amplitude in % of total resistance as a function of gate voltage for various magnetic fields. Insets : zoom in low gate region and normalized QMR for various gate voltages along the direction [001] and $[1\bar{1}0]$ respectively.

Finally, we discuss the gate voltage dependence of the BMR and QMR, shown in figure 4.8. Panel

a. shows the evolution of A_{QMR}, the QMR amplitude in percentage of total resistance, as a function of gate voltage, for various magnetic fields between 1 and 13 T for the direction [001]. The same is presented in panel **c.** for the direction $[1\bar{1}0]$. The lower inset is a zoom in the negative gate region and the upper inset is a representation of the QMR at 13 or 11 T for gates ranging from $V_G = -60\ V$ to $V_G = 80\ V$. Similarly, panel **b.** shows A_{BMR}, the BMR amplitude in % of total resistance, as a function of gate voltage for various magnetic fields along the direction [001]. The same is shown in panel **d.** for the $[1\bar{1}0]$ direction. The lower inset shows a zoom in the negative gate region of the amplitude of the BMR while the upper inset shows the normalized BMR for various gate voltages. For both orientations, the relative amplitude of the BMR and the QMR rapidly increases by two orders of magnitude when the 2DEG enters the overdoped regime, i.e. when $V_G > 0\ V$. For both the BMR and the QMR, part of this rapid increase can be attributed to their quadratic dependence with the elastic scattering time τ, since we know that for $V_G > 0\ V$ the second band is filled and has a larger mobility.

We investigate further the gate voltage dependence of the AMR measurements. From the QMR in equation 4.13 we can compute the elastic scattering time τ. Note that this cannot be done from the BMR in equation 4.12 since we ignore various quantities, the most important of which being the Rashba coupling constant. We propose to compare the scattering time extracted from the QMR to that extracted from a single band Drude model ($\tau^{-1} = ne^2 R_s/m^*$). The carrier density n is taken from figure 3.11 from chapter 3.

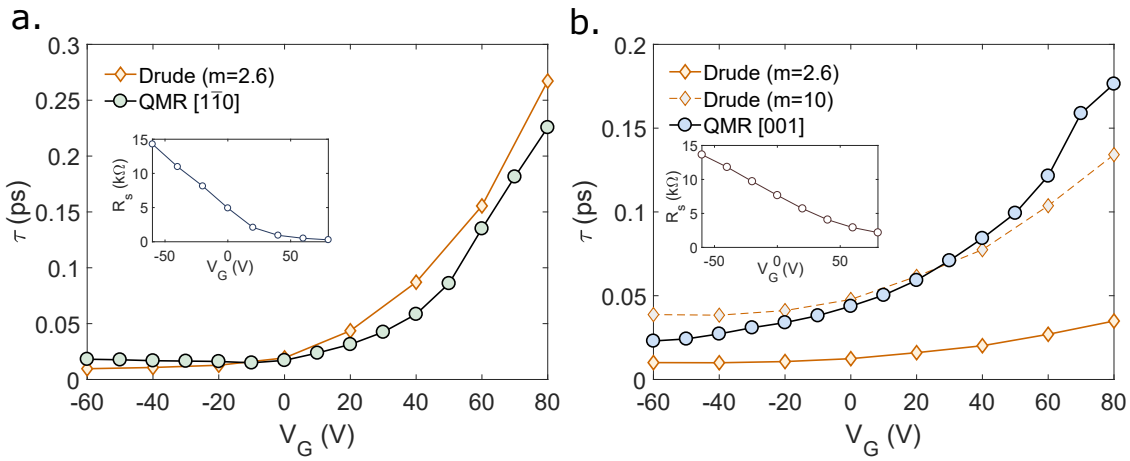

Figure 4.9: Elastic scattering time extracted from QMR data and comparison with Drude model in LAO/STO(110). **a.** along the $[1\bar{1}0]$ direction. **b.** along the [001] direction. Insets : sheet resistivity as a function of gate voltage.

We present our findings in panel **a.** in figure 4.9, for a sample oriented along the $[1\bar{1}0]$ direction and in panel **b.** for a sample oriented along the [001] direction. We have represented the scattering time, in picoseconds as a function of gate voltage, and the inset shows the sheet resistance as a function of gate voltage. Both directions have similar absolute values and trends for τ (in blue circles), varying from 0.02 ps at low doping to 0.3 ps at high doping. The scattering time expected from a single band Drude model coincides very well with τ from QMR for the $[1\bar{1}0]$ direction. The effective mass $m^* = 2.6\ m_e$ has been taken as an average of the in plane masses of both bands $\sqrt{3.1 \times 2.3}$. In the [001] direction however, the scattering from the Drude model is much lower than that extracted from QMR because of a much higher sheet resistance R_s (inset). A better agreement can be obtained considering $m^* = 10\ m_e$. However there is no justification for using a much higher mass. This discrepancy could be explained by the non-circular nature of the Fermi surface. Note that here we have chosen a Landé factor g=2, which can be an important source of error since it varies

from 0.5 to 5 in the literature in LAO/STO 2DEGs systems. Nevertheless, this potential error source can not explain the discrepancy between τ from QMR and τ from Drude in the [001] orientation, without invalidating the agreement between the two for the sample along the $[1\bar{1}0]$ direction at the same time.

4.2.5 Estimation of the Rashba coupling constant

The calculation carried out by Vaz et al. allows to compute the Rashba coupling constant α_R from the ratio of the normalized amplitude of the BMR and the QMR (eq. 4.14). The calculation is valid in the case of a single circular Fermi surface, which is not what we have at the LAO/STO(110) interface. The Fermi surface is composed of one or two orthogonal ellipses, depending on the filling. Nevertheless, equation 4.14 can provide an estimate of the effective Rashba coupling constant in the LAO/STO(110) 2DEG.

For the calculation, we assume $g = 2$. We estimate the Fermi energy using the formula $E_F = n\pi\hbar^2/m^*$ with $m^* = \sqrt{3.1 \times 2.3} \times m_e = 2.6\, m_e$ and n, varying from $0.7\times10^{14}\, cm^{-2}$ to $1.2\times10^{14} cm^{-2}$, as given in figure 3.11. The current density appearing in eq. 4.14 is equal to 4 A/m in our case. We show in figure 4.10 the gate dependence of the coupling constant, which varies from 5 meV.$\mathring{A}$ to 15 meV.$\mathring{A}$. For the sample along the $[1\bar{1}0]$ direction, the evolution is not monotonous: there is a maximum around $V_G = -10\ V$, a sharp decrease for higher gate voltages and another increase for $V_G > 40\ V$ up to a new maximum at $V_G = 80\ V$ along the $[1\bar{1}0]$ direction. For the [001] direction, the Rashba coupling is qualitatively different : α_R is almost gate-independent but sharply increases for $V_G > 60\ V$.

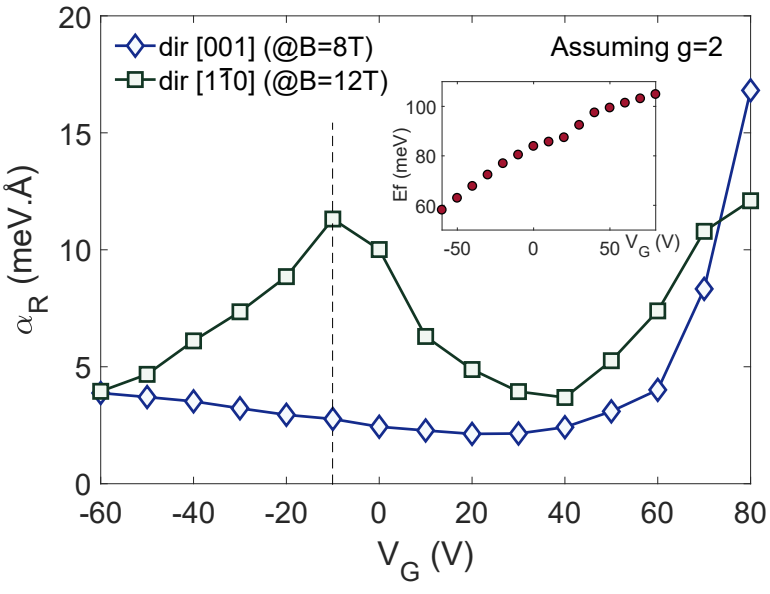

Figure 4.10: **Rashba coupling constant as a function of gate voltage in a LAO/STO(110) 2DEG.** Inset : Linear Fermi energy as a function of gate voltage used to compute α_R. Dashed line represents the Lifschitz transition where the Hall effect becomes non-linear.

Previous studies have noted that the Rashba effect is maximum at the Lifschitz transition [132], which is consistent with our result where α_R is maximum around the gate voltage at which the second band starts to be filled along the $[1\bar{1}0]$ direction. We currently do not have a clear picture

as to why the same is not observed along the [001] direction, but future theoretical developments should clarify that.

4.2.6 Lifschitz transition seen from QMR

An interesting quantity to investigate is what we will call from now on the absolute normalized QMR and BMR, which we will note $\tilde{Q}$ and $\tilde{B}$ respectively. These quantities are expressed as :

$$\tilde{B} = \frac{BMR(\varphi) - \min(BMR)}{\max(BMR) - \min(BMR)} \tag{4.15}$$

$$\tilde{Q} = \frac{QMR(\varphi) - \min(QMR)}{\max(QMR) - \min(QMR)} \tag{4.16}$$

These quantities vary between 0 and 1. This allows to compare the signal at the same scale whatever is the gate voltage or magnetic field. It is easier to observe the phase dependence with angle φ of the signal using this quantity plotted in polar coordinates.

We show the evolution of $\tilde{Q}$ in figure 4.11 at B=12 T along the [001] direction in panel **a.** and at B=13 T along the $[1\bar{1}0]$ direction in panel **b.**. The behavior of $\tilde{Q}$ at lower magnetic field is the same but the signal is noisier.

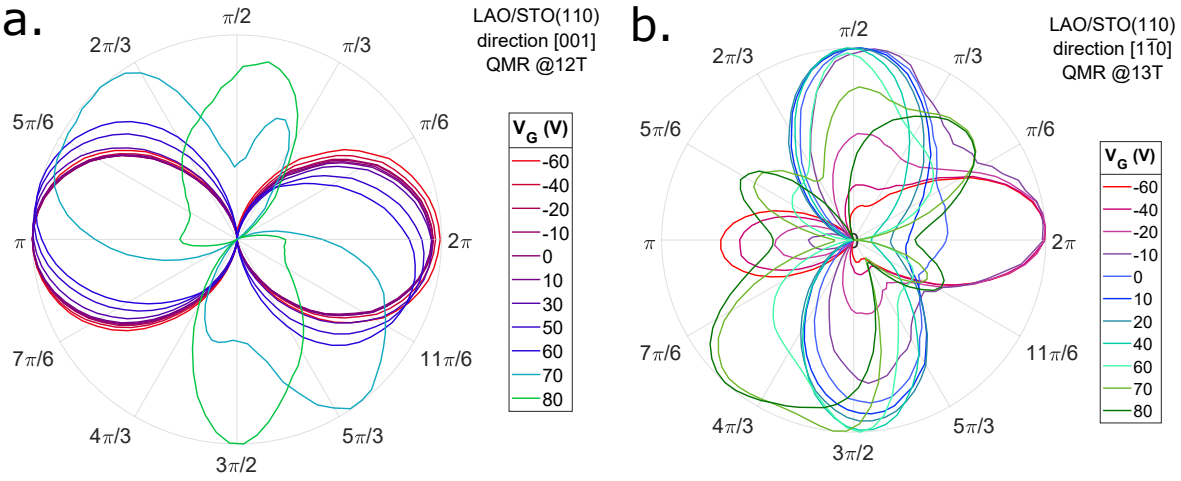

Figure 4.11: **Absolute normalized QMR a.** along the [001] direction at B=12 T, **b.** along the $[1\bar{1}0]$ direction at B=13 T.

Along the [001] direction, (figure 4.11**a.**), $\tilde{Q}$ shows maxima at π and 2π, and minima at $\pi/2$ and $3\pi/2$ in most of the gating range. For the two highest gate voltages, i.e. $V_G = 70$ and $80\ V$, the phase of the signal shifts by $\pi/2$ and small satellite peaks are visible around multiples of $\pi/3$. The most interesting feature happens in the sample along the $[1\bar{1}0]$ direction, shown in panel **b.** The absolute normalized QMR, $\tilde{Q}$, change regimes upon doping. We investigate this more closely in figure 4.12.

We have separated the $\tilde{Q}$ curves for the $[1\bar{1}0]$ direction into three regimes, corresponding to the three regimes observed in the evolution of the Rashba constant as seen figure 4.10. For $V_G \ll 0\ V$ (panel **a.**), $\tilde{Q}$ has a $\cos(2\varphi)$ like dependence, corresponding to an elongation along the [0,π] axis. For $V_G > 0\ V$ (panel b), $\tilde{Q}$ still has a $\cos(2\varphi)$-like dependence but shifted by $\pi/2$, corresponding

to an elongation along the $[\pi/2,3\pi/2]$ axis. The transition between the two regimes takes place at $V_G \approx -10\ V$ for which an intermediate shape of $\tilde{Q}$ is observed. Finally, when we overdope the 2DEG to V_G higher than 50 V, satellites peaks appears at angle $5\pi/6$ and $11\pi/6$.

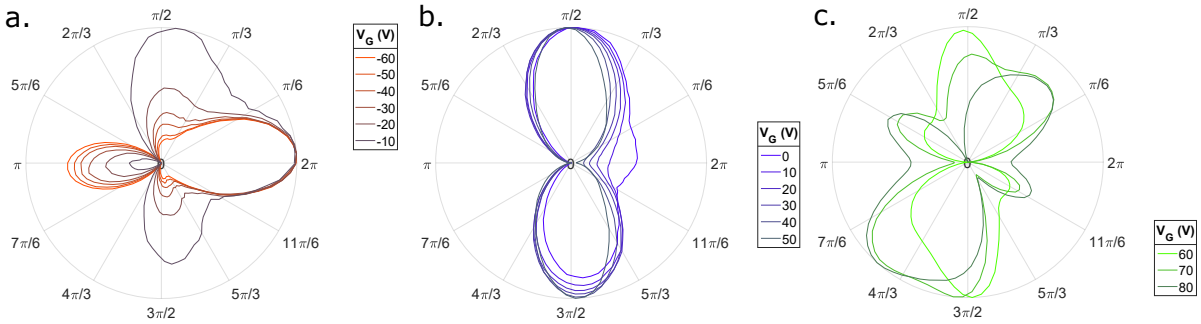

Figure 4.12: **Normalized QMR, $\tilde{Q}$, in polar coordinates, for a current applied in the direction $[1\bar{1}0]$ for different gate voltages. a.** Underdoped regime ($V_G \leq -10\ V$). **b.** Overdoped regime ($0 \leq V_G \leq 50\ V$). **c.** Highly overdoped regime ($V_G > 50\ V$). Data taken at $B = 11\ T$.

The abrupt change in the phase of the QMR signal between underdoped regime (panel **a.**) and overdoped regime (panel **b.**) coincides with the filling of the second band as seen in the Hall effect and correspond to the peak in α_R reported in figure 4.10. Qualitatively, our measurements of the QMR identifies the main Lifshitz transition in the band structure.

The orientation of the $\tilde{Q}$ pattern, with maxima along either the direction [001] at low doping or the direction $[1\bar{1}0]$ at high doping seems to be correlated to the direction of the two Fermi contours of ellipse shape. In figure 4.13**a.**, we show a scheme of the band structure when only the lowest degenerate $d_{xz,yz}$ band are populated, with $\tilde{Q}$ having maxima at 0 and π shown in inset. For $V_G > 0$ (4.13**b.**), the higher d_{xy} band start to be populated, making new kind of spin-dependent scattering possible, and in inset we show that $\tilde{Q}$ shift by $\pi/2$ in this regime. At larger gate voltages ($V_G > 60\ V$), additional $d_{xz/yz}$ or d_{xy} character subbands could also be filled, generating a new pattern for the QMR.

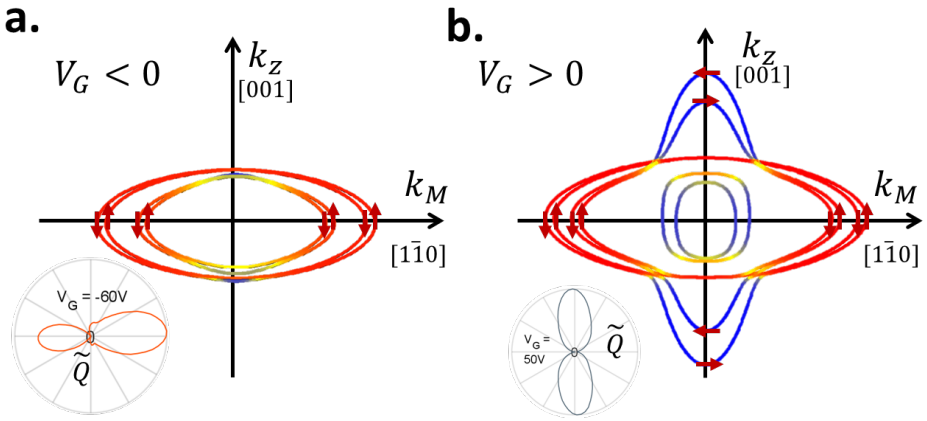

Figure 4.13: **Fermi surface of the LAO/STO(110)-2DEG a.** At low doping, only the lowest degenerate $d_{xz,yz}$ band are populated, here two subbans on the figure. The Rashba spin-splitting is visible, with arrow indicating the spin diretion. Inset shows $\tilde{Q}$ at $V_G = -60\ V$ with maxima at 0 and π. **b.** At higher dopind, the higher d_{xy} band is populated and also spin-splitted. The inset shows $\tilde{Q}$ at $V_G = 50\ V$ which is shifted by $\pi/2$ with respect to $\tilde{Q}$ in panel **a.**

To be more quantitative one needs to examine the spin-dependent scattering processes starting from a precise description of the spin-orbital texture of the band structure including the Zeeman effect. In reference [139], considering the (001)-orientated 2DEG, Boudjada et al. showed that the rotation of the magnetic field in plane, modifies the spin-texture which in turn affect the probability of scattering events. As a results, the QMR behavior is strongly determined by the SOC through the spin texture of the different bands. We have recently initiated a similar approach in collaboration with B. Göbel and I. Mertig (University of Halle) and A. Johansson (MPI Halle). The spin-orbital texture of the band structure is first derived using a tight-binding Hamiltonian which also includes an atomic SOC term, an orbital mixing term and a Zeeman term. Boltzmann transport calculations are then performed to obtain the MR.

4.3 Anisotropic magnetoresistance in $LaAlO_3/SrTiO_3(111)$

4.3.1 Magnetic transport properties

Before investigating the in-plane anisotropic magnetoresistance, we first discuss the gate voltage dependence of the sheet resistance and the Hall effect for the two LAO/STO(111) samples. Both samples were measured in the same run, using the same back gate. Figures 4.15**c.** and 4.14**c.** present the sheet resistance as a function of gate voltage for the two samples. The sheet resistance varies from few hundreds Ω to few kΩ between $V_G = -175\ V$ and $V_G = 175\ V$.

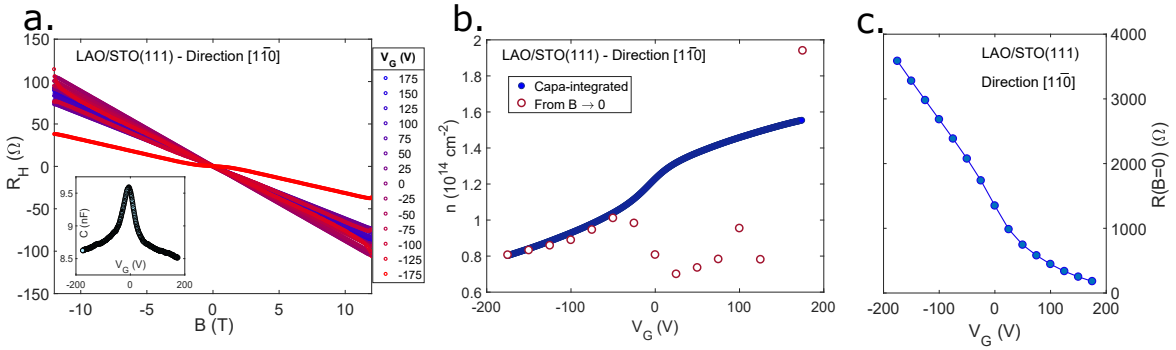

Figure 4.14: **Hall effect and sheet resistivity for a LAO/STO(111) sample cut along the [1$\bar{1}$0] direction a.** Hall resistance as a function of magnetic field for different gate voltages. Inset shows the gate capacitance measurement used to compute the carrier density **b.** Carrier density as a function of gate voltage deduced from the integration the capacitance (blue circle) compared to that extracted by linear Hall fit (red circle). **c.** Sheet resistance as a function of gate voltage.

Next, we have performed Hall effect and substrate capacitance measurements to assess the carrier density. Figures 4.14**a.** and 4.15**a.** show the Hall resistance R_H magnetic field dependence for the [1$\bar{1}$0] and [1$\bar{1}$2] orientation respectively. The inset presents the measurement of the gate capacitance. Finally figures 4.14**b.** and 4.15**b.** show the carrier density deduced from the low field linear Hall effect (red empty circle), and calculated by integrating the gate capacitance (blue circle), as already discussed in section 3.3.3 chapter 3. The typical Hall resistance varying between 30 to 100 Ω yields a carrier density between 1 and $2\times10^{14} cm^{-2}$. Overall, it seems that multiple carriers with different mobilities are at play here, since again the coefficient of the slope of the Hall effect does not vary monotonously. We notice that the Hall effect measurements are sometimes inconsistent between two consecutive gates (e.g in figure 4.15b. at $V_G = 100\ V$ and $175\ V$). While this gives problematic outliers in the carrier density extracted from linear low-field, it doesn't play a role in

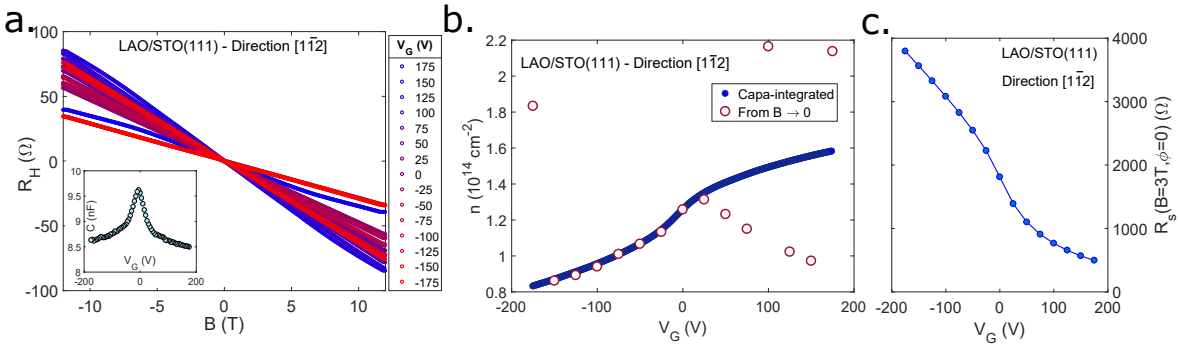

Figure 4.15: **Hall effect and sheet resistivity for a LAO/STO(111) sample cut along the [1$\bar{1}$2] direction a.** Hall resistance as a function of magnetic field for different gate voltages. Inset shows the gate capacitance measurement used to compute the carrier density **b.** Carrier density as a function of gate voltage deduced from the integration of the capacitance (blue circle) compared to that extracted by linear Hall fit (red circle). **c.** Sheet resistance as a function of gate voltage.

the capacitance-integrated density which only requires coherent data in the underdoped regime.

The carrier densities for the two directions are almost identical showing the consistency of the measurements. A small uncertainty in the determination of the absolute value of the Hall resistance is due to the fact that, in contrast with a patterned Hall bar, in our samples, the exact location of the contacts (which are aluminium wire bonds) is not very precise.

4.3.2 AMR measurements along the [1$\bar{1}$0] and [1$\bar{1}$2] direction

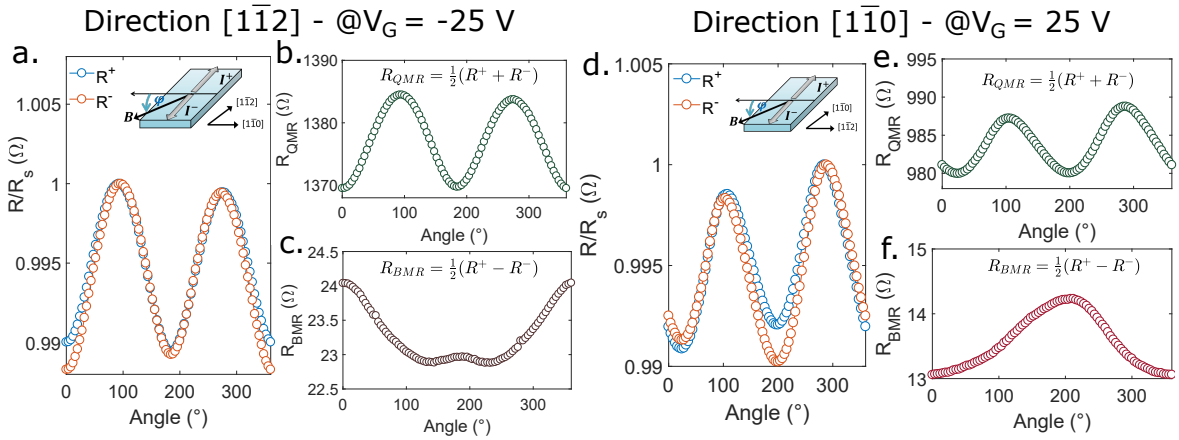

Figure 4.16: **AMR measurement in a LAO/STO(111) interface a.** In plane magnetoresistance $R^{\pm} = \rho_{xx}(I^{\pm})$ of the sample cut along the [1$\bar{1}$2] for the two current directions I^+ and I^- shown in inset. **b.** Quadratic magnetoresistance extracted from data in **a.** **c.** Bilinear magnetoresistance extracted from data in **a.** Panels **d.** **e.** and **f.** are the same as **a.** **b.** and **c.** for the sample cut along the [1$\bar{1}$0] direction. Data taken at $I = 2\ mA$ and $T = 3\ K$ for both directions, $B = 13\ T$ for [1$\bar{1}$2] and $B = 8\ T$ for [1$\bar{1}$0].

Transport measurements presented in this section have been performed in the same way as those presented in the previous section on the LAO/STO(110) samples. Figure 4.16 shows a typical AMR, BMR and QMR in a LAO/STO(111) 2DEG along both the [1$\bar{1}$2] direction for panels **a.** **b.** and

c. and the $[1\bar{1}0]$ direction for panels **d.** **e.** and **f.**. In panel **a.** and **d.**, we present the normalized anisotropic magnetoresistance as a function of in-plane angle between magnetic field and current, for two directions of the current. The inset defines the zero angle (corresponding in this case to $B \perp I$) as well as I^+ and I^-. We see a 1 to 1.2% relative variation between the maximum and absolute minimum for the two directions. When we sum R^+ and R^-, we obtain the quadratic magnetoresistance, displayed in panels **b.** and **e.**. It exhibits the expected $\cos(2\varphi)$ dependence, with a 15 Ω variation along the $[1\bar{1}2]$ direction at $V_G = -25\ V$ and a 10 Ω variation along $[1\bar{1}0]$ at $V_G = 25\ V$. When we take the difference between R^+ and R^-, we obtain the bilinear magnetoresistance, displayed in panels **c.** and **f.**. It has the expected $\sin(\varphi)$ dependence and a very small 1 to 2 Ω variation.

We will now present results of systematic measurements of the QMR and BMR for various gate voltages, magnetic fields, and currents.

4.3.3 Field dependence of the BMR and QMR

We first present the QMR in a LAO/STO(111) interface as a function of magnetic field, at $V_G = \pm 25\ V$ depending on the direction of the sample, in figure 4.17. In panel **a.** and **c.** we have plotted the QMR normalized by its value at $\pi/2$ for fields between 1 to 11 T, for the directions $[1\bar{1}2]$ and $[1\bar{1}0]$, respectively. The amplitude of the latter is reported in figure 4.17**b.** and **d.**, and a quadratic fit is provided in agreement with equation 4.11.

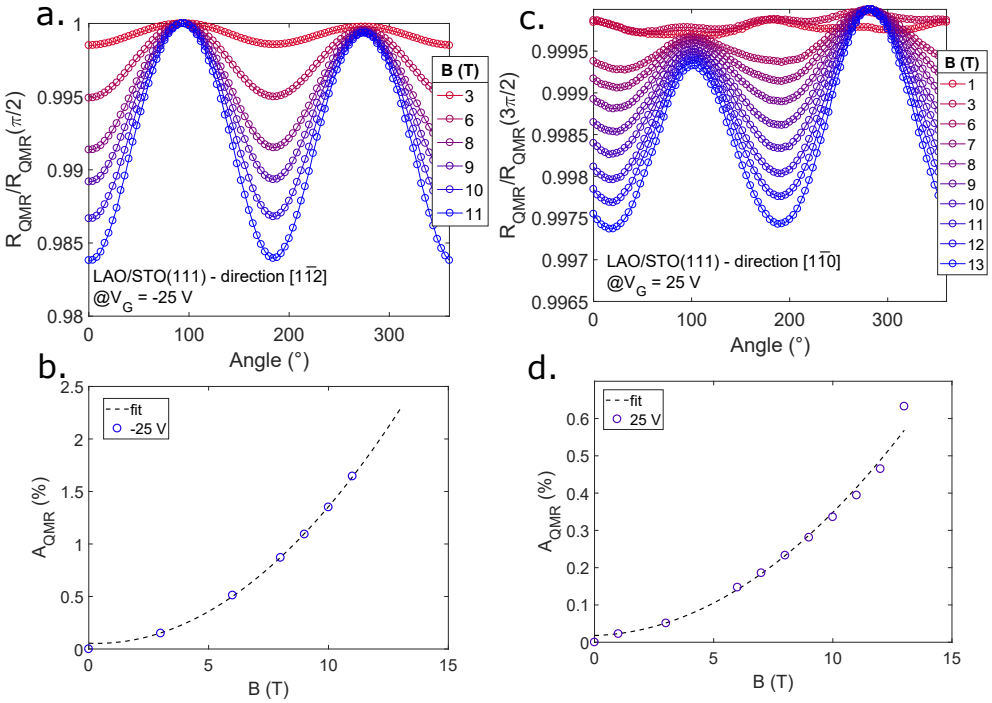

Figure 4.17: **Quadratic Magneto-Resistance (QMR) in a LAO/STO(111) sample. a.** Normalized resistance as a function of angle for various gate voltages for the sample oriented along the $[1\bar{1}2]$ direction. **b.** Evolution of the coefficient of the QMR oscillations (in %) as a function of magnetic field for the sample oriented along the $[1\bar{1}2]$ direction. **c. d.** Idem for the direction $[1\bar{1}0]$.

As for the LAO/STO(110) samples, the QMR shows a quadratic dependence in B and varies up

to a few % at high magnetic field for the gate voltage presented in figure 4.17.

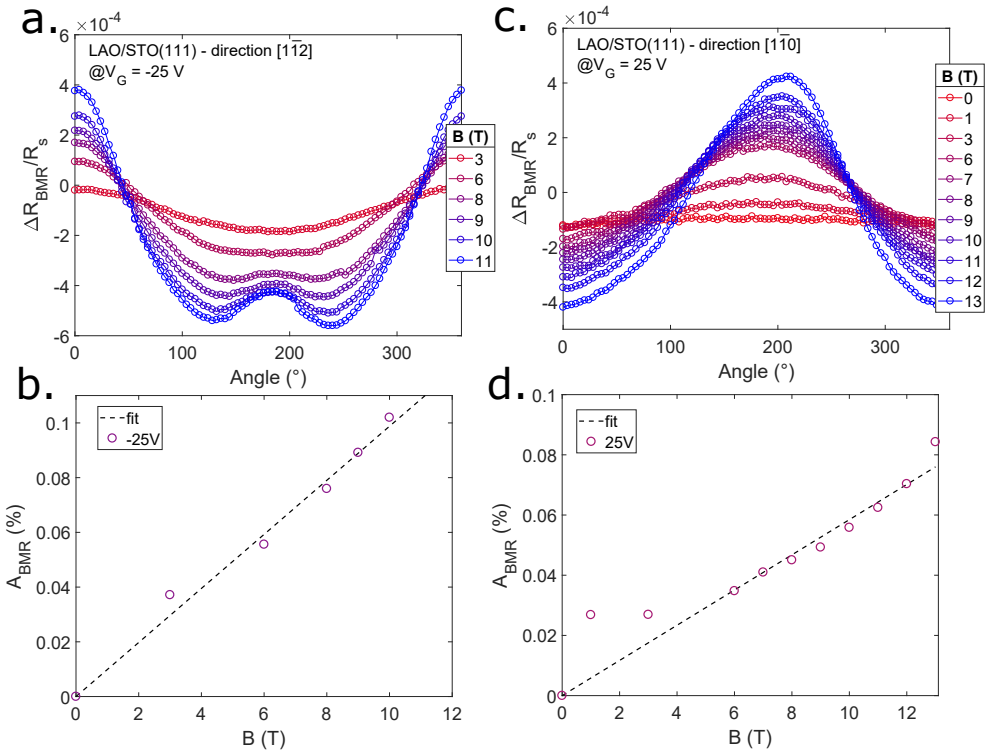

Figure 4.18: **Bilinear Magneto-Resistance (BMR) in a LAO/STO(111) sample. a.** Normalized bilinear magnetoresistance as a function of angle for different magnetic fields in the sample cut along the [1$\bar{1}$2] direction. **b.** Evolution of the coefficient of the BMR oscillations (in %) as a function of magnetic field. Panels **c. d.** are the same as panels **a. b.** but for the sample cut along the [1$\bar{1}$0] direction.

4.3.4 Current dependence of the BMR

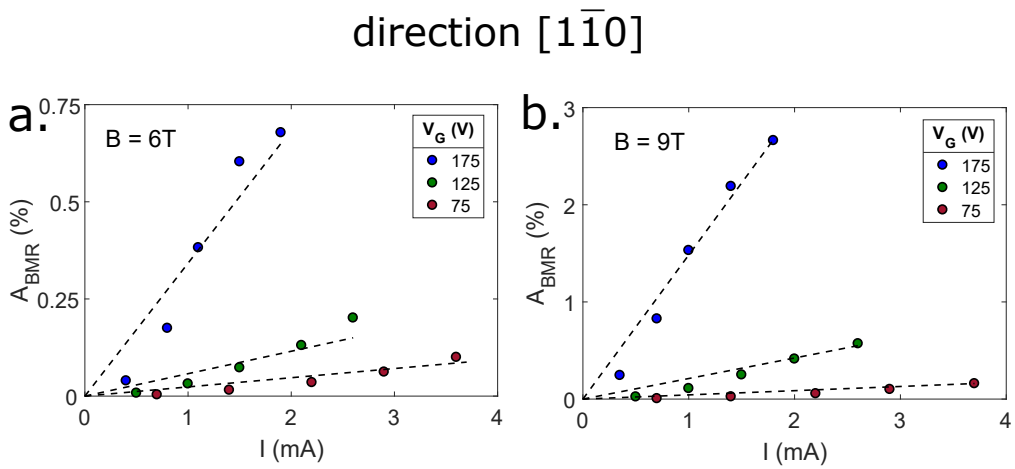

Figure 4.19: **Amplitude of the BMR as a function of current in a LAO/STO(111) sample along the [1$\bar{1}$0] direction for various gate voltages. a.** For B=6 T. **b.** For B=9 T.

Following the same procedure than for the LAO/STO(110) samples, we have analyzed the BMR amplitude as a function of current for both directions ([$1\bar{1}0$] and [$1\bar{1}2$]) in the LAO/STO(111) interface. We show our results in figure 4.19 panel **a.** for $B = 6\ T$ and panel **b.** for $B = 9T$, for measurements along the [$1\bar{1}0$].

A variation of the BMR amplitude is observed, in agreement with equation 4.10 and as already observed for the LAO/STO(110) sample.

4.3.5 Gate voltage dependence of the BMR and the QMR

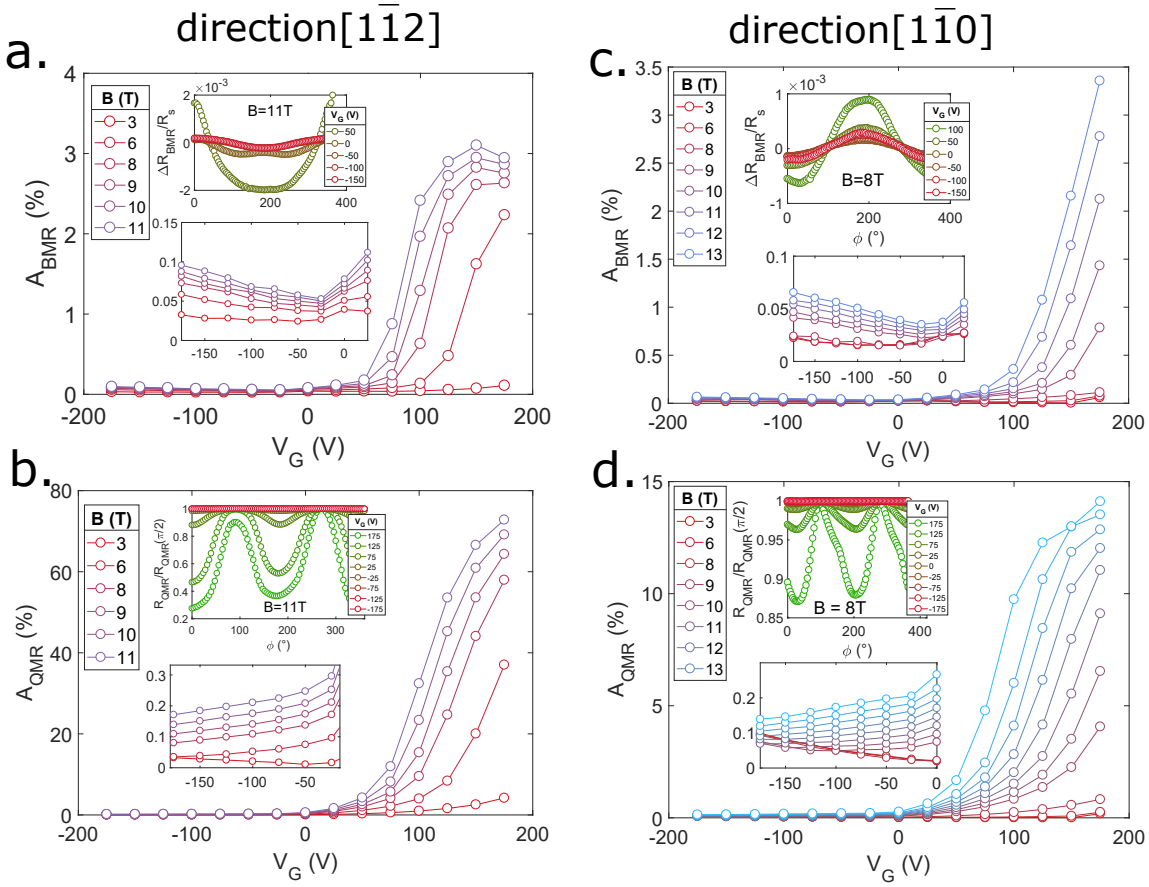

Figure 4.20: **Gate dependence of the BMR and QMR amplitude in a LAO/STO(111) sample** along directions [$1\bar{1}2$] (left) and [$1\bar{1}0$] (right) **a. c.** BMR amplitude in % of the total resistance as a function of gate voltage for different magnetic fields along the directions [$1\bar{1}2$] and [$1\bar{1}0$] respectively. Insets : zoom of the low gate voltages region and normalized BMR for various gate voltages. **b. d.** QMR amplitude in % of the total resistance as a function of gate voltage for different magnetic fields. Insets : zoom of the negative gate voltages region and normalized QMR for different gate voltages along the direction [$1\bar{1}2$] and [$1\bar{1}0$] respectively.

Next, we turn to the gate voltage dependence of the BMR and QMR, shown in figure 4.20. Panel **a.** shows the evolution of the QMR amplitude in (%) of the total resistance as a function of gate voltage, for different magnetic fields between 1 and 13 T for the direction [$1\bar{1}2$]. The same is presented in panel **c.** for the direction [$1\bar{1}0$]. The lower inset is a zoom in the negative gate region and the upper inset is a representation of the QMR at $B = 8\ T$ for sample [$1\bar{1}0$], for gate voltages ranging from

$V_G = -175\ V$ to $V_G = 175\ V$. Similarly, panel **b.** shows the BMR amplitude, in % of the total resistance, as a function of gate voltage for various fields along the direction $[1\bar{1}0]$, and the same in panel **d.** for the QMR amplitude along the $[1\bar{1}0]$ direction. The lower inset shows a zoom in the negative gate region of the amplitude of the BMR while the upper inset shows this normalized BMR for various gate voltages.

Both sample cut along the $[1\bar{1}0]$ and $[1\bar{1}2]$ direction shows similar trends in QMR and BMR amplitude as the LAO/STO(110) sample discussed in the previous section. A_{BMR} and A_{QMR} increase by two order of magnitude when the 2DEG enters the overdoped regime, i.e when $V_G > 0\ V$ which can be attributed to the filling of a high mobility band, as seen in transport measurement described chapter 3.

We now turn to the computation of the elastic scattering time τ from QMR and its comparison with a simple Drude model. The scattering time is plotted as function of gate voltage in figure 4.21, in panel **a.** for the sample cut along the $[1\bar{1}2]$ direction and in panel **b.** for the sample cut along the $[1\bar{1}0]$ direction. Equation 4.13 allows to extract τ from A_{QMR} that we compare to the scattering time derived from a single band Drude model ($\tau^{-}1 = ne^2R_s/m^*$). For n, we take data from figure 4.15**b.** and 4.14**b.**. For each direction, the scattering times from a single band Drude model for the two bands are shown in orange, the lower curve corresponds to the high mobility band and the upper curve corresponds to the low mobility band. Masses are taken from [72].

Both directions have similar increasing trends for τ as we increase the gate voltage. However the relative variation is four times higher along the direction $[1\bar{1}2]$ (from 18 to 800 fs) compared to the direction $[1\bar{1}0]$ (from 20 to 200 fs). Once again, the Landé factor is unknown and has been set to 2. Along the direction $[1\bar{1}2]$, τ from QMR follows a gate voltage dependence close to the average of the two bands. Along the $[1\bar{1}0]$ direction however, τ follows the trend expected from the low mobility carrier ($m^* = 2.2$). The main limitation of our approach is the non-circular nature of the Fermi surface which limits the validity of the use of equation 4.13.

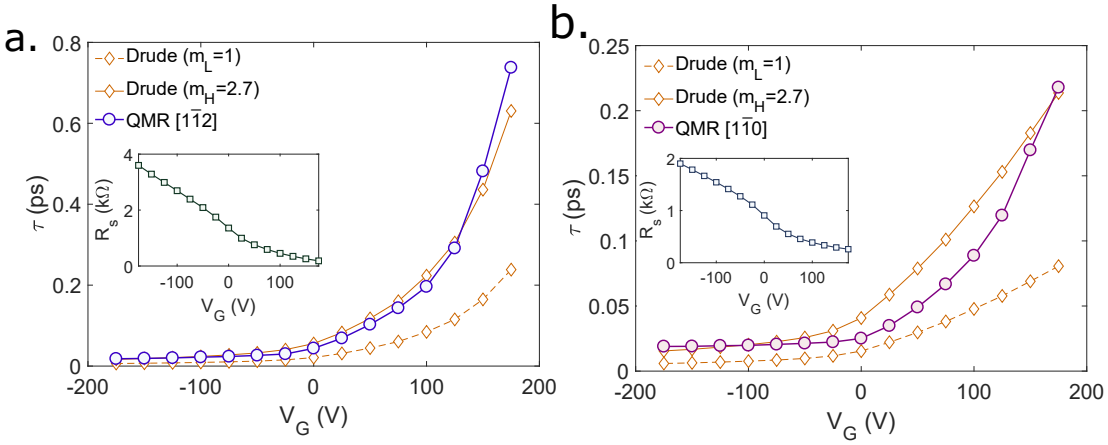

Figure 4.21: Elastic scattering time extracted from QMR data and comparison with Drude model in a LAO/STO(111) 2DEG. **a.** along the $[1\bar{1}2]$ direction. **b.** along the $[1\bar{1}0]$ direction. Insets : sheet resistivity as a function of gate voltage.

Note that we have chosen a particular field (8 T for the sample along $[1\bar{1}0]$ and 6 T for $[1\bar{1}2]$) to extract τ but we have checked that the results are consistent across all magnetic field values.

4.3.6 Estimation of the Rashba coupling constant

The calculation carried out by Vaz et al. (eq. 4.14) allows the computation of the Rashba coupling constant α_R from the ratio of the normalized amplitude of the BMR to the QMR. As already mentioned, in principle, the calculation is valid in case of a circular Fermi surface only, which is not the case at the LAO/STO(111) interface. The Fermi surface includes concentric 6-branch stars, depending on the filling.

For the calculation, we assume $g = 2$. We estimate the Fermi energy using the formula $E_F = n\pi\hbar^2/m^*$ with n, varying from $0.8\times10^{14}\ cm^{-2}$ to $1.5\times10^{14} cm^{-2}$ shown in figures 4.15 and 4.14. For the effective mass, we use the mass from ref [72], i.e. along the $[1\bar{1}0]$ direction the light band mass is 0.5 and the heavy band mass is 2.2 while along the $[1\bar{1}2]$ direction the light band mass is 1 and the heavy band mass is 7. We plot α_R for the average mass $m^* = \sqrt{m_L * m_H}$ along a given direction. The grey area corresponds to the two possible limiting cases where $m^* = m_L$ and $m^* = m_H$. The current density in eq. 4.14 is equal to 13 A/m. We show in figure 4.22 the gate voltage dependence of the coupling constant, which varies from 5 meV.$\mathring{A}$ to 50 meV.$\mathring{A}$.

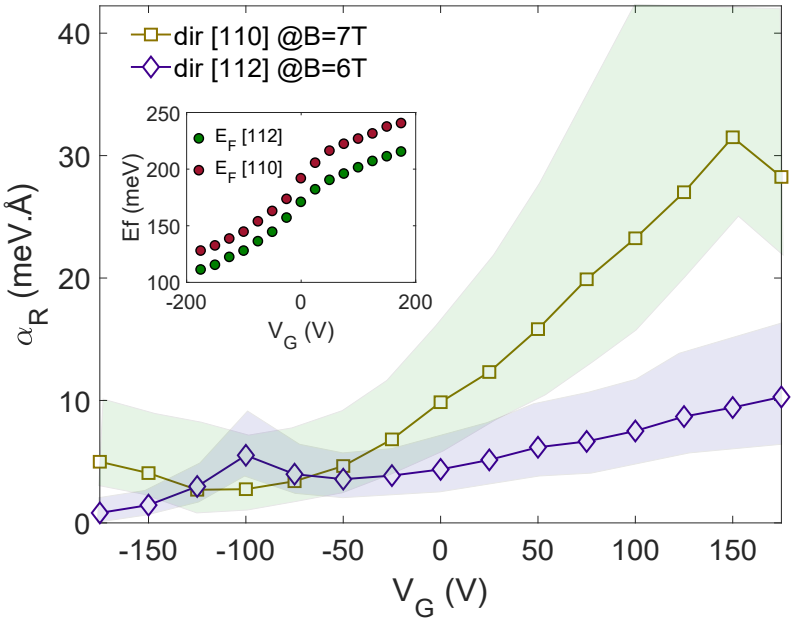

Figure 4.22: **Rashba coupling constant as a function of gate voltage.** Inset: Fermi energy as a function of gate voltage used to compute α_R. The shaded area represents the uncertainty linked to the effective mass, the lower bound corresponding to $m^* = m_H$ and the upper bound tp $m^* = m_L$.

The Rashba coupling constant along both the $[1\bar{1}0]$ direction and the $[1\bar{1}2]$ direction share similar trends: they steadily increase at high doping after a small decrease at low doping. However, the high doping value for the sample along the $[1\bar{1}0]$ direction is 5 times higher than the one along $[1\bar{1}2]$. This can be explained by the fact that the Rashba splitting is higher along the $[1\bar{1}0]$ direction. Here, the Lifshitz transition does not manifest istself by a peak in α_R, in contrast with observations on the (110) oriented sample.

4.3.7 Gate-Field phase diagram of the QMR

We start by discussing the gate voltage evolution of the $\tilde{Q}$ pattern for the direction $[1\bar{1}2]$ (figure 4.23**a.** and **b.**). For a rather weak magnetic field of 3 T (panel **a.**), at negative gate voltages, a regular $\cos(2\varphi)$ like pattern is observed, elongated along the direction $[\pi,2\pi]$. A transition takes place around $V_G = 0$ and a butterfly like pattern appears for positive gate voltages with maxima at $\pi/3$, $2\pi/3$, $4\pi/3$ and $5\pi/3$. This marks the filling of a new band of a different orbital character and spin texture. Surprisingly, the butterfly pattern is not seen at the higher magnetic field of 11 T (panel **b.**) for which a regular $\cos(2\varphi)$ like pattern is observed in the entire gating range. Although we do not have a quantitative understanding of the $\tilde{Q}$ yet, we anticipate that the Zeeman effect must play an important role here as it suppresses the contribution associated with the new band leading to the butterfly like pattern. For the $[1\bar{1}0]$ orientation (figure 4.23**c.** and **d.**), the situation is reversed at low magnetic field (3 T) since the butterfly like pattern is observed for negative gate voltages and disappears for $V_G > 0$ (panel **c.**). Again the contribution of the band generating the butterfly pattern is suppressed at higher magnetic field (11 T, panel **d**) most likely due to the Zeeman on the band structure and spin texture.

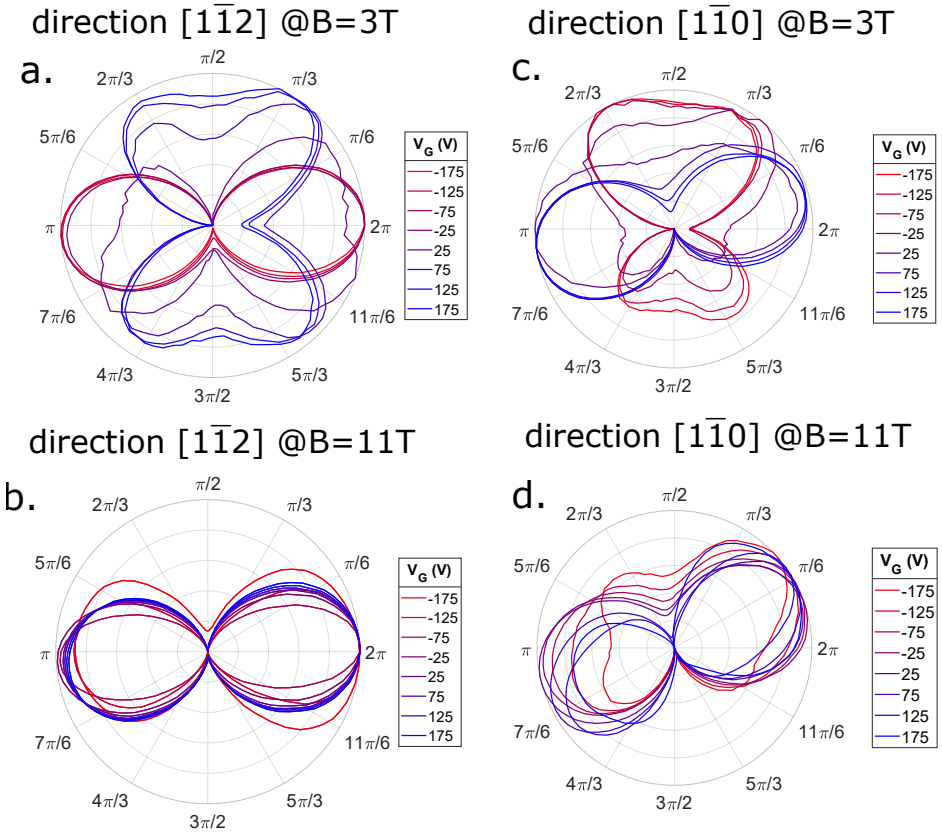

Figure 4.23: **Absolute normalized QMR** along the $[1\bar{1}2]$ direction **a.** at B=3 T, **b.** at B=11 T, and along the $[1\bar{1}0]$ direction **c.** at B=3 T, **d.** at B=11 T.

At the time of writing of this manuscript we haven't tried yet to model the spin-orbital texture of the band structure of the LAO/STO(111) interface. However, in the same spirit than for the LAO/STO(110) interface discussed previously we are confident that we can understand the different patterns of the $\tilde{Q}$ though Bolzman calculation of the spin-dependent scattering processes provided we include all the necessary ingredients in the band structure calculation (atomic SOC, orbital mix-

ing term and Zeeman effect). This will be done in collaboration with with B. Göbel and I. Mertig (University of Halle) and A. Johansson (MPI Halle).

4.4 Discussion

The study of the in-plane anisotropic magnetoresistance (AMR), in Rashba 2DEGs is a key method to measure the non-reciprocal transport that emerges in these systems. In particular, the associated bilinear magnetoresistance (BMR) and quadratic magnetoresistance (QMR) can be compared to prediction from spin dependent scattering for a given Fermi surface. These two quantities have been analytically derived by A. Drydal and D. Vaz [136] [132] in the limiting case of parabolic dispersion, or equivalently circular Fermi surface. They have predicted the dependencies of the QMR and BMR amplitude as a function of magnetic field, current, and elastic scattering time which are well reproduced in the non-circular Fermi surface of the LAO/STO(110) and LAO/STO(111) samples we have studied. In particular, the observation of the BMR which is linear both in current and magnetic field shows unambiguously the presence of Rashba spin-orbit coupling through a charge to spin conversion mechanism (Edelstein effect). Moreover, the study of the gate voltage dependence of the QMR allows the extraction of the elastic scattering time in good agreement with a single free electron Drude model. Finally, the Rashba coupling constant is calculated from the ratio of the BMR and the QMR, and even though the formula should only be valid for circular Fermi surface, we find a gate-dependent Rashba constant $\alpha_R \approx 10\ meV/\mathring{A}$, which is the correct order of magnitude for these 2DEGs. A maximum in Rashba coupling is seen for the sample oriented along the $[1\bar{1}0]$ direction as expected at the Lifschitz transition. However this is not seen in the other direction which remains to be understood.

The phase of the QMR oscillations with angle φ behaves differently depending on the sample and its orientation. The most striking feature revealed by our measurements is that for the LAO/STO(110) sample cut along the $[1\bar{1}0]$ direction, a $\pi/2$ shift is observed at the Lifschitz transition. We are confident that Boltzmann calculations of spin-dependent scattering under magnetic field initiated recently should be able to explain why the filling of the second band abruptly changes the sign of the QMR phase.

For the LAO/STO(111) samples, the variety of patterns observed for the QMR is even richer : while the pattern close to a $\cos(2\varphi)$ one remains unchanged at all gates for high enough magnetic fields, the low magnetic field measurements reveals a butterfly structure. Interestingly, for the direction $[1\bar{1}0]$, only the negative gate voltages curves exhibit the butterfly pattern at low magnetic field while for the other direction this pattern is only visible for positive gate voltages. We anticipate that this behavior is the result of a competition between the spin texture of the Fermi surface generated by Rashba coupling and the Zeeman effect that modifies the spin alignment in the complex band structure of the LAO/STO(111) interface. Note that in all our measurements, we have not observed the six-fold anisotropic magnetoresistance reported by Rout et al. [133]. The 2DEG at LAO/STO(111) exhibit a more complex phase diagram than the two other (001) and (110) orientations, and is subject to more complex electronic reconstruction [98], thus, the absence of replication of Rout's experiment could be due to different ground states of the sample.

In-plane anisotropic magnetoresistance is an accessible type of measurement which can provide numerous meaningful information on the 2DEG, the most important of which is the Rashba coupling constant. Combined with Boltzmann calculations of the scattering processes and band structure, it is a useful tool to design and test Rashba-2DEGs-based spintronic devices.

Chapter 5

Novel Oxide Interfaces

5.1 $AlO_x/SrTiO_3$

5.1.1 History

The Pulsed-laser deposition of a $LaAlO_3$ thin layer (or other e.g. $LaTiO_3$) on a $SrTiO_3$ substrate is a complex process, requiring a careful monitoring of the growth parameters (temperature, oxygen pressure, evaporation rate...). The properties of the resulting 2DEG strongly depends on the growth conditions, and ultimately PLD growth is not suitable for large scale production. To overcome this problem, in 2012 Delahaye and Grenet showed that is was possible to obtain a 2DEG at the STO(001) surface by simply depositing aluminium in a 10^{-6} mbar vaccum [140]. Motivated by the study of that 2DEG by ARPES, Santander's team in Paris Saclay University later proposed a similar "universal fabrication of 2DEG" [55]. The main idea is to deposit a thin layer of aluminium onto a clean STO substrate in an UHV chamber using a Knudsen cell (other evaporation methods such as sputtering for instance can also be used). The Al atoms are oxidized by pumping the oxygen atoms from the first top layers of STO, thus creating oxygen vacancies that dope the t_{2g}-based conduction bands. To form a capping layer, more Al is deposited and is exposed to an oxygen rich atmosphere to fully oxidize the top Al layer into AlO_x. The process is illustrated in figure 5.1**a.** They showed that the 2DEG formed by oxygen vacancies is very similar to that obtained at the LAO/STO interface, with a typical carrier density of 10^{14} cm^{-2} (see section 1.3.2). They have studied the band structure by ARPES and some of their results are reported in figure 5.1**b.** The top and bottom panels represent the linear vertical and linear horizontal polarization of the light respectively, which, depending on selection rules, interact with different t_{2g} bands. The top panel shows two light d_{xy} sub-bands while the bottom panel shows a single degenerate $d_{xz,yz}$ heavy band.

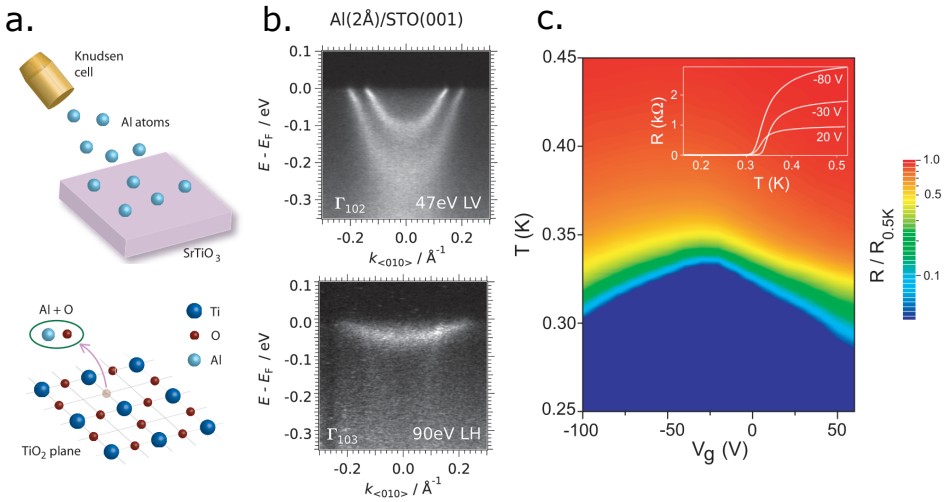

Figure 5.1: **$AlO_x/SrTiO_3$ 2DEG fabrication and electronic properties overview. a.** Schematic process of 2DEG formation from oxygen vacancies generated by Al deposition, from [57]. **b.** Two light bands and one heavy band in a $AlO_x/SrTiO_3$ 2DEG seen by ARPES, from [55]. **c.** Dome shaped superconducting phase diagram of an $AlO_x/SrTiO_3$ 2DEG, showing the normalized resistance in color scale as a function of temperature and back gate voltage, from [57].

Two years later, it was reported that the 2DEG formed at the AlO_x/STO interface is superconducting, with a similar T_c of 300 mK. Its density can also be tuned with a back gate voltage and a

relative variation of $\pm$30% of the electronic density was demonstrated [57]. The superconducting phase diagram as a function of gate is shown in figure 5.1**c.** The blue area corresponds to the superconducting phase. The resistive part is normalized by the resistance at 500 mK for better contrast. In the inset of figure 5.1**c.**, the authors present the resistance as a function of temperature for three different gate voltage.

As of today, it is still not clear whether or not the 2DEG at the $AlO_x/SrTiO_3$ made from oxygen vacancies is rigorously the same as the one at $LaAlO_3/SrTiO_3$ interface originating (at least partially) from the polar catastrophe. Still, the method of Al oxidation has proven to be efficient at creating superconducting 2DEG with strong spin orbit coupling using a simpler fabrication method compared to the PLD growth of a LAO/STO 2DEG. For this reason, Al-oxidized interfaces have gathered interest, notably in the spintronic community. In the following section I will present the results of our measurements of transport properties of a 2DEG made by the Oxitronics team at Thales-CNRS.

5.1.2 Fabrication

The samples were grown in CNRS-Thales using commercial TiO_2 terminated $SrTiO_3$ substrate according to the following recipe :

• The samples are grown using a commercial DC magnetron sputtering PLASSYS MP450S with a base pressure of about 9 x 10^{-8} mbar.

• The deposition rates of Al were deduced from X-ray reflectometry measurements (XRR) and AFM, the growth rate was 0.86 $\mathring{A}$/s.

• The conditions were fixed to DC current = 30 mA, Ar gas flow = 5.2 sccm (cubic centimeter per minute at standard conditions, room temperature and 1 atm of pressure).

• The resulting power during deposition was 10 W.

• The growth was carried out in three 10s steps.

The growth by step, instead of single shot, seems to give a lower carrier density, which is experimentally better for the existence of superconductivity in such 2DEGs. In the following section we will present the results obtained on an AlO_x(2.6nm)/$SrTiO_3$(001) sample in order to study the different aspects of its 2DEG.

5.1.3 Superconductivity

We first discuss the low temperature measurements of an $AlO_x/SrTiO_3$(001) interface performed in a dilution refrigerator at ESPCI. Figure 5.2 shows the superconducting transition with a critical temperature of about 200 mK, before the application of a gate voltage.

The field effect dependence of the superconductivity in this sample was also measured and is shown in figure 5.3 below. We performed a first polarization process, meaning that the back gate was swept to +200 V to allow an initial irreversible effect (electrons escaping the well) and to prevent subsequent hysteretic processes (see section 3.3.1). This explains why the 0 V resistivity curve in figure 5.3 is not the same as in figure 5.2. The left panel shows the resistance as a function of temperature for various gate voltages. The resistivity in the normal state varies between 4 kΩ at 200 V and 50 kΩ at -200 V. Upon doping, around V_G = 75 V, the 2DEG becomes superconducting with a T_c of approximately 180 mK. The right panel shows the same data but in the form of a 2D color

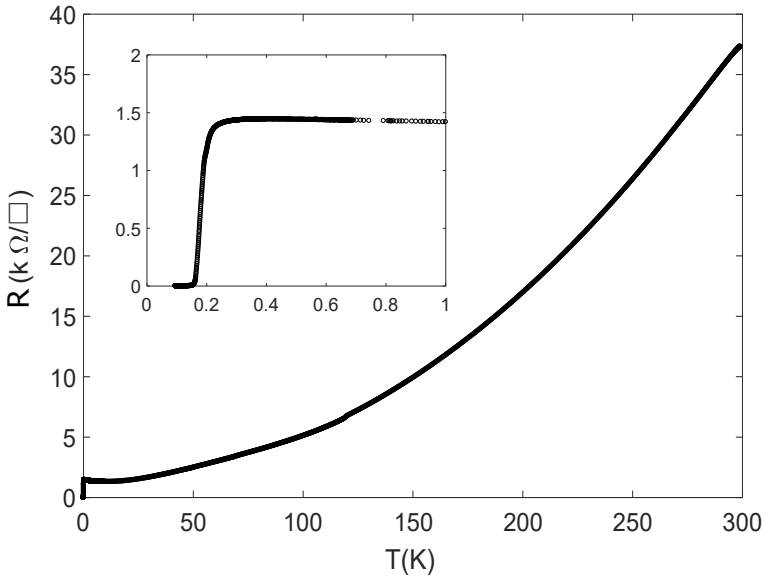

Figure 5.2: Sheet resistance of a 2DEG at Al(2.6 nm)/STO interface. Inset: superconducting transition around T_c = 250 mK. Taken before applying any gate voltage.

plot where the color scale represents the normalized sheet resistance. We clearly see the closing of the superconducting region around V_G = 50 V. This is, to our knowledge, the first report of a metal-to-superconducting transition driven by electric field effect in an $AlO_x/SrTiO_3$ 2DEG, since in previous measurements the T_c was not fully suppressed upon applying a gate [57].

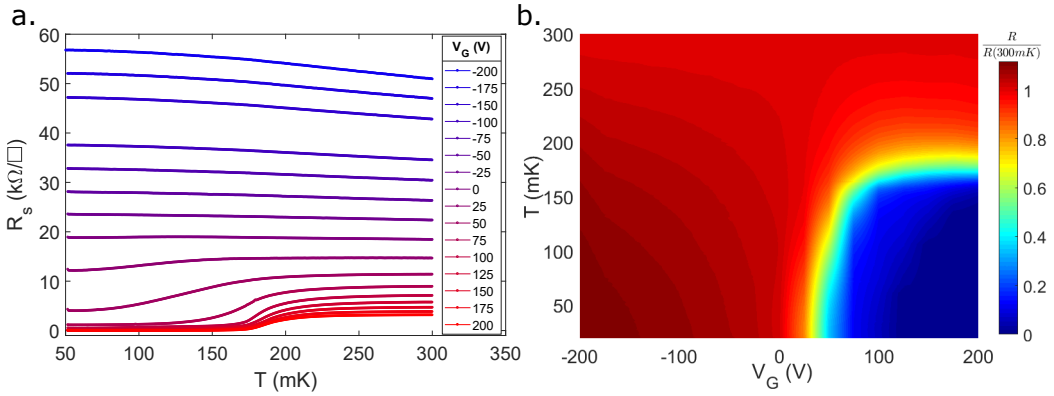

Figure 5.3: **Superconductivity in an AlO_x(2.6nm)/$SrTiO_3$ 2DEG. a.** R vs. T for different backgate voltages from +200 V to -200 V. **b.** Corresponding phase diagram, where resistance (in color scale) is normalized by its value in the normal state at 300 mK.

5.1.4 Critical magnetic field

We now look at the upper magnetic critical field H_{c2} dependence on temperature for various gate voltages in the superconducting region in order to extract the coherence length as described in section 1.1.1. Figure 5.4**a.** shows a typical measurement of resistance as a function of temperature

for different magnetic fields, at a given gate voltage $V_G = 175\ V$. We see that as we increase the field, superconductivity is progressively suppressed. As usual, we define the critical magnetic field as the magnetic field for which 80% of the normal resistance is recovered, i.e. $H_{c2}(T) = H(R(T) = 0.8\ R_s)$ and we plot H_{c2} as a function of T for each gate voltage in figure 5.4**b.** The interpolated zero temperature critical field gives the coherence length following the Ginzburg-Landau formula : $\xi = \sqrt{\frac{h}{4\pi e H_{c2}}}$. From figure 5.4**b.** we can extract the zero temperature superconducting coherence length $\xi_{GL} = 148$ nm for V_G = 25 V and 122 nm for V_G > 25 V. The mean free path at $V_G = 25\ V$ can be estimated to be $l_{MFP} = h/(e^2 R_s \sqrt{2\pi n}) = 24\ nm$. We are in the dirty limit since $\xi/l_{MFP} \approx 5 > 1$.

We then plot the normalized critical field $H_{c2}(T)/H_{c2}(0)$ as a function of the reduced temperature T/T_c in figure 5.4**c.**. We see that all $H_{c2}(T)$ curves collapse onto the single band WHH model (see section 3.4), suggesting that AlO_x/STO behaves as a single band superconductor. Given that the superconductivity only exists at $V_G > 25\ V$ (figure 5.3), we make the hypothesis that in $AlO_x/SrTiO_3$ interface just like in the $LaAlO_3/SrTiO_3$ ones, only the high energy $d_{xz,yz}$ band contributes to the superconductivity, hence the single gap superconductivity observed here.

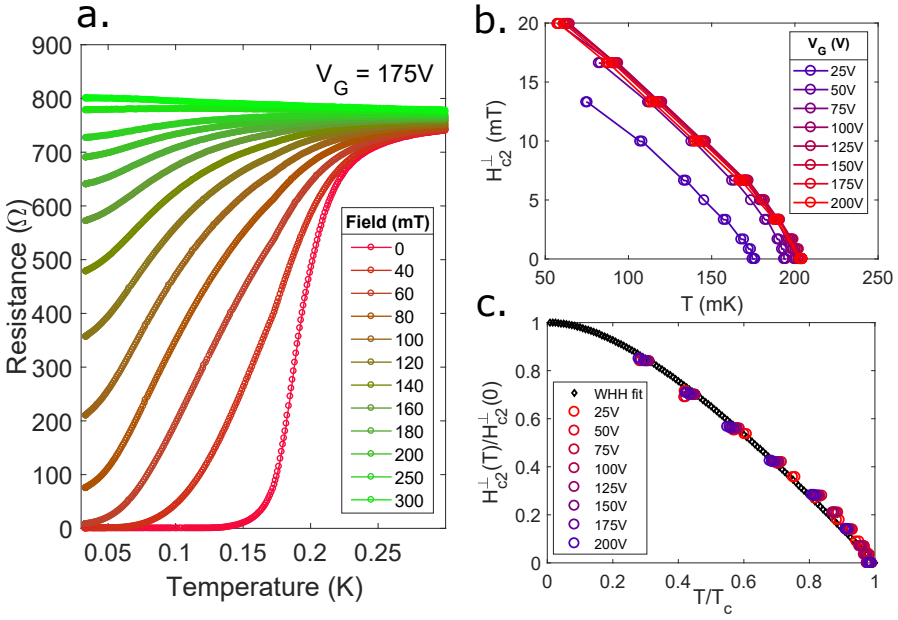

Figure 5.4: **Gate voltage dependence of the DC characteristic of a $AlO_x/SrTiO_3$ 2DEG under a perpendicular magnetic field.** **a.** Resistance vs. temperature for various magnetic field at $V_G = 175\ V$. **b.** Extracted $H_{c2}(T)$ curve. **c.** Fit with a single band WHH model of the normalized critical field $H_{c2}(T)/H_{c2}(0)$ described section 3.4.1.

5.1.5 Discussion

2DEGs fabricated by evaporation of Aluminium have proven to be a good alternative to the more complex pulsed laser growth of $LaAlO_3$. Their transport properties are similar to that of LAO/STO interfaces : gate tunable resistivity and carrier density, gate-driven metal-to-superconductor transition, single gap superconductivity seen from critical field. Noticeably, we could not achieve a clear Hall effect measurement on this sample, likely due to the contribution of the AlO_x layer which was maybe not fully oxidized.

5.2 $AlO_x/KTaO_3(111)$

5.2.1 History

Potassium-Tantalum oxide ($KTaO_3$) has been seen as a potential alternative to $SrTiO_3$ to host interfacial 2DEGs [141]. Both material are bulk-insulating transition metal perovskite crystals who can become semi-conducting or metallic upon doping. Just like STO, KTO is also an incipient ferroelectric/quantum paraelectric, with a large dielectric constant at low temperature. However, superconductivity was not evidenced in doped KTO bulk down to 10mK while it was known since 1967 that doped STO can be superconducting. There are numerous differences between the two materials as well : KTO has a dielectric constant $\simeq$ 4 times lower than STO at low temperature, STO undergoes a cubic to tetragonal transition at $\simeq$ 105 K while KTO remains cubic down to the lowest temperatures, and conduction in STO is insured by the 3d orbitals of the Titanium atoms while the Tantalum atoms in doped KTO has 5d character. Since Ta is much heavier than Ti, spin-orbit effects are also expected to be more intense in KTO. The interest for potential superconductivity in KTO started again in 2011 after that Ueno and collaborators discovered a superconducting 2DEG at the surface of KTO(100) doped with a ionic liquid technique. However, the critical temperature was very low ($\simeq$ 47 mK) [142] and the results have not been reproduced since. There have been successful attempts to generate a 2DEG at the $LaTiO_3/KTaO_3$ and $LaAlO_3/SrTiO_3$ interfaces but superconductivity has never been observed [143] [144].

2021 has been the year of superconductivity in $KTaO_3$ 2DEGs: in January, Z. Chen and collaborators reported a superconducting 2DEG at the $LaAlO_3/KTaO_3(110)$ interface with $T_c \simeq 0.9K$ [145]. In February, C. Liu and collaborators reported superconducting 2DEGs at $LaAlO_3/KTaO_3(111)$ interface with a T_c up to 1.47 K and superconducting 2DEGs at $EuO/KTaO_3(111)$ interface with T_c up to 2.2K, roughly an order of magnitude higher than the critical temperature of the conventional LAO/STO interface [83]. This is quite surprising since, in contrast with the LAO/STO interface for which superconductivity is most likely inherited from the intrinsic superconductivity in the bulk, doped bulk KTO can not be turned into a superconductor. Finally, in May 2021, Z. Chen et al. showed that the T_c at $LaAlO_3/KTaO_3(111)$ interface is gate-tunable, and that the key parameter being changed seems to be the mobility, and not so much the carrier density [146].

Bruno and collaborators [147] have calculated the band structure of the KTO(111) interface using DFT where the only free parameter, the potential at the interface, was found by matching their ARPES experiment with the model. They showed that KTO(111) and STO(111) interfaces both have t_{2g} orbitals responsible for conduction lower in energy than the e_g ones. However, due to the much larger atomic spin-orbit interacation in KTO, only the J=3/2 band contributes to conduction, as the J=1/2 band sits 400 meV higher. The resulting Fermi surface and band structure shows a star-like shape (panels **a.** **e.** in figure 5.5), with a spin texture detailed in figure 5.6 panels **a.** **b.** [147]. Figures 5.5**b.** and **f.** show the band dispersion along ΓM and ΓK and figures **c.** and **g.** show their respective energy distribution. The Fermi energy is about 130 meV and the two Fermi vectors estimated from figure 5.5 b) and e) are 0.14 and 0.26 $\mathring{A}^{-1}$ for the light and heavy band respectively. Along the ΓM direction, there are two types of bands, one light band with a predominant d_{xy} character, and one heavy band with an apparent equal mixture of d_{xz} and d_{yz} orbitals (panels **b.** and **d.**). In the other high symmetry direction ΓK, all bands have a similar behavior (panels **f.** and **h.**). On the right panel, we see that the Rashba spin splitting is stronger in $KTaO_3$ than $SrTiO_3$ but still hard to resolve (the splitting is below ARPES resolution).

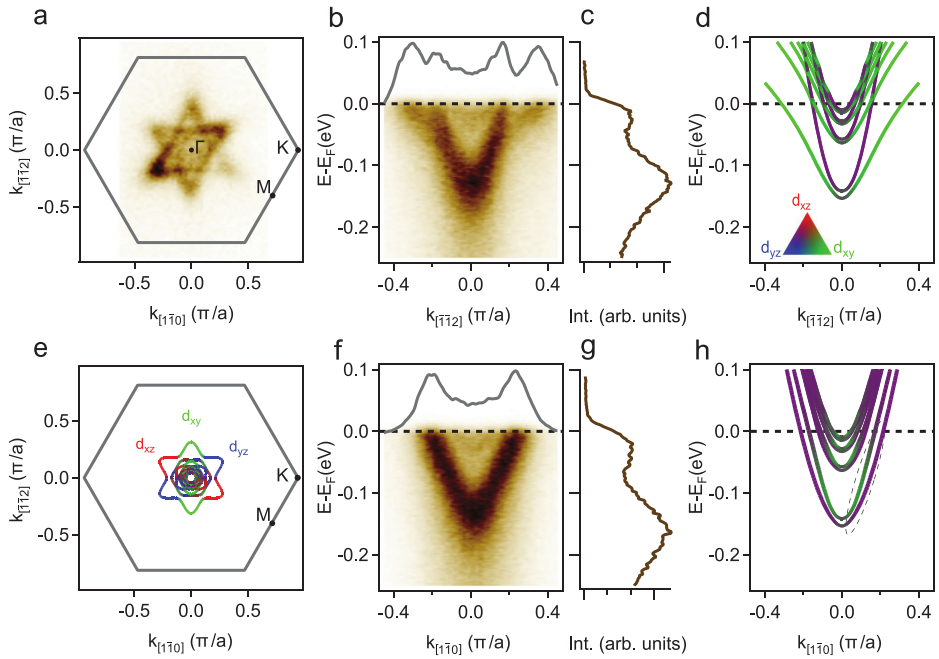

Figure 5.5: **ARPES measurement of KTO(111) surface a.** Fermi surface measured at 108 eV. **b. f.** Band dispersion along ΓM and ΓK respectively. **c. g.** Energy distribution along ΓM and ΓK respectively. Two subbands can be seen. **e.** Calculated Fermi surface of the 2DEG with orbital character of the band shown in color. **d.** Band energy dispersion along the ΓM direction. **h.** Band energy dispersion along the ΓK direction. Color code indicate the orbital character of the band as shown in the inset of panel **d.** From [147].

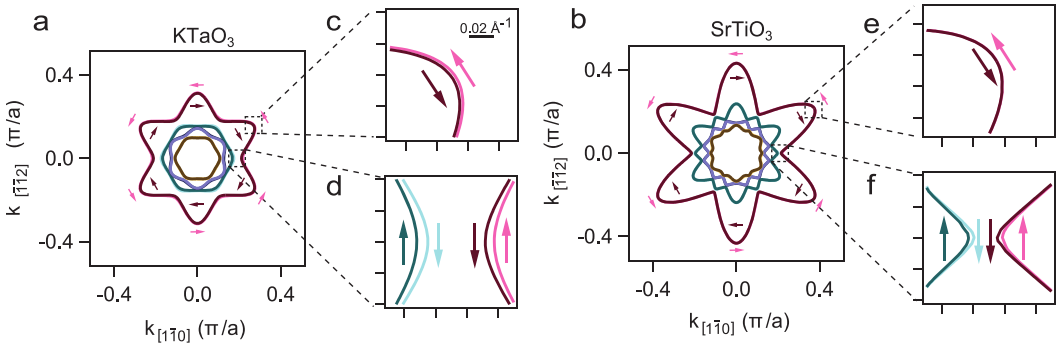

Figure 5.6: **Comparison of spin texture of the Fermi surface a.** in $KTaO_3$ and **b.** in $SrTiO_3$. The Rashba spin splitting is stronger in $KTaO_3$, shown at points of interest in **c. d.** than in $SrTiO_3$ **e. f.**. From [147].

5.2.2 Sample growth

During this thesis, we studied AlO_x/KTO(111) 2DEG generated by the deposition of a thin layer of Al as already described in section 5.1.2 for AlO_x/STO samples. The formation of the 2DEG thus relies on a pure redox mechanism. Samples were prepared by the Oxitronics team led by M. Bibes

in the CNRS-Thales lab following the recipe described below:

Prior to deposition, $KTaO_3(111)$ substrates from MTI corporation were annealed at 600 °C for 1 hour in vacuum. Then, the thin Al layer was deposited in a dc magnetron sputtering system (PLASSYS MP450S) under a base pressure lower than $5 \cdot 10^{-8}$ mbar. During Al deposition, the Ar partial pressure and the dc power were kept fixed at $5 \cdot 10^{-4}$ mbar and 10 W, respectively. The deposition rate for Al was 0.66 $\AA$/s until the thickness reaches 1.8 nm. The sample for which the superfluid stiffness has been analyzed has been grown in two steps: first 0.8 nm of Al under 500°C and the following 1.1 nm at room temperature.

The sample were then glued with silver paste onto a back gate, contacted with Al wire bounds and mounted on the mixing chamber of the dilution refrigerator. Table 5.1 presents the characteristics of KTO(111) samples whose results are discussed in this section.

Sample	K1806	K1808	PLAS1875
Measurements	DC (Hall effect, Superconducting phase diagram, Critical field H_{c2})	DC (Hall effect, resistance Critical field H_{c2})	DC (Hall effect, resistivity) RF measurement of J_s
Al thickness and deposition temperature	1.8 nm @ 600°C	1.8 nm @ 500°C	0.8 + 1.1 nm @500°C (second step at RT)

Table 5.1: Description of $AlO_x/KTaO_3$ samples presented in this chapter.

5.2.3 Resistance measurements

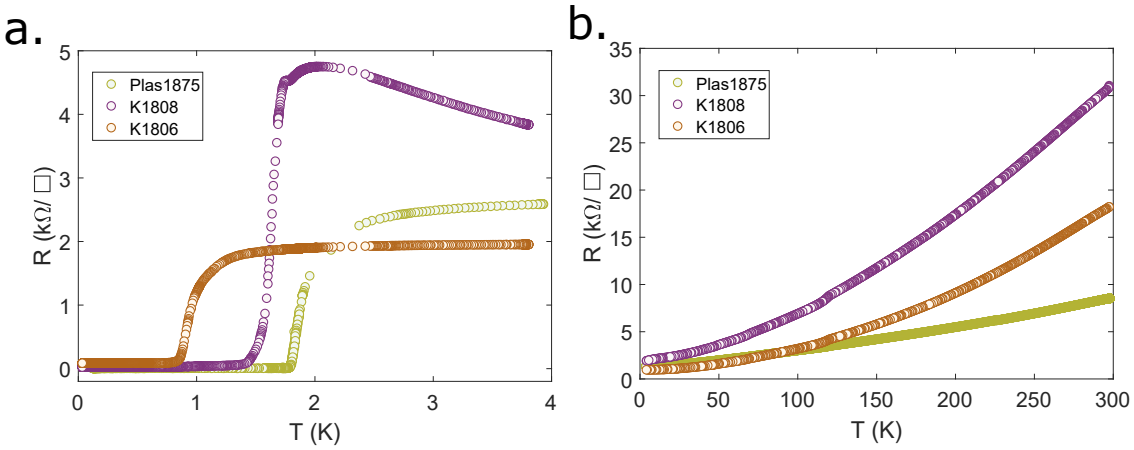

Figure 5.7: **Superconducting $AlO_x/KTaO_3(111)$ 2DEGs. a.** Sheet resistance vs. temperature for various superconducting $AlO_x/KTaO_3(111)$ samples. **b.** Zoom in the low temperature region to see the superconducting transition.

Figure 5.7**b.** shows the sheet resistance vs. temperature curves of all the AlO_x/KTO(111) samples discussed in this thesis down to 4 K. Panel **a.** shows that all sample are superconducting with critical temperature ranging from 700mK to 2K. The superconducting transition is not sharp and extends

to hundreds of mK. This is characteristic of disordered 2D superconductor, where inhomogeneities smooth the transition.

The critical temperature of the AlO_x/KTO(111) 2DEGs measured in this thesis T_c has been extracted and plotted as a function of the carrier density n. Our results reproduce the trend observed by Liu et al. ([83]) : T_c increases linearly with n in a certain doping range, and confirm that aluminium sputtering, which is an easier method than the molecular beam epitaxy deposition of EuO, is efficient at creating superconducting sample with similar T_c.

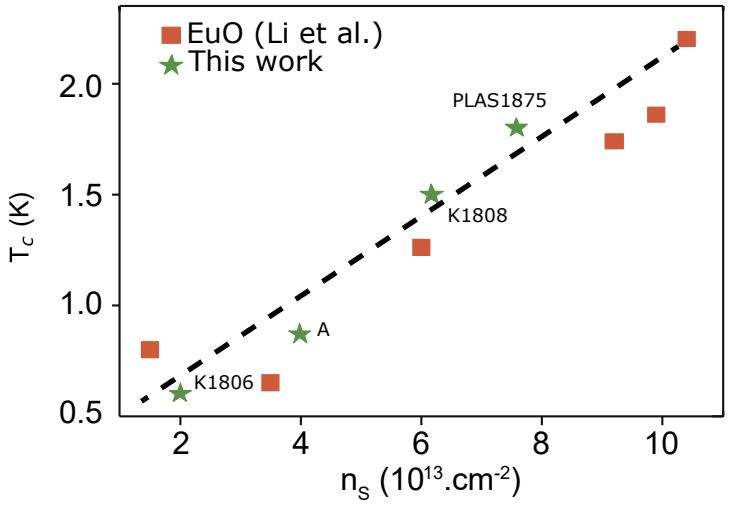

Figure 5.8: **Superconducting critical temperature versus carrier density for AlO_x/KTO(111).** The green star represent previous work by Liu et al. [83]. Sample A's superconducting transition or carrier density measurements are not presented in this manuscript.

5.2.4 Gate voltage dependence of Hall effect and carrier density

The electric field effect strength at a given gate voltage in a plane capacitor model is given by the ratio of the surface area to the distance between the two conducting planes. As $KTaO_3$ has a dielectric constant lower than $SrTiO_3$ ($\simeq$ 5000 compared to $\simeq$ 23000 for STO), it is not possible to achieve a similar carrier density modulation than in $SrTiO_3$ for the same geometry. To compensate this effect, the thickness of the KTO substrate of sample K1806 was reduced to 150 microns (instead of 500) by polishing, roughly compensating the difference in ϵ_r.

To assess the carrier density of the 2DEG, we performed a standard Hall effect measurement in a Van der Pauw geometry (see section 2.2.3), for different gate voltages (figure 5.9). We notice that the Hall resistance remains roughly linear, and its slope continuously decreases with the gate voltage, meaning that the carrier density continuously increases without apparent contribution of a second population of carriers. The situation is different from that observed in STO-based 2DEGs for which, above some doping threshold, non-linearity due to multi band transport is systematically observed. Although we know from band calculation and ARPES measurement that several bands are filled in KTO(111) interfaces, it is not possible to separate their different contributions in the Hall effect. A maximum of R_H = 80 to 220 Ω at $B = 13\,T$ correspond to a carrier density of $n = 3.5$ to $10 \times 10^{13} cm^{-2}$. Note that there is a strong uncertainty for the lowest gate voltage values due to very high contact resistance and noisy signal.

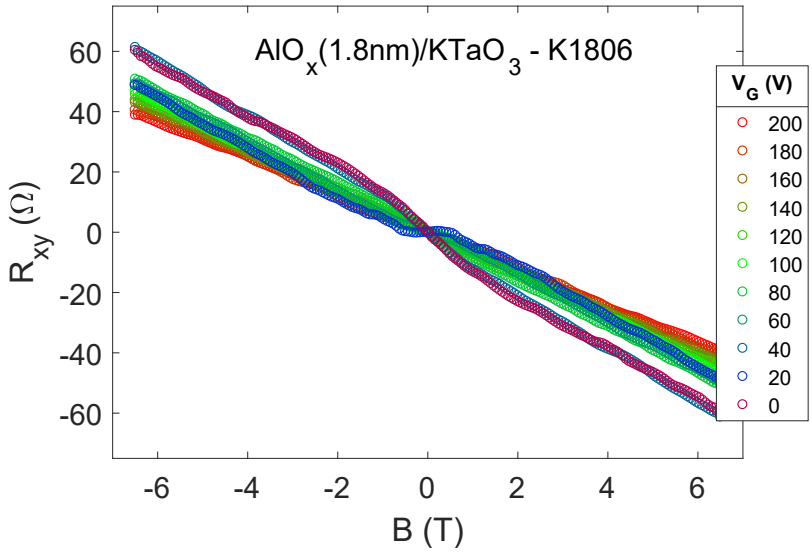

Figure 5.9: **Gate voltage evolution of the carrier density in a superconducting $AlO_x/KTaO_3$ sample (K1806)**. This 2DEG was obtained on a thinner substrate (150 micron thick instead 500 microns) to increase the electric field effect.

The gate dependence of the 2DEG carrier density extracted from the Hall effect is shown in figure 5.10. In contrast with previous measurements in superconducting 2DEGs at $KTaO_3$(111) interface, the doping in carrier here is stronger ($\delta n \simeq \pm 50\%$ vs. $\delta n \simeq \pm 9\%$ in [146]) and comparable to that reported at LAO/STO interfaces for thicker substrates.

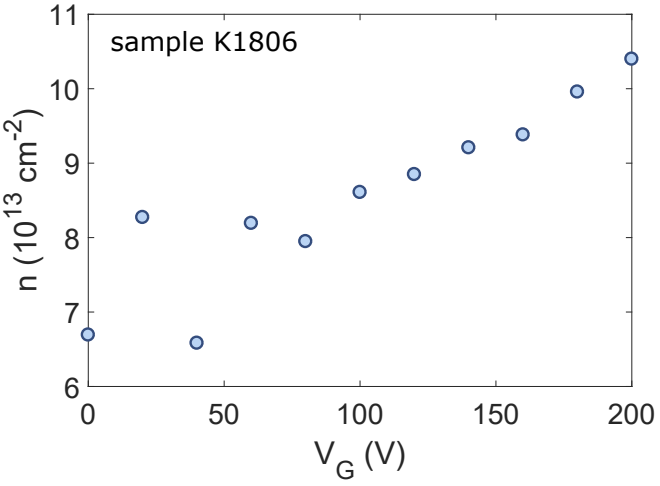

Figure 5.10: **Gate evolution of the carrier density in a superconducting $AlO_x/KTaO_3$ sample from Hall effect measurement.** The substrate has been polished down to 150 microns of thickness to enhance field effect.

5.3 Critical magnetic field H_{c2} measurements

We have performed upper critical magnetic field measurements in the dilution fridge in two AlO_x(1.8nm)/$KTaO_3$(111) 2DEGs (named K1806 and K1808). As for other critical field measurements presented in the manuscript, we have measured R(T) for various fields between 0 mT (in the superconducting state) and 1 T, a field much higher than H_{c2} (making the 2DEG normal/insulating). The measurement are presented figure 5.11.

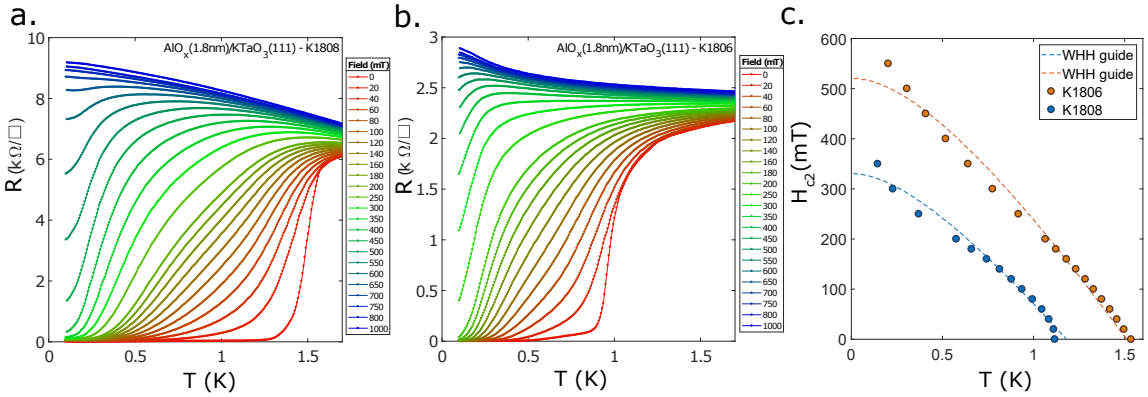

Figure 5.11: **Critical magnetic field measurements in a 2DEG at AlO_x/$KTaO_3$(111) interfaces.** **a.** Resistance as a function of temperature for different magnetic fields in sample K1808. **b.** Resistance as a function of temperature for different magnetic fields in sample K1806. **c.** Upper critical field H_{c2} as a function of temperature, from data in panels **a.** and **b.**

Resistivity as a function of temperature for different magnetic fields for two AlO_x/KTO(111) samples are shown in figure 5.11 panel **a.** for sample K1808 and panel **b.** for sample K1806. The temperature dependent critical magnetic fields for both samples, defined as the value of the field for which the resistance reverse 80% of the normal state value (at 1.8 K) are shown in figure 5.11**c.** A Werthamer-Helfand-Hohenberg (WHH) single band $H_{c2}(T)$ curve is added as a guide for the eye.

We see that the upper critical magnetic field H_{c2} of both samples are around 500 and 600 mT from extrapolation to $T = 0$. This corresponds to a zero temperature coherence length of the Cooper pair of $\xi \approx 23$ to 26 nm, which is similar to what has been found in other superconducting 2DEGs at $KTaO_3$ interface [145] [83] but lower than in LAO/STO(111) 2DEG as expected since the T_c is higher. Knowing the sheet resistance R_s and the carrier density n and assuming a single, parabolic, free electron model, we can compute a rough estimate of the mean free path.

$$l_{MFP} = \frac{h}{e^2 k_F R_s} = \frac{h}{e^2 (2\pi n)^{\frac{1}{2}} R_s} \approx 3.5nm$$

We verify that the 2DEG is indeed in the dirty limit since $\xi / l_{MFP} \approx 10 \gg 1$

5.3.1 Superconducting phase diagram

Figure 5.12 presents the results on gate tunable superconductivity. In panel **a.** we show the resistance as a function of temperature for various gate voltages between -40 and $200V$. In figure 5.12**b.** we show the resistivity normalized by its normal state value, as a function of temperature and carrier

density, from data in panel **a.** It seems that the T_c is constant when superconductivity is present. This can be explained as a result of 2D superconductivity (see section 1.1.3): in the simplest model the T_c only depends on the density of state, and not on the filling of the band. Panel **c.** shows the resistivity at 0.9 K used to normalize data in panel **b.**

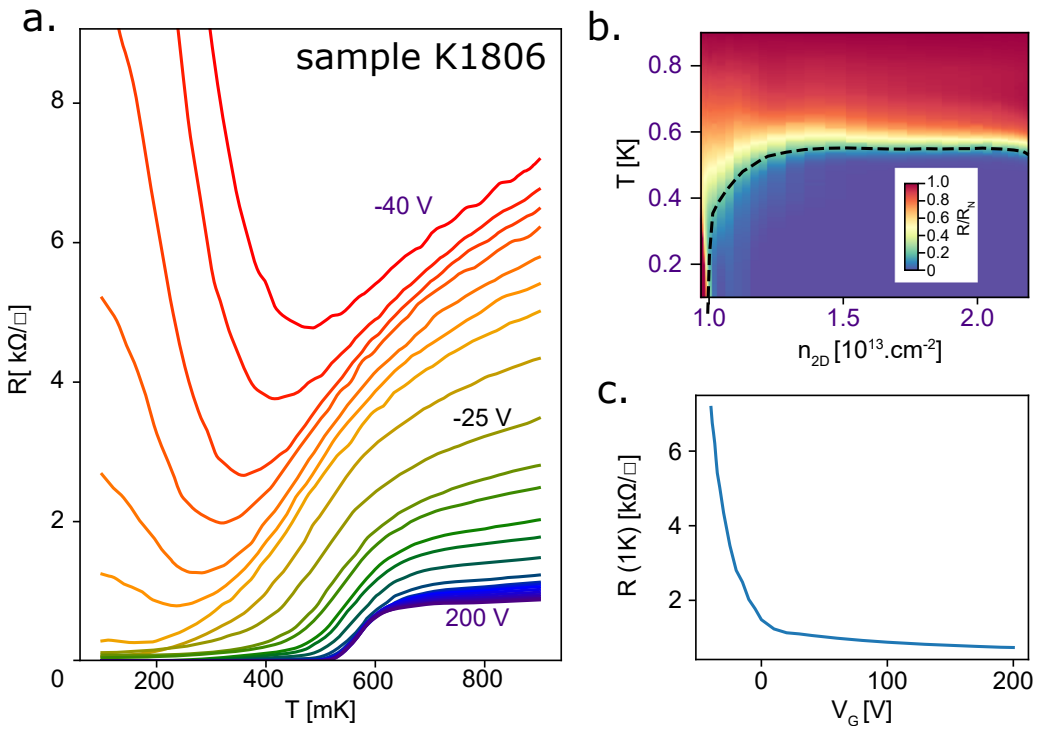

Figure 5.12: **Electric field and superconducting phase diagram in a KTO(111) 2DEG. a.** Sheet resistance as a function of temperature for various gate voltages in K1806. **b.** Corresponding normalized carrier density-temperature phase diagram (density is infered from Hall effect measurement, not shown). **c.** Sheet resistance at 1 K used to normalize data in **c.**

In figure 5.12**a.**, we see that for $V_G \geq -25\ V$, a true zero resistance superconducting state is reached while for $V_G \leq -25\ V$ an upturn in the resistance at very low temperature after the onset of a superconducting transition. This is characteristic of 2D disordered superconductors, in which superconductivity only exists locally in isolated islands surrounded by an insulating medium that precludes percolation. The upturn in resistance is interpreted as the opening of a gap within the excitation spectrum which prevents the emergence of long range superconductivity.

5.3.2 Microwave measurement of superfluid stiffness

In this section, we report the evolution of the superfluid stiffness as a function of temperature extracted from a resonant microwave measurement (section 2.3.2) for the PLAS1875 sample (AlO_x(1.8 nm)/$KTaO_3$). The same calibration procedure already used for LAO/STO samples and detailed in appendix A was applied to extract J_s from the shift in resonance frequency. Using a bias-tee, it was possible to simultaneously measure the dc resistance as a function of temperature. Our experimental results are shown in figure 5.13, where the dc resistivity is represented in orange diamond symbols and the superfluid stiffness (expressed in Kelvin unit) extracted from the resonant microwave measurement

is shown in blue circles.

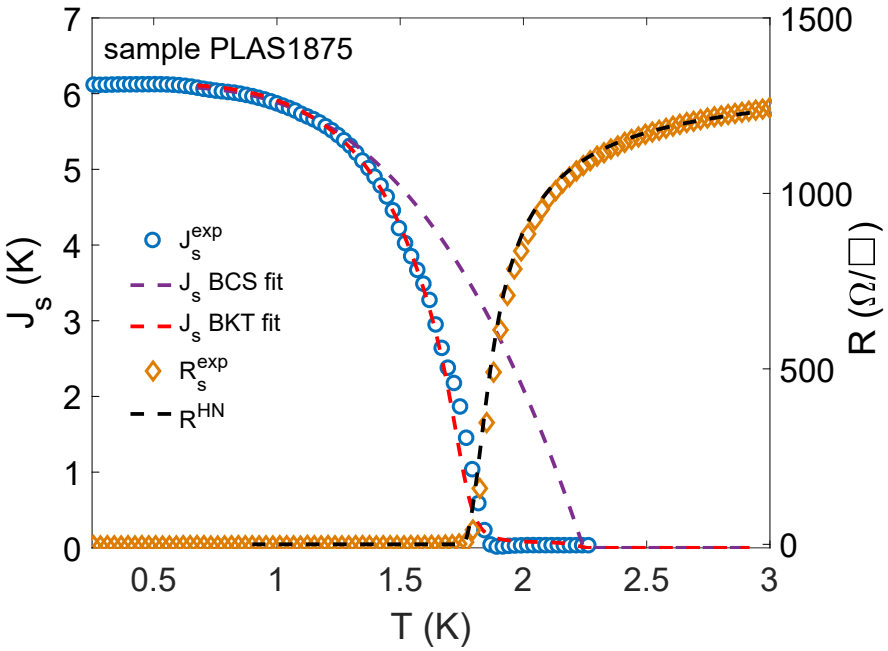

Figure 5.13: **Superfluid stiffness J_s^{exp} extracted from the resonance frequency as a function of the temperature.** The dashed purple line shows an attempt to fit the experimental data within a BCS model (J_s^{BCS}) in the strong coupling regime ($\Delta = 2.3 k_B T_c$), which provides a mean field critical temperature T_c^0 = 2.3 K. A better agreement is obtained by using a BKT model (J_s^{BKT}). On the right axis, the figure also shows the sheet resistance curve (R^{exp}) fitted with the Halperin and Nelson formula (R^{HN}).

The shift in the resonance frequency measured for the KTO sample PLAS1875 of almost 1 GHz, is much larger than what was observed for LAO/STO samples (a few 100 MHz). This translates into a larger superfluid stiffness J_s. Indeed, J_s reaches a maximum value of 6 K at zero temperature, which is indeed higher than 0.3 to 4 K in LAO/STO(110) that we showed in figure 3.21 or the 0.3 to 3 K shown in figure 3.47 for the LAO/STO(111) sample. The experimental stiffness can not be fitted by a single band BCS model, represented in purple dotted line in figure 5.13. This fit assumes a strong coupling $\Delta = 2.3 k_B T_c$, which is different from the weak coupling limit used for LAO/STO-2DEGs studied in chapter 3 ($\Delta = 1.76 k_B T_c$), from the fit of the low temperature data. Even in this strong coupling limit, the predicted T_c^0 is larger than the experimental one. Instead, our collaborator L. Benfatto from Sapienza University in Rome found a much better agreement with a BKT model including a low vortex diffusivity and finite frequency effects (red dotted line in figure 5.13). The resistance is consistently well fitted by a Halperin-Nelson model. In particular, finite frequency effects allows to reproduce the tail in J_s which extends to the non-zero resistance state. It is due to the fact that mean-field smooths all scales but probing at finite frequency ω defines a characteristic length via the vortex diffusivity constant. The three main ingredients for the fitting procedure, renormalization group flow equation for J_s, finite frequency effect and the effect of spatial inhomogeneities are discussed below.

BKT Renormalization Group Equations We want to account for the vortex excitation emerging from low temperature phase fluctuations, evidenced by Berezinsky, Kosterlitz and Thouless in a 2D XY model [**Kosterlitz1973**]. Considering a vortex with core energy μ and a fugacity $g = 2\pi e^{-\mu/(k_B T)}$, the BKT renormalization group equations describing the rescaled stiffness $K = \pi J_s / k_B T$ with the system scale l are :

$$\frac{dK}{dl} = -K^2 g^2 \tag{5.1}$$

$$\frac{dg}{dl} = (2 - K)g \tag{5.2}$$

where $l = \ln a/\xi_0$ is the RG lattice spacing with respect to the coherence length ξ_0 controlling the vortex size and used as a short-scale cut-off.

At low scale $l = 0$, $J(l = 0) = J^{BCS}$ and at large scale, when $l \longrightarrow \infty$, $J_s = (k_B T/\pi)K(l \longrightarrow \infty)$. The fit allows to find the vortex core energy μ, the vortex fugacity g and the vortex typical scale ξ_0.

Finite frequency effect When we probe the sample at finite frequency ω, even if $\hbar\omega < \Delta$ (where Δ is the superconducting gap), such that the excitation does not break Cooper pair, it can have a sizeable effect. The idea is that the mean field renormalization group smooths all scales, but probing at a finite frequency introduces a characteristic lengthscale $r(\omega) = \sqrt{\frac{14 D_v}{\omega}}$ where D_v is the vortex diffusion coefficient. Formally, a dynamical screening of the vortices is introduced via the frequency-dependant dielectric function $\epsilon(\omega)$ which enters in the complex conductivity of the film as $\sigma(\omega) = -\frac{4 J^{BCS} e^2}{i\omega\hbar^2 \epsilon(\omega)}$. At zero frequency, $\epsilon(\omega)$ is real and equals to $\epsilon_1(\omega) = K(0)/K(l \longrightarrow \infty) = J^{BCS}/J_s$ so we recover the static result. At finite frequency, $\epsilon(\omega)$ develop an imaginary part $\epsilon_2(\omega)$ due to vortex motion and can be expressed in first approximation [148] as $\epsilon_2 \approx (r(\omega)/\xi)^2$, where ξ is the vortex correlation length. The effect of ϵ_2 is to induce a small tail above T_{BKT} at finite frequency, given by $J_s = \hbar^2 \omega \sigma_2(\omega)/(4e^2)$, as we observe in figure 5.13. Following the same procedure as in [149], $\epsilon(\omega)$ has been computed and a vortex diffusion constant of $D_v = 10^{10} nm^2/s$ is found, much lower than the $10^{13} nm^2/s$ found in NbN thin films in ref [150].

Spatial inhomogeneity The Hallmark of BKT physics is the universal jump of superfluid stiffness at T_{BKT} with the ratio $J_s(T_{BKT})/T_{BKT} = 2/\pi$, which has indeed been observed in superfluid He films [151]. However, the suppression of the superconductivity near T_c itself close to T_{BKT} leads to an inhomogenous background of weakly superconducting puddles being turned metallic by the current, smearing out any clean superfluid jump. The suppression of superfluid jump at the superconducting transition due to inhomogeneity have indeed been observed in LAO/STO [149] and ultrathin NbN films [152]. While this signature has been observed via indirect probes such as the exponents of the I-V curve [39] [38], the few measurements of superfluid stiffness at STO-2DEG doesn't show a BKT jump [34] [75]. In the 2DEG studied here also there is no superfluid jump because of the smoothing induced by inhomogeneities.

5.3.3 Discussion

KTO(111)-based 2DEGs share many properties with their more studied counterpart STO-based 2DEGs. They both host a 2DEG which can become superconducting under the right conditions, they both

have a strong spin orbit coupling and their carrier density can be tuned by applying a gate voltage due to both substrates being quantum paraelectric at low temperature and thus displaying a large dielectric constant. Yet, upon closer investigation, several important differences can be found to help us understand the fundamentals of these multifonctional oxides.

First, while STO can host a superconducting 2DEG in each main crystallographic orientations (namely (001), (110) and (111)), superconductivity in KTO 2DEGs is only present in the (110) and (111) orientations, if we neglect the single report of superconductivity at very low temperature in KTO(001) induced by ionic liquid gating [142]. In this section, we have presented the superconducting R(T) curves of an AlO_x/STO(001) sample (figure 5.3) and of several samples of AlO_x/KTO(111) (figure 5.7). The critical temperature of KTO-based 2DEGs is also an order of magnitude higher than that of STO-based 2DEGs, making it a more robust system to develop mesoscopic devices. By polishing the substrate to increase its ability to be polarized via a back gate voltage, it is possible to generate a carrier density modulation comparable to that observed for LAO/STO interfaces, i.e. $\delta n \simeq \pm 50\%$ (figure 5.10) and induce a superconducting-to-metal transition (figure 5.12) when the 2DEG is depleted. The reentrant behavior of the resistivity curves at low doping suggests that the superconductivity in this regime is made of superconducting islands whose ability to percolate depends on the local homogeneity background. Contrary to STO(111) 2DEGs, we have not observed multiband physics neither in the Hall effect measurement (figure 5.9), nor the critical magnetic field measurements. Transport properties suggest that the gas is in a dirty limit which is expected for low dimensional materials.

Finally, we have successfully applied the microwave measurement of superfluid stiffness to a KTO(111) 2DEG. The measurement was somewhat challenging because the shift in resonance frequency was much higher than for STO 2DEGs (1 GHz). Nevertheless our set-up allowed us to capture the first report of J_s(T) in a KTO(111)-2DEG presented in figure 5.13. The first striking characteristic of J_s is that it strongly differs from the BCS prediction, even when assuming a non-weak coupling regime. Our collaborator L. Benfatto successfully managed to fit the $J_s(T)$ curve using a BKT model, with finite frequency effect and spatial inhomogeneities. The absence of jump in the stiffness and a small tail above T_{BKT} is explained by the two latter effects.

KTO-2DEGs are emerging as superconducting alter-ego of the widely studied STO-based 2DEGs in the last few years. Their similar carrier densities and larger SOC make them good candidates for spintronics applications. The T_c of KTO(111) 2DEGs is roughly 10 times larger than in STO 2DEGs and a fivefold enhancement of the Rashba coupling constant has been demonstrated compared to STO [153]. KTO 2DEGs thus appear largely superior to STO 2DEGs and may enable the realization of concepts formulated for STO but non achievable due to the weakness of the relevant energies.

Conclusion

This thesis focused on the transport properties of superconducting 2DEGs at oxide heterointerfaces such as LAO/STO(110), LAO/STO(111) or AlO_x/KTO(111). After introducing the reader to 2D superconductivity and bulk $SrTiO_3$ properties, we have reviewed the behavior of the conventional LAO/STO(001) which is used to compare our results with. We have discussed the band structure of the LAO/STO(111) and Poisson-Schrödinger simulations of the LAO/STO(110) interface, which have guided the interpretation of our results.

First, we have characterized two LAO/STO(110) samples. The gate voltage-temperature phase diagram of the resistance is different from that of the LAO/STO(001) interface: depleting the gas does not suppress the T_c, suggesting that the lowest energy band is superconducting. In addition, doping the gas with a positive gate voltage suppresses the T_c which is unexpected in a BCS picture. In this regime, the Hall effect measurements showed multiband physics and we have been able to extract the transport properties of the two different conducting bands. We have defined two regions : the underdoped regime (UD) corresponding to a depleted gas where only the lower d_{xy} band contributes and the T_c is constant, and an overdoped regime (OD) where the higher $d_{xz,yz}$ bands are also populated and the T_c decreases. Next, critical magnetic field H_{c2} measurements were presented and found to be consistent with a multicondensate model: while in the UD regime H_{c2} is fitted by a single band model (WHH), in the OD regime it is fitted by a two-condensate model with interband coupling. The validity of this model is strenghten by the comparison of the diffusivity coefficient from the fits with those expected from a Drude model. Resonant microwave measurements of the superfluid stiffness J_s in the range [100 MHz - 1 GHz] also demonstrated the presence of two-condensate superconductivity. In the UD regime, the J_s versus temperature curves follow a single gap BCS model, but the OD requires a multi-condensate model with interband coupling. The superconducting intraband ($\lambda_{11,22}$) and interband ($\lambda_{12,21}$) coupling constants from the two independent methods are almost identical. Finally, we discussed the origin of the decrease in T_c, which we explained by the formation of a s$\pm$-wave superconducting state with repulsive coupling between the two condensates for which interband diffusion is expected to strongly reduce the T_c. These results demonstrate a continuous and reversible single to two-condensate superconducting transition driven by gate voltage, a phenomena that could be exploited to generate exotic superconducting state in STO-based 2DEG devices.

We have then described the measurement of two LAO/STO(111) samples. The gate voltage-temperature phase diagram of the resistance is similar to that of the LAO/STO(110) interface, and so is the Hall effect. We thus also define an underdoped and overdoped regime, with a transition between the two around $V_G = 0\ V$. The critical magnetic field however did not show any sign of multicondensate superconductivity and its temperature dependence is consistent with that of a single band BCS superconductor for both the UD and the OD regimes. The superfluid stiffness measurements showed some kind of deviation from a BCS model at high doping, but this deviation could not be fitted with the two condensate model used for the LAO/STO(110) interface. We then compared the experimental stiffness to that expected from Mattis-Bardeen theory and have shown that the two coincide, confirming the dirty and 2D superconductivity nature of the system. To address whether the superconductivity in the OD regime in LAO/STO(111) is single or two gaps, one could set-up a tunneling spectroscopy experiment to probe the possible presence of a second gap, a method which have been successfully applied in LAO/STO(001) 2DEG but unfortunately without the necessary resolution.

In the next chapter, we studied in plane anisotropic magnetoresistance (AMR) for the LAO/STO(110) and LAO/STO(111) 2DEGs. When a current is applied, the Rashba effect at the interface gener-

ates a spin imbalance through the Edelstein effect. This spin imbalance generates non-reciprocal AMR from which two quantities are defined : the quadratic magnetoresistance (whose amplitude is quadratic in field) and the bilinear magnetoresistance (whose amplitude is linear in field and linear in current density). These quantities, when derived in the framework of a single parabolic band, are expressed in term of fundamental properties of the system, such as its Fermi level, elastic scattering time or more importantly, its Rashba coupling constant. The systematic analysis of the BMR and the QMR for various magnetic fields, gate voltages and current shows that they are indeed linear in current and field, and quadratic in field respectively. From the QMR, we extracted a scattering time which is found to be comparable to that predicted by a Drude model. From the ratio of the BMR and the QMR, we extracted a Rashba coupling constant as a function of gate voltage. We thus confirmed the existence of a tunable Rashba effect at the LAO/STO(111) interface. Finally, the modulation of the QMR with angle in LAO/STO(110) interface shows a $\pi/2$ shift at the Lifschitz transition. Meanwhile the modulation of the QMR in LAO/STO(111) interface shows a butterfly structure which seems to be switched off by the Zeeman effect. Ongoing calculations in the Halle University and MPI Halle should gives us a clearer picture of how combination between the spin orbital band texture and the external magnetic field generates these behavior beyond the single parabolic band model considered in this manuscript. We foresee that the characterisation of the spin-orbit interaction *via* AMR measurement could become standard for testing spintronic devices and candidates for spintronic applications.

In the last chapter, we have discussed the results of 2DEGs made by aluminium evaporation directly at the surface of the substrates in the oxytronic group at the UMphy CNRS-Thales. We first demonstrated that the 2DEG obtained at the AlO_x/STO(001) interface has a comparable superconducting phase diagram to that at the LAO/STO(001) phase diagram, and the critical magnetic field analysis reveals a single gap superconductivity. Aluminium sputtering is thus seen as an easier method to create 2DEGs at oxide interfaces. We then turned to 2DEGs at $AlO_x/KTaO_3$(111) interface which have been recently found to be superconducting with a $T_c \approx 1-2\ K$. We demonstrated that electric field effect doping is possible, and upon depletion of the gaz we show a quasi-reentrant behavior: the resistance first decreases and then upturns upon further cooling. This behavior is characteristics of disordered superconducting thin films in which superconductivity only exists locally forming a network of isolated islands surrounded by an insulating medium that precludes percolation. Both the Hall effect and critical field measurements are consistent with a single band conductor and a single gap superconductor. Finally, the superfluid stiffness was extracted from a resonant microwave measurement. The data could not be fitted with a simple BCS model, even assuming a strong coupling ($\Delta = 2.3 k_B T_c$). Instead, we found a good agreement with a BKT model that includes finite frequency effects and inhomogeneities. We predict that KTO-based 2DEGs will replace STO-based 2DEG for most of the research, since its superconducting gap is much higher than that of STO, and its spin-orbit interaction is also higher. Demonstration of superconducting KTO-based 2DEG devices such as quantum point contacts have yet to be done and could reveal insightful information which could have some impacts for STO as well.

Appendix A

Calibration procedure for resonant microwave measurement of the superfluid stiffness

So far, we have considered the reflection coefficient Γ defined at the sample circuit level. However, in our set-up we have only access to the transmission between port 1 and 2 (S21), which includes the contribution of the different microwave elements involved in the set-up (attenuation of the lines, attenuators, gain of amplifier...). In addition, small impedance mismatches between these elements generate oscillations in the microwave response due to standing waves.

Our measurement of S21 is related to Γ *via* complex coefficients α, β, γ and δ described in figure A.2. The calibration procedure consists in using three known points to calculate the transmission and reflection coefficients relating S21 to Γ. We assume that direct retro-transmission from port 2 to port 1 is negligible. The three calibration points can be one in the normal state, one in the superconducting state and one in between, or three points in the normal state at three different gate voltages. In any case, it requires a visible frequency shift between points, and the largest span of frequency between the first and third point [34] [154].

In the model presented in figure A.2, a_i and b_i are the complex amplitude of the incoming and outgoing microwave signals. Coefficients α, β, δ and γ are transmissions (or reflection for δ) probabilities. Based on this model, and continuity conditions, we can establish the following formula:

$$\begin{cases} a_3 = \delta b_3 + \alpha a_1 \\ b_2 = \gamma a_1 + \beta b_3 (1 - \delta) \end{cases} \tag{A.1}$$

Our quantities of interest, S21 and Γ are defined as:

$$S_{21} = \frac{b_2}{a_1}, \qquad \Gamma = \frac{b_3}{a_3}, \tag{A.2}$$

We can establish

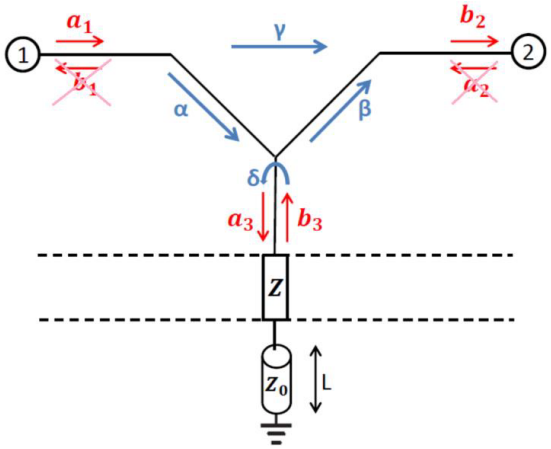

Figure A.1: Calibration circuit relating the sample circuit reflection coefficient Γ to the transmission between port 1 and 2 of the VNA. The reflection from port 2 to 1 is neglected as the VNA is perfectly matched. From [155].

$$\Gamma = \frac{1}{\delta - \frac{\alpha\beta(1-\delta)}{\gamma - S21}} \tag{A.3}$$

Equation A.3 shows that once we know the transmission coefficients α, β, γ and reflection coefficient δ we can deduce Γ from S21. To compute these coefficients, we follow the three points calibration procedure:

1) For a point above T_c, only the known SMD inductance contributes to the total inductance. We fit the S21 curve to find R_{TOT} and C_{STO}.

2) Once C_{STO} is known, we fit two other S21 curve, one inside the superconducting transition and one below (at temperature $T \simeq T_c$ and $T < T_c$) to find their respective R_{TOT} and L_{TOT}.

3) Having the RLC parameters for three different temperature points, we can compute the theoretical Γ from $\frac{Z_L(R,L,C)-Z_0}{Z_L(R,L,C)+Z_0}$

4) We then have to solve a system of three equations with three unknowns

$$\begin{cases} \gamma + \dfrac{\alpha\beta(1-\delta)\Gamma_1}{(1-\delta\Gamma_1)} - S21_1 = 0 \\ \gamma + \dfrac{\alpha\beta(1-\delta)\Gamma_2}{(1-\delta\Gamma_2)} - S21_2 = 0 \\ \gamma + \dfrac{\alpha\beta(1-\delta)\Gamma_3}{(1-\delta\Gamma_3)} - S21_3 = 0 \end{cases} \tag{A.4}$$

Where Γ_i and $S21_i$ (i=1,2,3) are the sample reflection (b_3/a_3) coefficients and the ones measured by the VNA (b_2/a_1) respectively for the three chosen temperature points.

Inverting the system give cumbersome expressions for α, β, γ and δ which are then used to compute Γ at each temperature points. Note that α and β are not independent as they always appear as a product, meaning we only need three equations instead of four if we consider the product $\alpha \times \beta$

as a single parameter.

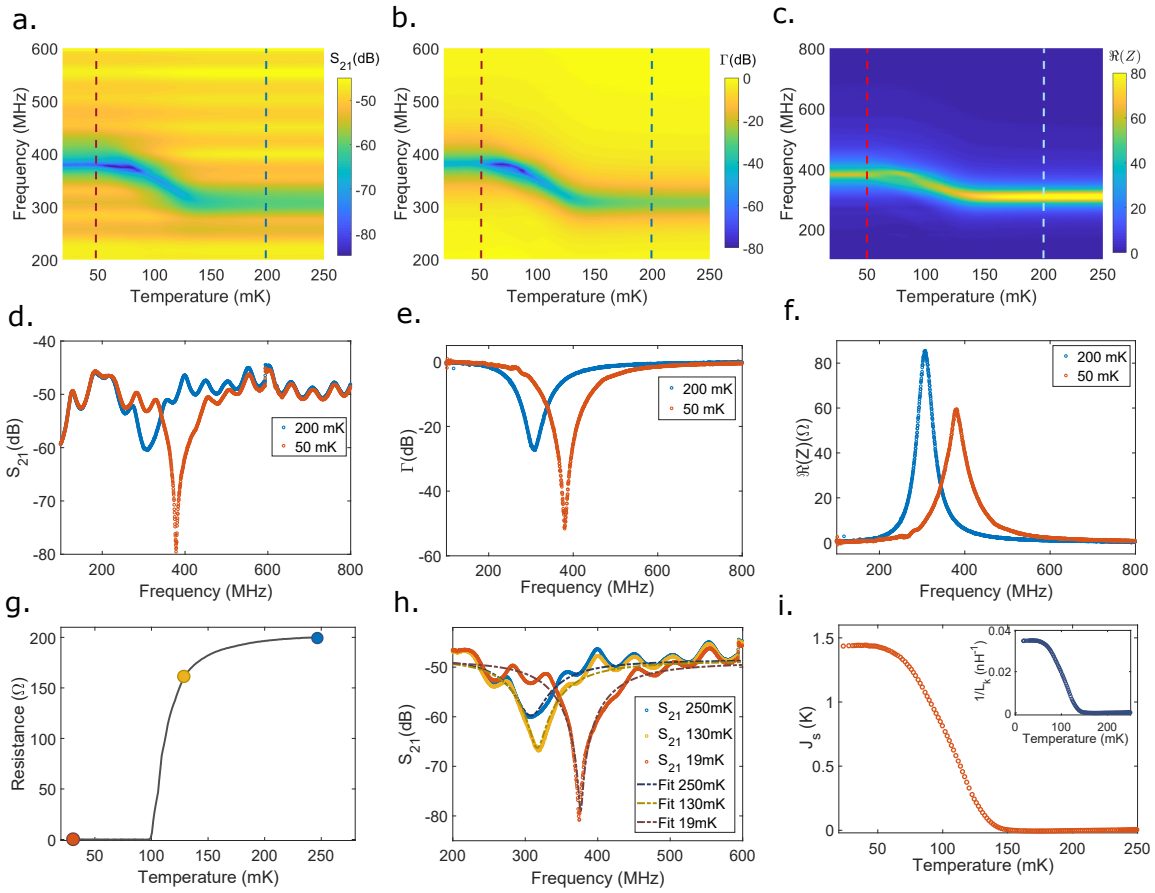

Figure A.2: **Example of calibration in LAO/STO(111) at Vg=+100V a.** Raw microwave signal $S_{21}(\omega)$ as a function of temperature. The temperature-independent standing wave of the setup are visible, and the relative depth of the signal is $\sim$ 20 dB at 19 mK. **b.** Calibrated microwave signal $\Gamma(\omega)$, it is $\sim$ 70 dB deep and the background standing wave has been removed by the calibration procedure. **c.** Temperature evolution of the real part of the complex impedance $Z(\omega)$ of the RLC circuit. **d.** Cut of S_{21} at 200 and 50 mK of figure **a.** **e.** Cut of Γ at 200 and 50 mK of figure **b.** **f.** Cut of $\Re(Z_L(\omega))$ at 200 and 50 mK. **g.** R(T) with the three calibration points used visible in color. **h.** Data used as calibration points with their fit visible. **i.** Extracted J_s(T) from the kinetic inductance eq. 2.5 shown as $1/L_k$ in inset, calculated from the temperature evolution of Z figure **c.**

A detailed example of the calibration procedure with actual data (discussed in more details in Chapter 3) is provided figure A.2. In panels **a.**, we see an example of raw S_{21} data, i.e S_{21} as a function of frequency for multiple temperatures, presented in a 2D color plot; and panel **d.** presents two cuts at two different temperatures. In panel **g.**, we show the temperature points used to calibrate the data, and their corresponding S_{21} are fitted in panel **h.** following the procedure described above, with the result of the fit in dashed lines. Once we have fitted the curve, we know the calibration coefficients which can be used to transform S_{21} (panel **a.**) into Γ (panel **b.**). Panel **e.** show the same temperature cuts for Γ as for $S21$ in panel **d.**, but after calibration. We see that the standing wave have been removed and the contrast is much better. Finally panels **c.** shows the real part of the circuit impedance Z_L (deduced from data in panel **b.**) in color plot as a function of temperature and frequency, from which L_k is extracted, and panel **f.** shows the same temperature cuts as in panels

d. and **e.** but for Z_L. Finally, panel **i.** shows the temperature dependence of the kinetic inductance of Cooper pairs, L_k.

Summary of superfluid stiffness measurement

In the previous section, we have described how a VNA is used to measure the reflection coefficients of the sample embedded in a RLC circuit (figure 2.10). A calibration, presented in figure A.2, requires the fitting of three transmission curves at three different temperatures. The measured reflection coefficient Γ is used to compute the complex impedance (equation 2.4) which relates directly to the kinetic inductance of the superconducting 2DEG Cooper pairs, inversely proportional to the superfluid stiffness J_s.

Bibliography

[1] Lev P. Gor'kov. "Superconducting transition temperature: Interacting Fermi gas and phonon mechanisms in the nonadiabatic regime". In: *Phys. Rev. B* 93 (5 2016), p. 054517. DOI: 10.1103/PhysRevB.93.054517.

[2] Lev P. Gor'kov. "Phonon mechanism in the most dilute superconductor n-type SrTiO3". In: *Proceedings of the National Academy of Sciences of the United States of America* 113.17 (2016), pp. 4646–4651. ISSN: 10916490. DOI: 10.1073/pnas.1604145113.

[3] C. A. Reynolds et al. "Superconductivity of isotopes of mercury [27]". In: *Physical Review* 78.4 (1950), p. 487. ISSN: 0031899X. DOI: 10.1103/PhysRev.78.487.

[4] A. Stucky et al. "Isotope effect in superconducting n-doped SrTiO 3". In: *Scientific Reports* 6.October (2016), pp. 1–9. ISSN: 20452322. DOI: 10.1038/srep37582. arXiv: 1610.10045.

[5] Jonathan M Edge et al. "Quantum Critical Origin of the Superconducting Dome in SrTiO 3". In: 247002.December (2015), pp. 1–5. DOI: 10.1103/PhysRevLett.115.247002.

[6] Michael Tinkham. *Introduction to superconductivity*. Courier Corporation, 2004.

[7] R. Kubo. "Statistical-Mechanical Theory of Irreversible Processes. I. General Theory and Simple Applications to Magnetic and Conduction Problems". In: *Journal of the Physical Society of Japan* 12 (1957), pp. 570–586.

[8] D. C. Mattis and J. Bardeen. "Theory of the anomalous skin effect in normal and superconducting metals". In: *Physical Review* 111.2 (1958), pp. 412–417. ISSN: 0031899X. DOI: 10.1103/PhysRev.111.412.

[9] M. Dressel. "Electrodynamics of metallic superconductors". In: *Advances in Condensed Matter Physics* 2013 (2013). ISSN: 16878108. DOI: 10.1155/2013/104379.

[10] Thomas Wolfram and Sinasi Ellialtioglu. *Electronic and optical properties of d-band perovskites*. Cambridge University Press, 2006.

[11] S. A. Hayward and E. K.H. Salje. "Cubic-tetragonal phase transition in SrTiO3 revisited: Landau theory and transition mechanism". In: *Phase Transitions* 68.3 (1999), pp. 501–522. ISSN: 01411594. DOI: 10.1080/01411599908224530.

[12] MC Gallardo et al. "Pressure-temperature phase diagram of SrTiO3 up to 53 GPa". In: *Physical Review B - Condensed Matter and Materials Physics* 81.5 (2010). ISSN: 10980121. DOI: 10.1103/PhysRevB.81.054115. arXiv: 0910.0710.

[13] T. T. Fister et al. "Octahedral rotations in strained LaAlO3/SrTiO3 (001) heterostructures". In: *APL Materials* 2.2 (2014). ISSN: 2166532X. DOI: 10.1063/1.4865160.

[14] J. F. Scott. "Soft-mode spectroscopy: Experimental studies of structural phase transitions". In: *Reviews of Modern Physics* 46.1 (1974), pp. 83–128. ISSN: 00346861. DOI: 10.1103/RevModPhys.46.83.

[15] R. C. Neville, B. Hoeneisen, and C. A. Mead. "Permittivity of strontium titanate". In: *Journal of Applied Physics* 43.5 (1972), pp. 2124–2131. ISSN: 00218979. DOI: 10.1063/1.1661463.

[16] K. A. Müller and H. Burkard. "SrTiO3: An intrinsic quantum paraelectric below 4 K". In: *Physical Review B* 19.7 (1979), pp. 3593–3602. ISSN: 01631829. DOI: 10.1103/PhysRevB.19.3593.

[17] H. E. Weaver. "Dielectric properties of single crystals of SrTiO3 at low temperatures". In: *Journal of Physics and Chemistry of Solids* 11.3-4 (1959), pp. 274–277. ISSN: 00223697. DOI: 10.1016/0022-3697(59)90226-4.

[18] M. Itoh et al. "Ferroelectricity induced by oxygen isotope exchange in strontium titanate perovskite". In: *Physical Review Letters* 82.17 (1999), pp. 3540–3543. ISSN: 10797114. DOI: 10.1103/PhysRevLett.82.3540.

[19] J. G. Bednorz and K. A. Müller. "Sr1-xCaxTiO3: An XY quantum ferroelectric with transition to randomness". In: *Properties of Perovskites and Other Oxides* 52.25 (2010), pp. 487–490. DOI: 10.1142/9789814293365_0008.

[20] Hiromoto Uwe and Sakudo Tunetaro. "Stress-induced ferroelectricity and soft phonon modes in SrTi03". In: *Journal of Chemical Information and Modeling* 53.9 (2013), pp. 1689–1699. ISSN: 1098-6596. DOI: 10.1017/CBO9781107415324.004. arXiv: arXiv:1011.1669v3.

[21] J. Hemberger et al. "Electric-field-dependent dielectric constant and nonlinear susceptibility in SrTiO3". In: *Physical Review B* 52.18 (1995), pp. 13159–13162. ISSN: 01631829. DOI: 10.1103/PhysRevB.52.13159.

[22] D. Satoh, K. Okamoto, and T. Katsufuji. "Magnetic impurities and itinerant carriers in doped SrTi O3: Anomalous Hall resistivity". In: *Physical Review B - Condensed Matter and Materials Physics* 77.12 (2008), pp. 2–5. ISSN: 10980121. DOI: 10.1103/PhysRevB.77.121201.

[23] L. F. Mattheiss. "Energy bands for KNiF3, SrTiO3, KMoO3, and KTaO3". In: *Physical Review B* 6.12 (1972), pp. 4718–4740. ISSN: 01631829. DOI: 10.1103/PhysRevB.6.4718.

[24] K. Van Benthem, C. Elsässer, and R. H. French. "Bulk electronic structure of SrTiO3: Experiment and theory". In: *Journal of Applied Physics* 90.12 (2001), pp. 6156–6164. ISSN: 00218979. DOI: 10.1063/1.1415766.

[25] D. Van Der Marel, J. L.M. Van Mechelen, and I. I. Mazin. "Common Fermi-liquid origin of T2 resistivity and superconductivity in n-type SrTiO3". In: *Physical Review B - Condensed Matter and Materials Physics* 84.20 (2011), pp. 1–11. ISSN: 10980121. DOI: 10.1103/PhysRevB.84.205111. arXiv: 1109.3050.

[26] Xiao Lin et al. "Fermi surface of the most dilute superconductor". In: *Physical Review X* 3.2 (2013), pp. 1–8. ISSN: 21603308. DOI: 10.1103/PhysRevX.3.021002. arXiv: 1211.4761.

[27] J. F. Schooley et al. "Dependence of the superconducting transition temperature on carrier concentration in Semiconducting SrTiO3". In: *Physical Review Letters* 14.9 (1965), pp. 305–307. ISSN: 00319007. DOI: 10.1103/PhysRevLett.14.305.

[28] J. F. Schooley, W. R. Hosler, and Marvin L. Cohen. "Superconductivity in Semiconducting SrTi03". In: *Physical Review Letters* 12.17 (1964), pp. 474–475. ISSN: 0031-9007. DOI: 10.1103/PhysRevLett.12.474.

[29] C. S. Koonce et al. “Superconducting Transition Temperatures of Semiconducting SrTiO3”. In: *Physical Review* 163.2 (1967), pp. 380–390. ISSN: 0031899X. DOI: 10.1103/PhysRev.163.380.

[30] W. L. MCMILLAN. “Transition Te1nperature of Strong-Coupled Superconductors”. In: *Physical Review* 167.2 (1968), pp. 326–331. ISSN: 0031899X. DOI: 10.1103/PhysRev.167.326.

[31] J. Appel. “Soft-mode superconductivity in SrTiO3-x”. In: *Physical Review* 180.2 (1969), pp. 508–516. ISSN: 0031899X. DOI: 10.1103/PhysRev.180.508.

[32] Yasutami Takada. *Theory of Superconductivity in Polar Semiconductors and Its Application to N-Type Semiconducting Srtio3*. 1980. DOI: 10.1143/JPSJ.49.1267.

[33] G. Binnig et al. “Two-band superconductivity in Nb-Doped SrTiO3”. In: *Physical Review Letters* 45.16 (1980), pp. 1352–1355. ISSN: 00319007. DOI: 10.1103/PhysRevLett.45.1352.

[34] G. Singh et al. “Competition between electron pairing and phase coherence in superconducting interfaces”. In: *Nature Communications* 9.1 (2018), pp. 1–8. ISSN: 20411723. DOI: 10.1038/s41467-018-02907-8. eprint: 1704.03365.

[35] Markus Thiemann et al. “Single-Gap Superconductivity and Dome of Superfluid Density in Nb-Doped SrTiO3”. In: *Physical Review Letters* 120.23 (2018), p. 237002. ISSN: 10797114. DOI: 10.1103/PhysRevLett.120.237002. eprint: 1703.04716.

[36] Adrian G. Swartz et al. “Polaronic behavior in a weak-coupling superconductor”. In: *Proceedings of the National Academy of Sciences of the United States of America* 115.7 (2018), pp. 1475–1480. ISSN: 10916490. DOI: 10.1073/pnas.1713916115. arXiv: 1608.05621.

[37] A Ohtomo and H Y Hwang. “A high-mobility electron gas at the LaAlO 3 / SrTiO 3 heterointerface”. In: *Nature* 427.January (2004), pp. 423–427.

[38] N. Reyren et al. “Superconducting Interfaces Between Insulating Oxides”. In: *Science* August (2007), pp. 1196–1200. DOI: 10.1126/science.1146006.

[39] A. D. Caviglia et al. “Electric field control of the LaAlO3/SrTiO3 interface ground state”. In: *Nature* 456.7222 (2008), pp. 624–627. ISSN: 14764687. DOI: 10.1038/nature07576. arXiv: 0807.0585.

[40] S. Thiel et al. “Tunable Quasi–Two-Dimensional Electron Gases in Oxide Heterostructures”. In: *Science* 313.September (2006), pp. 1942–1946. DOI: doi.org/10.1126/science.1131091.

[41] Liping Yu and Alex Zunger. “A polarity-induced defect mechanism for conductivity and magnetism at polar-nonpolar oxide interfaces”. In: *Nature Communications* 5 (2014), pp. 1–9. ISSN: 20411723. DOI: 10.1038/ncomms6118. arXiv: 1402.0895.

[42] Naoyuki Nakagawa, Harold Y. Hwang, and David A. Muller. “Why some interfaces cannot be sharp”. In: *Nature Materials* 5.3 (2006), pp. 204–209. ISSN: 14764660. DOI: 10.1038/nmat1569.

[43] Z. Q. Liu et al. “Origin of the Two-Dimensional Electron Gas at LaAlO3=SrTiO3 Interfaces: The Role of Oxygen Vacancies and Electronic Reconstruction”. In: *Physical Review X* 3.2 (2013), pp. 1–9. ISSN: 21603308. DOI: 10.1103/PhysRevX.3.021010. arXiv: 1305.5016.

[44] M. Basletic et al. "Mapping the spatial distribution of charge carriers in LaAlO 3/SrTiO3 heterostructures". In: *Nature Materials* 7.8 (2008), pp. 621–625. ISSN: 14764660. DOI: 10.1038/nmat2223.

[45] Rossitza Pentcheva and Warren E. Pickett. "Avoiding the polarization catastrophe in LaAlO3 overlayers on SrTiO3(001) through polar distortion". In: *Physical Review Letters* 102.10 (2009), pp. 3–6. ISSN: 00319007. DOI: 10.1103/PhysRevLett.102.107602. arXiv: 0812.0550.

[46] Yun Li et al. "Formation of oxygen vacancies and charge carriers induced in the n-type interface of a LaAlO 3 overlayer on SrTiO 3(001)". In: *Physical Review B - Condensed Matter and Materials Physics* 84.24 (2011), pp. 1–6. ISSN: 10980121. DOI: 10.1103/PhysRevB.84.245307.

[47] Jun Zhou et al. "Interplay of electronic reconstructions, surface oxygen vacancies, and lattice distortions in insulator-metal transition of LaAlO3/SrTiO3". In: *Physical Review B - Condensed Matter and Materials Physics* 92.12 (2015), pp. 4–9. ISSN: 1550235X. DOI: 10.1103/PhysRevB.92.125423.

[48] J. Biscaras et al. "Two-dimensional superconducting phase in LaTiO 3/SrTiO 3 heterostructures induced by high-mobility carrier doping". In: *Physical Review Letters* 108.24 (2012), pp. 1–5. ISSN: 00319007. DOI: 10.1103/PhysRevLett.108.247004.

[49] A. Joshua et al. "Gate-tunable polarized phase of two-dimensional electrons at the LaAlO3/SrTiO3 interface". In: *Proceedings of the National Academy of Sciences* 110.24 (2013), pp. 9633–9638. ISSN: 0027-8424. DOI: 10.1073/pnas.1221453110.

[50] Y. Lei et al. "Visible-light-enhanced gating effect at the LaAlO3/SrTiO3 interface". In: *Nature Communications* 5 (2014), pp. 1–7. ISSN: 20411723. DOI: 10.1038/ncomms6554.

[51] G. Herranz et al. "High mobility in LaAlO3/SrTiO3 heterostructures: Origin, dimensionality, and perspectives". In: *Physical Review Letters* 98.21 (2007), pp. 3–6. ISSN: 10797114. DOI: 10.1103/PhysRevLett.98.216803. arXiv: 0704.2523.

[52] A. Brinkman et al. "Magnetic effects at the interface between non-magnetic oxides". In: *Nature Materials* 6.7 (2007), pp. 493–496. ISSN: 14764660. DOI: 10.1038/nmat1931.

[53] Alexey Kalabukhov et al. "Effect of oxygen vacancies in the SrTiO3 substrate on the electrical properties of the LaAlO3 SrTiO3 interface". In: *Physical Review B - Condensed Matter and Materials Physics* 75.12 (2007), pp. 2–5. ISSN: 10980121. DOI: 10.1103/PhysRevB.75.121404.

[54] A. F. Santander-Syro et al. "Two-dimensional electron gas with universal subbands at the surface of SrTiO 3". In: *Nature* 469.7329 (2011), pp. 189–194. ISSN: 14764687. DOI: 10.1038/nature09720.

[55] Tobias Chris Rödel et al. "Universal Fabrication of 2D Electron Systems in Functional Oxides". In: *Advanced Materials* 28.10 (2016), pp. 1976–1980. ISSN: 15214095. DOI: 10.1002/adma.201505021.

[56] Sang Woon Lee et al. "Creation and control of two-dimensional electron gas using Al-based amorphous oxides/SrTiO 3 heterostructures grown by atomic layer deposition". In: *Nano Letters* 12.9 (2012), pp. 4775–4783. ISSN: 15306984. DOI: 10.1021/nl302214x.

[57] Shamashis Sengupta et al. “Gate-tunable superconductivity at SrTiO 3 surface realized by Al layer evaporation”. In: *Journal of Applied Physics* 124.21 (2018), pp. 1–15. ISSN: 10897550. DOI: 10.1063/1.5049363. arXiv: 1810.08069.

[58] Diogo Castro Vaz. “Spin-to-charge current conversion in SrTiO3-based two-dimensional electron gases”. In: (2020). URL: https://tel.archives-ouvertes.fr/tel-03058916.

[59] Sébastien Lemal, Nicholas C. Bristowe, and Philippe Ghosez. “Polarity-field driven conductivity in SrTiO3/LaAlO3: A hybrid functional study”. In: *Physical Review B* 102.11 (2020). ISSN: 24699969. DOI: 10.1103/PhysRevB.102.115309. arXiv: 2005.12771.

[60] Pouya Moetakef et al. “Electrostatic carrier doping of GdTiO 3/SrTiO 3 interfaces”. In: *Applied Physics Letters* 99.23 (2011). ISSN: 00036951. DOI: 10.1063/1.3669402.

[61] Yanwu Xie et al. “Control of electronic conduction at an oxide heterointerface using surface polar adsorbates”. In: *Nature Communications* 2.1 (2011), pp. 1–5. ISSN: 20411723. DOI: 10.1038/ncomms1501.

[62] Zhicheng Zhong, Anna Tóth, and Karsten Held. “Theory of spin-orbit coupling at LaAlO3/SrTiO3 interfaces and SrTiO3 surfaces”. In: *Physical Review B - Condensed Matter and Materials Physics* 87.16 (2013), pp. 1–5. ISSN: 10980121. DOI: 10.1103/PhysRevB.87.161102. arXiv: 1209.4705.

[63] J. Biscaras et al. “Multiple quantum criticality in a two-dimensional superconductor”. In: *Nature Materials* 12.6 (2013), pp. 542–548. ISSN: 14761122. DOI: 10.1038/nmat3624. URL: http://dx.doi.org/10.1038/nmat3624.

[64] Alexis Jouan. “DC and AC transport in field-effect controlled LAAlO3/SrTiO3 interface”. PhD thesis. 2011.

[65] Younghyun Kim, Roman M. Lutchyn, and Chetan Nayak. “Origin and transport signatures of spin-orbit interactions in one- and two-dimensional SrTiO3-based heterostructures”. In: *Physical Review B - Condensed Matter and Materials Physics* 87.24 (2013), pp. 1–11. ISSN: 10980121. DOI: 10.1103/PhysRevB.87.245121.

[66] R. Bistritzer, G. Khalsa, and A. H. MacDonald. “Electronic structure of doped d0 perovskite semiconductors”. In: *Physical Review B - Condensed Matter and Materials Physics* 83.11 (2011), pp. 1–8. ISSN: 10980121. DOI: 10.1103/PhysRevB.83.115114.

[67] A. D. Caviglia et al. “Tunable Rashba Spin-Orbit Interaction at Oxide Interfaces”. In: *Physical Review Letters* 104.12 (2010), pp. 1–4. ISSN: 00319007. DOI: 10.1103/PhysRevLett.104.126803. arXiv: 0912.3731.

[68] N. Reyren et al. “Gate-controlled spin injection at LaAlO 3/SrTiO 3 interfaces”. In: *Physical Review Letters* 108.18 (2012), pp. 1–5. ISSN: 00319007. DOI: 10.1103/PhysRevLett.108.186802.

[69] Yi Wang et al. “Room-Temperature Giant Charge-to-Spin Conversion at the SrTiO3-LaAlO3 Oxide Interface”. In: *Nano Letters* 17.12 (2017), pp. 7659–7664. ISSN: 15306992. DOI: 10.1021/acs.nanolett.7b03714.

[70] G. Herranz et al. “High mobility conduction at (110) and (111) LaAlO 3/SrTiO 3 interfaces”. In: *Scientific Reports* 2.110 (2012), pp. 3–7. ISSN: 20452322. DOI: 10.1038/srep00758.

[71] T. C. Rödel et al. "Orientational Tuning of the Fermi Sea of Confined Electrons at the SrTiO3 (110) and (111) Surfaces". In: *Physical Review Applied* 1.5 (2014), pp. 1–5. ISSN: 23317019. DOI: 10.1103/PhysRevApplied.1.051002.

[72] S. McKeown Walker et al. "Control of a Two-Dimensional Electron Gas on SrTiO3 (111) by Atomic Oxygen". In: *Physical Review Letters* 113.17 (2014), pp. 1–5. ISSN: 10797114. DOI: 10.1103/PhysRevLett.113.177601. arXiv: 1405.3201.

[73] C. Richter et al. "Interface superconductor with gap behaviour like a high-temperature superconductor". In: *Nature* 502.7472 (2013), pp. 528–531. ISSN: 00280836. DOI: 10.1038/nature12494. URL: http://dx.doi.org/10.1038/nature12494.

[74] D. Valentinis et al. "Modulation of the superconducting critical temperature due to quantum confinement at the LaAlO3/SrTiO3 interface". In: *Physical Review B* 96.9 (2017), pp. 1–6. ISSN: 24699969. DOI: 10.1103/PhysRevB.96.094518. arXiv: 1611.07763.

[75] Julie A. Bert et al. "Gate-tuned superfluid density at the superconducting LaAlO 3/SrTiO 3 interface". In: *Physical Review B - Condensed Matter and Materials Physics* 86.6 (2012), pp. 1–5. ISSN: 10980121. DOI: 10.1103/PhysRevB.86.060503.

[76] G Singh et al. "Gap suppression at Lifshitz transition in a multi-condensate superconductor". In: *Nature materials* (2019). DOI: 10.1038/s41563-019-0354-z.

[77] Nicola Manca et al. "Bimodal Phase Diagram of the Superfluid Density in LaAlO3/SrTiO3 Revealed by an Interfacial Waveguide Resonator Supplementary Material". In: (2018), pp. 1–10. DOI: 10.1103/PhysRevLett.122.036801.

[78] S. Caprara et al. "Multiband superconductivity and nanoscale inhomogeneity at oxide interfaces". In: *Physical Review B - Condensed Matter and Materials Physics* 88.2 (2013), pp. 1–5. ISSN: 10980121. DOI: 10.1103/PhysRevB.88.020504. arXiv: 1304.2970.

[79] N. Reyren et al. "Anisotropy of the superconducting transport properties of the LaAlO 3 / SrTiO3 interface". In: *Applied Physics Letters* 94.11 (2009), pp. 1–4. ISSN: 00036951. DOI: 10.1063/1.3100777.

[80] J. Biscaras et al. "Two-dimensional superconductivity at a Mott insulator/band insulator interface LaTiO3/SrTiO3". In: *Nature Communications* 1.7 (2010). ISSN: 20411723. DOI: 10.1038/ncomms1084. arXiv: 1002.3737.

[81] A. M.R.V.L. Monteiro et al. "Two-dimensional superconductivity at the (111) LaAlO3/SrTiO3 interface". In: *Physical Review B* 96.2 (2017), pp. 1–4. ISSN: 24699969. DOI: 10.1103/PhysRevB.96.020504. arXiv: 1703.04742.

[82] Beena Kalisky et al. "Locally enhanced conductivity due to the tetragonal domain structure in LaAlO3/SrTiO3 heterointerfaces". In: *Nature Materials* 12.12 (2013), pp. 1091–1095. ISSN: 14761122. DOI: 10.1038/nmat3753.

[83] Changjiang Liu et al. "Two-dimensional superconductivity and anisotropic transport at KTaO3 (111) interfaces". In: *Science* 371.6530 (2021), pp. 716–721. ISSN: 10959203. DOI: 10.1126/science.aba5511.

[84] P Schnabel. "Four-Point Method for Measuring the Anisotropy of Resistivity". In: *R498 Philips Res. Repts* 19 (1964), pp. 43–52.

[85] L. B. Valdes. "Resistivity Measurements on Germanium for Transistors". In: *Proceedings of the IRE* 42.2 (1954), pp. 420–427. ISSN: 00968390. DOI: 10.1109/JRPROC.1954.274680.

[86] D. Pesquera et al. "Two-dimensional electron gases at LaAlO3/SrTiO3 interfaces: Orbital symmetry and hierarchy engineered by crystal orientation". In: *Physical Review Letters* 113.15 (2014). ISSN: 10797114. DOI: 10.1103/PhysRevLett.113.156802.

[87] Gervasi Herranz et al. "Engineering two-dimensional superconductivity and Rashba spin-orbit coupling in LaAlO3/SrTiO3 quantum wells by selective orbital occupancy". In: *Nature Communications* 6 (2015), pp. 1–8. ISSN: 20411723. DOI: 10.1038/ncomms7028.

[88] Zhiming Wang et al. "Anisotropic two-dimensional electron gas at SrTiO3(110)". In: *Proceedings of the National Academy of Sciences of the United States of America* 111.11 (2014), pp. 3933–3937. ISSN: 10916490. DOI: 10.1073/pnas.1318304111.

[89] Bruce C. Russell and Martin R. Castell. "Reconstructions on the polar SrTi O3 (110) surface: Analysis using STM, LEED, and AES". In: *Physical Review B - Condensed Matter and Materials Physics* 77.24 (2008), pp. 1–9. ISSN: 10980121. DOI: 10.1103/PhysRevB.77.245414.

[90] David Doennig, Warren E. Pickett, and Rossitza Pentcheva. "Massive symmetry breaking in LaAlO3/SrTiO3(111) quantum wells: A three-orbital strongly correlated generalization of graphene". In: *Physical Review Letters* 111.12 (2013), pp. 1–5. ISSN: 00319007. DOI: 10.1103/PhysRevLett.111.126804.

[91] Mathias S. Scheurer, Daniel F. Agterberg, and Jörg Schmalian. "Selection rules for Cooper pairing in two-dimensional interfaces and sheets". In: *npj Quantum Materials* 2.1 (2017), pp. 1–8. ISSN: 23974648. DOI: 10.1038/s41535-016-0008-1. arXiv: 1503.03646.

[92] Di Xiao et al. "Interface engineering of quantum Hall effects in digital transition metal oxide heterostructures". In: *Nature Communications* 2.1 (2011). ISSN: 20411723. DOI: 10.1038/ncomms1602. arXiv: 1106.4296.

[93] S. Davis et al. "Magnetoresistance in the superconducting state at the (111) LaAlO 3/ SrTiO 3 interface". In: *Physical Review B* 96.13 (2017), pp. 1–6. ISSN: 24699969. DOI: 10.1103/PhysRevB.96.134502. arXiv: 1707.03029.

[94] S. Davis et al. "Anisotropic multicarrier transport at the (111) LaAlO3/ SrTiO3 interface". In: *Physical Review B* 95.3 (2017), pp. 1–11. ISSN: 24699969. DOI: 10.1103/PhysRevB.95.035127. arXiv: 1603.04538.

[95] S. Davis et al. "Signatures of electronic nematicity in (111) LaAlO 3/ SrTiO 3 interfaces". In: *Physical Review B* 97.4 (2018), pp. 1–6. ISSN: 24699969. DOI: 10.1103/PhysRevB.97.041408. arXiv: 1708.04809.

[96] S. Davis et al. "Anisotropic superconductivity and frozen electronic states at the (111) LaAlO3/SrTiO3 interface". In: *Physical Review B* 98.2 (2018), pp. 21–23. ISSN: 24699969. DOI: 10.1103/PhysRevB.98.024504.

[97] Udit Khanna et al. "Symmetry and Correlation Effects on Band Structure Explain the Anomalous Transport Properties of (111) LaAlO3/SrTiO3". In: *Physical Review Letters* 123.3 (2019), p. 36805. ISSN: 10797114. DOI: 10.1103/PhysRevLett.123.036805. eprint: 1901.10931.

[98] Nazim Boudjada, Gideon Wachtel, and Arun Paramekanti. "Magnetic and Nematic Orders of the Two-Dimensional Electron Gas at Oxide (111) Surfaces and Interfaces". In: *Physical Review Letters* 120.8 (2018), p. 86802. ISSN: 10797114. DOI: 10.1103/PhysRevLett.120.086802.

[99] J. Biscaras et al. "Limit of the electrostatic doping in two-dimensional electron gases of LaXO3(X = Al, Ti)/SrTiO3". In: *Scientific Reports* 4 (2014), pp. 1–7. ISSN: 20452322. DOI: 10.1038/srep06788.

[100] Yin Long Han et al. "Two-dimensional superconductivity at (110) LaAlO3/SrTiO3 interfaces". In: *Applied Physics Letters* 105.19 (2014), pp. 3–8. ISSN: 00036951. DOI: 10.1063/1.4901940. URL: http://dx.doi.org/10.1063/1.4901940.

[101] A. Annadi et al. "Anisotropic two-dimensional electron gas at the LaAlO3 /SrTiO3 (110) interface". In: *Nature Communications* 4.May (2013), pp. 1–7. ISSN: 20411723. DOI: 10.1038/ncomms2804.

[102] Ashcroft Mermin. *Solid State Physics*. Brooks/Cole, 1976.

[103] N. R. Werthamer, E. Helfand, and P. C. Hohenberg. "Temperature and purity dependence of the superconducting critical field, Hc2. III. Electron spin and spin-orbit effects". In: *Physical Review* 147.1 (1966), pp. 295–302. ISSN: 0031899X. DOI: 10.1103/PhysRev.147.295.

[104] J. M. Edge and A. V. Balatsky. "Upper critical field as a probe for multiband superconductivity in bulk and interfacial STO". In: *Journal of Superconductivity and Novel Magnetism* 28.8 (2015), pp. 2373–2384. ISSN: 15571947. DOI: 10.1007/s10948-015-3052-3. arXiv: 1401.5318.

[105] A. Gurevich. "Limits of the upper critical field in dirty two-gap superconductors". In: *Physica C: Superconductivity and its Applications* 456.1-2 (2007), pp. 160–169. ISSN: 09214534. DOI: 10.1016/j.physc.2007.01.008.

[106] J. Bardeen, L. N. Cooper, and J. R. Schrieffer. "Theory of Superconductivity". In: *Physical Review* 108.5 (1957). DOI: doi.org/10.1103/PhysRev.108.1175.

[107] L. P. Gor'Kov. "Microscopic derivation of the Ginzburg-Landau equations in the theory of superconductivity". In: *J. Exptl. Theoret. Phys. (U.S.S.R.)* 36.6 (1959), pp. 1364–1367. URL: http://www.jetp.ac.ru/cgi-bin/dn/e_009_06_1364.pdf.

[108] Gert Eilenberger. "Transformation of Gorkov's equation for type II superconductors into transport-like equations". In: *Zeitschrift für Physik* 214.2 (1968), pp. 195–213. ISSN: 14346001. DOI: 10.1007/BF01379803.

[109] Klaus D Usadel. "Generalized diffusion equation for superconducting alloys." In: *Physical Review Letters* 6 (1970), pp. 7–9. DOI: 10.1103/PhysRevLett.25.507.

[110] A. Gurevich. "Enhancement of the upper critical field by nonmagnetic impurities in dirty two-gap superconductors". In: *Physical Review B - Condensed Matter and Materials Physics* 67.18 (2003), pp. 1–13. ISSN: 1550235X. DOI: 10.1103/PhysRevB.67.184515. arXiv: 0212129 [cond-mat].

[111] R. M. Fernandes et al. "Two-band superconductivity in doped SrTiO3 films and interfaces". In: *Physical Review B - Condensed Matter and Materials Physics* 87.1 (2013), pp. 1–6. ISSN: 10980121. DOI: 10.1103/PhysRevB.87.014510. arXiv: 1208.3134.

[112] Meservey and Tedrow. “Measurements of the Kinetic Inductance of Superconducting Linear Structures”. In: *Journal of Applied Physics* 40.5 (1969), pp. 2028–2034. DOI: 10.1063/1.1657905.

[113] V. G. Kogan, C. Martin, and R. Prozorov. “Superfluid density and specific heat within a self-consistent scheme for a two-band superconductor”. In: *Physical Review B - Condensed Matter and Materials Physics* 80.1 (2009), pp. 1–8. ISSN: 10980121. DOI: 10.1103/PhysRevB.80.014507.

[114] Yunkyu Bang and G. R. Stewart. “Superconducting properties of the s +−wave state: Fe-based superconductors”. In: *Journal of Physics Condensed Matter* 29.12 (2017). ISSN: 1361648X. DOI: 10.1088/1361-648X/aa564b. eprint: 1701.00320.

[115] A. Golubov and I. Mazin. “Effect of magnetic and nonmagnetic impurities on highly anisotropic superconductivity”. In: *Physical Review B - Condensed Matter and Materials Physics* 55.22 (1997), pp. 15146–15152. ISSN: 1550235X. DOI: 10.1103/PhysRevB.55.15146.

[116] Thaís V. Trevisan, Michael Schütt, and Rafael M. Fernandes. “Unconventional Multiband Superconductivity in Bulk SrTiO3 and LaAlO3/SrTiO3 Interfaces”. In: *Physical Review Letters* 121.12 (2018), pp. 1–5. ISSN: 10797114. DOI: 10.1103/PhysRevLett.121.127002. eprint: 1803.02389.

[117] Furkan Öztürk. “BCS to BEC Evolution”. In: *Harvard University website* (2019).

[118] D. Bucheli et al. “Metal-superconductor transition in low-dimensional superconducting clusters embedded in two-dimensional electron systems”. In: *New Journal of Physics* 15 (2013). ISSN: 13672630. DOI: 10.1088/1367-2630/15/2/023014.

[119] Xiaoyong Wei et al. “Abnormal C-V curve and clockwise hysteresis loop in ferroelectric barium stannate titanate ceramics”. In: *Materials Science and Engineering B: Solid-State Materials for Advanced Technology* 120.1-3 (2005), pp. 64–67. ISSN: 09215107. DOI: 10.1016/j.mseb.2005.02.002.

[120] M. Ben Shalom et al. “Tuning Spin-Orbit Coupling and Superconductivity at the SrTiO3/LaAlO3 Interface: A Magnetotransport Study”. In: *Physical Review Letters* 104.12 (2010), pp. 1–4. ISSN: 00319007. DOI: 10.1103/PhysRevLett.104.126802.

[121] M. Ben Shalom et al. “Shubnikov-de Haas oscillations in SrTiO3/LaAlO3 interface”. In: *Physical Review Letters* 105.20 (2010), pp. 1–4. ISSN: 00319007. DOI: 10.1103/PhysRevLett.105.206401. eprint: 1008.4975.

[122] B. S. Chandrasekhar. “A note on the maximum critical field of high-field superconductors”. In: *Applied Physics Letters* 1.1 (1962), pp. 7–8. ISSN: 00036951. DOI: 10.1063/1.1777362.

[123] M. Kim et al. “Intrinsic spin-orbit coupling in superconducting δ-doped SrTiO 3 heterostructures”. In: *Physical Review B - Condensed Matter and Materials Physics* 86.8 (2012), pp. 1–6. ISSN: 10980121. DOI: 10.1103/PhysRevB.86.085121. eprint: 1106.5193.

[124] W Thomson. “On the electro-dynamic qualities of metals: Effects of magnetization on the electric conductivity of nickel and of iron”. In: *Proceedings of the Royal Society of London* 8 (1857), pp. 546–550. ISSN: 0370-1662. DOI: 10.1098/rspl.1856.0144.

[125] M. N. Baibich et al. “Giant magnetoresistance of (001)Fe/(001)Cr magnetic superlattices”. In: *Physical Review Letters* 61.21 (1988), pp. 2472–2475. ISSN: 00319007. DOI: 10.1103/PhysRevLett.61.2472.

[126] G. Binasch et al. “Enhanced magnetoresistance in layered magnetic structures with antiferromagnetic interlayer exchange”. In: *Physical Review B* 39.7 (1989), pp. 4828–4830. ISSN: 01631829. DOI: 10.1103/PhysRevB.39.4828.

[127] Nitesh Kumar et al. “Extremely high magnetoresistance and conductivity in the type-II Weyl semimetals WP2 and MoP2”. In: *Nature Communications* 8.1 (2017), pp. 1–8. ISSN: 20411723. DOI: 10.1038/s41467-017-01758-z.

[128] M. Diez et al. “Giant Negative Magnetoresistance Driven by Spin-Orbit Coupling at the LaAlO3 /SrTiO3 Interface”. In: *Physical Review Letters* 115.1 (2015), pp. 1–5. ISSN: 10797114. DOI: 10.1103/PhysRevLett.115.016803. eprint: 1412.5614.

[129] Kulothungasagaran Narayanapillai et al. “Interfacial Rashba magnetoresistance of the two-dimensional electron gas at the LaAlO3 / SrTiO3 interface”. In: *Physical Review B* 96.6 (2017), pp. 1–6. ISSN: 24699969. DOI: 10.1103/PhysRevB.96.064401.

[130] M. Ben Shalom et al. “Anisotropic magnetotransport at the SrTiO3/LaAlO3 interface”. In: *Physical Review B - Condensed Matter and Materials Physics* 80.14 (2009), pp. 3–6. ISSN: 10980121. DOI: 10.1103/PhysRevB.80.140403.

[131] A. Fête et al. “Rashba induced magnetoconductance oscillations in the LaAlO 3-SrTiO3 heterostructure”. In: *Physical Review B - Condensed Matter and Materials Physics* 86.20 (2012), pp. 1–4. ISSN: 10980121. DOI: 10.1103/PhysRevB.86.201105.

[132] D. C. Vaz et al. “Determining the Rashba parameter from the bilinear magnetoresistance response in a two-dimensional electron gas”. In: *Physical Review Materials* 4.7 (2020), pp. 1–7. ISSN: 24759953. DOI: 10.1103/PhysRevMaterials.4.071001. eprint: 2007.03354.

[133] P. K. Rout et al. “Six-fold crystalline anisotropic magnetoresistance in the (111) LaAlO3/SrTiO3 oxide interface”. In: *Physical Review B* 95.24 (2017), pp. 1–5. ISSN: 24699969. DOI: 10.1103/PhysRevB.95.241107.

[134] Pan He et al. “Bilinear magnetoelectric resistance as a probe of three-dimensional spin texture in topological surface states”. In: *Nature Physics* 14.5 (2018), pp. 495–499. ISSN: 17452481. DOI: 10.1038/s41567-017-0039-y.

[135] J. C. Rojas-Sánchez et al. “Spin to Charge Conversion at Room Temperature by Spin Pumping into a New Type of Topological Insulator: α -Sn Films”. In: *Physical Review Letters* 116.9 (2016), pp. 1–6. ISSN: 10797114. DOI: 10.1103/PhysRevLett.116.096602.

[136] A. Dyrdał, J. Barnaś, and A. Fert. “Spin-Momentum-Locking Inhomogeneities as a Source of Bilinear Magnetoresistance in Topological Insulators”. In: *Physical Review Letters* 124.4 (2020), pp. 1–6. ISSN: 10797114. DOI: 10.1103/PhysRevLett.124.046802.

[137] Sheng Chun Shen et al. “In-plane anisotropy in two-dimensional electron gas at LaAlO3/SrTiO3(110) interface”. In: *Chinese Physics B* 25.7 (2016). ISSN: 16741056. DOI: 10.1088/1674-1056/25/7/076802.

[138] Jine Zhang et al. “Anisotropic bilinear magnetoresistance in (110) SrTiO 3 -based two-dimensional electron gas”. In: *Physical Review B* 104.045114 (2021), pp. 1–8. DOI: 10.1103/PhysRevB.104.045114.

[139] Nazim Boudjada, Ilia Khait, and Arun Paramekanti. "Anisotropic magnetoresistance in multiband systems: Two-dimensional electron gases and polar metals at oxide interfaces". In: *Physical Review B* 99.19 (2019), pp. 1–12. ISSN: 24699969. DOI: 10.1103/PhysRevB.99.195453.

[140] Julien Delahaye and Thierry Grenet. "Metallicity of the SrTiO3 surface induced by room temperature evaporation of alumina". In: *Journal of Physics D: Applied Physics* 45 (2012), p. 315301. DOI: 10.1088/0022-3727/45/31/315301.

[141] J. R. Thompson, L. A. Boatner, and J. O. Thomson. "Very low-temperature search for superconductivity in semiconducting KTaO3". In: *Journal of Low Temperature Physics* 47.5-6 (1982), pp. 467–475. ISSN: 00222291. DOI: 10.1007/BF00683987.

[142] K. Ueno et al. "Discovery of superconductivity in KTaO 3 by electrostatic carrier doping". In: *Nature Nanotechnology* 6.7 (2011), pp. 408–412. ISSN: 17483395. DOI: 10.1038/nnano.2011.78.

[143] K. Zou et al. "LaTiO3/KTaO3 interfaces: A new two-dimensional electron gas system". In: *APL Materials* 3.3 (2015). ISSN: 2166532X. DOI: 10.1063/1.4914310.

[144] Hui Zhang et al. "Highly Mobile Two-Dimensional Electron Gases with a Strong Gating Effect at the Amorphous LaAlO3/KTaO3 Interface". In: *ACS Applied Materials and Interfaces* 9.41 (2017), pp. 36456–36461. ISSN: 19448252. DOI: 10.1021/acsami.7b12814.

[145] Zheng Chen et al. "Two-Dimensional Superconductivity at the LaAlO3/KTaO3 (110) Heterointerface". In: *Physical Review Letters* 126.2 (2021), pp. 1–6. ISSN: 10797114. DOI: 10.1103/PhysRevLett.126.026802.

[146] Zheng Chen et al. "Electric field control of superconductivity at the LaAlO3/KTaO3(111) interface". In: *Science* 372.6543 (2021), pp. 721–724. ISSN: 10959203. DOI: 10.1126/science.abb3848.

[147] Flavio Y. Bruno et al. "Band Structure and Spin–Orbital Texture of the (111)-KTaO 3 2D Electron Gas". In: *Advanced Electronic Materials* 5.5 (2019), pp. 1–7. ISSN: 2199160X. DOI: 10.1002/aelm.201800860.

[148] V. Ambegaokar et al. "Dynamics of superfluid films". In: *Physical Review B* 21.5 (2019), pp. 9–25. DOI: 10.1103/PhysRevB.21.1806.

[149] L. Benfatto, C. Castellani, and T. Giamarchi. "Broadening of the Berezinskii-Kosterlitz-Thouless superconducting transition by inhomogeneity and finite-size effects". In: *Physical Review B - Condensed Matter and Materials Physics* 80.21 (2009), pp. 1–11. ISSN: 10980121. DOI: 10.1103/PhysRevB.80.214506. arXiv: 0909.0479.

[150] Rini Ganguly et al. "Slowing down of vortex motion at the Berezinskii-Kosterlitz-Thouless transition in ultrathin NbN films". In: *Physical Review B - Condensed Matter and Materials Physics* 91.5 (2015), pp. 1–9. ISSN: 1550235X. DOI: 10.1103/PhysRevB.91.054514.

[151] D. McQueeney, G. Agnolet, and J. D. Reppy. "Surface Superfluidity in Dilute 4He-3He Mixtures". In: *Physical Review Letters* 52.15 (1984), pp. 1325–1328. DOI: doi.org/10.1103/PhysRevLett.52.1325.

[152] Jie Yong et al. “Robustness of the Berezinskii-Kosterlitz-Thouless transition in ultrathin NbN films near the superconductor-insulator transition”. In: *Physical Review B - Condensed Matter and Materials Physics* 87.18 (2013), pp. 1–8. ISSN: 10980121. DOI: 10.1103/PhysRevB.87.184505.

[153] Luis M. Vicente-Arche et al. “Spin–Charge Interconversion in KTaO3 2D Electron Gases”. In: *Advanced Materials* 33.43 (2021). ISSN: 15214095. DOI: 10.1002/adma.202102102.

[154] L. Dumoulin M. Aprili C. A. Marrache-Kikuchi F. Couëdo1 L. Bergé and J. Gabelli. “Metallicity of the SrTiO3 surface induced by room temperature evaporation of alumina”. In: *AIP Advances* 9 (2019), p. 075005. DOI: 10.1063/1.5097897.

[155] François Couedo. “Transitions de phase quantiques dans les systèmes désordonnés de basse dimension”. PhD thesis. 2014.

RÉSUMÉ

Ce manuscrit présente les propriétés de transport modifiable par application d'une tension de grille des gaz d'électrons bidimensionnels (2DEG) supraconducteurs à l'interface de SrTiO3 avec d'autres oxydes. Premièrement, nous rapportons les propriétés de transport statiques telles que les champs critiques et la densité de porteurs dans les orientations non conventionnelles du substrat que sont les systèmes LaAlO3/SrTiO3(110) et LaAlO3/SrTiO3(111). Nous complétons ces résultats par des mesures micro-ondes de la rigidité superfluide, que nous analysons dans le cadre théorique de la théorie BCS/Mattis-Bardeen. En particulier, nous montrons que l'orientation du substrat modifie la structure de bande interfaciale et peut conduire à une supraconductivité multibande dans certains cas. Dans une deuxième partie, nous analysons la magnétorésistance anisotrope dans le plan de ces 2DEG comme une sonde pour l'interaction spin-orbite et comme un moyen d'évaluer qualitativement la surface de Fermi. Dans la dernière partie, nous discutons des propriétés de nouvelles interfaces telles que les 2DEG supraconducteurs récemment découverts aux interfaces d'oxydes avec KTaO3(111). Nous fournissons une mesure des propriétés de transport et de la rigidité superfluide, qui est étudiée à la lumière de la théorie Berezinskii-Kosterlitz-Thouless.

MOTS CLÉS

Superconductivité, oxyde, micro-ondes, 2DEG.

ABSTRACT

This manuscript presents the gate tunable transport properties of superconducting two-dimensional electron gases (2DEG) in SrTiO3-based oxide interfaces. In the first part, we report on the dc transport properties of the LAO/STO(110) and LAO/STO(111) including the superconducting Tc, the carrier density, and the critical magnetic field. We complement these results by microwave measurements of the superfluid stiffness, which we analyze within the theoretical framework of the BCS/Mattis-Bardeen theory. In particular, we show that the substrate orientation modifies the interfacial band structure and can lead to multiband superconductivity in some cases. In the second part, we analyse the in-plane anisotropic magnetoresistance of these 2DEGs as a probe for the Rashba spin-orbit interaction and as a way to qualitatively assess the Fermi surface. Finally, in the last part, we discuss the properties of novel interfaces such as the recently discovered superconducting 2DEG KTaO3(111) based oxide interfaces. We provide transport and superfluid stiffness measurements, which are discussed in light of the Berezinskii-Kosterlitz-Thouless theory.

KEYWORDS

Superconductivity, oxide, microwave, 2DEG.